

Report No. CG-D-55-79

LEVEL

12

AD A 077073

EXPERIMENTS INVOLVING POOL AND VAPOR FIRES FROM
SPILLS OF LIQUEFIED NATURAL GAS ON WATER



DDC
RECEIVED
NOV 16 1979
REGISTERED
E

FINAL REPORT

Document is available to the public through the
National Technical Information Service,
Springfield, Virginia 22161

MARCH 1979

DDC FILE COPY

Prepared for

U.S. DEPARTMENT OF TRANSPORTATION
United States Coast Guard
Office of Research and Development
Washington, D.C. 20550

79 11 19 026

NOTICE

This document is disseminated under the sponsorship of the Department of Transportation in the interest of information exchange. The United States Government assumes no liability for its contents or use thereof.

The contents of this report do not necessarily reflect the official view or policy of the Coast Guard; and they do not constitute a standard, specification, or regulation.

This report, or portion thereof may not be used for advertising or sales promotion purposes. Citation of trade names and manufacturers does not constitute endorsement or approval of such products.

15 [N7A12-78-C-1718
N60534-78-C-1142]

Technical Report Documentation Page

18 715 CG D-55-79	2 Government Accession No.	3 Recipient's Catalog No.
6 Experiments involving pool and vapor fires from spills of liquefied natural gas on water.	4 Title and Subtitle	7 Report Date
10 Phani P.K. Raj, Albert N. Moussa and Krishna Aravamudan	5 Author(s)	8 Performing Organization Code
Arthur D. Little, Inc. Acorn Park Cambridge, Massachusetts 02140	9 Performing Organization Report No.	10 PA Unit No. (TRAIS)
12 Sponsoring Agency Name and Address U. S. Navy at the Naval Weapons Center Explosives Technology (Code 3262) China Lake, California 93555	11 Sponsoring Agency Code	13 Type of Report and Period Covered
13 Supplementary Notes The U.S. Coast Guard Office of Research and Development's technical representative for the work performed herein was Dr. M. C. PARNAROUSKIS	14 Sponsoring Agency Code	15 Final Report
16 Abstract (12) 258 A series of 16 tests have been conducted at the Naval Weapons Center involving the spill and ignition of liquefied natural gas (LNG) on water. Two kinds of fires have been studied; namely, pool fires and vapor cloud fires. The principal objective of the tests was to measure the thermal characteristics. The quantities of spilled LNG varied between 3 and 5.5 m ³ with spill durations from 30 to 250 s. Thermal radiation from the fires was measured using wide-angle and narrow-angle radiometers and a spectrometer. The data from the tests have been analyzed for pool spread, liquid regression rate, flame heights, thermal radiative output and LNG fire spectra. Models useful for evaluating LNG fire hazards are indicated. Mean flame emissive power measured is about 210 kW/m ² and estimated flame temperature is 1500 K. CO ₂ , H ₂ O, and soot appear to be the principal radiating species. Vapor cloud burning was close to the ground with a propagating plume fire. The velocity of propagation was a function of the wind speed. A peculiar fire halting behavior noticed is discussed.	17 Key Words Pool fire, vapor fire, thermal radiation, fire spectrum, flame height, emissive power	18 Distribution Statement Document is available to the public through the National Technical Information Service, Springfield, Virginia 22161.
19 Security Classif. (of this report) Unclassified	20 Security Classif. (of this page) Unclassified	21 No. of Pages 257
22 Price		

Form DOT F 1700.7 6-77

Reproduction of completed page authorized

208850

51u

ACKNOWLEDGEMENT

This study was performed by Arthur D. Little, Inc. for the U. S. Navy at the Naval Weapons Center, China Lake, California under Contract No. N60530-78-C-0192.

Dr. C. Douglas Lind was the technical monitor representing the U. S. Navy. His very helpful support and constructive advice are gratefully acknowledged. The project team at Arthur D. Little, Inc. was headed by Dr. P. K. Raj and included Drs. A. Moussa, K. Aravamudan, Messrs. P. Von Thuna, I. A. Sheikh and P. J. Marchessault. Dr. E. M. Drake provided significant support in the technical review and critique of the report.

The careful review and the valuable comments made on the draft report by Lt. Michael Flessner, Lt. Guy Collona, Drs. Michael Parnarouskis and Allan Schneider of the U. S. Coast Guard, Dr. John Ceece of the Department of Energy, Mr. Sami Atallah of the Gas Research Institute, and Dr. Douglas Lind of the U. S. Navy are gratefully acknowledged. The encouragement and support provided by LCDR. Michael W. Taylor of the U. S. Coast Guard during the initial phase of this project is thankfully acknowledged.

Accession Number
NTI
Date
Title
Author
Subject
Notes
Classification
Indexing
Remarks

TABLE OF CONTENTS

	<u>Page</u>
EXECUTIVE SUMMARY	0- 1
1. INTRODUCTION	1- 1
1.1 Background	1- 1
1.2 Objectives of the Experiments	1- 4
1.3 Scope of the Test Program	1- 4
2. SURVEY OF LITERATURE CONCERNING THERMAL RADIATION FROM LNG AND OTHER TURBULENT DIFFUSION FLAMES	2- 1
2.1 Behavior of LNG on Water	2- 1
2.2 Past LNG Fire Experiments	2- 2
2.2.1 Experiments Before 1972	2- 2
2.2.2 American Gas Association Tests	2- 3
2.2.3 Recent Tests and On-Going Tests	2- 5
2.3 Modeling Fire Radiation	2- 5
2.4 Scaling Laws	2- 9
2.4.1 Size Scaling	2- 9
2.4.2 Radiation Scaling	2-11
2.5 Unconfined Vapor Fires	2-12
3. TEST SITE AND EXPERIMENTAL PROCEDURE	3- 1
3.1 Description of Test Site and Spill Equipment	3- 1
3.2 Instrumentation	3- 5
3.3 Experimental Procedure	3- 9
4. LNG FLAME RADIATION SPECTRUM	4- 1
4.1 Introduction	4- 1
4.2 Experimental Spectral Data	4- 1
4.3 Instrument and Calibration	4- 4
4.3.1 Description of the Instrument	4- 4
4.3.2 Calibration Procedure and Scale Factor	4- 4
4.4 Atmospheric Absorption	4- 7
4.5 Analysis of Spectral Data	4-13
4.5.1 Analysis of a Specific Spectral Scan	4-16
4.5.2 Changes in Spectral Data with Burn Time	4-20
4.5.3 Estimation of Soot Temperature and Emissivity	4-22
4.5.4 Estimation of Flame Emissive Power	4-27
4.5.5 Comparison with Other LNG Flame Spectra	4-33
4.6 Discussion	4-37
4.7 Conclusions	4-41

TABLE OF CONTENTS (continued)

	<u>Page</u>
5. ANALYSIS OF LNG POOL FIRES	5- 1
5.1 Introduction	5- 1
5.2 Analysis of Pool Spread	5- 2
5.3 Analysis of Pool Fire Data	5-16
5.3.1 Qualitative Observations on Pool Fire Behavior	5-16
5.3.2 Quantitative Data from Pool Fire Experiments	5-19
5.3.3 Correlation of the Visible Flame Length Data	5-21
5.3.4 Flame Tilt by Wind	5-27
5.4 Thermal Radiation Data and Their Analysis	5-29
5.4.1 Limitations of the Measured Radiometer Data	5-32
5.4.2 Analysis of Narrow-Angle Radiometer Data	5-34
5.4.3 Wide-Angle Radiometer Data	5-39
5.4.4 Analysis of Wood Charring Data	5-49
5.5 Discussion of Results	5-53
5.6 Conclusions	5-60
6. ANALYSIS OF LNG VAPOR FIRES	6- 1
6.1 Introduction	6- 1
6.2 Test Conditions	6- 3
6.3 Listing of Data Collected	6- 7
6.4 Spill, Cloud Formation, and Ignition	6- 7
6.5 Vapor Fire Development	6- 7
6.5.1 Stage 1: Transient Flame Growth	6-15
6.5.2 Stage 2: Stationary Flame Near Pond Edge	6-19
6.5.3 Stage 3: Transient Burn-out	6-22
6.5.4 Flame Length/Width Ratio	6-22
6.6 Radiation Analysis	6-24
6.6.1 Data Collection and Evaluation	6-24
6.6.2 View Factor Calculations	6-27
6.6.3 Flame Emissive Power	6-29
6.7 Hydrocarbon Gas Analysis	6-32
6.8 Main Results and Conclusions	6-34
7. COMPARISON OF RESULTS AND RECOMMENDATIONS	7- 1
7.1 Comparison of Flame Emissive Power Results from Pool Fires and Vapor Fires	7- 1
7.2 Suggested Model for Use in Assessing Thermal Radiation Hazards from LNG Pool Fires on Water	7- 6
7.2.1 Illustrative Example	7- 8
7.3 Suggested Model for Assessing Thermal Radiation Hazards from Unconfined Vapor Cloud Fires	7-10
7.3.1 Illustrative Example	7-11
7.4 Recommendations	7-12

TABLE OF CONTENTS (concluded)

	<u>Page</u>
Nomenclature	N- 1
References	R- 1
APPENDIX A	A- 1
APPENDIX B	B- 1
APPENDIX C	C- 1
APPENDIX D	D- 1

LIST OF FIGURES

	<u>Page</u>
3.1 Schematic Diagram of the Test Site	3- 3
4.1 NWC Spectrum Scan #47, at 15 sec. after Ignition	4- 2
4.2 NWC Spectrum Scan #92, at 40 sec. after Ignition	
4.3 Schematic Diagram illustrating the Principle of Michelson Interferometer	4- 5
4.4 Theoretical and Measured Spectrum of a Black Body at 1116 K During Calibration	4- 6
4.5 Field of View of Spectrometer at 236 m and the Relative Location of the Flame in the View	4- 8
4.6 Variation of Precipitable Water Content of Atmosphere with Temperature, Humidity and Path Length	4-11
4.7 LNG Pool Fire Radiation Spectrum Taken at 20 Seconds after Ignition and Calculated Atmospheric Transmissivity at Different Wave Lengths for a 200 m Path Length	4-15
4.8 Percent of Total Black Body Energy Below a Given Wave Length vs. the Wave Length	4-21
4.9 Ratio of CO ₂ to Soot Emission vs. Burn Time	4-23
4.10 Comparison of Soot Emission with Black Body Spectra at Different Temperatures	4-26
4.11 Comparison of AGA Test Spectra with NWC Test Spectrum	4-34
5.1 Location of Various Instruments for LNG Pool Fire Tests #1 through 6	5- 4
5.2 Location of Various Instruments for LNG Pool Fire Tests #12, 13, and 14	5- 5
5.3 Observed Pool Dimensions for LNG Test #5	5- 7
5.4 Observed Pool Dimensions for LNG Test #12	5- 9
5.5 The Variation of Maximum Pool Diameter with Spill Rate	5-12
5.6 The Variation of Burning Rate with Spill Rate	5-13
5.7 The Measured Cloud Length as a Function of Time for Delayed Ignition Pool Fires	5-15
5.8a Schematic View of the Starting Thermal Stage of Fire Plume Development	5-18
5.8b Instantaneous Flame Shape for a Fully Developed Fire	5-18
5.9 Instantaneous Height of the Visible Flame as a Function of Time for LNG Test #12	5-20
5.10 Instantaneous Length of the Visible Flame as a Function of Time for LNG Test #3	5-22
5.11 Instantaneous Length of the Visible Flame as a Function of Time for LNG Test #4	5-23
5.12 Instantaneous Length of the Visible Flame as a Function of Time for LNG Test #5	5-24
5.13 Measured Flame Lengths and Their Variation with the Estimated Burning Rates	5-26
5.14 Nondimensional Flame Length vs Dimensionless Burning Rate	5-28
5.15 Flame Tilt Angle as a Function of Dimensionless Wind Velocity	5-30

LIST OF FIGURES (continued)

	<u>Page</u>
5.16 Narrow-Angle Radiometer Data for Pool Fire Test #12	5-35
5.17 Narrow-Angle Radiometer Data for Pool Fire Test #5	5-36
5.18 Narrow-Angle Radiometer Data for Delayed Ignition Pool Fire Test #13	5-37
5.19 Narrow-Angle Radiometer Data for Delayed Ignition Pool Fire Test #14	5-38
5.20 The Variation of Measured Thermal Flux with Time after Spill for Various LNG Pool Fires	5-40
5.21 Transmissivity of Atmosphere for Thermal Radiation from LNG Flames	5-41
5.22 The Emissive Power for Various LNG Pool Fires Determined Using Narrow-Angle Radiometer Data	5-42
5.23 Wide-Angle Radiometer Data for Pool Fire Test #12	5-44
5.24 Variation of the Measured Thermal Flux with Distance from the Surface of the Fire for Pool Fire Test #12	5-45
5.25 Emissive Power Calculated Using Wide-Angle Radiometer Data for Test #12	5-48
5.26 Variation of Fractional Combustion Energy Radiated with Spill Rate	5-58
6.1 Plot Plan Showing Instrumentation and Wind Direction for Tests No. 8, 9, 10, and 11.	6- 5
6.2 Plot Plan Showing Instrumentation and Wind Direction for Tests No. 16 and 17.	6- 6
6.3 Vapor Fire Development in Test #9	6-10
6.4 Vapor Fire Development in Test #10	6-11
6.5 Vapor Fire Development in Test #16	6-12
6.6 Vapor Fire Development in Test #17	6-13
6.7 Schematic of Main Stages of Vapor Fire	6-14
6.8 Turbulent Flame Speed Relative to Gas in Vapor Cloud vs. Mean Wind Speed	6-18
6.9 Fire Behavior at Pond Edge	6-20
6.10 Dimensions of the Burning Zone	6-23
6.11 Typical Radiometer Output	6-26
A-2 Schematic Representation of a Spectrometer	A- 2

LIST OF TABLES

	<u>Page</u>
3.1 List of Measuring Instruments Used in the Tests	3- 6
4.1 Constituent Gases in the Atmosphere and Their Concentrations	4- 9
4.2a Total Absorption Band Width for 1.87 μ m and 2.7 μ m Water Bands at 300 K	4-12
4.2b Total Absorption Band Width for 4.3 μ m CO ₂ Band at 300 K	4-12
4.3 Variation of Transmissivity of Atmosphere with Wave Length for the Conditions of the Experiment	4-14
4.4 Estimation of Soot Temperature and Soot Emissivity	4-25
4.5 Variation of Estimated Soot Emissivity with Time for Different Assumed Flame Temperatures	4-28
4.6 True Flame Emissive Power Estimated from 4.3 μ m CO ₂ Band Spectral Data (Scan #56, 20 s into the Burn)	4-32
5.1 Description of Conditions of LNG Pool Fire Tests	5- 3
5.2 Geometric Characteristics of Pool	5-10
5.3 Measured Visible Flame Lengths for Pool Fires	5-25
5.4 Location and Orientation of Radiometers	5-31
5.5 The Available Radiometer Data for Pool Fires	5-33
5.6 Wood Charring Data for Test #12	5-50
5.7 Sensitivity Analysis on LNG Pool Fire Test #12 Data	5-54
5.8 Fraction of Combustion Energy Radiated by Pool Fires	5-59
6.1 Test Conditions of Vapor Fire	6- 4
6.2 Raw Data for Vapor Fires	6- 8
6.3 Characteristics of Main Stages of Vapor Fire Development	6-16
6.4 Radiometer Arrangements for Vapor Fires	6-25
6.5 Flame Dimensions for View Factor Calculations	6-28
6.6 Emissive Power Calculations for Vapor Fires	6-30
6.7 Emissive Power Based on only Narrow-Angle Radiometer Data	6-33
7.1 Flame Emissive Power Measurements from LNG Fire Tests	7- 2
7.2 Recommended Values for Various Physical Parameters for use in Models	7- 7

LIST OF PLATES

3.1 A View of the Test Site	3- 2
5.1 Photographs of the Pieces of Wooden Stakes After Exposure to Pool Fire	5-51

EXECUTIVE SUMMARY

INTRODUCTION

The United States Coast Guard has statutory responsibility for regulating the marine transportation of hazardous chemicals, including liquefied natural gas (LNG). LNG is transported by ship as a very cold liquid (110 K) at just slightly above atmospheric pressure. If it is spilled from its well-insulated container, it will boil rapidly and produce natural gas vapors which are composed primarily of methane. Some ethane, propane, and other compounds may also be found in LNG. The vapors are flammable between 5% and 15% volume concentrations when mixed with air. With the current start-up of two new LNG import terminals and pending plans for additional import projects, there is an increasing need for regulatory and accident-response personnel to understand the hazardous consequences that might be associated with marine spill accidents.

In the past, experimental programs involving LNG spills and fires on land have been conducted in the U. S. and abroad. Further, a series of LNG spill tests was conducted on water to study flammable vapor dispersion in the absence of ignition. The information obtained from these tests, coupled with theoretical models, had been used to develop techniques for predicting the hazard zones surrounding LNG fires on water. However, these predictions were without experimental verification prior to the test program described in this report.

To provide experimental verification and additional information, the U. S. Coast Guard requested the U. S. Navy at the Naval Weapons Center (NWC), China Lake, California, to perform field experiments involving LNG spills and fires on water. Additional tests under a 2nd phase program were funded by the Department of Energy under interagency agreement EE-77-A-28-3248. These tests were performed between September 1976 and June 1978. Arthur D. Little, Inc. (ADL) staff, under contract to the U. S. Navy, provided consulting services to the NWC during the experimental program and also performed the analysis of the experimental results. This report describes the details of the test program, the experimental data, and the findings.

THE EXPERIMENTAL PROGRAM

The test facility at the Naval Weapons Center consists of an excavated pond located in the midst of a fairly flat desert terrain. The pond is about 50 m x 50 m with a 1 m depth. Quantities of LNG in the 3-5 m³ range were spilled at rapid but controlled rates through a pipe onto the center of the pond. In "pool fire" tests, an igniter was activated near the spill point as soon as LNG hit the water surface. This produced nearly immediate ignition and resulted in an initially expanding, burning pool of LNG with a tall-fire plume above. In "vapor fire" tests, the LNG was spilled and allowed to vaporize producing a cloud of gas that was carried downwind. When the vapors reached a point about 70 m downwind, flaming igniters at that distance were activated. The resulting fire burned back toward the spill point, burned for a significant duration of time at the edge of the pond, and finally burned back to the spill point after liquid flow had ceased. Three tests of an intermediate type, termed "delayed ignition pool fires" were also run. In these tests, a vapor cloud was allowed to form in the vicinity of the spill pool before the igniter was activated. The early stages of these tests resembled a vapor fire but pool fire behavior was quickly established thereafter.

The instrumentation for gathering the data during the experiments included narrow- and wide-angle radiometers to measure the emissive power of specific parts of the flame and the overall emissive power; movies to show the visible flame dimensions and behavior; spectrometer (1 pool fire test only) to study the wave length distribution of energy radiated by the fire; and information from gas sensors, weather instrumentation, thermocouples, and spill equipment monitoring and control instrumentation. In two tests, wooden stakes were arrayed radially at different locations from the spill point to allow the effects of the radiation on wood to be evaluated qualitatively. The conduct of field experiments is quite difficult, especially when sensitive instrumentation must be used. In the first series of tests, a number of instrument problems occurred; a subsequent series of tests was performed with most of these early problems corrected.

FINDINGS: Pool Fire Experiments

Based on theory and information for LNG fires on land, prior to this program LNG pool fires on water were expected to spread and vaporize at a rate equivalent to a decrease in liquid level of a confined pool of about 6×10^{-4} m/s ("regression rate"). This rate is consistent with most of the experimental regression rates for the spill tests in this program. These rates were deduced from the fire diameter observed in movie records after the fire stabilized. However, for the two fastest spills (3 m^3 in about 30 seconds and 5 m^3 in about 50 seconds), vaporization rates seemed to increase by about 50%. We believe that this is probably due to the rapid interaction between the jet and the water which produces fragmentation and increased heat transfer area. This effect, if it should occur in an accident, would tend to produce a smaller diameter, but taller fire. The total radiating area, however, would be reduced.

The movie films also provided data on visible flame height. We found that these heights could be well correlated using a relationship known as Thomas' equation which relates flame length to a parameter involving pool diameter and fuel vaporization rate.

Narrow-angle radiometer data from the pool fire tests indicated flame emissive powers near the flame base in the $212 \pm 20 \text{ kW/m}^2$ range. Wide-angle data, which are subject to more uncertainty, indicated the average emissive power of the entire flame surface to be about $220 \pm 47 \text{ kW/m}^2$. (These values obtained from LNG pool fires on water are higher than those measured in earlier AGA experiments of LNG pool fires on land.)

However, the data obtained in the one test where a spectrometer was used to analyze the flame emissions, provide substantial insight into the behavior of LNG fires. In the combustion of LNG (primarily methane), water and carbon dioxide are formed as products of combustion. Further, incomplete combustion results in the formation of some luminous soot. Some unburned gases or carbon monoxide may also be present. While the soot behaves essentially as a "grey emitter" with radiant emission continuously distributed over the entire infrared spectral range, the water and carbon dioxide emit energy at a series of discrete bands centered at specific wave lengths. As this energy is transmitted through the atmosphere, water vapor

and carbon dioxide in the ambient atmosphere are effective at absorbing radiation in these same bands.

From the limited spectral data, we estimate that the soot is radiating at a temperature of about 1500 K and that water vapor and carbon dioxide in the fire plume exist at concentrations corresponding to burning with no excess air. The fires in these tests were typically up to 15 m in diameter and thus were not "optically thick" over the entire infrared wavelength range. An optically thick LNG fire at 1500 K would have a surface emissive power of about 287 kW/m^2 . When corrections are made to account for the limited thickness of the test fires, the spectral flame model gives an equivalent average emissive power of about 210 kW/m^2 which is in good agreement with the narrow-angle radiometer data.

Several tests conducted in wind showed flame tilt angles similar to those that would be predicted by correlations developed for pool fires on land.

Finally, if the ratio of the fraction of energy radiated to the total energy of combustion possible is estimated, the ratio decreases as the spill rate increases. This suggests that in very rapid spills where heat transfer area between the spilled LNG and water is enhanced due to liquid fragmentation, a larger fraction of the vapor produced escapes from the plume unburned. We hypothesize that a large vapor core rises in the center of the fire. Further we suggest that the fire core may entrain combustion products from the outer burning zone that subsequently inhibit its combustion in the top regions of the fire plume. Therefore, a significant part of the mass of vapor produced may escape at the top of the fire.

FINDINGS: Vapor Fires

Ignition of dispersed vapors from an LNG spill on water produced a fire that spread back along the ground over the land toward the pond spill source. "Fireball" type of burning, where burning gas lifts off from the ground, was not observed.

The rate of fire spread through the vapor cloud increases with wind speed at least for winds up to 7 m/s. The correlations, for flame speed

the intensity of the surrounding thermal radiation field. In the case of assessing hazards for vapor fires, the extent of spread of flammable vapor, the rapidity of flame travel after ignition and the thermal radiation output need to be known. Also in the case of vapor fires, structures lying within the flame travel path may be ignited or experience damage from sudden (but moderate) pressure differences. The latter could be caused by the combustion of any vapors that have diffused into the buildings or external pressure difference caused by flame travel. Evaluation of "safe distances" for preventing hazards to people, damage to structures and ignition of wooden buildings is of great concern to both regulatory bodies of the government and liquefied natural gas industry. The understanding of the consequences of accidental spills of LNG on water and the assessment of the potential risks posed to the public safety from such spills form important aspects of the regulation of LNG transportation.

Several studies have been undertaken in recent years both in the U.S. and abroad to investigate the fire hazards from LNG. In a series of tests conducted for the American Gas Association by a consortium of companies including ADL, (AGA-1974), radiation from LNG pool fires on land was measured and analyzed. Gaz de France has conducted tests on land to study the distance over which the LNG vapor cloud generated by a land spill is flammable. The U. S. Navy and the U. S. Coast Guard have investigated the detonability of methane air mixtures. However, no experiments had been conducted prior to the present study measuring the radiation from LNG pool fires on water.* This problem is of utmost importance because it represents the most probable situation consequent to an accidental spill of LNG from a tanker. Several questions remain to be answered before a reasonable estimate of the thermal radiation hazard from such an expanding, burning, and short-lived fire can be made. Some of these questions are: (1) can a flame be sustained on the boiling LNG during its rapid boiling and spread on water? (2) Will the flame remain in one piece on the pool or will it break up into small flamelets of low height? (3) Will the height of flame be equal to the height of a non-expanding pool flame of the same base dimensions?

* There have been some limited, small-scale tests involving LNG fires on water conducted by the Bureau of Mines and the simulated water spills conducted by University Engineers, Inc.

(4) Finally, will the transient conditions have any bearing on the burning and/or flame characteristics? Only a theoretical model (Raj and Kalelkar, 1973) presently exists to predict the hazard from burning LNG pool on water.

Similarly, there exist no experimental data to indicate the extent of radiation hazard due to the burning of a large flammable vapor cloud (as may be formed from dispersion of the LNG vapors) spread over a wide area. What theoretical analysis exists is very cursory (Raj and Emmons, 1975).

The United States Coast Guard (USCG) has the primary statutory responsibility to regulate the marine transportation of hazardous chemicals including LNG and to ensure safety within the territorial waters and in the ports of the United States. The U. S. Navy (USN) does not have regulatory authority for LNG shipping; however, the USN may be called upon to assist the USCG or assume a primary role in emergency situations involving the shipping of energy fluids. The chemical hazard response information system (CHRIS) was developed by the U. S. Coast Guard to better assess potential hazards from chemical spills on water and to provide guidance for contingency planning. CHRIS contains several models to predict the behavior of spilled chemicals. One of the models deals with the behavior of LNG on water, especially the thermal radiation from pool fires. However, many of the CHRIS models are based on theoretical derivations without experimental verification.

The USCG and USN recognized the fact that quantitative knowledge on the behavior of LNG on water and the thermal radiation output from such fires was unavailable. Theoretical models for the scenarios of pool fires and the burning of LNG vapor clouds were available without experimental verification. Therefore, a field scale experimental program involving LNG spills onto water followed by ignition was initiated by the USCG.

The experiments were performed by the USN at the Naval Weapons Center (NWC) at China Lake, California, under contract from the U. S. Coast Guard. The USN personnel at NWC were completely in charge of the planning, design and conduct of the tests.

The professional staff of Arthur D. Little, Inc. (ADL) provided, under contract to the USN (Contract #s N00123-76-R-1718 and N60530-78-C-0192), consulting services during the design of tests and their execution. In

addition, ADL was contracted to perform the analyses of the experimental data, develop correlations and generate the report covering the LNG spill test program. This report indicates the details of the test program and the findings.

1.2 OBJECTIVES OF THE EXPERIMENTS

The principal objectives of the experimental program, described in this report, were to understand the behavior of two kinds of LNG fires: namely, pool fires on water and fire propagation in unconfined clouds of dispersed LNG vapor. Specifically, the purpose of the experiments was to obtain data on the characteristics of the LNG fires on water including the thermal radiative output, the fire size, and the fire spread velocity (in the vapor fire). The data measured were intended for use in verifying or modifying existing physical models or in developing additional ones for use in hazard prediction calculations.

1.3 SCOPE OF THE TEST PROGRAM

To achieve the above objectives, a two-phase experimental test program was conducted at the Naval Weapons Center, California. A total of 11 tests were included in the first phase. These involved 6 pool fire tests, 1 delayed-ignition pool fire and 4 vapor fire tests. In the second phase, a total of 5 tests were conducted involving 1 pool fire, 2 delayed-ignition fires, and 2 vapor fire tests. The second phase was initiated after the data from the first phase indicated significant problems with calibration and positioning of some of the instruments.

Each experiment was recorded on a motion picture film from each of at least three different directions. Other measurements included radiation flux at different distances from the fire, using wide-angle and narrow-angle radiometers. In one experiment the spectral characteristics of the pool fire were also measured. Also measured routinely in each experiment were meteorological data such as wind speed, wind direction, relative humidity and ambient temperature. Other important and relevant data such as the spill time, ignition time, tank pressure, liquid depth in the tank, etc., were also measured.

Chapter 2 in this report covers a review of past experiments and analyses pertaining to LNG fires. Also discussed in the review chapter are models from the combustion literature relating to turbulent flame behavior, radiation and scaling laws. In Chapter 3 are described the details of the test site, experimental equipment, measuring instruments and the test procedures. The spectral data obtained in one of the pool fire experiments are described and analyzed in Chapter 4. Chapter 5 deals with the pool fire data and their analyses. The vapor fire experimental data are discussed in Chapter 6. A general discussion of the overall findings from this experimental program and recommendations for hazard estimation techniques are indicated in Chapter 7. Recommendations and suggested future research areas are given in Chapter 8.

2. SURVEY OF LITERATURE CONCERNING THERMAL RADIATION FROM LNG AND OTHER TURBULENT DIFFUSION FLAMES

The burning of a large pool of liquid in the open is a complex phenomenon involving the entrainment of ambient air, turbulent mixing of fuel vapor and the entrained air, liberation of heat by combustion, loss of heat by radiation and heat transfer to the evaporating pool by radiation and convection. In a steady burning pool of liquid there is dynamic equilibrium amongst the various interacting phenomena. However, even in such a case, precise prediction of the heat output from the flame in the form of thermal radiation, from purely theoretical considerations is virtually an impossibility. This is because of the complexity of the chemical reactions, the diverse nature of the radiating species, and the lack of a good model to describe turbulence in large fires. To circumvent the difficulties in theoretical predictions, semi-empirical models have been developed. Some of these models are reviewed from the point of view of thermal radiation transfer from fires as well as from the point of view of physical size scaling. The emphasis in this review is on LNG fires. First we review past LNG fire experiments, their results and the models that have been developed. Subsequently, other general models available in the combustion literature for describing large turbulent diffusion flames are reviewed. The scaling laws for size scaling and for radiative transfer are also discussed.

2.1 BEHAVIOR OF LNG ON WATER

The behavior of an LNG spill on water is significantly different from that of a spill on land for two principal reasons. In the case of spill on a large body of water, first the liquid spreads because there is no confinement. Secondly, the heat transfer occurs from the water at a relatively high rate. The rate of transfer of heat per unit area has been found to be approximately constant from previous experimental data. For a pool on fire, there is also heat transfer from the fire. The high heat transfer rates together with the increasing area of contact with water results in rapid evaporation of the liquid. For an instantaneous spill of a given volume, the pool is expected to increase in size until all of the LNG has evaporated. In a continuous spill, on the other hand, the pool size will reach a maximum area commensurate with the evaporation rate and the spill rate.

The water spill has to be contrasted with the behavior of an LNG spill on land. While unconfined spreading is possible on flat ground, in most cases of interest, the potential land spill areas are diked. This confinement, therefore, limits the size (diameter) of the pool. Secondly, the heat transfer rate from the ground decreases with time. Should there be a fire over a diked LNG pool, the burning rate (after an initial transient of a minute or so) will be primarily dependent on the radiative feedback from the fire. This is unlike the situation on open water where heat transfer from the water remains significant until the pool is evaporated.

2.2 PAST LNG FIRE EXPERIMENTS

Over the years several groups both within the U. S. and abroad have conducted tests to study the radiative and other characteristics of LNG fires. A review of the tests conducted before 1972 and their results are presented in another report (see Section G, AGA; 1974). However, all of these fire tests have been on land. The series of tests described in this report is unique in that it consists of LNG fire tests on water. LNG spill tests on water have been performed and only one involved ignition.

Previous LNG fire tests can be divided into three broad categories: 1) those that were conducted before 1972, 2) the tests in the AGA sponsored series between 1971-74, and 3) tests after 1974. The significant findings from the different tests are discussed below.

2.2.1 Experiments Before 1972

Several research groups have performed LNG tests on land. These groups include the Bureau of Mines, University Engineers, Inc., TRW, Enso, Gaz de France, Tokyo Gas, Osaka Gas, et al. A review of the details of these tests and their results is given in another report (Section G, AGA 1974), and is therefore not discussed in detail. However, to keep the current series of tests in perspective, the following features of the past tests are noted.

- The test sizes ranged from laboratory scale (15 cm diameter) to large field fires (10 m x 13 m pools). Some qualitative observations of the 200 m diameter fire resulting from the 1944 Cleveland LNG accident are also available.

- The flame radiative power* deduced from the measured radiometer data ranged from 90 kW/m^2 to 160 kW/m^2 . Some researchers have expressed the flame output in terms of the base area of the flame. This number varied between 600 kW/m^2 and 850 kW/m^2 .
- The fraction of combustion energy which was radiated in these various tests ranged between 19% and 40%.

2.1.2. American Gas Association Tests

During 1971-74 a series of land pool fire tests was conducted under the sponsorship of the American Gas Association (AGA, 1974). The tests involved the rapid spillage of LN₂ onto compacted ground in a diked area, ignition of the pool, measurement of the thermal radiation from the fire at different distances from the fire center. Three different dike diameters were used in the tests. These were 1.8 m (6 ft), 6 m (20 ft), and 24 m (80 ft)** in diameter. Also measured in these tests were the liquid regression rate in the pool, and the direct radiation from the flame to the pool. The former was measured with a depth gage and the latter using four wide-angle radiometers located in the dike aimed vertically upward. Motion picture records of the fires were also made.

The important results that were generated by the AGA tests are as follows:

- The liquid regression rate varied with time (due to varying heat transfer rate from the ground). The quasi-steady state liquid pool regression rate varied with dike size. It was $1.5 \times 10^{-4} \text{ m/s}$ (0.35 in/min) in 1.8 m diameter fires, $2.2 \times 10^{-4} \text{ m/s}$ (0.52 in/min) in 6 m fires and $2.3 \times 10^{-4} \text{ m/s}$ [†] (0.55 in/min) for the 24 m fire. The portion of this rate that was due to back radiation from the fire was estimated to be $0.2 \times 10^{-5} \text{ m/s}$ (.12 in/min) in the 1.8 m diameter fires and $1.5 \times 10^{-4} \text{ m/s}$ (0.34 in/min) in the 6 m diameter fires.

* The common terminology encountered in the study of radiative transfer from fires and flames are indicated and defined in Appendix C. Also given in the Appendix are the values of constants in SI units.

** Only one test of the 24 m size was conducted. The results from this test are suspect because of accidental ignition of vapors outside the pool and the consequent destruction of cables and measuring instruments.

† Estimated value for the 24 m fire.

- The average flame to pool radiation flux was 3.3 kW/m^2 in the 1.8 m fires and 4.2 kW/m^2 in the 6 m fires. These represented, respectively, 35% and 66% of the total heat transfer to the liquid (from flame and ground). The dominance of radiative transfer in the larger fire was clearly seen.
- The angle of tilt of the flame plume by wind could be correlated by:

$$\cos \theta = \begin{cases} 1 & \text{for } u^* < 1 \\ \frac{1}{\sqrt{u^*}} & \text{for } u^* > 1 \end{cases} \quad (2.1)$$

$$u^* = \frac{u_{\text{wind}}}{\left[\frac{\dot{m}''}{\rho_v} 8D \right]^{1/3}} = \text{Dimensionless wind velocity} \quad (2.2)$$

where θ = tilt of the axis of flame with respect to the vertical,

\dot{m}'' = the liquid burning rate per unit area, ($\text{kg/m}^2 \text{ s}$)

ρ_v = the vapor density at ambient pressure, and (kg/m^3)

D = the fire diameter, (m).

Another somewhat more elaborate correlation has also been proposed to fit the data. The difference between the tilt angle estimated by using the two correlations is very small (see Section C, AGA, 1974).

- The height of the visible flame could be correlated using Thomas' correlation (see Section 2.3.1). However, in the 24 m test, the flame heights measured were about three times the diameter. This is about 30% more than that predicted by Thomas' relationship.

Two different groups analyzing the AGA fire data came to somewhat different conclusions. One group (ADL) concluded that the AGA test data indicated the flame height to diameter ratio was essentially 3 and the flame emissive power was 100 kW/m^2 . The corresponding conclusions from the other group (UE) were that the visible flame heights could be adequately explained by Thomas' correlation (see below) and that the flame emissive power was 140 kW/m^2 .

Spectral measurements of the infrared emission from the flame were also made in these experiments. While no conclusions were drawn from the flame spectral measurements, it was indicated that a significant fraction of radiation from the fires (especially the 6 m and the 24 m) could be attributed to luminous soot. The fraction of radiation attributed to soot was reported to be in the 0.6 to 0.8 range. The percent of heat energy liberated by combustion which is emitted as radiation was calculated to be about 20% for the 1.8 m fires, 25% for the 6 m fires and about 23% for the 24 m fire. These values are well within the range generally quoted in the combustion literature for radiation from large fires. However, what is less certain is the magnitude of this percentage for a very large fire, or how it changes with the higher hydrocarbon contents of the LNG.

The principal conclusion from the AGA test experiments was that LNG fire was highly radiative because of luminous soot. There was, however, difference of opinion on the magnitude of the emissive power. General models for predicting thermal radiation hazards from diked LNG pool fires were proposed.

2.2.3 Recent Tests and On-Going Tests

Since the completion of the AGA test series there have been no large scale LNG fire experiments within the U. S. designed specifically to study the thermal radiation output. Tests conducted by University Engineers, Inc., (UE, 1974) were primarily intended to study the effects of extinguishing agents on LNG dike fires. Other LNG fire tests in the open have been conducted in the last few years in Japan (Tokyo Gas), and in England (British Gas Corporation). Many of these tests involved spills into precooled dikes. In addition, several LNG fire fighting schools routinely produce LNG fires for training programs.

2.3 MODELING FIRE RADIATION

The degree of sophistication used in determining the magnitude of thermal radiation field around a fire depends on the accuracy to which the radiation field has to be described for the end use of the information. For example, contingency planning in the transportation of flammable fluids

involves estimating the extent of hazard zones from potential fire accident scenarios. In such cases it may suffice to use simple models because the accidental release parameters may not be known precisely. On the other hand, in developing siting criteria (such as spacing between adjacent storage tanks) it is desirable to use as accurate a model as is available.

There are basically two models to describe the thermal radiation field around a fire. The first model, which is very simple, is called the "Inverse Square Law" model. The second but more sophisticated model is called the "solid flame" model. The state of the art in calculating thermal radiation hazards from LNG fires has been discussed in a recent review paper (Raj, 1977). More detailed analysis of these models are included in the review paper.

The Inverse Square Law model is based on the fact that the flux of radiant energy at any distance from a point source varies as the inverse square of the distance from the source. Based on this model the thermal flux (\dot{q}'') at any distance (X) from a fire is calculated by the formula:

$$\dot{q}'' = \frac{\dot{Q}}{4\pi X^2} \quad (2.3)$$

where $\dot{Q} = n \dot{Q}_c$ = Thermal energy radiated in unit time (W) (2.4)

In the above equation \dot{Q}_c is the rate of energy released by the combustion of fuel, and n is the fraction of combustion energy released in the form of thermal radiation. The above model assumes the fire to be a point source of energy. The model does not account for the absorption of radiation by the intervening atmosphere.

The value of the fractional energy radiated cannot be determined theoretically. A reasonable value would be 25%, even though the estimated value from measurements varies between about 15% and 35% (see the reviewed values in Raj, 1977).

The second approach generally used in the literature to evaluate the thermal field around a fire is based on recognizing the fact that the radiation from a fire originates from the hot gases in the plume and sig-

nificant energy is radiated from regions which form the visible flame. In short: this model takes into account the effects of size and shape of fire and the specie concentration in the fire. A simplified version of this model is called the solid flame model and is used widely for describing LNG fire radiation (AGA, 1971; AGA, 1974). The solid flame model assumes the flame to be a cylinder with diameter equal to fire base diameter and axial length equal to the length of the visible fire plume. Also the flame is assumed to radiate uniformly over the entire surface of the cylinder. The thermal radiative flux at any position (X) from the flame center is then given by:

$$\dot{q}'' = E F \tau \quad (2.5)$$

where E is the rate of energy radiation per unit nominal flame surface area (emissive power), F is a geometric view factor between the flame and the receiver and τ is the atmospheric transmissivity for thermal radiation from the fire. The view factor calculation is in general very tedious because it depends on the flame geometry, relative position of the receiver and the orientations of the receiver and the flame. Methods for calculating the view factors for general cases are given by Hottel and Sarofim (1967), Sparrow (1973) and for specific cases by Rein et al. (1970), Raj et al. (1974), and Raj (1977).

The determination of the emissive power E of a flame is more difficult. The thermal radiation from a fire emanates from both gaseous species such as water vapor, carbon dioxide and carbon monoxide as well as from luminous soot particles. The gaseous species emit radiation in certain spectral bands (non-luminous radiation) whereas the soot radiation is continuous over the entire spectral range of importance. The theories of gas radiation and the models developed to describe the band emission from various gases are described in most text books on radiative transfer (see Hottel and Sarofim, 1967). Recently, deRis (1978) has reviewed these models from the point of view of fire radiation predictions. Modak (1978) has developed simplified calculation procedures for obtaining the gas emissivities. Markstein (1975) has proposed a model which considers a fire as a two-specie emitter whose total radiance is equal to the weighted sum of the radiance

due to gas emission and that due to soot. Using a unique laboratory experimental procedure, Markstein has measured the radiances of ethane and propane flames (laminar and turbulent). Markstein's data indicate that turbulent fires are less radiative than laminar fires. Also his data seem to confirm some earlier findings that in fires the heat release rate per unit volume of flame is constant and independent of fuel types. This value was found to be about $2 \times 10^6 \text{ W/m}^3$ (in a 1 m high flame). Based on this significant finding deRis (1976) has attempted to develop a cascade combustion model for buoyant diffusion flames with a view to predicting the fraction of combustion energy that is radiated. This model explains qualitatively the relative insensitivity of the fraction radiated to the fuel flow rate.

It is known generally that a significant fraction of the fire radiation originates from the luminous soot. Markstein's data for turbulent fires of propane and ethane indicate that in very large fires about 98% of radiation is emitted by luminous soot. The emissivity of soot depends on the mean volume fraction of soot, the temperature and the flame size. The soot spectral absorption-emission coefficient is approximately proportional to the inverse of wavelength and can be expressed by (Dalzell and Sarofim, 1969):

$$k_{s,\lambda} = B_s f_v / \lambda \quad (2.6)$$

where B_s is a dimensionless constant of magnitude between 4 and 10 (generally assumed to be 7) and f_v is the volume fraction of soot. deRis (1978) has shown that based on the above equation the emissivity of soot is:

$$\epsilon_s = 1 - (15/\pi^4) \psi^{(3)}(1 + B_s f_v X T / C_2) \quad (2.7)$$

where $\psi^{(3)}$ is the penta gamma function,* X is the path length for radiation and C_2 is the Planck second constant. There are no comprehensive models to describe the formation of soot or to estimate the amount of soot present in a given fire. Therefore, the use of the above equations is limited.

* Penta Gamma function is defined by:

$$\psi^{(2)}(z) = \int_0^\infty \frac{t^3 e^{-zt}}{(1-e^{-t})^2} dt,$$

See Abramowitz and Stegun (1964), p. 260.

Current fire radiation models are at a stage where given the temperature of the gases, the partial pressures of gaseous species, the soot concentration and the size of fire it is possible to predict the emissive power of the fire with at least an accuracy sufficient for engineering calculations. Unfortunately, however, none of these values are known a priori in a large diffusion fire and that is why the prediction of radiative output from such fires is difficult. This difficulty has been overcome in many instances by direct measurements of emissive power in experiments. This certainly is the case with LNG fires.

2.4 SCALING LAWS

In extrapolating the results from small-scale experiments for prediction of the hazards to large-scale spill fires, it is essential to know the laws of scaling. Reviewed in this section are the scaling laws for the physical size of the fire as well as the scaling of radiative characteristics of turbulent diffusion flames. The emphasis in the review of physical size scaling laws is on LNG spills on water.

2.4.1 Size Scaling

Pool Size

In the size scaling of a LNG fire on water, the parameters of importance are the volume of spill, the duration of spill, and the rate of mass loss per unit area (vaporization or regression rate). The maximum diameter of the pool at the base of the fire is given by (Raj et al., 1974):

$$D = 2 \left[\frac{V^3}{t^2} \frac{g \Delta}{\rho} \right]^{1/6} \quad \text{for instantaneous spills} \quad (2.8)$$

and

$$D = \left[\frac{V}{t} \frac{4}{\rho \dot{y}} \right]^{1/2} \quad \text{for continuous spills} \quad (2.9)$$

where V is the volume of liquid spilled, \dot{y} is the regression rate, Δ the liquid fractional density defect and t is the duration of spill when the volume V is spilled continuously at a constant rate. Other researchers have also obtained similar expressions which differ only in the magnitude of the constant factor (for a review see Otterman, 1975). Expressions

for the size of the pool during the transient spreading phase are also available (see Raj, 1977; Raj and O'Farrel, 1978). In a recently published paper (Raj, 1979), the issue of classifying spills into instantaneous and continuous has been discussed and a criterion has been derived. A spill is classified as "instantaneous" if:

$$\underbrace{t_s}_{\text{Duration of spill of volume V}} < \underbrace{t_c}_{\text{A critical time}} \quad (2.10)$$

where for LNG spills on water (spill volume in the range $1000 \text{ m}^3 - 50,000 \text{ m}^3$) the critical time is given by:

$$t_c = 2 \times 10^{-3} \frac{V^{1/3}}{\dot{y}} \quad (2.11)$$

If equation 2.10 is not satisfied, the spill is assumed to be a continuous spill.

Visible Flame Height

The height (or length of plume) of a visible flame is dependent on several parameters including the size of the fire (diameter), the mass flow rate of fuel vapor, the nature of the fuel and other ambient conditions. Different correlations exist relating the visible length-to-diameter ratio for other parameters. Thomas et al. (1965) derived the following correlation to a free-burning turbulent fire, dominated by self-induced buoyancy forces and self-generated turbulence.

$$\frac{L}{D} = 42 \left(\frac{\dot{m}''}{\rho_a \sqrt{g D}} \right)^{0.61} \quad (2.12)$$

where \dot{m}'' is the mass burning rate per unit pool area, and ρ_a is the density of air. Steward (1970) and more recently, Becker and Liang (1978) have developed flame length correlations based on laboratory data.*

* AGA flame height data did not agree with Steward's correlation. A cursory look at the data from present experiments did not check the Becker and Liang correlation (which gives $L/D = 11$ for pool sizes tested, whereas observed values are in the 3 to 4 range). Therefore, the details of these correlations are not discussed.

It should be noted that the visible flame does not represent the complete radiative surface. In the upper portion of the flame, both flame temperature and soot concentration decrease with height so that the contribution to the radiometric data by the infrared portion of the spectrum becomes increasingly dominant (Markstein, 1976). However, at this stage, the flame may not be visible. The difference between visible surface and the IR radiating surface is a small fraction of the total; for many practical purposes, the distinction can be ignored.

2.4.2 Radiation Scaling

The amount of energy emitted per unit area by a black body is proportional to the fourth power of temperature. The temperatures of fuel fires, in general, do not vary significantly and are in the 1200 K - 1500 K range. From a radiative point of view, both temperature and emissivity are important. Emissivity for a continuum (or grey) emitter can be expressed by:

$$\epsilon = 1 - e^{-kD} \quad (2.13)$$

where k is the mean absorption coefficient (m^{-1}) and D the flame size. For band emitters (such as H_2O and CO_2) the relationship is not simple. The emissivity depends on the temperature and partial pressure beam length product.

$$\epsilon_{band} = f(pL, T) \quad (2.14)$$

Graphical representations of the above function for different species are available in radiative transfer text books (see Hottel and Sarofim, 1967). If dynamic similarity exists between an experimental fire in the laboratory and a fire in the open then emissivities can be scaled using the above equations. Of course, beyond a certain size the emissivity may be almost unity. For fuel fires, this thickness ranges from about 3 m for propane and 5 m for ethane, to about 10 m for methane (Markstein, 1976).

For turbulent diffusion fires generated by controlled fuel vapor flow, scaling laws describing the physical dimensions of the fire and the radiative output have been developed by Markstein (1976). The validity of these scaling laws for a pool fire, in which the evaporation rate of the pool (i.e., the

vapor flow rate) is itself dependent on the radiative characteristics of the fire and its size, has not been demonstrated.

Radiative transfer in fires is an area of continuing research. While significant progress is being made in several areas (such as developing a comprehensive combustion model for a buoyant turbulent fire) many other problems have not been investigated adequately. One of these, for example, which has significant relevance to large LNG spill fires on water, is the question of size stability. If one kept on increasing the size of the pool, is there a critical size beyond which no single diffusion flame is sustained on the pool, but instead would one find a cluster of smaller pool fires? In such a case, what are the parameters that influence this critical size? The question is not academic; for if the flame size (and therefore the flame height) is reduced but yet the flame is optically thick, the radiation hazard zone will be significantly reduced.

2.5 UNCONFINED VAPOR FIRES

Vapor fire experiments have been conducted before (Gaz de France, 1972, AGA); however, these were not intended for studying either the flame propagation in vapor clouds or the thermal radiation from such fires. The data that could be gathered from these tests were reviewed by Raj and Emons (1975). Also developed in the same paper is a model for the propagation of turbulent fire in an unconfined vapor cloud and for estimating fire size. Another type of vapor burning in the form of a fire ball has been proposed by Fay (1975), Fay and Desgroseilliers (1978), and Lewis (1978). The propagating fire model and the fire ball model have been discussed by Raj (1977) in the review article. Harder et al. (1978) have also developed a simple fire ball model. Small-scale experiments in the 0.1 - 10 kg range (with pure methane and premixed methane air mixtures at ambient temperature) have been performed. The experimental fire balls were smaller than the theoretical predictions. Combustion times seem to agree better.

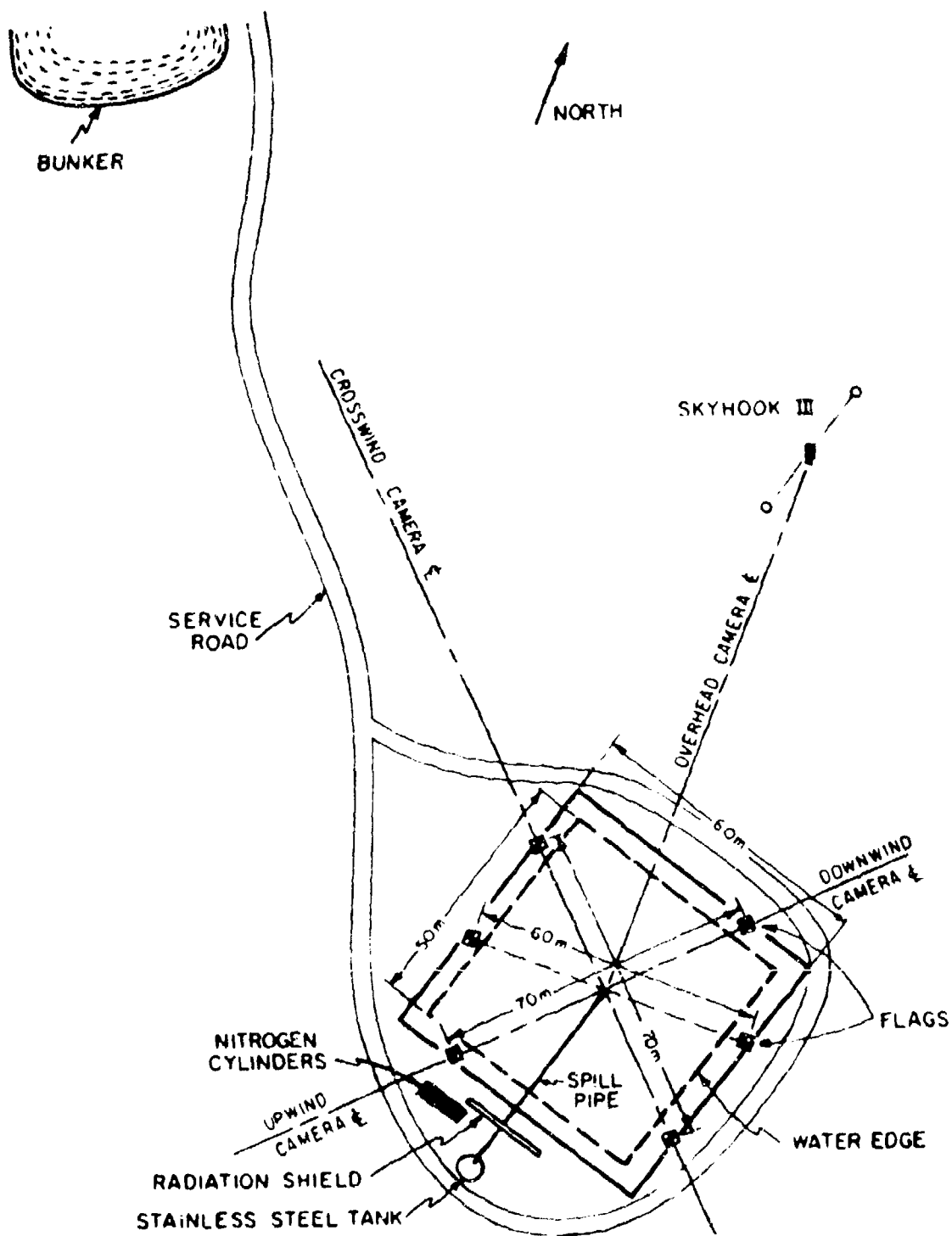


FIGURE 3.1: SCHEMATIC DIAGRAM OF THE TEST SITE

system. The tank is a vertical cylinder of nominal capacity -- 6 m^3 (2 m diameter x 4 m height) and is insulated on the outside with about 0.2 m thick polyurethane foam. The insulation is painted white (silver) to reduce the radiative heat leak. The tank is located about 15 m away from the center of the southern edge of the pond. The spill line starts inside near the tank bottom and extends through the top of the tank. External to the tank, it is basically an insulated 0.15 m (6 inch) diameter pipe except towards the discharge end where its diameter increases to 0.2 m (8 inches). Transfer is accomplished by introducing nitrogen into the tank vapor space thus forcing liquid through the spill line. The ullage space in the tank is connected to nitrogen cylinders through remotely operated pressure reduction valves. The nitrogen cylinders are on a flat bed truck which can be seen in Plate 3.1.

The spill line over the pond rests on a pipeway supported on a trestle. The center line of the horizontal section of the pipe is 2.2 m above the water line. The discharge end of the pipe has an elbow with a short vertical section exactly above the center of the pond. The exit section of pipe is 1 m above pond water surface and discharges liquid vertically down. A circular metal plate (0.5 m diameter) is suspended from the pipe with the plate surface just beneath the water surface. This plate is intended to prevent the LNG jet from impinging on the bottom of the shallow spill pond. A radiation shield is provided between the stainless steel tank and the pond edge to minimize heat radiation to the tank from the LNG fire on the pond. Also provided is another thermal shield to protect the thermocouple junctions and other instruments from fire radiation.

Meteorological data are recorded from two stations. One station for wind speed and direction is on top of the bunker. The other is located at about 10 m upwind from the SW corner of the pond. This station records wind speed and direction 2 m above ground, temperature, pressure, and relative humidity. In addition, for test #12 and later tests, wind direction and velocity at 10 m above ground and lapse rate up to 15 m were recorded at pond station.

For the initial two tests a matrix of thermocouples was provided underneath the water to measure the heat transfer from the water to LNG (by noting the instantaneous temperature of water). This matrix consisted

of 6 thermocouples located vertically beneath the water surface at 2 mm intervals. There were 5 such vertical arrays arranged at 2 m spacing along the downwind (NE) direction from the spill point. Seven additional surface thermocouples were also provided. These thermocouples were not used in the later tests because the surface temperature data obtained in the first two tests were very noisy probably due to wave effects and no sense could be made of them. Thermocouples lower in the water registered no observable temperature changes.

The test equipment also included electrically initiated flares. For igniting the pool fire, an ignitor was provided about 1/2 m behind the exit section of the spill pipe. The number of ignition flares for the vapor fire tests varied between 2 and 3, and these were located on land on the downwind side. Their exact locations in each vapor fire experiment are described in Chapter 6. A safety flare was also provided midway between the bunker and the pond. This was intended to ignite any vapors that might blow in the direction of the bunker.

3.2 INSTRUMENTATION

The principal instruments used in the series of tests described in this report were designed to measure the thermal radiation output from the LNG pool fires on water and the LNG vapor fires. In addition, photographic, meteorological, spectral, and some gas concentration data were obtained. Table 3.1 gives a summary list of the instruments used, their type and manufacturers, significant specifications, number of instruments used and other special information.

Two types of instruments were used to measure the radiative output of the fires. These were the wide-angle radiometers (with view angle of 150°) and narrow-angle radiometers (view angle 7°). Both radiometers were water cooled instruments. The instruments were provided with windows (quartz, sapphire) to prevent the air currents from affecting the sensing elements. The actual types of windows used on each radiometer are indicated in Chapters 5 and 6. Since the wide-angle radiometers view the entire flame, their output gives an average value of the total emission from different parts of the flame. The narrow-angle radiometers indicate

TABLE 3.1

LIST OF MEASURING INSTRUMENTS USED IN THE TESTS

Item #	Instrument	Type, Manufacturer and Specifications	Total # Used	Test #s in Which Used	Remarks
1	Wide-angle radiometer	Hy-Therm water cooled radiometer, Hy-Cal Engineering Model # R-8015-C-ZZ-YYY View 150° with Bezel in place, 180° with window removed	4 or 5	All tests	In Phase I of test series (up to Test #11), only 4 were used - in Phase II (tests 12-17) 5 radiometers were used.
2	Narrow-angle radiometer	Hy-Therm "H" Radiometer, water cooled, Hy-Cal Engineering Model R-8101-B View angle: 7° full cone	2	All tests	
3	Movie cameras	Wide-angle cameras. In most tests the speed was 100 frames per second.	3	All tests	One camera was used for each of crosswind, downwind (or upwind) and over-head view. In test #17, 5 cameras were used.
4	Wind speed and direction		2	All tests	One station located on top of the bunker, another station 10 m upwind from edge of pond.
5	Spectrometer	Michelson fast-scanning type 0.5 sec/scan	1	Only in test # 5 (pool fire).	Infrared spectrum, only between 1.5 μ m and 5.5 μ m is measured.

TABLE 3.1 (concluded)

Item #	Instrument	Type, Manufacturer and Specifications	Total # Used	Test #s in Which Used	Remarks
6	Hydrocarbon sensor		5	Used only in vapor fire tests (8 through 11, 16 and 17).	These worked properly only in tests 16 and 17.
7	Thermal imaging camera		1	Test #	This instrument was used on an experimental basis.
8	Still camera	70 mm, 10 f/s	1	Used in many tests	
9	Close-circuit TV camera		1	All tests Recorded from test #12 on.	All decisions during the progress of the test were based on observations over the TV camera.
10	Data logger	Model 120-122 made by Datum, Inc., Anaheim, CA, 30 channels + 50 mv D.C. scan time = 250 ms for one sweep of all channels	1	All tests	All of the inputs from thermocouples were connected to the data logger.
11	High-speed instrumentation tape recorder.		1	All tests	Data from hydrocarbon sensors and radiometers recorded on this device.

the emission from a specific area of the flame. In the experiments, the wide-angle radiometers were set up with the axes of the instruments horizontal and aimed mostly on a vertical line directly over the spill point. In the case of narrow-angle radiometers, the "aim" was different in different experiments and these are indicated in Chapters 5 and 6.

In only one experiment (Test #5), a spectrometer was used to measure the flame infrared spectrum. This instrument was mounted on a mobile trailer and located a distance of 236 m from the pool fire. The spectrometer (a fast-scanning Michelson type) had a scan speed of 0.5 s.

All of the tests were recorded on movie films viewed from three different directions. The movie cameras were located on the cross-wind direction to get a side view, on the upwind (or downwind) to get a second orthogonal horizontal view. Another camera was suspended on a guy wire between two poles held aloft at about 80 m above ground. This overhead camera was arranged to record an overhead view of the experiments, but the full field of view was sometimes reduced since the camera tended to sway in the wind. All of the cameras recorded the experimental events at a speed of 100 frames per second.* Two of the pool fire tests were also recorded on 70 mm still films.

For the vapor fire tests, hydrocarbon sensors were located at 5 downwind locations on land. The sensors were installed about 0.6 m above-ground. These instruments were intended to measure the vapor concentrations before the ignition of the vapors by flares.

The electrical signal outputs from all of the measuring instruments were connected to a data logger and to the high speed tape recorder located in the instrument bunker by cables. The data logger is capable of taking in 30 channels of input. All channels can be scanned in 250 ms. In experiments 1-11, wind speed and wind direction were recorded on two channels each (on the tape recorder), one channel each of ambient temperature, pressure and relative humidity were also recorded. From Test #12 on, additional data such as wind speed (1 channel), wind direction (1 channel), ambient temperature (1 channel) and temperature differences (4 channels) in the atmosphere were also noted.

* In only one experiment - a vapor fire experiment, two additional movies were taken, one at 24 frames per sec and the other at 100 frames per sec.

The progress of the experiment was also monitored from a close-circuit television in the instrument bunker. The television camera was mounted on top of the bunker and had the ability to zoom on any specific spot. Also the camera could be panned.

Thermal imaging films of the vapor cloud were made in one experiment. Thermal imaging indicates the temperature distribution within the cloud. The principle of thermal imaging is based on the fact that the transmissivity of the various parts of the cloud for thermal radiation from a background source (such as the desert) is a function of the temperature. Because of the significant expense in the use of the thermal imaging camera, its use was discontinued after a single vapor fire test.

Additional instruments used included pressure gages to monitor the tank pressure, and a liquid depth gage to record the liquid level in the tank. These instruments were also monitored remotely from the instrument bunker.

3.3 EXPERIMENTAL PROCEDURE

The experimental procedures followed for both pool fire tests and vapor fire tests were similar up to a certain time, beyond which they differed because of the nature of the tests. In brief, the test procedure consisted of the following sequential steps.

1. Based on the wind direction and wind speed requirements for the test, an appropriate day for the test was chosen using the meteorological prognosis as a guide.*
2. The cryogenic tank was cooled by LNG. If the tank was at ambient temperature, it was first cooled by adding LNG slowly and cooling the tank by vaporizing the LNG until the tank reached the LNG boiling point. The tank was then drained to remove enriched LNG and loaded with fresh charge. If the tank was cold from a previous test, it was first drained to remove residue and loaded with fresh LNG.

* Significant delays were experienced in the test schedule, waiting for the wind to blow from the proper direction. Tests were not conducted for reasons of safety when the wind was blowing towards the bunker. Also because of the peculiar weather patterns over California during 1977, meteorological predictions on wind directions proved to be inaccurate.

3. On the day of the test all instruments were checked and the wind speed and direction were monitored for at least 2 to 3 hours before the test time. Also the tank was pressurized to between 2 and 6 atm (depending on required LNG flow rate) with nitrogen. When all systems were found to be in order and the wind was in the proper direction, the LNG spill initiation sequence was begun. The wind direction was less of a consideration (than wind speed) in pool fire tests.
4. The spill line was precooled by remotely opening the cool-down valve and allowing a small amount of LNG to flow down the spill line. All the recording instruments were turned on. The spill was initiated by electrically opening the solenoid valve located in the discharge pipe about 1/3 of the pipeline length from the tank. The time at which the valve opened was recorded. During the liquid discharge from the tank the pressure inside the tank was maintained to assure constant liquid flow rate. The pressure was preset at a value commensurate with the desired rate of flow.
5. The spill was monitored on the TV screen in the instrument bunker. In the case of pool fire tests, the flare was ignited at the same time the spill valve was opened. There is an inherent delay between the time the flare is ignited and fire appears from the flare case. In addition, there is a further delay until an ignitable gas mixture reaches the flare.

In the case of vapor fires, ignition was not effected at the spill point. The vapor cloud formed was allowed to drift over land. The land based flares were ignited when it appeared from the TV view and from the hydrocarbon sensor data that an ignitable mixture had reached them.
6. The spill valve on the discharge pipe was closed when the volume of liquid in the tank reached 1 m^3 . This "heel" was left in the tank to keep it cold until the next test.

7. The data obtained during the test were visually monitored and later processed on the NWC computer. Print out of the signal strength (in mv) in individual channels with time were obtained. Also plotted from the digitized data were the radiometer data (mv vs time).
8. The motion picture films were retrieved and processed. The data obtained in the experiments, significant observations on the behavior of the different fires and other information on the experiments are discussed in detail in the subsequent chapters.

4. LNG FLAME RADIATION SPECTRUM

4.1 INTRODUCTION

An understanding of the infrared radiation emission spectrum from an LNG flame is important from the point of view of knowing the distribution of energy in various bands and how this energy distribution is affected by the flame size, flame constitution and by the meteorological conditions. The knowledge of the total irradiance from the flame and the energy distribution in various wave lengths can then be utilized along with the absorption characteristics of the atmosphere (water vapor and carbon dioxide) to estimate the distances from the flame at which various levels of radiation hazards are produced.

In the current series of LNG fire experiments described in this report, only in one experiment (test #5, pool fire) was the fire radiation spectrum measured. In this chapter the details of the measured spectrum and its analysis are described.

The principal products that result from the (stoichiometric) combustion of methane and air are water vapor, CO_2 and nitrogen. In addition, in the case of hydrocarbon diffusion flames where the rate of entrainment of air is determined by the characteristics of the fire, soot formation occurs. Hence, the principal thermal emitters in an LNG fire are expected to be water vapor, CO_2 and soot. However, there may also be other emitters such as CO, CH_4 and other intermediate reaction products.

4.2 EXPERIMENTAL SPECTRAL DATA

A series of one hundred twenty eight (128) fast scan spectra were measured during test #5 involving a pool fire on water. The duration of each scan was about 0.5 seconds. The instrument was located at 236 m (775 ft) from the spill point mounted on an instrument truck parked just behind the bunker at the test site. The spectral range scanned wave lengths from 1.5 μm to 5.5 μm with a resolution of 7.7 cm^{-1} . The data obtained from different scans have been reduced at approximately 5 second intervals starting with the first at 5.4 s after the initiation of ignition.

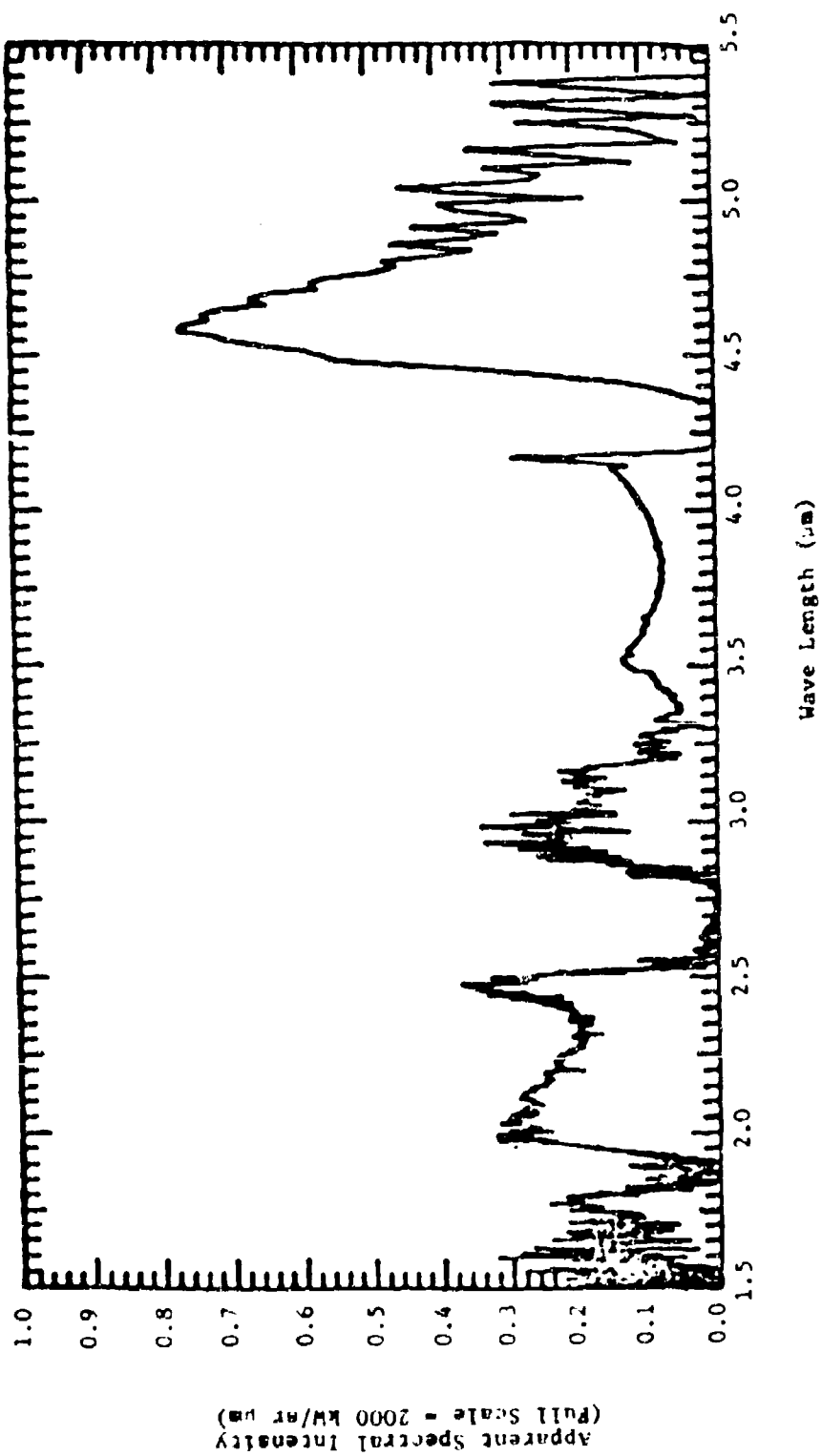


FIGURE 4.1: NWC SPECTRUM SCAN #47, AT 15 SEC. AFTER IGNITION

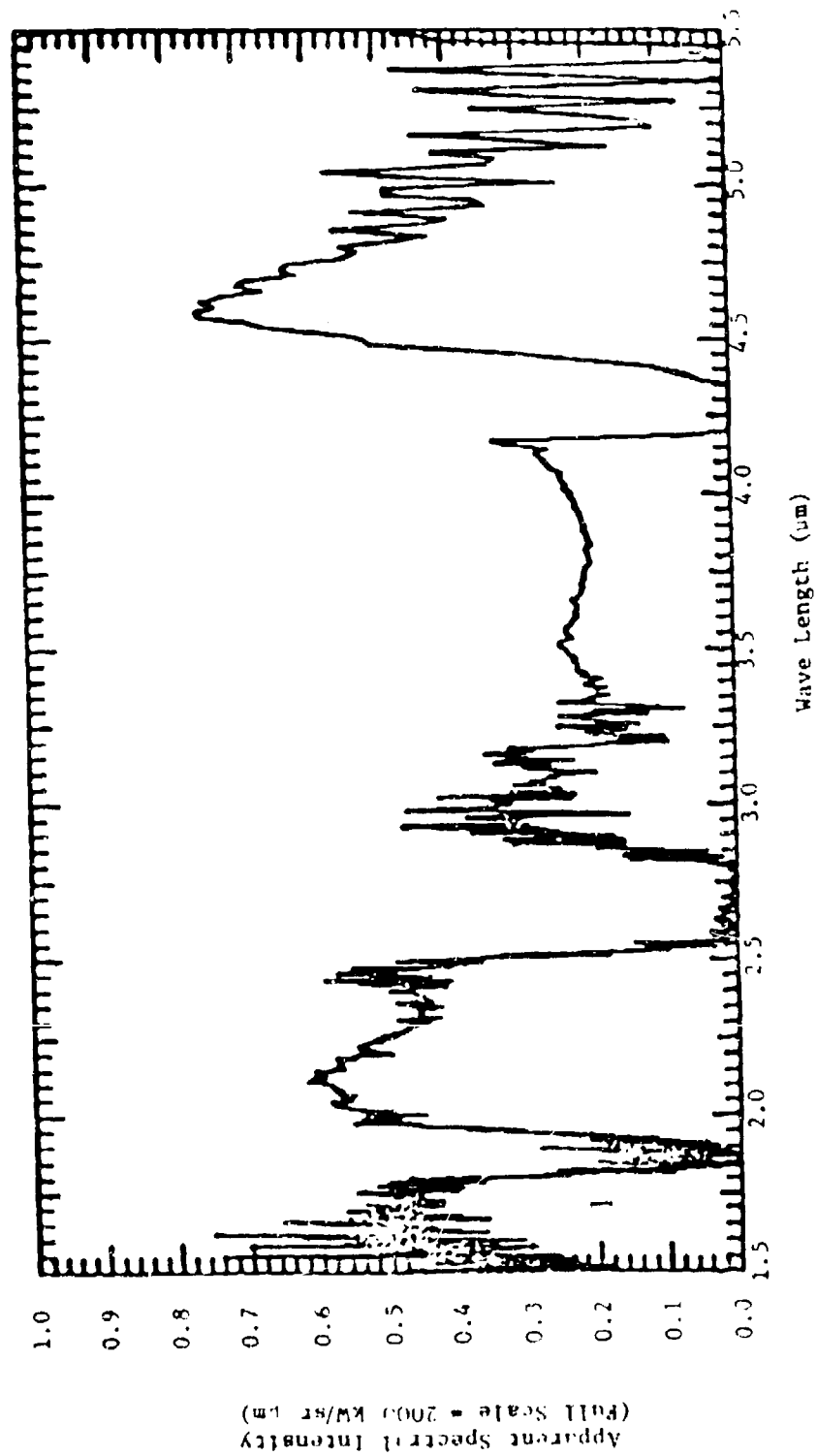


FIGURE 4.2: NWC SPECTRUM SCAN #92, AT 40 SEC. AFTER IGNITION

Figures 4.1 and 4.2 show two typical spectra measured at about 15 seconds and 40 seconds respectively, after ignition. A complete package of the reduced spectral data from the experiment is given in Appendix D.

4.3 INSTRUMENT AND CALIBRATION

4.3.1 Description of the Instrument

The instrument used for the spectral measurements was the fast scanning Michelson Interferometer, made originally by General Dynamics and subsequently modified. No fore optics were used either during the calibration or during the measurement. The field of view was, therefore, defined by the detector lens and the mask on the face of the detector to a 6° (full cone) angle. The detector was a liquid nitrogen cooled InSb diode and the beam splitter was made of KBr. The choice of the detector limited the interferometer to wave lengths (λ) less than $5.5 \mu\text{m}$. The spectrometer had two Intran 2 windows and two PbSe field lenses. A schematic diagram indicating the salient features of the interferometer used is indicated in Figure 4.3. The workings of the spectrometer are described in Appendix A.

4.3.2 Calibration Procedure and Scale Factor

A spectrometer must be calibrated in both wave length and energy. In the case of the fast-scanning Michelson interferometer that was used in the experiment, wave length calibration is based on the built-in He-Ne laser which controls the sampling rate of the recording of the interferogram. The instrument is thus inherently calibrated in wave length.

The spectrometer used in the test was calibrated against a standard black body source at 1116 K. The details of the calibration and the equations for determining the scale factor when the spectrometer is used to view the flame are described in part 2 of Appendix A.

The theoretical black body curve for a 1116 K temperature source and the measured spectrum are indicated in Figure 4.4. It is seen that the measured spectrum and theoretical spectrum are in excellent agreement over most of the wave lengths. The wide scatter in the measured spectrum between $1.5 \mu\text{m}$ and $2.0 \mu\text{m}$ is probably due to noise generated by instrument problems. The line structure at $2.5 \mu\text{m}$ is due to water absorption lines. The significant

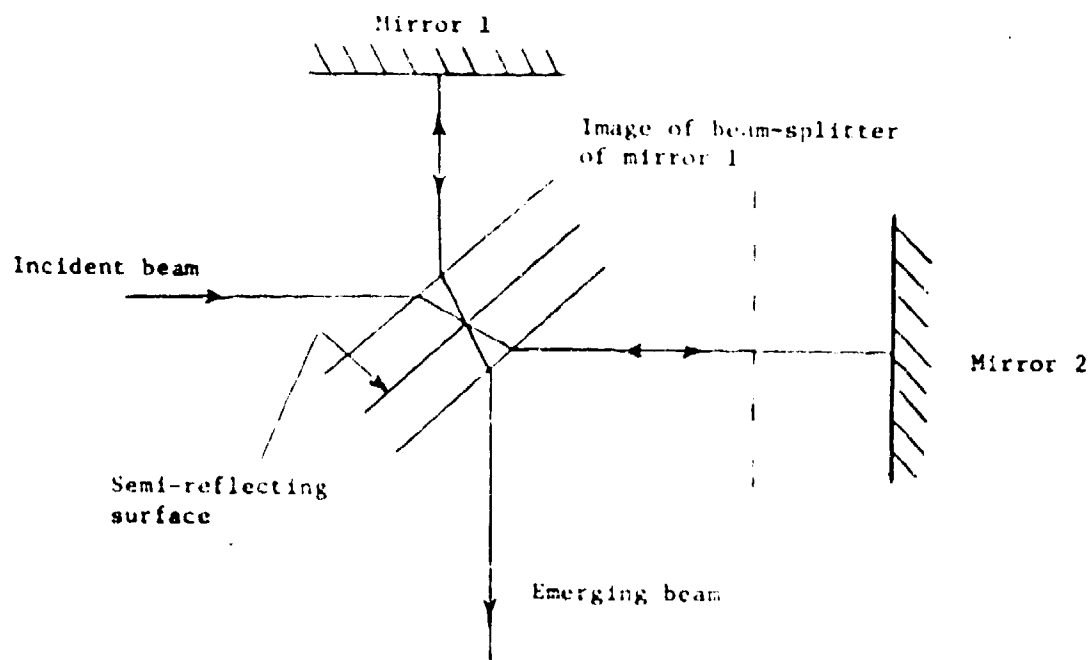


FIGURE 4.3: SCHEMATIC DIAGRAM ILLUSTRATING THE PRINCIPLE OF MICHELSON INTERFEROMETER

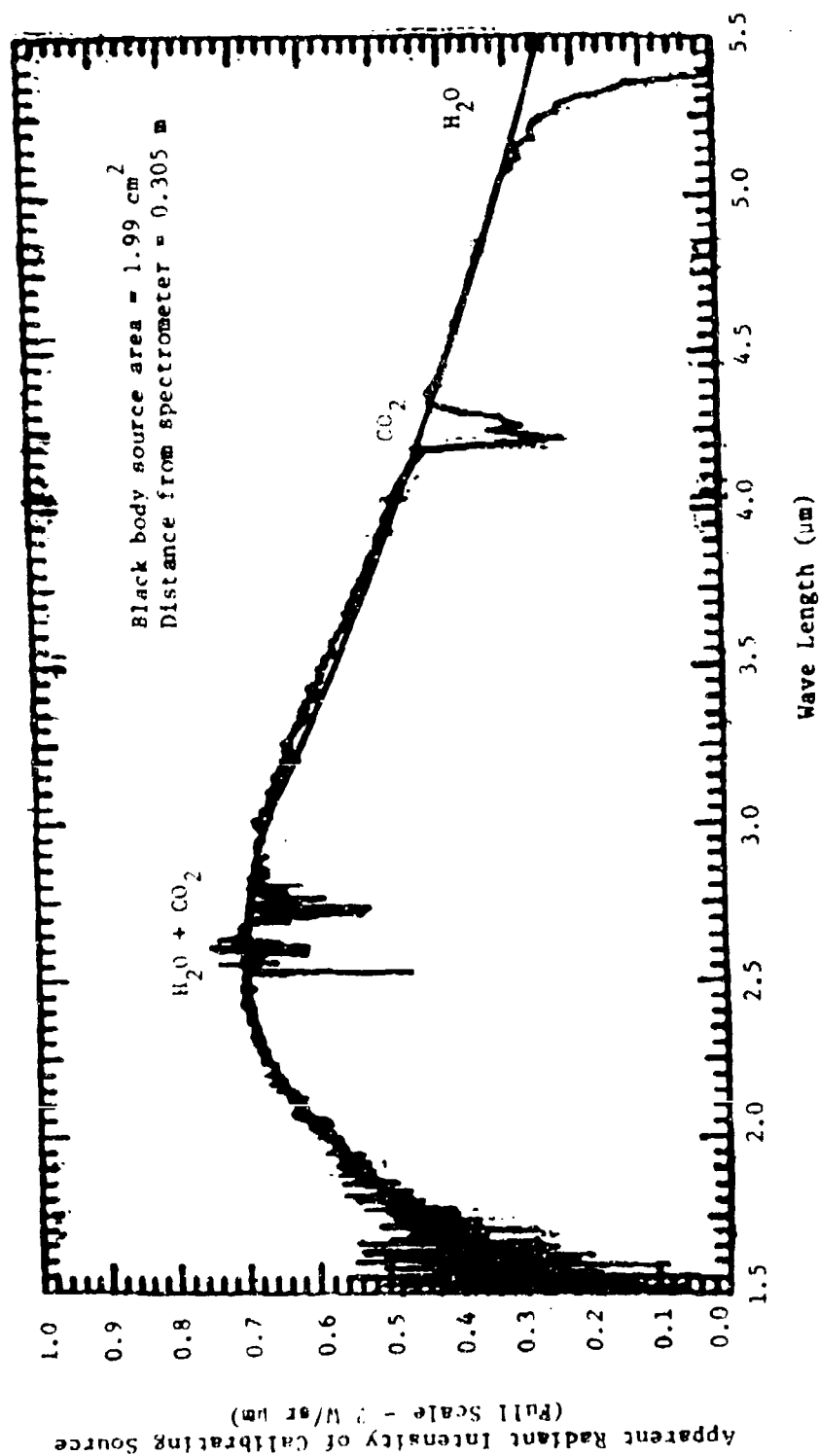


FIGURE 4.4: THEORETICAL AND MEASURED SPECTRUM OF A BLACK BODY AT 1116 K DURING CALIBRATION

dip at 4.3 μm (CO_2 absorption) seems to be inexplicably large, considering the calibration was done at short range to minimize atmospheric absorption.

The spectrometer calibrated as above was aimed at the flame in Test #5 from a distance of 236 m. The resulting spectra are presented with the full scale on the graphs representing an apparent spectral radiant intensity of 2,000 $\text{kW}/\text{sr}\mu\text{m}$. (NWC, 1976.)

At a range of 236 m (774 ft) and a full cone angle of 6° , the field of view covers a diameter of about 24.75 m. The center of the field of view of the spectrometer was aimed at between 3 and 5 m above the spill point. A schematic of the field of view at the instrument aperture is shown in Figure 4.5. The actual flame shapes seen by the crosswind movie camera at about 20 seconds (± 0.5 s) are also shown in Figure 4.5. It is estimated from the motion picture films of the experiment (see details in the next chapter) that the flame diameter is about 13 m. The view is such that a part of the reflection of the flame in water is also "seen" by the spectrometer. Some energy received (by the spectrometer) therefore represents the reflected energy from the water pool. However, this represents a small fraction of total energy received because of the comparatively small flame area "seen" in reflection. Also, the reflectivity of water is only on the order of 20% from 1 - 6 μm (with the exception of a peak of 40% at 3 μm). Therefore, we estimate the projected flame surface area seen by the spectrometer to be about $213 \text{ m}^2 \pm 13 \text{ m}^2$, assuming that the aim of the axis of the spectrometer is 4 ± 1 m above spill point.

Based on the above estimate for the area of the flame seen by the spectrometer, the spectral radiance represented by the full scale on the spectral graphs are

$$\text{Spectral radiance (full scale)} = \frac{2,000}{213} = 9.4 \pm \frac{0.60}{0.54} \text{ kW/m}^2 \text{ sr}\mu\text{m}$$

4.4 ATMOSPHERIC ABSORPTION

The principal constituents of the atmosphere that absorb thermal radiation are the water vapor (H_2O) and carbon dioxide (CO_2). Table 4.1 indicates the composition of various gases in the atmosphere.

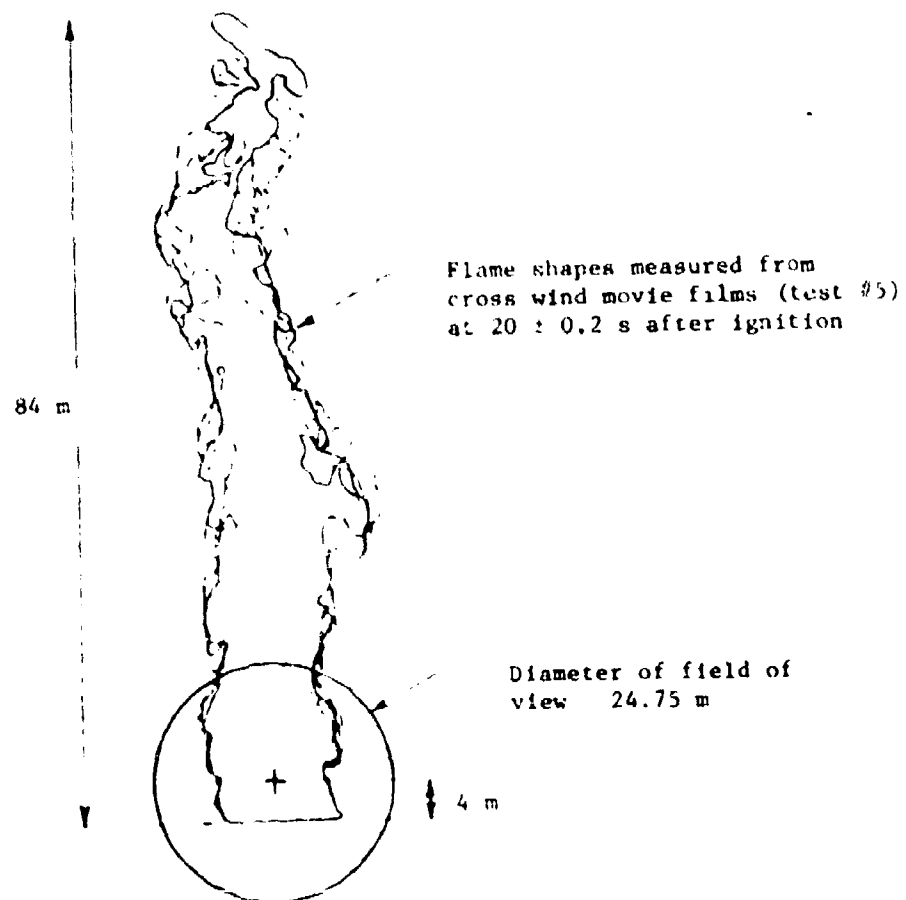


FIGURE 4.5: FIELD OF VIEW OF SPECTROMETER AT 236 m AND THE
RELATIVE LOCATION OF THE FLAME IN THE VIEW.

TABLE 4.1: CONSTITUENT GASES IN THE
ATMOSPHERE AND THEIR CONCENTRATIONS

Constituent Gas	Concentration in Atmosphere (% by volume)
Nitrogen	78.088
Oxygen	20.949
Argon	0.93
Carbon Dioxide	0.033
Neon	1.8×10^{-3}
Helium	5.24×10^{-4}
Methane	1.4×10^{-4}
Krypton	1.14×10^{-4}
Nitrous Oxide	5.0×10^{-5}
Carbon Monoxide	2.0×10^{-5}
Xenon	8.6×10^{-6}
Hydrogen	5.0×10^{-6}
Ozone	Variable
Water Vapor	Variable (depends on temperature and relative humidity).

* Source: Wolfe (1965)

The CO_2 content in the atmosphere is in general constant at about 330 ppm by volume, water vapor content varies strongly with temperature and humidity. On the day of test #5 for which the spectral data are available, the ambient temperature was 294 K (21°C) and relative humidity, 54%. Figure 4.6 indicates the relationship between atmospheric temperature, relative humidity and the amount of precipitable water vapor in a given path length. Using this figure and a path length of 236 m (775 ft), the precipitable water vapor is estimated to be 2.3 mm.

The principal absorption bands for water vapor are at 1.87 μm , 2.7 μm , and 6.27 μm (Wolfe, 1965). Minor absorption bands also exist at 0.94 μm , 1.1 μm , 1.38 μm , and 3.2 μm . Strong absorption by CO_2 exists in the 2.7 μm region, the 4.3 μm region, and the region between 11.4 μm , and 20 μm . Weaker absorption bands are present at 1.4 μm , 1.6 μm , 2.0 μm , 4.8 μm , 5.2 μm , 9.4 μm , and 10.4 μm . As the temperature of the emitting or absorbing species increases, the bands tend to broaden.

A useful concept for the quick estimation of atmospheric absorption of continuum radiation is the "equivalent bandwidth of complete absorption." One calculates the integral of absorption over an absorption band and interprets the result as the width of a "rectangular" complete absorption band equivalent to the real band profile. For a continuum source, the effect of such opaque bands is then easy to estimate. Three absorption bands, in the range of interest (1.5 μm through 5.5 μm) can be described in this way. These are the water bands at 1.87 μm and 2.7 μm and the 4.3 μm CO_2 band. The water absorption beyond about 4.7 μm is not as readily dealt with since the band structure is not narrow compared to the range of interest. However, the fraction of total energy from a 1300 K black body that lies beyond 4.7 μm is about 25% and that beyond 5.5 μm is only 19%. The results of total absorption bandwidth calculations for the above three bands of interest are given in Table 4.2a and 4.2b. The calculations are based on the data available in the Infrared Handbook (Wolfe, 1965). Also given in the tables are the fractions of a 1300 K black body energy that will be absorbed in each of the bands. Atmospheric temperature is assumed to be 300 K in these tables.

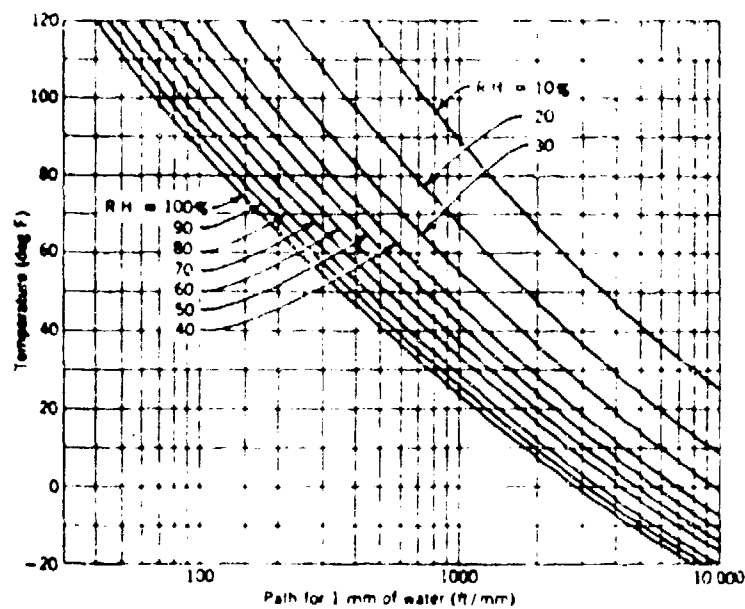


FIGURE 4.6: VARIATION OF PRECIPITABLE WATER
CONTENT OF ATMOSPHERE WITH TEMPERATURE,
HUMIDITY AND PATH LENGTH

* Source: Kruse, et al. (1962)

TABLE 4.2a: TOTAL ABSORPTION BAND WIDTH FOR 1.87 μm
AND 2.7 μm WATER BANDS AT 300 K

Precipitable Water (mm)	1.87 μm Band		2.7 μm Band	
	Total Absorption Band Width $\Delta\lambda$ (μm)	Fraction of 1300 K Black Body Energy Absorbed	Total Absorption Band Width $\Delta\lambda$ (μm)	Fraction of 1300 K Black Body Energy Absorbed
5	0.16	.04	0.58	.16
2	0.12	.03	0.51	.14
1	0.1	.03	0.45	.12
0.1	0.033	.01	0.22	.06
0.01	0.01	.003	0.07	.02

TABLE 4.2b: TOTAL ABSORPTION BAND WIDTH FOR 4.3 μm
CO₂ BAND AT 300 K

Path Length Through the Atmosphere (m)	Total Absorption Band Width $\Delta\lambda$ (μm)	Fraction of 1300 K Black Body Energy Absorbed
1000	.28	.04
236	.24	.03
100	.22	.03
10	.17	.02
1	.065	.01
0.3	.033	.004

The detailed calculations of the atmospheric transmissivity for different wave lengths is a tedious job. Fortunately, the absorption is minimal except at certain bands. The atmospheric absorption tables for different path lengths, bands and humidity conditions are available in the literature (see Hudson, 1969; Wolfe, 1965). Utilizing these tabulated values* we have estimated the transmissivity variation in the atmosphere with wave length for a path length of 236 m and 21°C, 54% relative humidity (2.3 mm precipitable water vapor).

Table 4.3 shows the transmissivity of H₂O (2 mm of precipitable water) and CO₂ (200 m path length) and the total transmissivity as a function of the wave length of radiation. The total transmissivity is plotted in Figure 4.7. This transmissivity is construed as the one applicable to interpreting the spectral data. The error due to the use of data for a 200 m path length for CO₂ (instead of the actual 236 m) and for 2 mm precipitable water (instead of the actual 2.3 mm) is expected to be small.

4.5 ANALYSIS OF SPECTRAL DATA

During the experiment, 128 spectral scans were made (each scan of duration 0.5 seconds). Data from 12 representative spectra have been reduced, spaced about 5 seconds apart. The duration of the intense fire in this test lasted only for about 26 seconds, and the spectral data covered this duration and beyond. Figures 4.1 and 4.2 are typical spectral records representing an early stage and latter stage of the fire. All of the 12 spectral records measured and reduced are given in Appendix D. Only one record is analyzed in detail for making quantitative estimates of fire radiation and for the purposes of discussions.

* At a wave length of 1.9 μ m and 2 mm precipitable water, the fraction of energy absorbed in the atmosphere, according to the table in Hudson (1969), is 0.175. However, this is in conflict with the measured spectrum where the absorption is about 98%, and it is also in conflict with the data in the IR Handbook (Wolfe, 1965).

TABLE 4.3: VARIATION OF TRANSMISSIVITY OF ATMOSPHERE WITH
WAVE LENGTH FOR THE CONDITIONS OF THE EXPERIMENT

Wave Length	Transmissivity			Wave Length	Transmissivity		
(μm)	H ₂ O	CO ₂	Total	(μm)	H ₂ O	CO ₂	Total
1.5	0.98	1.0	0.98	3.6	0.97	1.0	0.97
1.6	0.11	1.0	0.11	4.0	0.99	1.0	0.99
1.8	0.24	1.0	0.24	4.1	0.98	0.97	0.96
1.9	0.82	1.0	0.82	4.2	0.97	0.55	0.53
2.0	0.93	0.95	0.88	4.3	0.95	0.016	0.015
2.1	0.98	1.00	0.98	4.4	0.91	0.32	0.29
2.2	0.99	1.00	0.99	4.5	0.87	0.95	0.83
2.3	0.98	1.0	0.98	4.6	0.82	1.0	0.82
2.4	0.91	1.0	0.91	4.8	0.74	0.97	0.72
2.5	0.69	1.0	0.69	5.0	0.63	1.00	0.63
2.6	0.002	1.0	0.002	5.2	0.38	0.98	0.37
2.8	0.001	0.8	0.001	5.4	0.12	1.00	0.12
3.0	0.4	1.0	0.4	5.6	0.002	1.00	0.002
3.2	0.67	1.0	0.67				
3.4	0.88	1.0	0.99				

- Reference Kruse et al. (1962), Hudson (1969)
- Conditions of the experiment 21°C, 54% RH (2.3 mm precipitable water vapor).
- Table is based on 2 mm water vapor and 200 m path length for CO₂

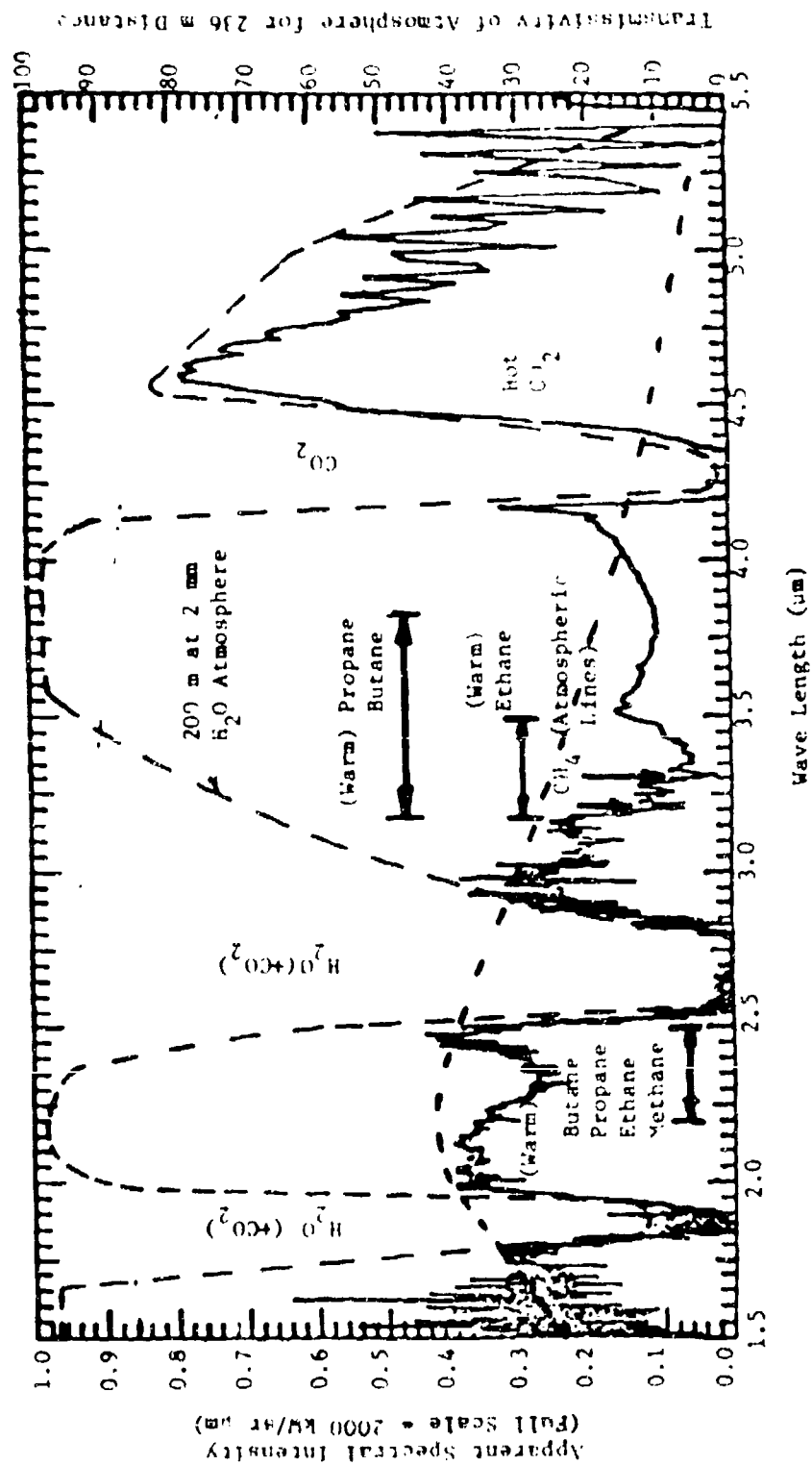


FIGURE 4.7: LNG POOL FIRE RADIATION SPECTRUM TAKEN AT 20 SECONDS AFTER IGNITION AND
CALCULATED ATMOSPHERIC TRANSMISSIVITY AT DIFFERENT WAVELENGTHS FOR A
200 M PATH LENGTH.

4.5.1 Analysis of a Specific Spectral Scan

Figure 4.7 shows the radiation spectrum measured in scan #56 at about 20 seconds after the ignition of the spill.* The motion picture records of the experiment and the radiometer data (see Chapter 5) indicate that at 20 seconds after ignition, the burning is "intense" and quasi steady.

The figure clearly shows the atmospheric absorption of the radiation by the 1.87 μm and 2.7 μm water bands and by the 4.3 μm CO_2 band. The flame has no resemblance, spectrally, to a black or grey body emitter. This is not merely due to the atmospheric and other absorption spectra superimposed on it but chiefly due to the fact that a very large part of the radiation originates from gaseous species, chiefly H_2O and CO_2 . The remainder of the total emission comes from luminous soot particles. Even the latter will not necessarily emit as an isothermal black body radiator because the outer layers of the flame will be at different temperatures than the inner ones. The soot particles, in general, are much smaller (1000 \AA^2) than the wave lengths corresponding to the peak emission intensity of a black body in the temperature range of 1300 K - 1500 K (2.3 μm - 1.9 μm). Therefore, wave length dependent effects and the non-uniform temperature effects can be expected to influence the emission from optically thin luminous soot layers. In particular, peculiar spectral brightness changes for the particular wave length can be expected toward the limb of the flame in contrast to a uniform Lambertian radiator. A Lambertian radiator is one in which radiance falls off strictly with the cosine of the angle of emission with respect to the direction of view.

Our analysis of the spectrum shown in Figure 4.7 indicates the following:

* The full-scale value of the ordinate in the figure is equal to an apparent flame intensity of 2000 kW/Sr μm . To get the actual radiance at any wave length, the measured radiance has to be divided by the transmissivity of the atmosphere.

1.5 - 1.75 μm

The line spectrum indicated in this region is probably due to the noise in the instrument. This is also apparent in the calibration, as can be seen in Figure 4.4. However, the mean level of the noise can be interpreted as due to soot emission.

1.75 - 2 μm

This region is dominated by the 1.87 μm water (and some CO_2) absorption band. The shape of the spectrum agrees with known atmospheric spectra, but not with the atmospheric absorption tables indicated by Hudson (1969). According to Plass in I.R. Handbook (Ref. Wolfe, 1965), the equivalent total absorption bandwidth* at 1.87 μm is 0.12 μm . In fact, it is seen from the data that the totally absorbed band has a width about this value.

2.0 - 2.6 μm

Since most of the water vapor and CO_2 emissions from the flame are absorbed by the same species in the atmosphere before reaching the spectrometer, most of the spectral record obtained (Figure 4.7) can be interpreted as indicating the luminous soot emission modified by atmospheric absorption. The most probable soot emission is indicated in Figure 4.7. The peak spectral intensity due to soot emission is probably within the 2 μm to 2.3 μm wave lengths. It is seen that the soot is assumed to be a grey emitter, its temperature is between 1450 K and 1260 K. The absorption between 2.2 - 2.5 μm is probably caused by hydrocarbons (butane, propane, ethane, and methane) at an intermediate temperature. Considering the probable soot line indicated in Figure 4.7, and the actually observed spectrum, it is seen that the minimum transmission is about 70% through the atmosphere. This occurs at 2.35 μm at the above wave length. Therefore, if the absorption were due to low concentration, cold hydrocarbon gases one would see more line structure than has been observed. It can, therefore, be inferred that what is observed is due to hot (< 1300 K) relatively high concentration gases, which may be optically thick. We are unable to explain where these gases may be located in the flame.

* For the amount of precipitable water vapor (2.3 mm) contained on the day of the experiment between the flame and spectrometer.

2.6 - 4.3 μm

This region is dominated by the total absorption water vapor band at 2.7 μm . As can be seen from Table 4.2a, the total absorption bandwidth is about 0.5 μm , (for 2 mm water). Hence, one expects the "well" to occur between 2.45 μm through 2.95 μm . The actually observed "well" is only between 2.55 μm - 2.75 μm . The spikes of emission seen on both sides of the absorption band at 2.7 μm are the partially absorbed hot water vapor emissions from the flame. These penetrate through the absorption band spectrum of cold water vapor in the air to some degree because the spectral line positions for hot and cold water vapors do not precisely coincide.

Sharp methane lines at 3.2 and 3.3 μm are probably of atmospheric origin rather than due to methane vapors generated by LNG vaporization. Also noticed is a broad absorption band between 3.2 and 4 μm . The absorption in the 3.2 - 3.5 μm can be identified as due to intermediate temperatures, high concentration optically thick hydrocarbons. The bands are nearly "bottomed" and no line structure is present. It is possible that the soot radiation in this region is almost completely absorbed and what we are seeing is the emission from warm hydrocarbon (propane, ethane, and butane) gases that are optically thick.

The region between 3.5 - 4 μm is very interesting in that it exhibits no line structure at all (note the spectral resolution is 7.7 cm^{-1} or $1.12 \times 10^{-2} \mu\text{m}$). Also, the transmissivity for soot radiation seems to be about 40%. This absorption must be due to cold hydrocarbon gases possibly on the outside of the flame.

Finally, in this region the pronounced "blue spike" is noticeable at 4.15 μm . This is due to hot CO_2 emission lines not occupied by cold, atmospheric, CO_2 absorption lines.

4.3 - 5.5 μm

The strongest CO_2 emission and absorption bands are centered around 4.3 μm . The spectral band associated with the atmospheric CO_2 absorbs much of the energy emitted by hot CO_2 and CO in the flame. However, as

indicated in Table 4.2b the bandwidth for total absorption for a 236 m path through the atmosphere is about 0.2 μm . Hence, any CO_2 emission from the flame in the 4.18 μm - 4.42 μm should be absorbed completely, as is indeed noticed in the spectral record shown in Figure 4.7. The total bandwidth for CO_2 emission from the flame at 4.3 μm is dependent on the flame temperature and the partial pressure - beam length product. Neither of these quantities was, however, measured. But it can be stated qualitatively, that the emission bandwidth at flame temperature is much larger than the atmospheric absorption bandwidth. Hence, some of the CO_2 emission will get through. This is indeed observed with a peak recorded at 4.6 μm . The thermal emission spectrum from the vibrational band of hot CO_2 is distorted considerably by water vapor in the atmosphere, beyond about 4.5 μm . The region between 4.5 and 5 μm is commonly referred to as the "red spike" and is seen in many other atmospheric measurements.

At about 4.6 μm the atmosphere is relatively transparent. For the spectrometer distance, the atmospheric transmissivity is 0.82 (see Table 4.3). The apparent spectral radiance at the above wave length is 7.25 kW/m^2 or μm , which corresponds to a black body temperature of 1425 K. Accounting for the atmospheric absorption, the flame spectral intensity at 4.6 μm is 8.83 kW/m^2 or μm which corresponds to a black body of 1550 K. The true temperature of the flame, is of course, greater than this temperature if the spectral emissivity of the CO_2 at 4.6 μm is less than unity. This calculation seems to indicate that the vibrational band emission of CO_2 is in equilibrium with the thermal motions of the molecules in the flame. As such, assigning a "temperature" to the flame is valid. This aspect is covered in the Discussion Section.

From 4.7 μm , a strong water absorption band with a resolved line spectrum begins. The atmosphere becomes completely opaque at about 5.5 μm . According to Plass (Wolfe, 1965) this water band is strong enough to be opaque even at water concentrations much below 1 mm of precipitable water. Radiation in this wave length range will be absorbed completely in tens of meters rather than hundreds of meters.

5.5 μm - 25 μm

No spectral data were measured in regions beyond 5.5 μm . In Figure 4.8 the percent of total black body energy emitted within a given wave length is plotted as a function of the wave length with temperature as a parameter. It is seen from this figure that the fraction of total energy in wave lengths beyond 5.5 μm ranges from about 26% at 1100 K to about 14% at 1500 K. The atmosphere is practically opaque (water absorbtion band) in the entire region 5.4 μm through 7.4 μm (Wolfe, 1965). The second important absorption band is one due to CO_2 at 15 μm . For a 300 m path through the atmosphere the complete absorption bandwidth centered at 15 μm is about 1.5 μm (from 14 to 15.5). Finally, there is a significant H_2O absorption between 20 μm and 23 μm with total absorption beyond 23 μm .

4.5.2 Changes in Spectral Data with Burn Time

A review of the twelve spectral records (given in Appendix D) taken at 5 second intervals starting from about 5 seconds after ignition of the LNG pool indicates the following features:

1. The CO_2 emission in the 4.3 μm band dominates the emission in the early stages. As much as 45% of total energy received by the spectrometer is accounted for by the CO_2 band.
2. The soot emission gradually increases and dominates towards the end of the fire life. This may be due to the increased luminous soot formation by the combustion of propane, butane, and ethane during the final stages of the LNG fire. In this test, the LNG was about 75% methane, 19% ethane, and 6% propane.
3. The strong absorption bands due to an outer layer of hydrocarbons, seen in early spectral records, disappear completely during the last 15 seconds of burning. The first to disappear is propane + butane absorption at about 15 seconds before the end, followed by that of ethane, 5 seconds later.

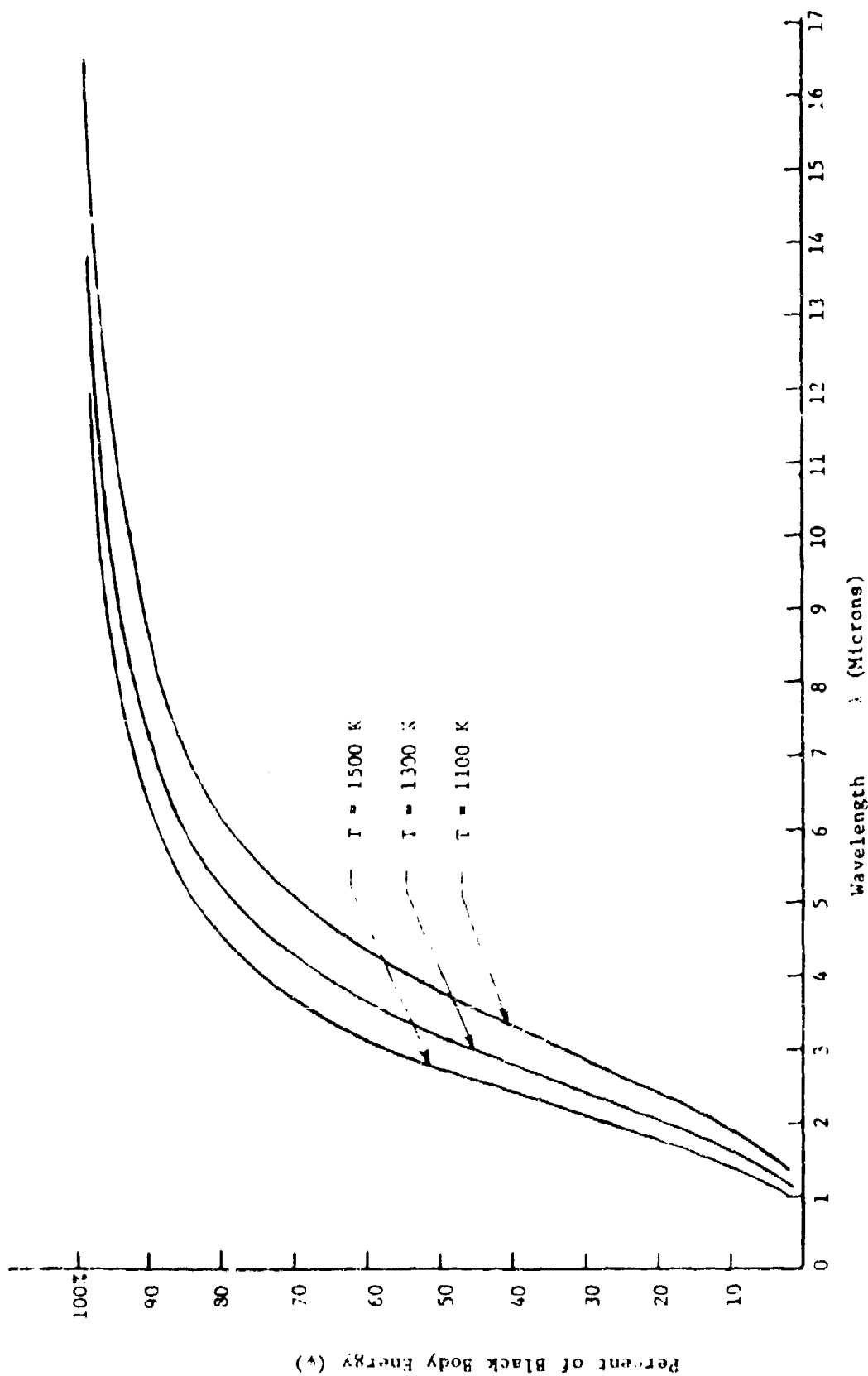


FIGURE 4.8: PERCENT OF TOTAL BLACK BODY ENERGY BELOW A GIVEN WAVE LENGTH VS. THE WAVE LENGTH

To compare the relative importance of CO_2 emission and luminous soot emission received by the spectrometer, their ratio is plotted versus burn time. This is shown in Figure 4.9. The area under the measured spectral curve between 1.5 and 4 μm is assumed to represent the radiance due to soot.* The area under the spectral curve beyond 4 μm is assumed to be due to CO_2 . It is seen that the CO_2 emission relative to that of soot increases up to about 30 seconds; subsequently CO_2 emission is lower compared to that of soot. Also observed is a sudden jump in the spectral intensity of the soot, by almost 50%, between scan #83 (at 35 seconds into the burn) and scan #92 (at 40 seconds). The visible flame in the motion pictures do not exhibit any noticeable differences between 35 s and 40 s.

One possible explanation for such a sudden increase in luminous soot emission could be the burning of increased quantities of ethane and propane. It has been found in other experiments in the laboratory (Valencia and Reid, 1979) that during the boiling of LNG on water, the rate at which different fractions evaporate changes drastically. Initially methane evaporates preferentially. After a certain duration of time, the methane fraction in the vapor decreases drastically, and there is a sudden increase in ethane fraction. Similarly after most of the ethane is evaporated, the propane starts to vaporize. This phenomenon of preferential evaporation should also be occurring in the case of the pool of LNG on fire.

4.5.3 Estimation of Soot Temperature and Emissivity

Except for the CO_2 band emission at 4.3 μm , the rest of the energy received by the spectrometer can be construed to be due to the luminous soot emission modified by the atmospheric absorption. The water vapor emissions from the flame are almost completely absorbed in the atmosphere. The inspection of scan 56 spectral record (shown in Figure 4.7) does not give direct information on the soot conditions. It is difficult

* The choice of 4 μm is somewhat arbitrary. However, since the purpose of figure is to illustrate the relative strengths of soot and CO_2 emission, this arbitrariness is not expected to affect the conclusions.

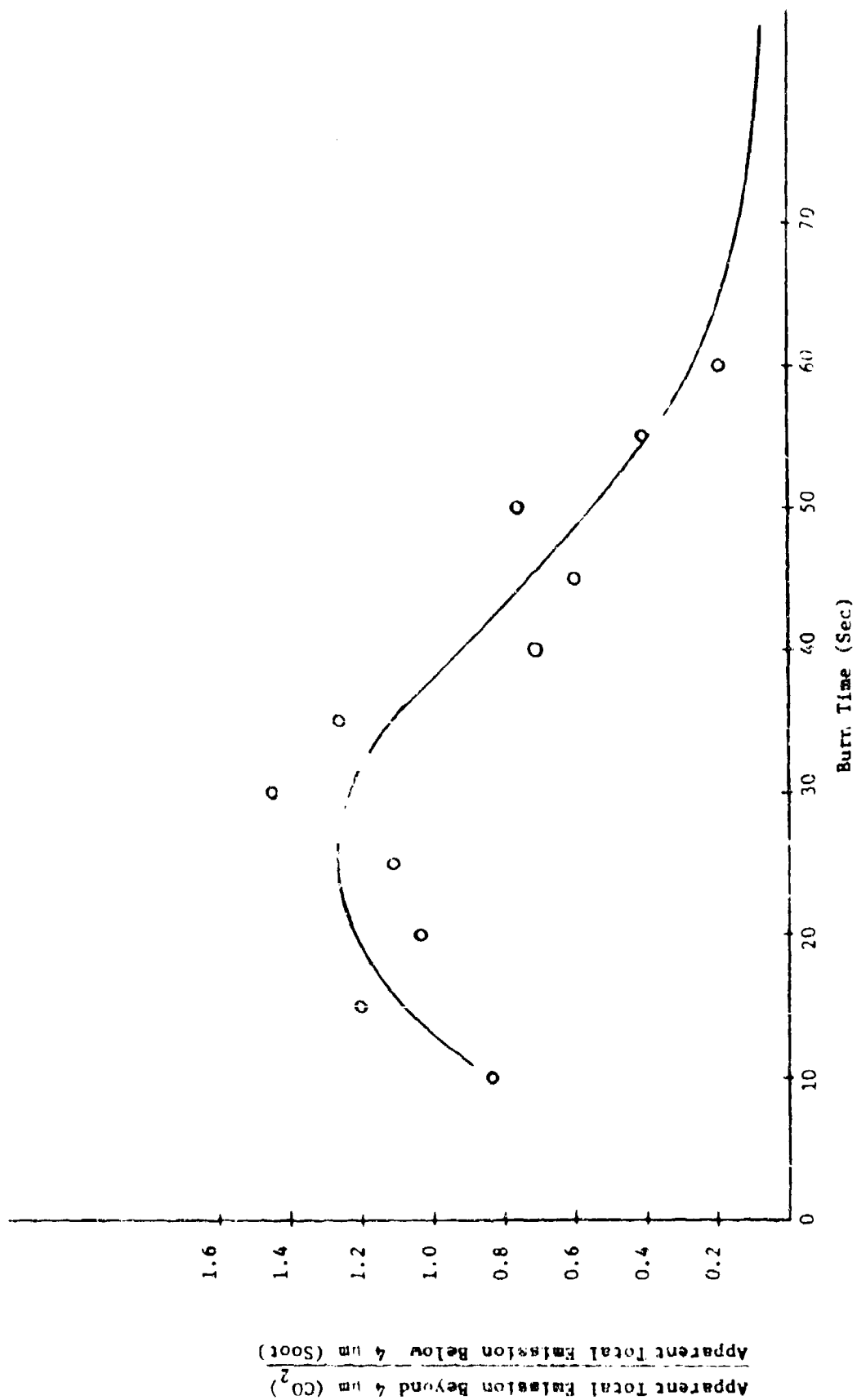


FIGURE 4.9: RATIO OF CO₂ TO SOOT EMISSION VS. BURN TIME

to estimate the magnitude of maximum spectral intensity from the soot as well as the location of this maximum. We have, therefore, tried to fit the observed soot radiation by comparing it with grey body emitters of different temperatures. In Table 4.4 are shown the assumed soot temperature, the wave length at which spectral intensity is a maximum, the magnitude of maximum spectral intensity of a black body, and the estimated soot emissivity. In Figure 4.10 the comparison between the emission from grey bodies at different temperatures and the observed soot spectral radiance are compared. The theoretical curves are all normalized with respect to maximum spectral intensity. These curves are generated by the Planck equation (see equation 3, Appendix A).

As can be seen from Figure 4.10, the luminous soot temperature cannot be estimated very precisely. Our estimating technique is based on noting the wave length at which we think the peak intensity from soot is located and comparing this with the wave length at which maximum intensity occurs for a theoretical grey body emission. We recognize the difficulty in this judgmental procedure and also the fact that atmospheric absorptivity is not a constant over the wave length region of interest. However, recognizing the above uncertainty, it can be argued that the luminous soot temperature is between 1300 and 1400 K. From Table 4.4 we see that the calculated luminous soot emissivity in this temperature range varies between 0.28 and 0.19, respectively. In this calculation, it is assumed that the value of peak spectral radiance observed in the luminous soot emission is $4.27 \text{ kW/m}^2 \text{ sr } \mu\text{m}$.

The above values for the luminous soot emissivities are somewhat greater than the value of 0.1 suggested by Hottel and Sarofim (1967, p. 247) to account for luminous soot emissivities in methane gas fired furnaces. It is possible that in diffusion flames in the open, a larger fraction of the fuel forms soot, hence higher soot emissivities.

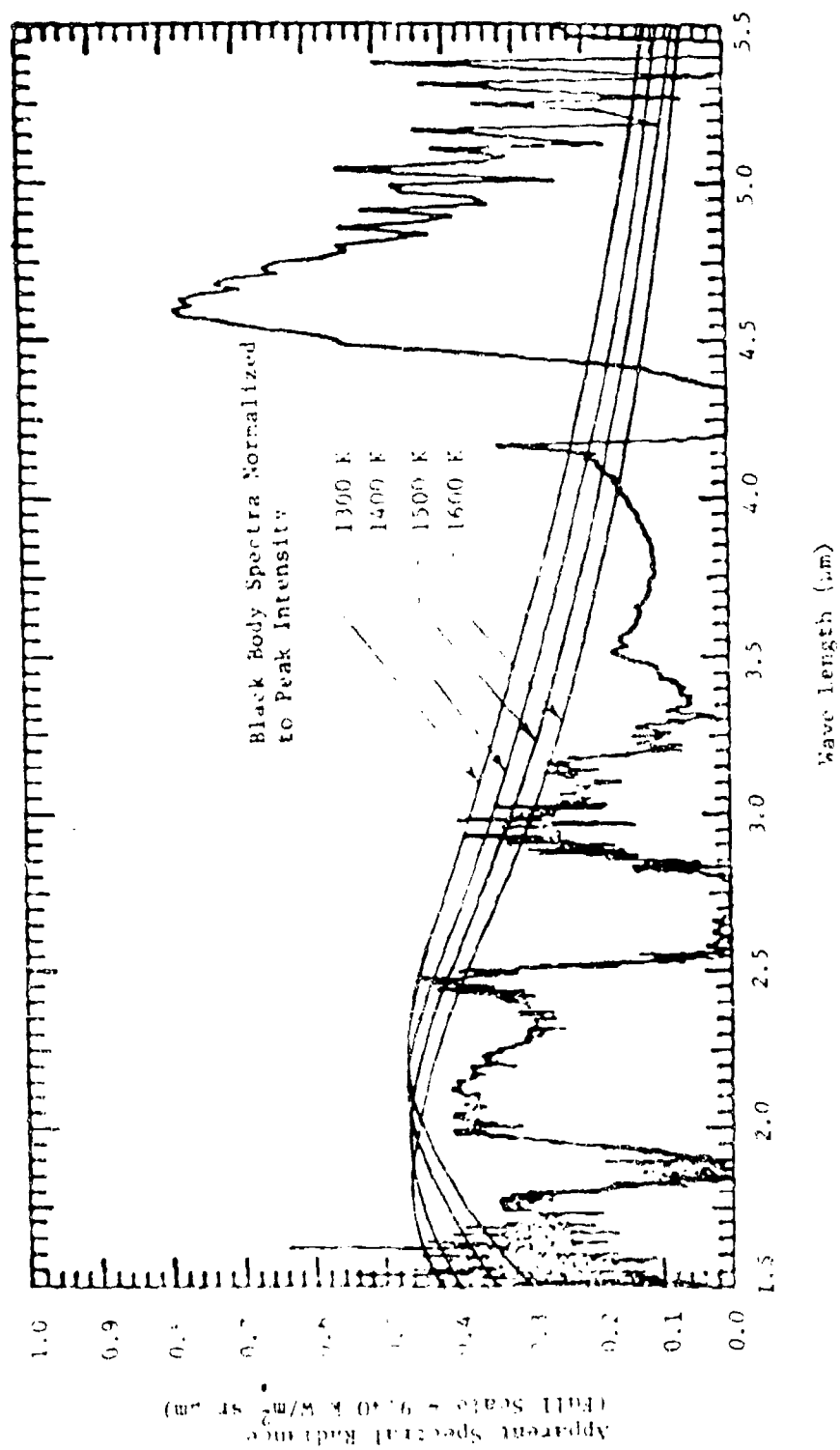
The soot emissivity indicated in Table 4.4 refers to the value at peak radiance corresponding to the temperature chosen. It is, however, known for hydrocarbon fires that the soot emissivity does change with wave length (Burgess and Hertzberg, 1974). The spectral emissivity

TABLE 4.4: ESTIMATION OF SOOT TEMPERATURE AND SOOT EMISSIVITY

Assumed Soot Temperature (K)	Wave Length at Maximum Spectral Intensity (μm)	Magnitude of Maximum Spectral Intensity ($\text{kW}/\text{sr } \mu\text{m}$)	Observed Maximum Spectral Intensity ($\text{kW}/\text{sr } \mu\text{m}$)	Estimated Emissivity of Soot* (ϵ_{soot})
1200	2.415	2169.3	910	0.42
1300	2.229	3237.0	910	0.28
1400	2.070	4688.8	910	0.19
1500	1.932	6620.3	910	0.14
1600	1.811	9141.6	910	0.10

+ Based on an area of flame of 213 m^2 observed in the field of view of the spectrometer.

* Soot emissivity = $\frac{\text{observed maximum spectral intensity}}{\text{maximum spectral intensity of a black body}}$



* Apparent Peak Spectral Radiance at all temperatures = 0.45

FIGURE 4.10: COMPARISON OF SOOT EMISSION WITH BLACK BODY SPECTRA AT DIFFERENT TEMPERATURES

of soot varies as

$$E_{\lambda, \text{ soot}} \propto \lambda^{-0.77} \quad (4.1)$$

If this relationship is applicable, then the spectral emissivity of the soot (in scan #56) at a wave length of 5.5 μm , and flame temperature of 1400 K will be 0.09 instead of 0.19 as indicated in Table 4.4.

The variation of estimated soot emissivity with burn time is given in Table 4.5 for (assumed) different flame temperatures. It is interesting to note that the soot emissivity increases with time. This may be a result of the burning of higher hydrocarbon fractions such as ethane, propane, and butane. (The variation in the spectral characteristics with time was discussed in Section 4.5.2.) This observation of increased radiation from the flame with time is also indicated by the narrow angle radiometer data (see Chapter 5, Figure 5.17). We note, however, that both instruments were looking at the lower sections of the flame where significant soot formation may not occur, compared to the middle and top sections of the flame which may have relatively high soot concentrations.

4.5.4 Estimation of Flame Emissive Power

The estimated field of view of the spectrometer and the portion of the LNG flame in the field of view are shown in Figure 4.5. It is not certain as to how much of the reflection of the flame in the pond water was "seen" by the spectrometer. It is conceivable that the lower half of the field of view intersected some land also. Because of these uncertainties the exact area of the flame (emitting radiation) seen by the spectrometer cannot be ascertained. For the purposes of evaluating the flame emissive power we assume that only that part of the flame area above the water surface seen by the spectrometer radiates the energy intercepted by the spectrometer. Hence, the radiating area of the flame (A_f) is $13 \text{ m} \times 16.4 \text{ m} \approx 213 \text{ m}^2$.

The flame emissive power (E) is now calculated using the equation:

$$E = \frac{\pi}{A_f} \int_{\lambda=0}^{\infty} \frac{N_{\lambda}}{\tau_{\lambda}} d\lambda \quad (4.2)$$

TABLE 4.5

VARIATION OF ESTIMATED SOOT EMISSIVITY WITH TIME
FOR DIFFERENT ASSUMED FLAME TEMPERATURES

Assumed Flame Temperature (K)	Soot Emissivity (ϵ_s) Obtained from Spectral Scans		
	Scan #47 (15 s after burn)	Scan # 56 (20 s after burn)	Scan # 92* (40 s after burn)
1200	0.30	0.42	0.58
1300	0.20	0.28	0.39
1400	0.14	0.19	0.27
1500	0.10	0.14	0.19
1600	0.07	0.10	0.14

* The spectrum does not change significantly between that at 20 s (Scan #56) and that at 35 s (Scan #59).

where N_λ is the spectral intensity measured by the spectrometer (kW/sr μm) at wave length λ (μm), and $\bar{\tau}_\lambda$ the total atmospheric transmissivity between the flame and the spectrometer.

In applying equation 4.2 to the measured spectrometer data we recognize two problems. The first is the fact that spectral data are available only in the 1.5 - 5.5 μm wave length range. Therefore, any estimate of the emissive power is probably lower by about 25% when compared to the actual emissive power (see Figure 4.8). The second and perhaps the more serious problem is the total absorption of water band emissions (1.87, 2.7 μm) and the partial absorption of CO_2 emission (4.3 μm). Since the energy received by the instrument in these bands is essentially zero and since the atmospheric transmissivity for the path length to the spectrometer is also zero, the integrand in equation 4.2 becomes indeterminate at the above bands. The physical meaning of this result is that the actual emission intensities in these bands cannot be estimated using the spectrometer data.

4.5.4.1 Apparent Emissive Power of the Flame

For purposes of illustration and to compare with the emissive power calculated from radiometer data, we have estimated the "apparent" flame emissive power using the formula:

$$E_{\text{apparent}} = \frac{\int_{1.5}^{5.5 \mu\text{m}} N_\lambda d\lambda}{\bar{\tau}} \quad (4.3)$$

where the integral represents the area under the apparent intensity - wave length curve (measured in the experiment) shown in Figure 4.7. The term $\bar{\tau}$ represents the mean atmospheric transmissivity excluding the 1.87, 2.7, and 4.3 μm bands.

For the spectral data of scan #56, the total area under the spectral curve is equal to 1820 kW/sr. Therefore,

$$\begin{aligned} \text{Apparent radiance of the} \\ \text{fire* (based on energy} \\ \text{received by the spec-} \\ \text{trometer).} \end{aligned} = \frac{1820}{213} = 8.55 \text{ kW/m}^2 \text{ sr} \quad (4.4a)$$

* radiance = emissive power in a unit solid angle.

Apparent emissive power

$$E = \text{(corrected for absorption in the atmosphere not including H}_2\text{O and CO}_2\text{)}^* = \frac{8.55 \times \pi}{0.75} = 35.8 \text{ kW/m}^2 \quad (4.4b)$$

4.5.4.2 True Emissive Power

The true emissive power of that part of the fire seen by the spectrometer may be estimated from the information contained in the 4.3 μm CO_2 band. The calculation is based on the principle of estimating the partial pressure path length product (pl) for CO_2 in the flame using the observed emission. This involves calculating the energy in the 4.3 μm band emission absorbed by the intervening atmosphere, adding this absorption to the measured (received) energy and then estimating the magnitude of emission from the flame in the above band. The band emissivity is then calculated for the assumed flame temperature and hence the $(\text{pl})_{\text{CO}_2}$ can be estimated. Once this is done, the $(\text{pl})_{\text{H}_2\text{O}}$ and total emissivities of CO_2 and H_2O can be obtained from Hottel's charts (Hottel and Sarofim, 1967). With estimated values of soot emissivity (Tables 4.4 and 4.5) the true emissive power of the flame is calculated.

The calculation of CO_2 partial pressure in the flame from the known 4.3 μm band energy received and the assumed flame temperature is tedious. The calculation procedure is illustrated in part 1 of Appendix B. The calculation methodology is in part an inverse procedure to that developed by Edwards and Balakrishnan (1973) for estimating total emissivities of gases from known (pl) values for individual species and the temperature of gases. The uncertainties in the calculation and the sensitivity of the result to certain parameters are also discussed in that appendix.

The conclusion from the calculation indicated in part 1 of Appendix B is that the flame temperature should be assumed to be 1500 K and the corresponding partial pressure of CO_2 in the flame should be assumed

* This value is obtained by averaging the atmospheric transmission curve indicated in Figure 4.7. Note, however, the bands 1.87, 2.7, and 4.3 are not included in the averaging process.

to be 0.094 atm^* (see discussions in part 1, appendix 3).

Based on the above result and invoking the relationship that the partial pressure of H_2O is twice the partial pressure of CO_2 in the combustion of methane, we have estimated the emissive power of the flame. The result is obtained by using the emissivity charts of Hottel and Sarofim (1967) and is illustrated in Table 4.6. The emission per unit nominal area of the flame is calculated to be 175 kW/m^2 . This value is to be compared with the apparent emissive power of 35 kW/m^2 obtained earlier.

The above two numbers indicate the importance of the absorption by the water vapor CO_2 and other gases in the atmosphere. Calculations based on the methods of Edwards and Balakrishnan (1973) give for the atmospheric absorptivity over 236 m distance a value of 0.285. Using Hottel charts, this number is 0.33. Therefore, the apparent flame radiance as measured by the spectrometer should be:

$$\begin{aligned}\text{Apparent radiance} &= (E_b/\pi) \times [\epsilon_{\text{C,H}} + \epsilon_{\text{S}} - a_{\text{atm}}] \\ &= \left(\frac{287}{\pi}\right) [(0.35 + 0.19 - 0.07) + 0.14 - 0.33] \\ &= 25.6 \text{ kW/m}^2 \text{ sr}\end{aligned}$$

Based on the integration of spectral data, the apparent radiance is $8.55 \text{ kW/m}^2 \text{ sr}$ (see equation 4.4a). We are unable to explain this significant discrepancy. Absorption by atmospheric gases other than water vapor and CO_2 may account for considerable absorption over the 236 m path length.** However, the magnitude of the absorption seems to inexplicably large.

The partial pressure values used for the CO_2 and H_2O are their stoichiometric values for the combustion of methane in air. In reality, these partial pressures may be less than the stoichiometric values due to

* This is equal to the value of CO_2 partial pressure corresponding to a stoichiometric combustion of methane in air.

** It has been suggested that the steam produced by the evaporation from the pond water surface (due to radiant heat from the fire) may account for additional absorption. This hypothesis is unacceptable because (i) the steam produced would be sucked into the fire and (ii) radiometer readings were not affected significantly.

TABLE 4.6

TRUE FLAME EMISSIVE POWER ESTIMATED FROM 4.3 μ CO_2 BAND
SPECTRAL DATA (Scan #56, 20 s into the Burn)

T	E_b	P_{CO_2}	Y	$P_{\text{H}_2\text{O}}$	Partial Emissivities	Total Emissivity	Estimated Soot Emissivity (6)	Total Flame Emissivity (6)	True Flame Emissive Power E_f (kW/m^2)
Assumed Flame Temperature (K)	Beam Emissive Power (kW/m^2)	Partial Pressure Length Product ($\text{atm} \cdot \text{m}$)	Calculated Percent Excess Air in Combustion (1)	Pressure Length Product ($\text{atm} \cdot \text{m}$)	of Each Spec (4)				
1500	25	1.44	3	2.50	0.10	0.37	0.14	0.61	175

1. Details of calculation in Appendix B - See Table 3.1

2. Percent excess air (above stoichiometric requirement) = $100 \times \left[\frac{0.105}{0.052} - 1.105 \right]$

3. $\text{CH}_2\text{OL} = 27.00$ for beam length $L = 1.1$ m

4. Based on a mean beam length = flame diameter (11 mm) and using Hottel charts (Hottel and Sarofim, 1967).

5. From Table 4.5 corresponding to 20 s after ignition.

6. $E_f = E_{\text{CO}_2} + E_{\text{H}_2\text{O}} + E_s$ - the correction for CO_2 and H_2O band overlap (taken to be 0.07).

7. $E_f = 0.7 E_b$

excess air entrainment. Since no direct measurements were made of the CO_2 and H_2O content within the fire, it is not possible to evaluate whether the assumption of stoichiometric values are justifiable. However, this assumption leads to the maximum emissivities for the species for a given optical path length through the fire and hence may be a conservative assumption.

The results from the spectral calculations on predicting the flame temperature and CO_2 partial pressure are applied to predicting the value of the radiant flux at the location of one of the wide-angle radiometers. These calculations are indicated in part 2 of Appendix B.

4.5.5 Comparison with Other LNG Flame Spectra

A review of the literature indicated that except for the AGA test data (AGA, 1974) no spectra have been published for methane-air diffusion flames. The AGA test data were obtained for LNG fires on land; the fire diameters were 1.8 m (6 ft), 6 m (20 ft), and 24 m (80 ft). A relatively slow scanning grating spectrometer was used in these experiments. Hence, the spectra measured were severely affected by intensity fluctuations in the flame.

A comparison of the flame radiation spectrum measured in the current series at NWC and those obtained in the AGA tests is shown in Figure 4.11. The NWC data is from scan #56, corresponding to about 20 s after ignition. The AGA data plotted are the ones from the 1.8 m diameter test (AGA test LNG 023) and 6 m diameter test (AGA test # LNG 029). The spectrum from the 24 m diameter test is not given in Figure 4.11 because valid data were not obtained.* In the AGA 023 test, the spectrometer was located about 14 m from the center of the dike and had a 33° (full cone) angle view of the flame. The mean flame height was about 3.7 m. The field of view was not filled by the flame - on the contrary, the entire flame was visible within the field of view. In the AGA 029 test, the spectrometer was 36.5 m from the center of the dike and had a 25° (full cone) angle view. The mean flame height was about 16.75 m. The field of view probably covered the entire height of the flame.

The ordinate shown in Figure 4.11 is in the units of flame spectral radiance ($\text{kW/m}^2 \text{ sr } \mu\text{m}$). The spectral data in the AGA report (1974) are

* In the 24 m experiment, premature ignition occurred and the spill truck tires burned producing a very dark, sooty flame.

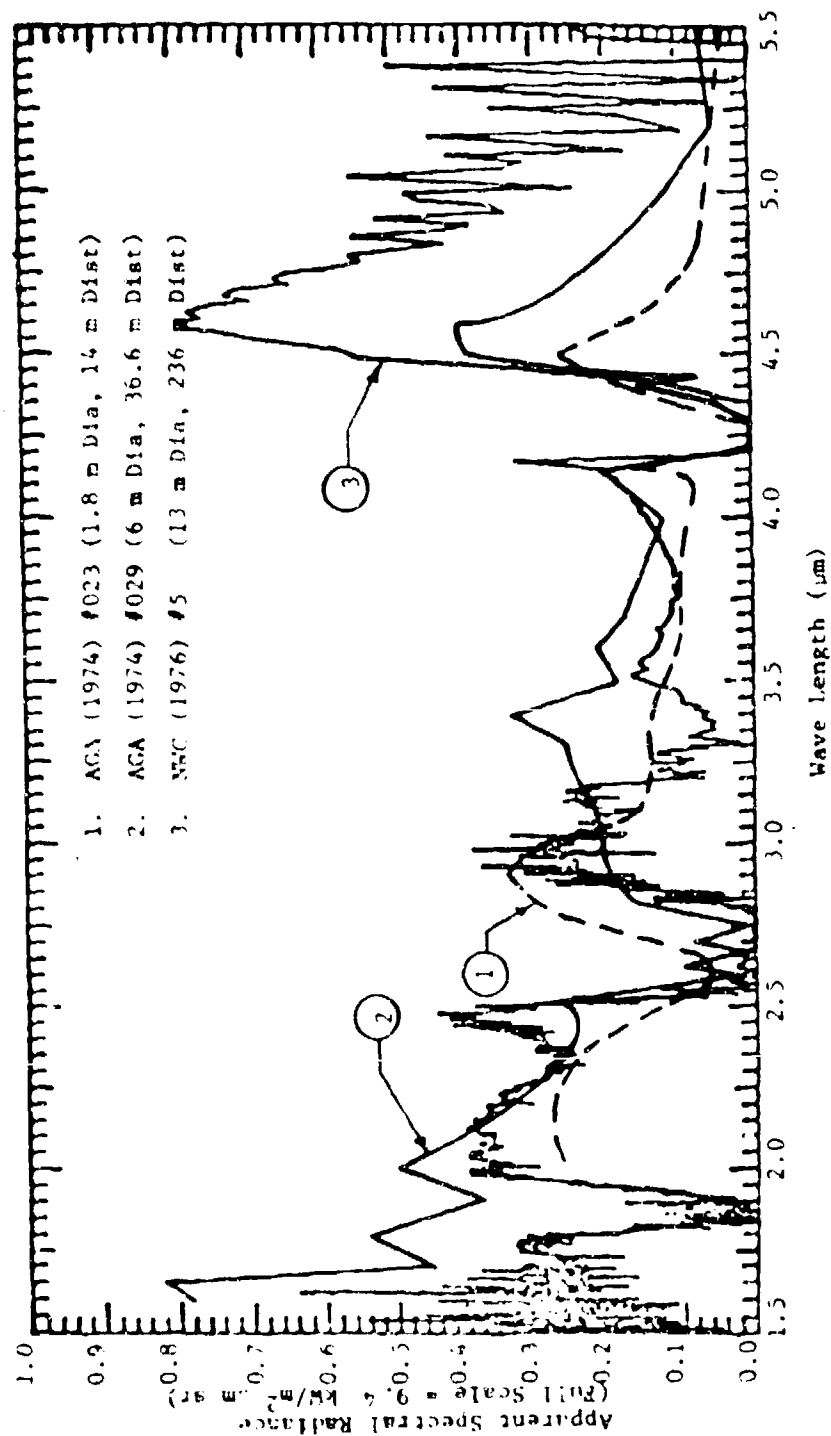


FIGURE 4.11: COMPARISON OF AGA TEST SPECTRA WITH NWC TEST SPECTRUM

indicated in the units of spectral irradiance H_λ ($\text{W/m}^2 \cdot \mu\text{m}$) at the location of the spectrometer. These are converted to apparent flame spectral radiance by using the following equation:

$$I_\lambda(\text{apparent}) = \frac{H_\lambda X^2}{A_f} \quad (\text{kW/m}^2 \cdot \mu\text{m} \cdot \text{sr}) \quad (4.5)$$

Where X is the distance to the spectrometer from the flame center and A_f is the flame projected area seen by the spectrometer.

The value of full scale apparent intensity in the NWC spectrum is 2000 $\text{kW/sr} \cdot \mu\text{m}$ (see Section 4.3.2) which on the basis of 200 m^2 of flame area translates to the spectral radiance of $9.40 \text{ kW/m}^2 \cdot \text{sr} \cdot \mu\text{m}$. All the plots shown in Figure 4.11 are on the basis of "apparent" flame spectral radiance. That is, the correction for transmissivities in the atmosphere over the various distances to the spectrometers in the different experiments, have not been included. While this may cause some error in comparing the results, the magnitude of the error is expected to be small because the atmosphere is essentially transparent (except in H_2O and CO_2 bands) for the distances where the spectrometers were located.

It is seen from Figure 4.11 that there is reasonable agreement between the NWC spectrum and the two AGA spectra. There are some significant differences also. The resolution obtained in the NWC spectrum is significantly higher than in the AGA spectra. The NWC spectrum (13 m diameter fire) seems to agree more closely with the AGA, 1.8 m fire spectrum than with the AGA 6 m fire spectrum. However, the apparent spectral radiance in the NWC test seems to be higher. If the atmospheric transmissivity effect is taken into account, the NWC spectral radiance values will be even higher. This is because the absorption in the atmosphere over 236 m distance in the NWC test would be much more than in AGA tests where the spectrometers were only 14 m and 36 m away respectively from the 1.8 m diameter and 6 m diameter fires. This indicates that the NWC fire was much more radiative. It is possible that the higher radiance is a direct consequence of the greater optical depth in the 13 m fire.

The strong water band absorption at 2.7 μm is noticed in all three spectra. Considering that the spectrometer for the AGA test # 023 (1.8 m diameter) was only 14 m away from flame center, the water absorption in this band is very significant. Similarly, the very strong CO_2 absorption at 4.3 μm is noticed in all three spectra. The CO_2 emission peak occurs at about 4.6 μm , in both NWC and AGA 6 m fires. In the 1.8 m fire the peak in this band occurs at 4.5 μm . Also noticed is the significant differences in the apparent peak spectral radiance of CO_2 band. As explained earlier (see Section 4.5.1) the temperature corresponding to the observed CO_2 peak at 4.6 μm in the NWC spectrum is about 1550 K. The peak radiances in the AGA spectra at this wave length are almost one half to one third (in the 6 m and 1.8 m fires, respectively) the peak in the NWC spectrum. The conclusion that can be drawn from this comparison is that the 1.8 m and 6 m AGA fires were not optically thick.

There are other important differences that can be observed in the three spectra. It is surprising that there is better agreement between soot emissions from the 1.8 m AGA and the 13 m NWC fires in the 2.8 - 4.2 μm region than between the 6 m AGA and 13 m NWC fires in the same wave-length region. In this region, the 6 m fire soot emissions are not only consistently higher but also there is a spike at 3.4 μm . This has been attributed to a "possible hydrocarbon emission" (AGA 1973, Section H.). Also noticeable is the significant difference in the 1.5 - 2.5 μm region between the 6 m AGA and 13 m NWC spectra. The high spectral intensities indicated in the AGA results are suspect. The reasons for the very high intensity close to 1.5 μm are not obvious to us. One possible explanation is that the spectrometer malfunctioned in the lower wave-length region. However, it should be kept in mind that the AGA spectra presented in the report (AGA, 1974) are the "averaged-over-a-large-number-of-scans" lines. The fine structure of the spectrum seen in NWC data is not available for the AGA data because of the way in which the spectra were obtained in the AGA tests by "averaging" data from different scans.

4.6 DISCUSSION

The spectrometer used in the experiment had no fore optics. The use of fore optics would focus the field of view on the detector condenser lens, rather than on the detector itself. The detector, in turn, would image the exit pupil of the fore optics on the detector. In the experiment the flame did not completely fill the field of view of the spectrometer (see Figure 4.5). Unfortunately, since the fore optics was not used and the uniformity of sensitivity of the detector over its entire area is uncertain, it is possible that any minor misalignment of the spectrometer which shifted the image of the flame in the field of view may contribute to the variation of signal output. We are unable to estimate whether the spectral data indeed had errors due to the above misalignment problems. However, based on the analysis of the data, it seems highly unlikely that such errors were present in the spectral data.

In scanning Michelson interferometers, a phenomenon called "aliasing" occurs when the signal source fluctuates in intensity. If the fluctuations happen at frequencies at which the fringes occur in the scanning interferometer, spurious spectral features appear in the spectrum. The detector output frequency and wave number are linearly related for a given mirror velocity:

$$f = 2 \lambda v \text{ (Hz)}$$

$$v = \text{mirror velocity (cm/sec)}$$

$$\lambda = 1/\nu = \text{wave number (cm}^{-1}\text{)}$$

A mirror velocity of 0.54 cm/sec was used to cover wave lengths from 1.5 to 5.5 μm , leading to fringe frequencies at the detector of:

$$1963 < f < 7200 \text{ (Hz)}$$

Fluctuations in the flame emission are principally due to small scale turbulent eddies. The frequencies of these flickers are significantly lower than the above aliasing limits. Hence, aliasing cannot be expected to be a problem. The spectrometer, however, seems to have significant noise in the wave length close to 1.5 μm . This can be clearly seen from the calibration curve in Figure 4.4. The results from other wave lengths are accurate because of the high scanning speed (0.5 s) of the spectrometer.

The single important feature of the measured spectra is the total absorption of the 1.87 μm , and 2.3 μm water bands as well as the partial absorption of the 4.3 μm CO_2 band by the intervening atmosphere. Because of this absorption (and the consequent loss of vital information) the true emission characteristics of the flame cannot be ascertained. Only indirect inferences can be drawn using the available record. Such an indirect approach has been utilized to bracket the soot temperature in the flame.

Soot temperature is estimated to be between 1300 K and 1500 K. More precise evaluation cannot be made because of the relative insensitivity of the wave length for maximum intensity (see Table 4.4) with temperature. Also it is uncertain as to where the maximum soot emission intensity is in Figure 4.10. The soot emissivity calculations shown in Table 4.4 indicate that it is in the 0.28 to 0.14 range. We do however notice that the soot emissivity increases with burn time increasing for example, from 0.14 at 15 s to 0.27 at 40 s after ignition (see Table 4.5) for an assumed flame temperature of 1400 K. This may be a consequence of the increased soot formation by the combustion of ethane, butane, and propane fractions in the LNG.

There is no a priori way of estimating the luminous soot emissivity. Hottel and Sarofim (1967) suggest that for radiation calculations from gaseous flames the effect of luminous soot radiation can be accounted for by increasing the gas emissivity by 0.1. The inference from present measurements on soot emissivity imply that soot emissivities lie between 0.1 and 0.2. This result is in disagreement with the conclusions from the AGA experiments (see Section G, AGA 1974) in which the soot emissivity was estimated (from radiometer data) to be close to unity for flame sizes larger than 3 m diameter. The AGA data indicate that between 60 and 80% of the energy received by the spectrometer in the 6 m test was attributable to soot. This does not, however, give any indication of soot emissivity because the energy radiated by H_2O and CO_2 and later absorbed by the atmosphere is not precisely known. Therefore, the question of the magnitude of soot emissivity remains unresolved.

The 4.3 CO_2 emission band in all of the spectra is quite prominent. It is argued by Hottel and Sarofim (1967, p. 205) that because the average collision time between molecules is of the order of 10^{-10} s and the relaxation time for excited vibrational energy levels is of the order of 10^{-1} to 10^{-3} seconds, the chance of not having redistribution of vibrational energy into translational energy is small. In effect, equilibrium exists in a flame and the term "temperature" is meaningful.

The apparent spectral radiance at 4.6 μm corresponds to a black body temperature of 1,425 K. If the atmospheric absorption correction is taken into account, the effective temperature is found to be 1550 K. This calculation of course assumes that the line emissivity is unity. The importance of this calculation is in indicating that the CO_2 emission is also a thermal emission.

The emissive power calculation indicated in Section 4.5.4.2 and described in detail in part 1 of Appendix B is probably the only way of determining the energy emission from the flame using the present spectral data. The principal difficulty arises due to the complete absorption in the intervening atmosphere of the water vapor emissions and partial absorption of CO_2 emissions from the flame. The method indicated in Appendix B is quite sensitive to the input information, especially to the value of 4.3 μm CO_2 band energy received by the spectrometer after attenuation in the atmosphere (for a detailed discussion on this see Appendix B). It has been argued in Appendix B that the spectral data, both luminous soot emission and the 4.3 μm CO_2 band emission could be adequately described by a 1500 K flame and the combustion occurring under stoichiometric conditions. That is the partial pressures of CO_2 and H_2O in the fire have their stoichiometric values corresponding to the combustion of methane in air.

Based on the 1500 K fire, stoichiometric combustion and observed soot emissivity corresponding to 1500 K (Table 4.4) the LNG fire emissive power is calculated to be 175 kW/m^2 (see Table 4.6). This agrees remarkably well with the narrow-angle data for test #5 (see Figures 5.23 and 5.24) which are described in greater detail in Chapter 5.

The wide-angle radiometer data for the same test indicated higher emissive power than the above 175 kW/m^2 (see Section 5.4.3). Also a calculation has been made in Part 2, Appendix B, using flame characteristics determined (by using the spectral data) to estimate the radiant flux at the 60 m location of a wide-angle radiometer. After accounting for the various band absorptivities in the atmosphere for a weighted path length of 40 m (see part 2 of Appendix B), the radiant flux at the wide-angle radiometer position is calculated to be 8.6 kW/m^2 . The measured flux is close to 18.4 kW/m^2 . It is very difficult to explain this significant difference.* However, certain arguments can be made to explain why the wide-angle radiometer reading could be higher than that calculated. The spectrometer is aimed at the lower position of the flame where soot concentrations may be low and consequently the luminous soot emissivity could also be lower. It is entirely possible that middle and upper parts of the flame have higher luminous soot concentrations. Since the wide-angle radiometer receives energy from the entire flame (in contrast to the narrow-angle radiometer and the spectrometer), it may receive energy from the flame which has higher soot emissivity. We do note here that visible motion picture records do not indicate any significant variation of the flame brightness with height. It is, of course, highly unlikely that the soot emissivity will increase with height in the flame to such an extent as to substantially increase the radiative emission from the top parts of the fire. It is unfortunate that spectra from different parts of the flame (with height) were not measured.

The amount of excess air to the fire calculated from the spectral data is found to be negligible. This may be in keeping with the fact that the chemical reaction between a fuel vapor and oxygen in air occurs only at stoichiometric conditions. It is noted, however, that the laboratory scale experiments of Thomas et al. (1965) have shown that the total mass of air moving vertically up over the entire horizontal section in space corresponding to the top of the flame is about an order of magnitude larger than the stoichiometric value. Thomas et al. did not infer that this was the value of air entrained within the visible flame.

* especially since the same model overpredicts flux at 236 m.

One of the unresolved questions that has resulted from the spectral data is the absorption of soot radiation by warm, optically thick hydrocarbon gases. We have been unable to explain where in the flame these gases are and how they absorb soot radiation. Perhaps the physical picture of a core of warm fuel vapor in the fire surrounded by a reaction zone (flame) containing luminous soot could explain the above discussed absorption.

4.7 CONCLUSIONS

The significant conclusions from the analysis of the spectral data are the following:

1. The flame temperature cannot be determined precisely, but it is in the range of 1300 K - 1500 K. This is estimated from the location of peak soot emission. The calculations based on $4.3 \mu\text{m}$ CO_2 band emission indicate that the temperature is probably closer to 1500 K.
2. The LNG flame, for the size investigated (13 m diameter) is a band emitter with significant emissions in the H_2O and CO_2 bands. Water vapor emission constitutes about 50% of the total, CO_2 , about 25%, and the remainder by the soot.
3. The flame emissive power (total energy emitted per unit nominal flame surface area) is about 175 kW/m^2 . This value agrees well with estimates based on other measurements (narrow-angle radiometer).
4. Estimated soot emissivities during the major part of burning time are in the range of 0.14 to 0.19. These are much lower than the 0.5 to 0.6 reported in the AGA experiments. Soot emissivity increases towards the end of the burning period. At 1500 K the maximum soot emissivity observed is 0.19.
5. For a given distance the atmospheric transmissivity for the LNG flame radiation is much lower than for a radiation from a black body with the same emissive power. This is due to the band emission from H_2O and CO_2 in a LNG fire and the strong absorption by the same species in the atmosphere.

6. Actual atmospheric absorptivity is greater (by almost a factor of two) than that calculated based on principal H_2O and CO_2 bands. This may be due to the effect of other weaker bands and also due to other gases. However, the magnitude of this absorption is inexplicably large.
7. If, as spectral data suggest, the flame is assumed to be emitting at a temperature of 1500 K and to contain stoichiometric quantities of water vapor and CO_2 , and if water and CO_2 absorption in the atmosphere are estimated using standard methods, flux estimates do not agree well with experimental data. At a distance of 40 m the data from the wide-angle radiometer indicate more than twice the radiation predicted; at 236 m the spectrometer receives about 1/3 the radiation predicted.
8. While a model describing flame emission in terms of soot, water vapor, and CO_2 species should provide an improved description of radiation from an LNG fire, not enough spectral data are yet available to define the characteristics of such a model. The role of unburned vapor in the core of the fire plume, if any, may have significant effect on the radiative characteristics.

5. ANALYSIS OF LNG POOL FIRES

5.1 INTRODUCTION

In the past, hazard models dealing with thermal radiation from LNG pool fires on water have been based on theory and experimental data from LNG pool fires on land. The tests described in this section are the first extensive set of experiments involving LNG pool fires on water.

In an LNG pool fire, the burning rate is determined by the rate of vaporization of LNG. The vaporization rate is based on two primary factors: heat transfer to the pool from the underlying surface and the radiation back into the pool from the fire above it. For a land spill, the solid substrate beneath the pool cools rapidly, so the burning rate decreases with time. However, the boiling rate of unignited LNG on water remains relatively constant and thus the burning rate per unit area of LNG on water would be expected to remain fairly constant until the fuel is consumed.

Pool fires on land have been studied in diked enclosures where the pool area remains constant during the burning period. In a water spill, the pool is not contained and thus spreads rapidly as it burns.

The height of pool fires observed in land spill tests was found to be about three times the pool diameter early in tests where LNG was spilled into a warm dike. The height subsequently decreased to about twice the pool diameter. The latter height to diameter ratio was also observed in pool fire tests conducted in precooled dikes. Existing models for LNG pool fires on water are generally based on the assumption that flame heights would be comparable to those observed in the early stages of a pool fire on land.

The tests conducted at the Naval Weapons Center included three types of LNG fire tests. The first type involved rapid spills of LNG and essentially immediate ignition resulting in an expanding pool fire. The second type of test involved a small delay in the time of ignition so that a vapor cloud was formed in the vicinity of the pool before ignition occurred. In the third type of test, the spill generated a

vapor cloud which was allowed to drift downwind a significant distance before it was ignited at a downwind location. These latter tests are described in Chapter 6. In this chapter we review experimental data only from the "pool fire" and "delayed pool fire" experiments.

The series of pool fire tests consisted of 7 tests in which the spilled LNG was ignited immediately and 3 tests where the ignition was delayed. The quantity of LNG and the duration of spill were varied and the appropriate meteorological conditions at the test site were measured. In Table 5.1 is given a summary description of the conditions associated with each of the experiments. The thermal radiation resulting from the pool fires was measured with narrow angle and wide angle radiometers placed at various locations. In test #5, a spectrometer was placed at a distance of 236 m from the spill point to measure the spectral characteristics of the flame. Three movie cameras were located at various distances from the spill point to obtain two orthogonal side views and an overview of the fire. In Figure 5.1 are shown the locations of the instruments used for pool fire test #1 through test #6. In Figure 5.2 are shown the locations of instruments for pool fire tests #11, 13 and 14.

5.2 ANALYSIS OF POOL SPREAD

When LNG is spilled on water, it spreads and evaporates. Spreading enhances total evaporation by providing more surface area for heat transfer. Spreading of a nitrogen or water is governed by the interaction of the fluid dynamical phenomenon of liquid spreading and the thermal phenomenon of heat transfer at the interface. Several theoretical models are available in the literature to determine the extent of spreading. A review of these models is available in the literature (see Section 2). In all of these models, the important parameter determining the maximum extent of the spread and the spread rate is the liquid regression rate of LNG on water, \dot{V} . The dimensions of \dot{V} are m/s and physically this represents the rate of decrease in the height of a pool of LNG on water due to evaporation. This is a direct function of the heat transfer from the water to the pool of LNG. In addition, the

TABLE 5.1

DESCRIPTION OF INCIDENTS OF LSG PULFIB 71-75

Incident No.	Type	Date	Spill Quantity (lb)	Spill Duration (seconds)	Average Spill Rate (lb/hr)	Air Temp (°F)	Relative Humidity (%)	Wind Vel. (ft/min)	Wind Direction at Time of Spill	Gas Composition by Volume, %		
										Methane	Ethane	Propane
1	Pool	9-17-76	5.3	25	0.02	26	34	alm	-			
2	Pool	9-27-76	5.3	5	0.10	30	44	alm	10			
3	Pool	9-30-76	4.2	40	0.09	29	52	alm	-			
4	Pool	10-1-76	4.2	24	0.32	31	52	alm	9	29.0	3.0	
5	Pool	10-1-76	1.0	3	0.99	21	51	alm	140	25.4	10.4	3.0
6	Pool	11-14-76	5.7	34	0.11	24	41	alm	91	25.6	12.0	5.0
7	Delayed Ignition	4-27-77	5.7	35	0.06	24	24	1	10			
12	Pool	5-25-79	5.68	41	0.07	22	32	alm	-	96.1	3.0	4.1
13	Delayed Ignition	5-26-79	5.7	40	0.07	21	36	alm	10	94.0	3.0	4.0
14	Delayed Ignition	6-1-79	5.5	84	0.07	20	34	alm	-	94.3	3.5	4.2

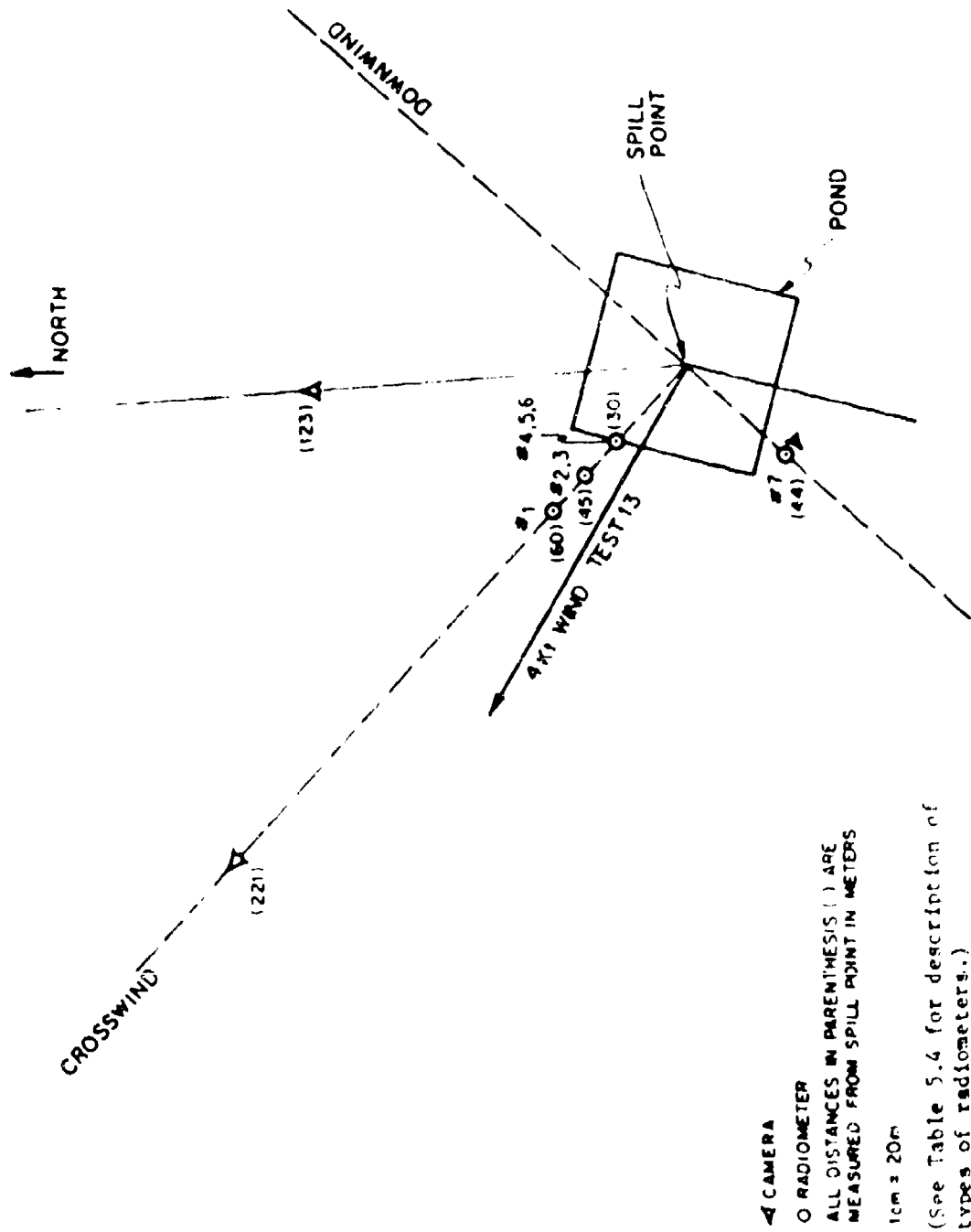


FIGURE 5.2: LOCATION OF VARIOUS INSTRUMENTS FOR INC POOL FIRE TESTS #12, 13 and 14

boiling rate is also sensitive to the chemical composition of LNG. The heat transfer from the water to the LNG pool is further influenced by formation of ice (if any) on water surface. Solid ice typically does not form in unconfined spills of LNG on water.

Once the pool of LNG is ignited, the heat transfer from the flame to the surface of the pool increases the rate of vaporization. The "burning rate" thus depends both on back radiation from the flame and the boiling rate of water. In large scale experiments, the variation in burning rate with time cannot be determined easily. While theoretical estimates of back radiation from the flame are possible in principle, they require knowledge of the distribution of the flame temperature and the gas concentration within the fire. Only average values of the burning rate can be determined by knowing the total volume of fuel and the duration of burning.

In Figure 5.3 are shown the observed dimensions of the pool^{*} for LNG test #5 which was one of the more rapid spills. The dimensions of the pool were measured using the downwind and the crosswind cameras. As can be seen from Figure 5.3, the pool is not radially symmetric. In fact, the shape of the pool in most pool fire experiments was observed to be closer to an ellipse with "fingers" emerging from the outer periphery.

* The pool dimensions were inferred by assuming the liquid pool boundary before extinction to be the same as the boundary of the white vapor cloud at the water level. Further, the actual measurement of the dimensions of the pool from the motion picture data is rather subjective because of the lack of contrast on the screen between the pool and the background. Because of these uncertainties in the measurement of pool dimensions, we have performed a sensitivity analysis on the measured data. The details of this analysis are presented in Section 5.7.

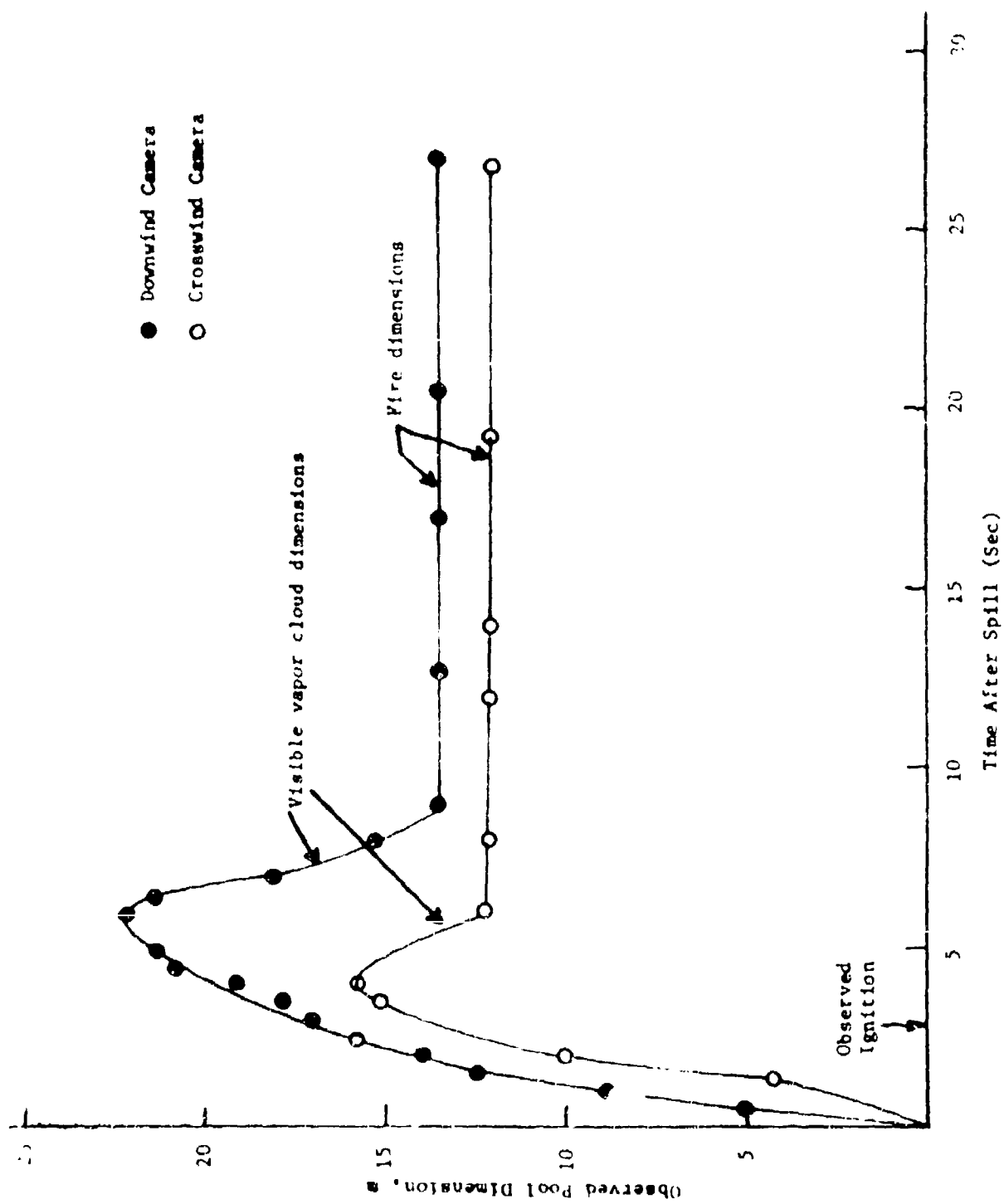


FIGURE 5.3: OBSERVED POOL DIMENSIONS FOR LNG TEST #5

The exact dimensions of these fingers could not be determined by the available motion picture data. For simplicity, we assumed that the pool was elliptical in shape, with dimensions along the major and minor axes given by the downwind and the crosswind cameras, respectively. The average pool diameter was determined to be the diameter of a circle of equivalent area. Since the view from the movie camera always indicated the width of the pool normal to the field of view of the camera, the diameter of the pool determined by this method provides an upperbound on the extent of pool spread.

As can be seen from Figure 5.3, the initial spread rate of the pool is high. The igniter, in these tests, was activated within about 1 second after liquid first contacted the pool. The arrow shown in Figure 5.3 indicates the first evidence of visible flame from the movie records. The peak in the diameter at about 5 seconds is based on a measurement of the visible vapor cloud and may not actually represent the true pool diameter which subsequently stabilizes at about 13 m. Figure 5.4 shows similar data for test #12 which was at a spill rate about 20% lower than that for test #5, but which continued for 81 seconds (compared to 37 seconds for test #5). The pool diameter in test #12 stabilized at about 14 m.

The measured stabilized dimensions of the LN₂ pool on water for various tests are shown in Table 5.2. The last column in Table 5.2 shows the range of estimated burning rates for LN₂ pool fires on water. To make an estimate of this quantity we have made the following assumptions:

- The duration of intense burning is used to determine the burning rate. This was determined by the motion picture data and the radiometer data. In determining the duration of intense burning, we ignored the initial transient period of the fire in which the flame height was increasing and the final stages of the fire where the height of the visible flame was steadily decreasing.

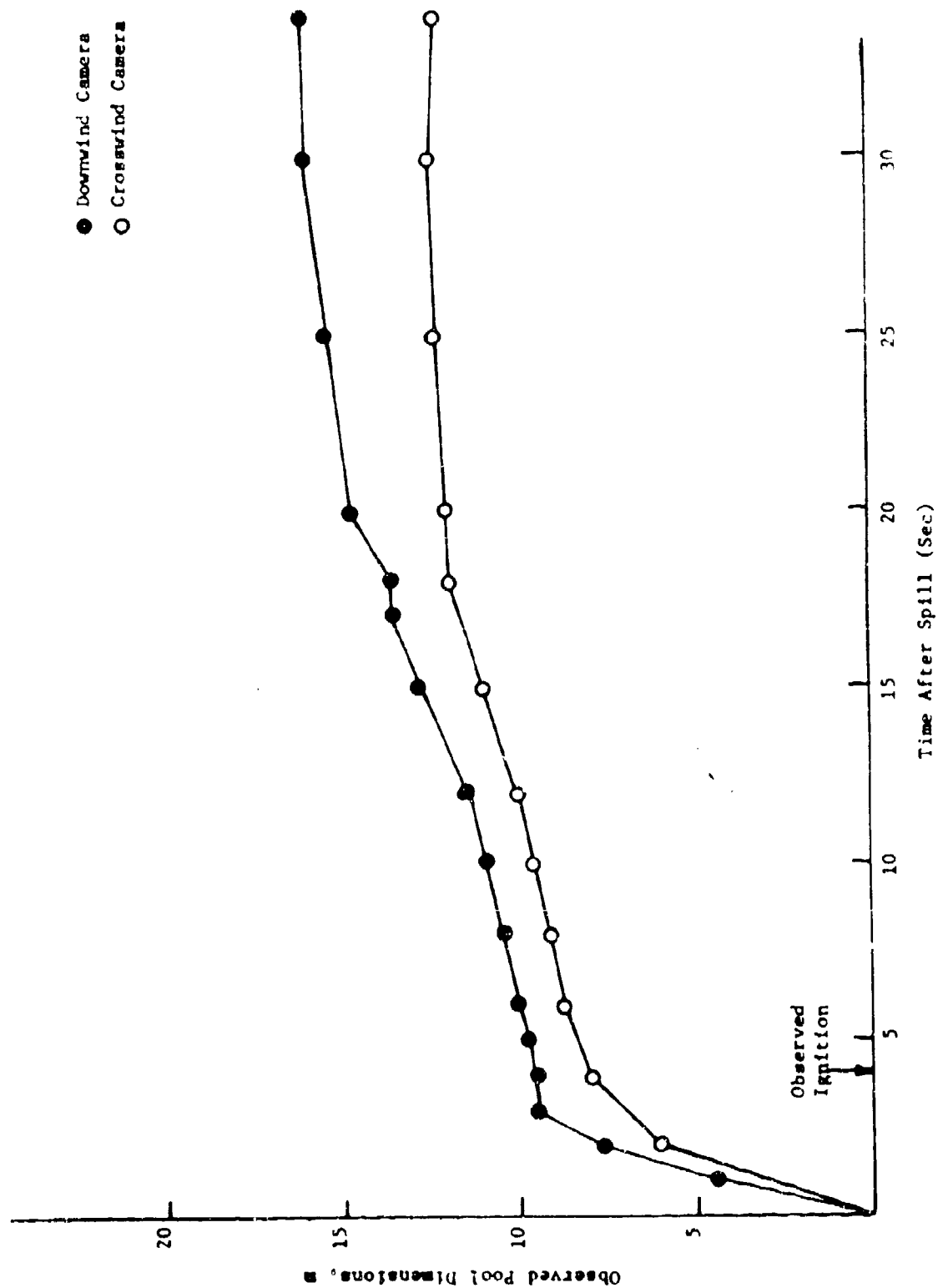


FIGURE 5.4: OBSERVED POOL DIMENSIONS FOR LNG TEST #12

TABLE 5.2

GEOMETRIC CHARACTERISTICS OF POOL

Test #	Quantity collected (g)	Solid Time (sec)	Solid Rate (g/sec)	Pool Width (m)		Average Flame Height (m)	Still Velocity (m/sec)	Duration of Intense Burning (sec)	Estimated Burning Rate ^a (m/s)	
				Camera	Downwind Camera				Lower Limit	Upper Limit
1	5.3	55	0.096	4.7	8.5	8.5	3.4	10	4.4×10^{-4}	5.5×10^{-4}
2	5.3	52	0.102	-	-	-	3.8	-	-	-
3	4.2	49	0.086	12.1	11.6	11.5	4.9	45	9.5×10^{-4}	12.0×10^{-4}
4	4.2	44	0.097	9.0	9.0	9.0	3.0	105	3.4×10^{-4}	4.1×10^{-4}
5	3.0	32	0.094	12.7	13.6	12.8	3.3	29	9.0×10^{-4}	11.0×10^{-4}
6	5.2	52	0.110	14.6	14.6	14.6	4.2	40	8.1×10^{-4}	10.0×10^{-4}
7	5.7	75	0.076	16.8	-	16.8	4.3	75	3.4×10^{-4}	4.2×10^{-4}
12	5.68	91	0.062	11.2	16.0	14.0	4.0	74	4.9×10^{-4}	6.0×10^{-4}

^a This looks like a delayed ignition; the entire pool burns in a very short time and in an unusual manner. High wind initially blew vapor away from the igniter. Data could not be readily interpreted.

^b The wind velocity was about 5 m/sec. There are great fluctuations in pool widths. The pool used dimensions are for steady burning.

^c Burning rate is calculated based on the duration of intense burning.

^d This is a delayed ignition pool fire.

- The actual area of the pool is likely to be less than the area indicated by the maximum pool dimensions. We, therefore, have used both the average diameter and 90% of the average diameter in order to obtain respectively the lower limits and the upper limits for the burning rates.

The burning rate is estimated by dividing the total volume of LNG by the calculated area of the pool and the duration of the burning.

If the burning rate were constant, the maximum pool radius should increase with the square root of the spill rate. In the AIA (1974) pool fire tests, the burning rate due to back radiation from the fire was found to be about 1.44×10^{-4} m/s (0.34 in/min) for the 6 m diameter tests and was estimated to be about 1.57×10^{-4} m/s (0.37 in/min) for the 24 m diameter test. If we assume a typical value of 1.48×10^{-4} m/s (0.35 in/min) and add this to the typical regression rate of 4.23×10^{-4} m/s (1 in/min) for LNG boiling on water, we would expect the pool fires on water of the scale studied at China Lake to have a regression rate of about 5.7×10^{-4} m/s (1.35 in/min).

Observed average pool diameters are plotted as a function of spill rate in Figure 5.5. Also shown is the theoretical line if the regression rate remained a constant at 5.7×10^{-4} m/s. From this figure it appears that the pool diameter is less than would be expected at the high spill rates.

If, however, it is assumed that the observed diameters represent the dimension of the LNG-water pool surface contact area, then apparent burning rates can be estimated. These rates are presented as a function of spill rate in Figure 5.6. The rates are in the range expected for the tests of spill rates up to about $0.07 \text{ m}^3/\text{s}$; however, they seem to increase substantially for the highest spill rate tests.

While data are not available to identify the reason for this apparent increase in burning rate with spill rate, it seems likely that the effect is due to a surface area enhancement-effect associated with the discharge jet reaching a high enough velocity to cause fragmentation of liquid as it impinges on the flat plate designed to deflect

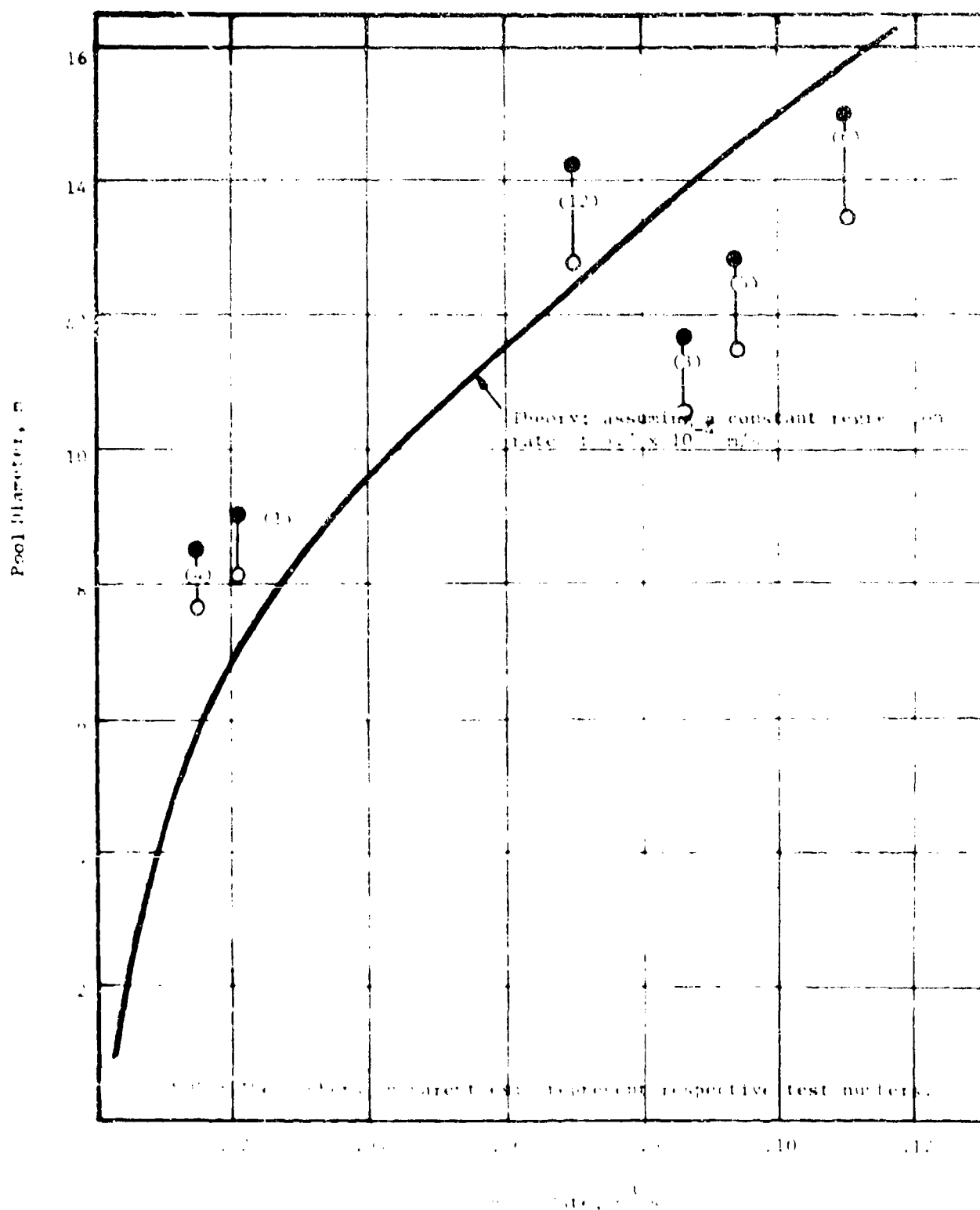


FIGURE 1. THE VARIATION OF MAXIMUM POOL DIAMETER WITH SPILL RATE

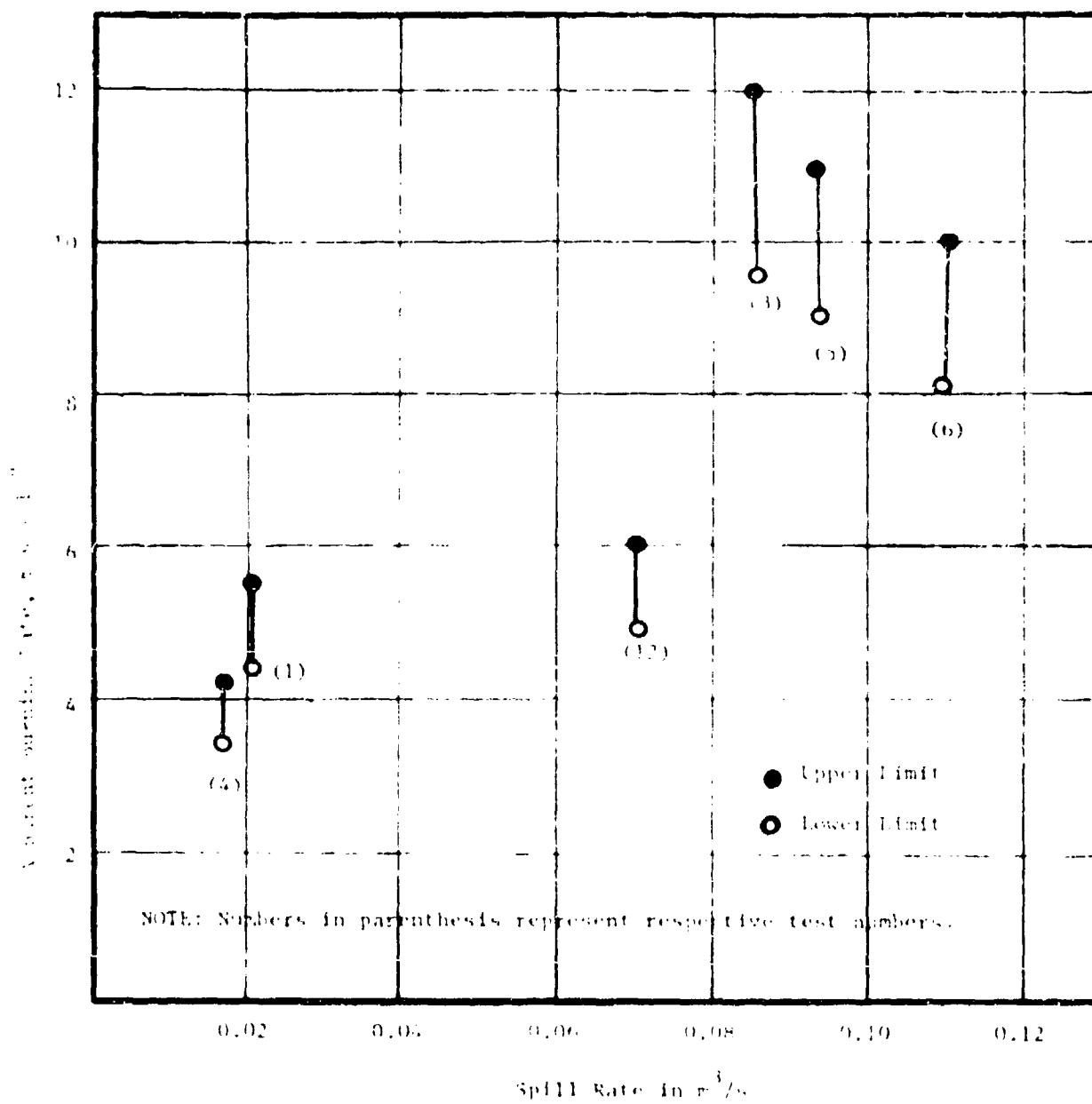


FIGURE 5.6: THE VARIATION OF BURNING RATE WITH SPILL RATE

the jet. Rapid spill of LNG onto the water from a LNG ship caused by an accident may also exhibit a similar effect.

In Figure 5.7 are plotted the visible measured cloud lengths as a function of time after spill for delayed ignition pool fire tests #13 and #14. The rates of spill for these tests were $0.066 \text{ m}^3/\text{s}$ and $0.005 \text{ m}^3/\text{s}$, respectively. The liquid pool was allowed to spread and evaporate. The dense vapor cloud of LNG was seen to spread well beyond the edge of the pond. The dimensions of the vapor cloud were measured from the motion picture data. Ignition was initiated at about 24 seconds and 30 seconds after the spill for tests #13 and #14, respectively. In both cases, the source of ignition was located several meters away from the spill point. At first the edge of the vapor cloud started burning. Once the periphery of the vapor cloud was completely burned, the fire started to move towards the center of the cloud. The length of the vapor cloud steadily decreased with time. Once the flame became concentrated at the center of the cloud, the characteristics of the fire resembled those observed in other pool fire tests. As can be seen from Figure 5.7 the dimensions of the fire during this stage of burning stabilized briefly at about 11 m in each test. (In test #12 at about the same spill rate, the stabilized fire diameter was about 14 m.)

In Table 5.2 and in Figure 5.8 and 5.9 we have not included the data taken for pool fire test #2. This is primarily because the behavior observed during this test indicated that it was not a normal pool fire. The data log indicated that this was to be a conventional pool fire test but that high wind blew vapors away from the igniter. The spill rate was fairly high (5.3 m^3 in 52 seconds), but ignition occurred about 40 seconds after the spill instead of the 3-5 seconds typical of other pool fire tests. Soon after ignition, the vapor cloud which developed and moved downwind burned intensely in a very short duration (of 4 to 5 seconds). For the remainder of the film, after a brief period of almost normal pool fire burning, a very short, sooty fire which resembled the last stage of the flame of other pool fire tests was observed. The radiometer data showed a sharp rise in measured radiation, which lasted only for 2 or 3 seconds, soon after the ignition. The measured radiation for the remainder of the

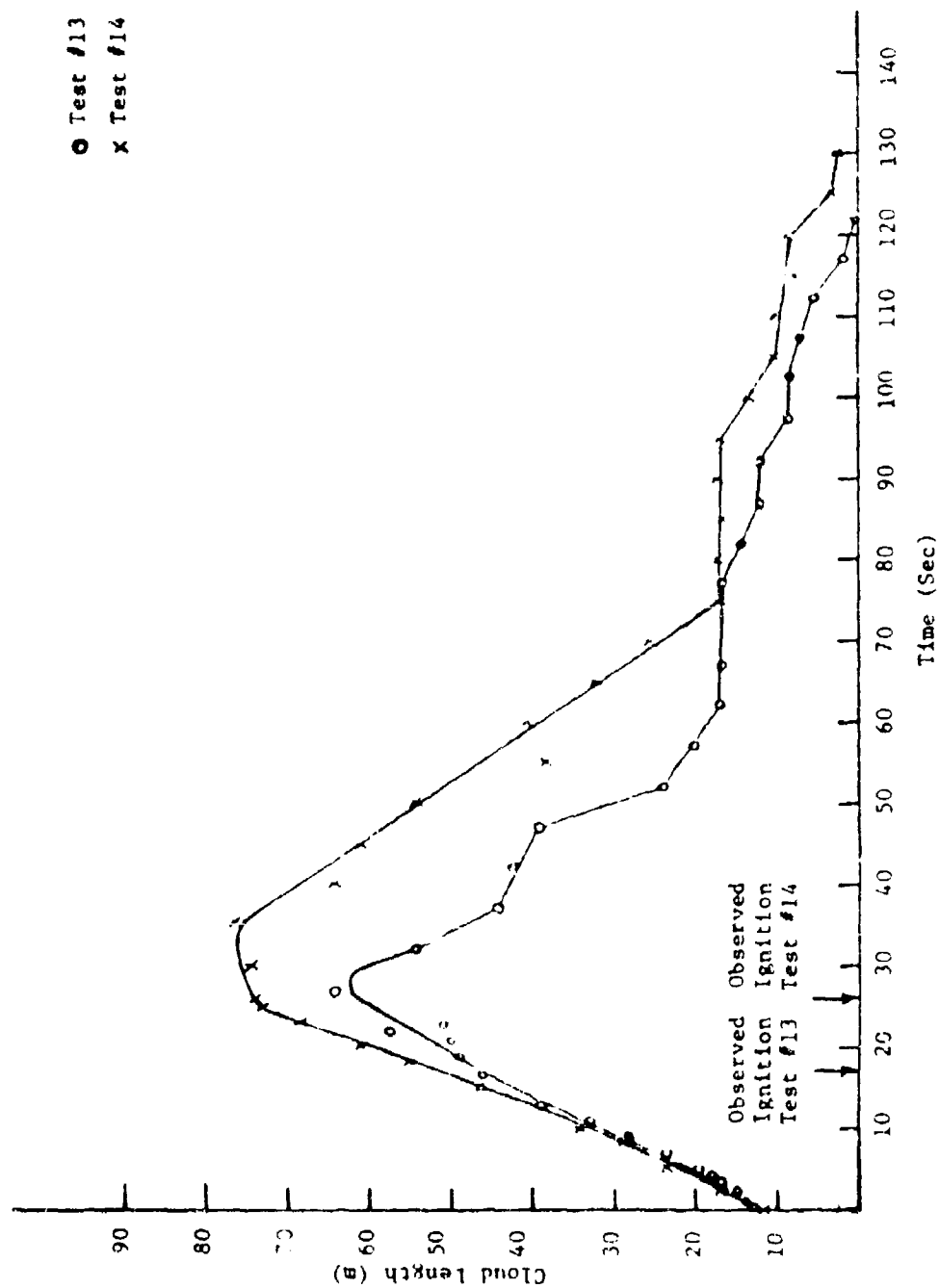


FIGURE 5.7: THE MEASURED CLOUD LENGTH AS A FUNCTION OF TIME FOR DELAYED IGNITION POOL FIRES

fire was much smaller than the measured peak value. This test was conducted with winds in the 6-8 knot range and we have used flame tilt data from the brief pool fire segment. This is one of three tests conducted with wind. However, we have not used the radiometer data since considerable data are available from other pool fire tests which followed the conventional test sequence.

5.3 ANALYSIS OF POOL FIRE DATA

In this section we discuss observations on the physical characteristics of the pool fire. First, we describe the qualitative observations made from the motion picture films. Then quantitative data obtained from measurements of motion picture records are analyzed and correlated.

5.3.1 Qualitative Observations on Pool Fire Behavior

As soon as the LNG first impinges on the water, one observes streaks of white vapor shooting out in all directions, completely masking the spill pipe (which is about 2 m above water level). Igniters are activated in pool fire tests in about 1 second after the spill contacts the water; however, there usually is a delay of a few seconds before flame is visible on the film record. The flame does not spread very rapidly through the established cloud. In fact, even when most of the vapor (and perhaps the pool) is on fire, one can still notice some "stray" white clouds on the periphery. It is likely that these clouds contain vapor concentrations below the lower flammable limit which are visible because of the high relative humidity close to the water.* Alternatively, another explanation for the "slow" consumption of the visible cloud of vapor is that it contains significant amounts of condensed water (fine fog or ice droplets) which act as a quenching medium for flame. While these may not completely quench the flame, they may significantly affect the flame propagation.

* The visible cloud is due to condensation of water vapor as the LNG vapor cools air. The flammable vapor zone may lie within the visible zone if the air is fairly humid.

The second stage in the development of the pool fire is the formation of the visible plume (of fire). The formation of the plume is characterized by a leading head followed by a tail. The head disappears very soon establishing only the tail. This behavior, which is observed in many other situations where buoyancy is suddenly turned on and maintained, is termed (Turner, 1972) the "Starting Thermal." From the time of ignition to the establishment of a fire plume, we estimate the duration to be about 5 s.

The third stage of burning, which lasts for the longest duration of time, is the steady state burning. This period is characterized by the presence of a tall yellowish flame whose height oscillates at almost a regular period. The base diameter has a constant size. Another important feature noticed in this period is the release at regular intervals (between 3 s to 4 s period) of large spherical blobs of burning zones which move up the visible plume. In fact the periodicity of height variation coincides with the release of these blobs of fluid. It is our premise that this phenomenon is the result of flame instability which results in periodic increase and decrease of vaporization rate of fuel from the pool surface. This stage lasts for almost 75% of the spill duration.

Schematic representations of the fire development stage ("starting thermal") and a well established plume fire are given in Figures 5.8a and 5.8b, respectively. The latter figure has been traced from a movie record.

In the fourth stage of burning the flame becomes sooty (most probably due to the burning of heavier hydrocarbons such as propane, ethane, butane). The color of the fire changes from yellow to brick red and finally black soot can be seen at the top third of the flame. The flame height finally decreases, presumably because of the rapid decrease in the evaporation rate. This is seen to occur soon after the flow of LNG is turned off.

In the final stage of burning we see small flamelets on water burning on what appears to be "black" ice. After all of the little flames have died out one notices an area (on the pond water), roughly equal to the size of the LNG pool, which looks black. This may be the

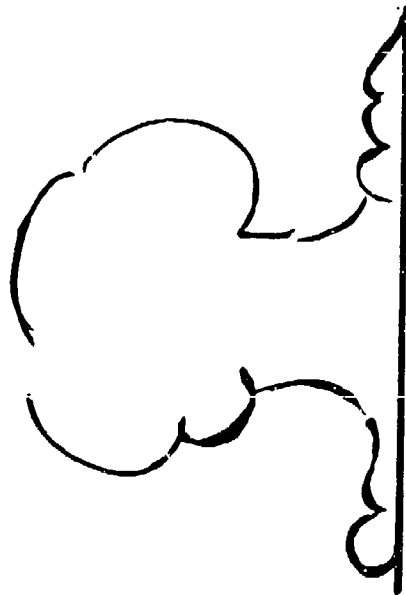


FIGURE 5.8a: SCHEMATIC VIEW OF THE STARTING
THERMAL STAGE OF FIRE PLUME
DEVELOPMENT

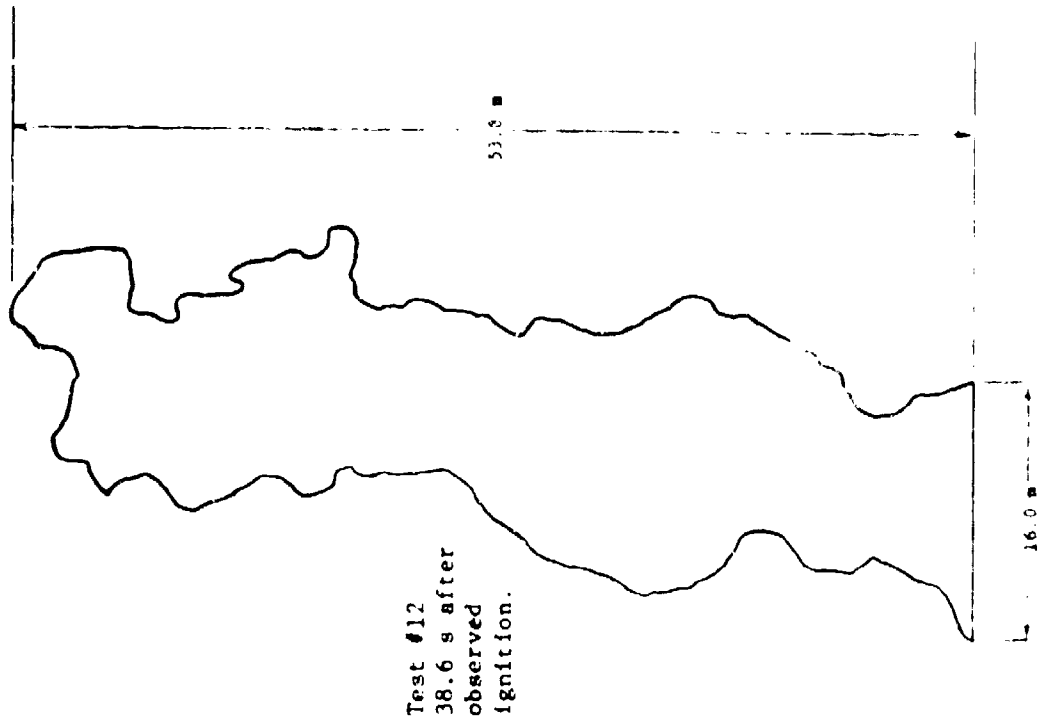


FIGURE 5.8b: INSTANTANEOUS FLAME SHAPE FOR
FULLY DEVELOPED FIRE

remnants of some kind of a LBA water hydrate. By the time anyone could approach the pond after the test, his black patch had completely disappeared.

5.3.2 Quantitative Data from Pool Fire Experiments

As indicated earlier, the visible flame height varies periodically with time. The flame, though vertical, in the absence of wind, is far from being a perfect cylinder.

As can be seen from Figure 5.8b, the flame is tall and slender, but the lateral dimensions are by no means uniform. In fact, the observations of the motion picture data indicate that large turbulent eddies are formed at the lower part of the flame and rise gradually to the upper part of the flame. During their ascent, the eddies grow in size and slowly dissipate into "flamelets." For purposes of analysis, we have used the "instantaneous height" of the visible flame, which by definition is the height of the solid flame from the pool base. In determining the instantaneous height, we have ignored the sheets of the flame that escape from the main body of the flame.

In Figure 5.9 are shown the measured instantaneous heights varying with time for test #12. As can be seen from the Figure, the height of the flame steadily increases to about 50 m in less than 5 seconds after ignition. This corresponds to the rise of the initial head. The diameter of the head was estimated to be about 18 m and the height to be about 11 m. The average velocity of rise of the center of the head was about 11 m/s. The tail of the flame forms the beginning of the pool fire and it rises to a height of about 50 m in about 10 seconds. The mean height of the flame was seen to be steady for a long time and started to decrease steadily around 85 seconds after ignition. Hence, we have estimated the duration of intense burning as 75 seconds which corresponds to the time difference between the beginning of the pool fire (after the formation of the initial head) and the end of the steady state burning indicated by the rapid decline in the flame height.

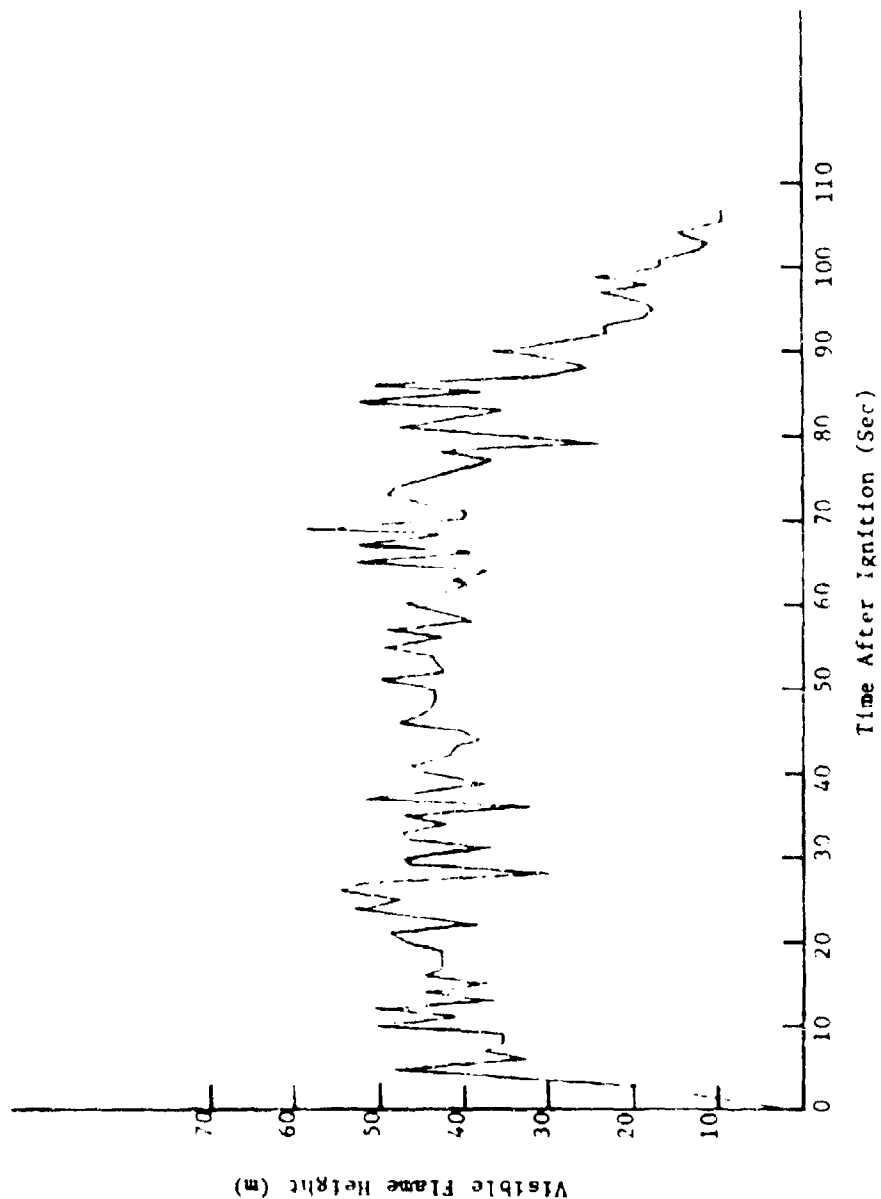


FIGURE 5.9: INSTANTANEOUS HEIGHT OF THE VISIBLE FLAME AS A
FUNCTION OF TIME FOR LNG TEST #12

During the period of intense burning, the flame height fluctuates rapidly. There appears to be a predominant frequency to this fluctuation with a period of about 2-3 seconds. The peak-to-peak fluctuation in height is less than 10 m during the steady burning period. An arithmetic average of the flame lengths over the duration of intense burning was calculated. In Figures 5.10, 5.11 and 5.12 are shown the variation in instantaneous visible flame length as a function of time for LNG tests #3, 4, and 5, respectively. In Table 5.3 are given the duration of intense burning, average and standard deviation of measured visible flame lengths for various LNG tests.

5.3.3 Correlation of the Visible Flame Length Data

It was pointed out earlier in Section 5.2 that the apparent average burning rate of LNG on water varied significantly for the various tests. In Figure 5.13 are plotted the measured mean lengths of the flames as a function of the estimated burning rates. It should be noted that there is inherent uncertainty in the estimated rate of burning because of the subjective evaluation of the duration of intense burning and the asymmetry of the burning pool. The purpose of Figure 5.13 is merely to indicate that there is a definite relationship between the rates of burning and the average flame height measured using the motion picture data.

Thomas (1963) developed a correlation for the visible mean height of turbulent diffusion flames (in the absence of wind) based on dimensional analysis and data from laboratory scale crib fires. The correlation for a circular liquid pool fire can be written as follows:

$$\frac{L_f}{D} = 42 \left[\frac{1}{a} \frac{\dot{y}}{\sqrt{gD}} \right]^{0.61} \quad (5.1)$$

where \dot{y} is the total liquid regression rate.

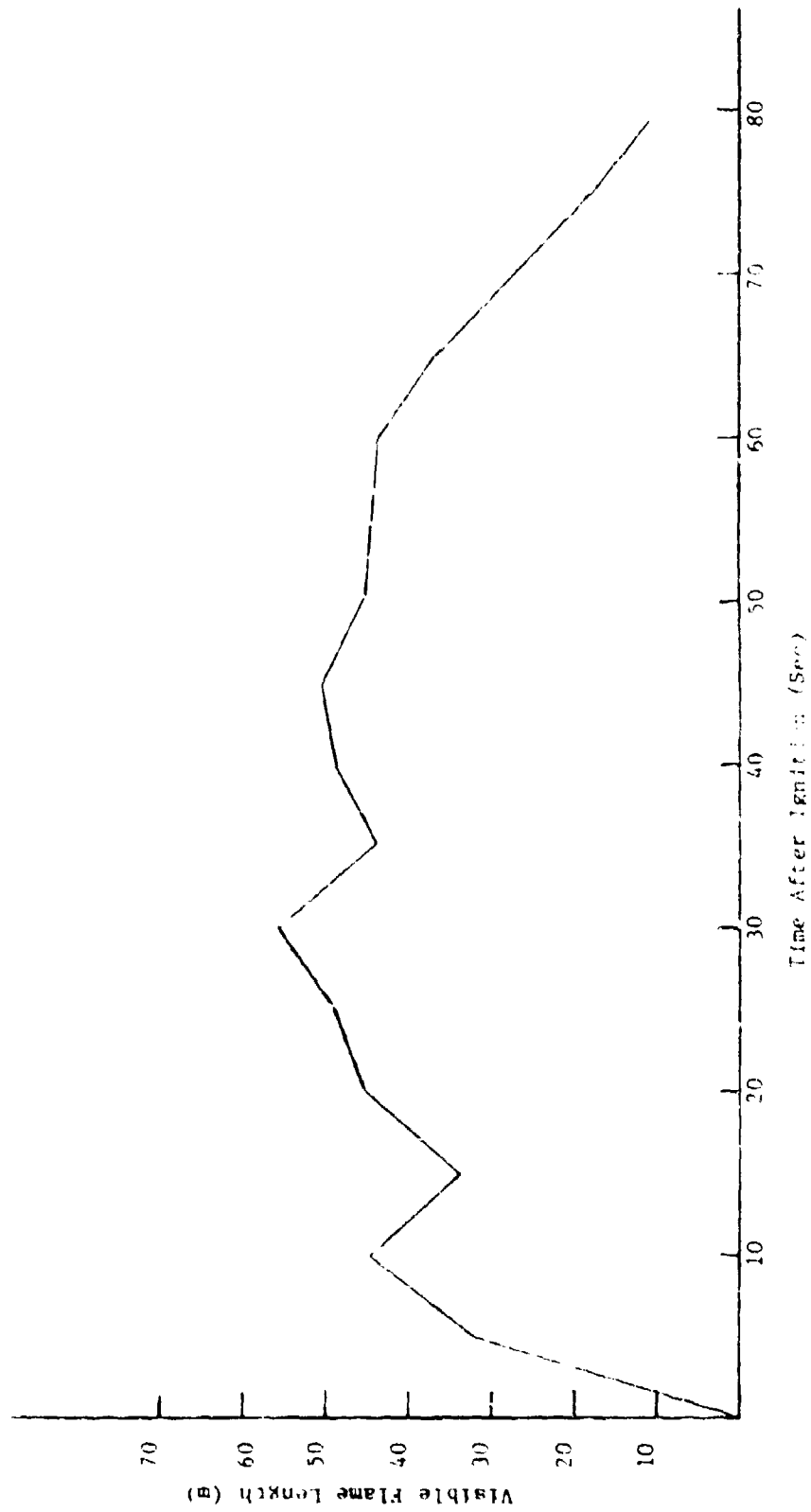


FIGURE 5.10: INSTANTANEOUS LENGTH OF THE VISIBLE FLAME AS A
FUNCTION OF TIME FOR LNG TEST #3

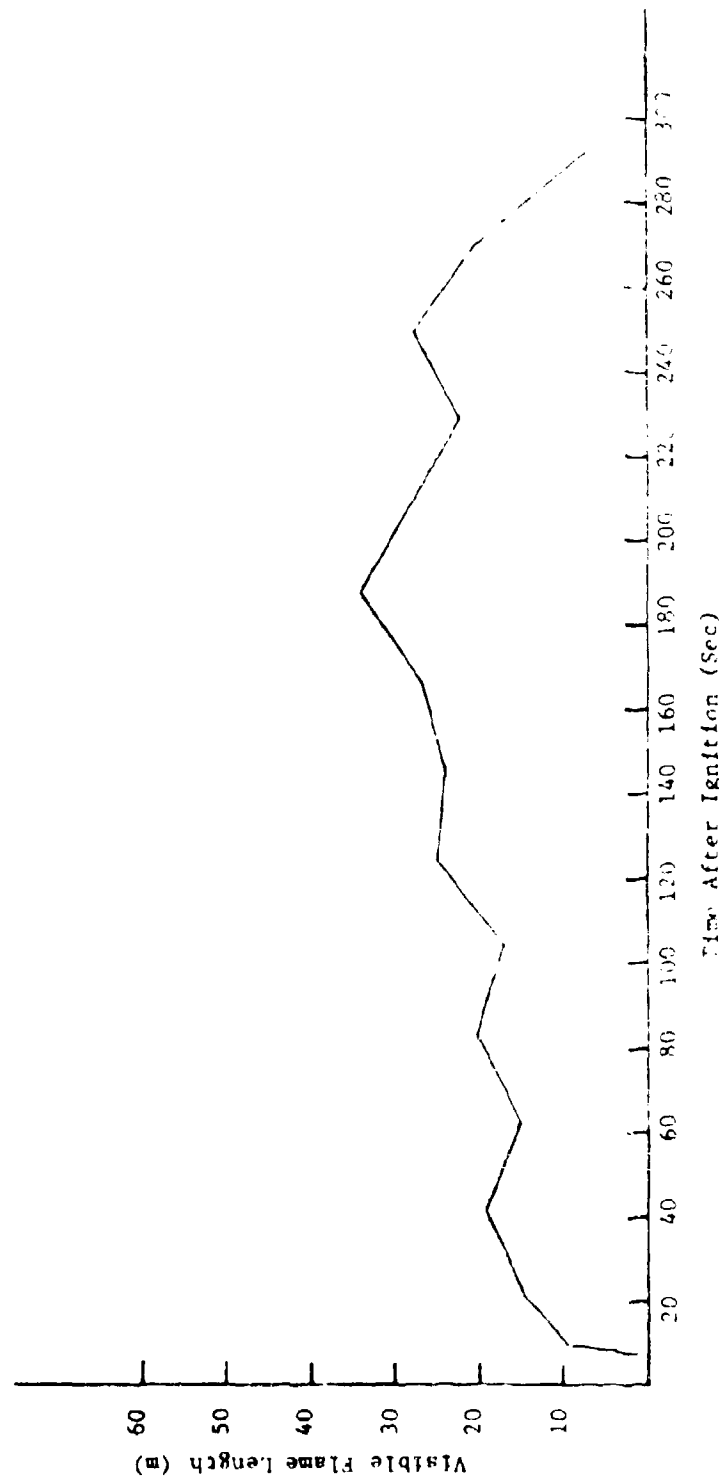


FIGURE 5.11: INSTANTANEOUS LENGTH OF THE VISIBLE FLAME AS A
FUNCTION OF TIME FOR LNG TEST #4

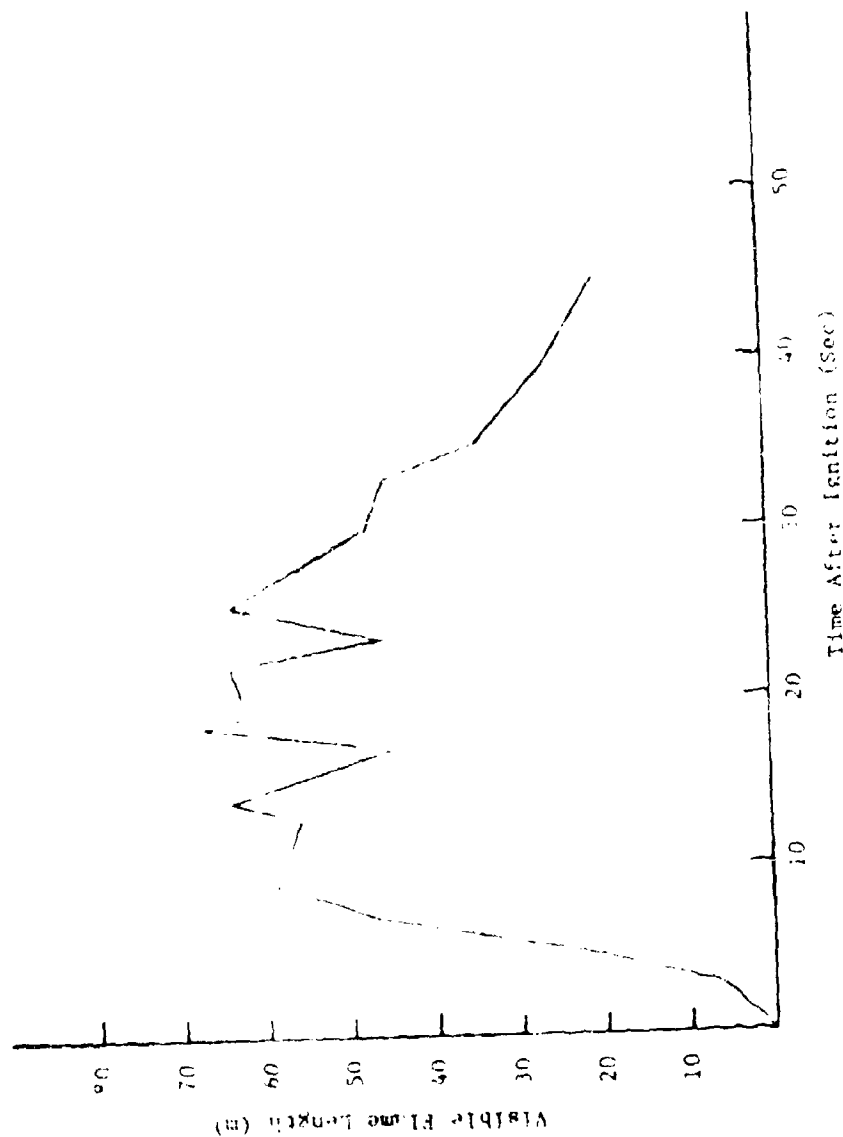


FIGURE 5.1.2: INSTANTANEOUS LENGTH OF THE VISIBLE FLAME AS A FUNCTION OF TIME FOR LAC TEST #3

TABLE 5.3

MEASURED VISIBLE FLAME LENGTHS FOR POOL FIRES

Test #	Average Spill Rate (m^3/s)	Duration of Intense Burning (s)	Average* Flame Length L_f (m)	Standard Deviation of Flame Length (m)	Pool Diameter D (m)	L/D
1	0.021	210	24.0	2.7	8.5	2.8
3	0.086	42	47.2	3.9	11.5	4.1
4**	0.017	195	25.5	6.3	9.0	2.8
5	0.094	26	55.0	8.5	12.6	4.3
6**	0.110	40	42.0	6.4	15.0	2.8
12	0.070	75	44	6.3	14.0	3.1

* Average flame length was obtained by calculating the arithmetic average of the length of the visible flame sheet during the period of intense burning.

** Flames in tests 4 and 6 were tilted by wind of 2.6 and 2.2 m/s velocity respectively. Flame length is the slant height.

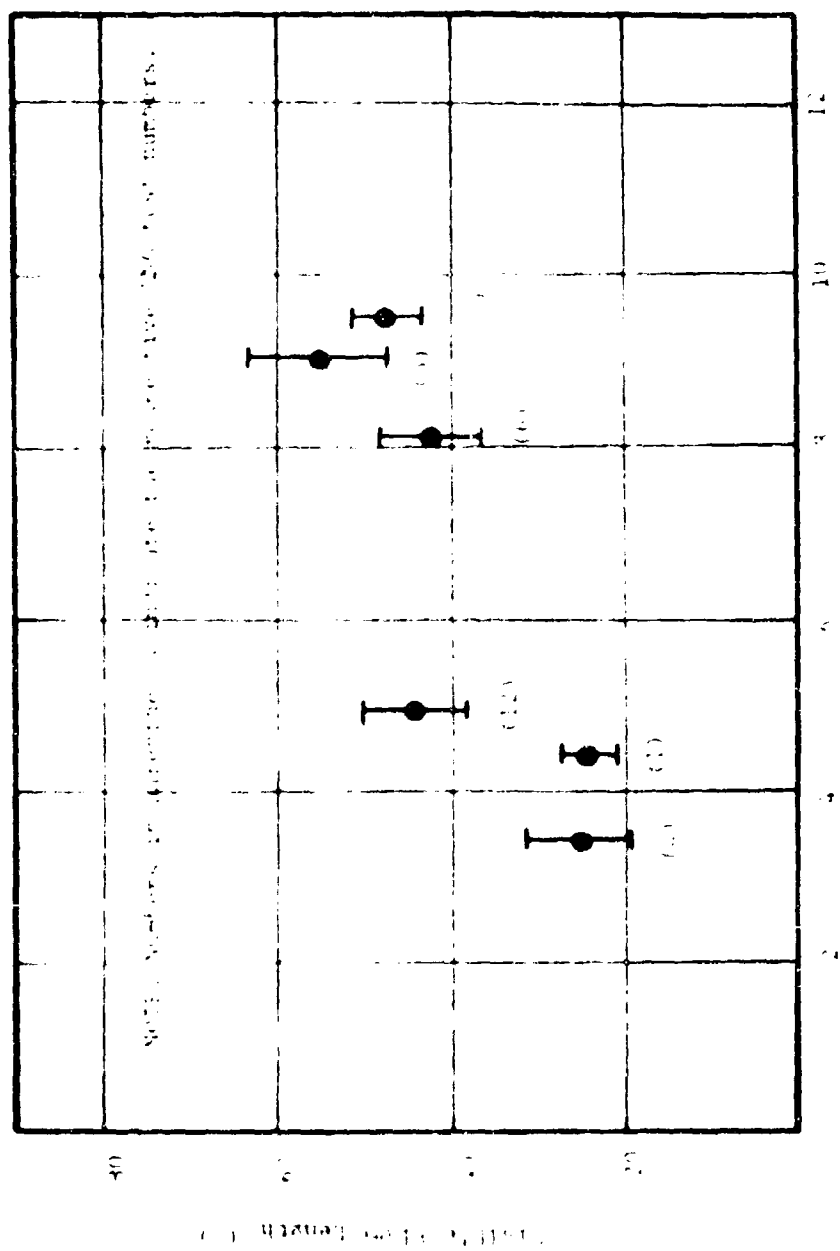


Figure 5.13: Graph of Lengths and Their Variation with the Estimated Burning Rates

Thomas' analysis involves some fundamental assumptions:

1. The flame is characterized by a single temperature and a specified gas composition at the flame tip regardless of the flame size or soot concentration in the flame.
2. The correlation does not take into account either the differences in fuel properties or the differences in their flame radiation properties.
3. The correlation is valid only if the turbulence is generated by the heat source itself and not if the ambient turbulence is convected into the fire plume. This may be a very serious limitation, since ambient turbulence is always convected into the fire plume for a fire in the open, such as for a burning pool of LNG on water.

Despite these limitations, Thomas' correlation seems to predict the height-to-diameter ratios of large-scale LNG pool fires very well. In Figure 5.14 the flame height data from the current series of pool fire tests are plotted in dimensionless coordinates and are compared with Thomas' correlation. The scatter in the measured flame heights is indicated whereas the diameter is assumed to be constant. In using Thomas' correlation, we have utilized the estimated values of the apparent average burning rates of LNG on water. As can be seen from Figure 5.14, the predicted flame heights agree reasonably well with the measured flame heights.

5.1.4 Flame Tilt by Wind

Wind tilting of LNG pool fire plume has been studied by AGA (1974) using the data obtained in the AGA experiments with LNG fires on land. The correlation obtained from these data is similar to one developed by Thomas (1964) and is given by:

$$\cos \alpha = \begin{cases} 1 & \text{for } u^* < 1 \\ \frac{1}{\sqrt{u^*}} & \text{for } u^* > 1 \end{cases} \quad (5.2)$$

where:

$$u^* = \frac{U_w}{(\frac{1}{2} g D / \nu)^{1/3}} \quad (5.3)$$

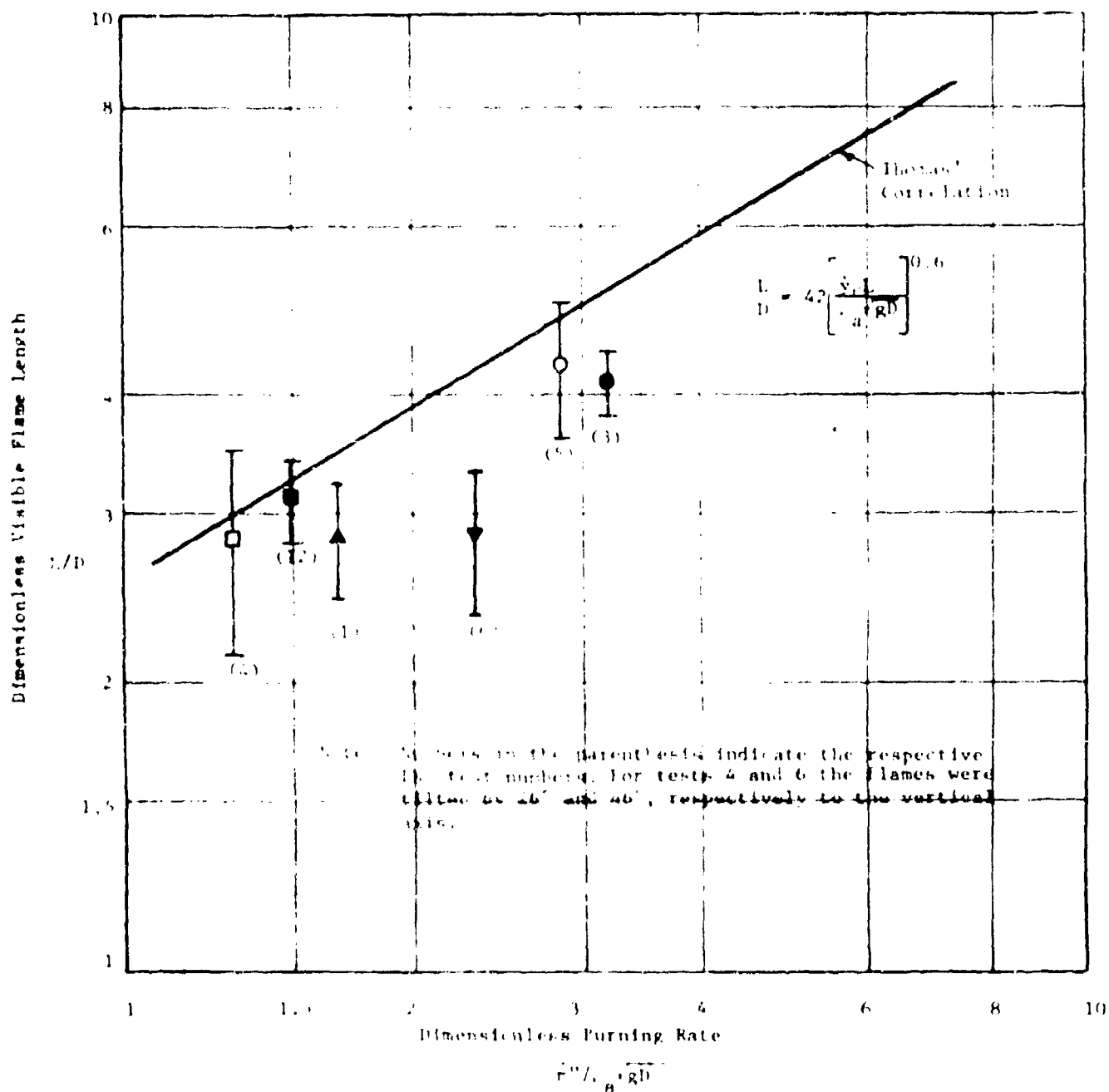


FIGURE 5.1.1: NONDIMENSIONAL FLAME LENGTH VS DIMENSIONLESS BURNING RATE

Where U_g is the wind velocity in m/s measured at a height of 1.5 m above ground.

In Figure 5.15 is shown the correlation indicated by equation (5.2). Indicated in the figure are the two experimental points obtained from the pool fire tests #4 and 6. The instantaneous flame tilt angles were measured from the motion picture data. Since the camera was not normal to the direction of the wind, the measured angles were corrected using simple trigonometric relationships to obtain the tilting of the flame by the wind in the vertical plane containing the wind vector. The scatter in the measured data is due to fluctuations in wind speed. The measured wind velocities over the pond were about 2.64 m/s for tests #2 and #6 and 2.20 m/s for test #4. The measured mean flame tilt angles from the vertical axis were 37°, 26.5° and 46.3° for tests #2, 4, and 6 respectively.

5.4 THERMAL RADIATION DATA AND THEIR ANALYSIS

In the pool fire experiments the radiative outputs of the fires were measured using radiometers, both the narrow-angle type and the wide-angle type. In one experiment, (test #5) a spectrometer was also used to measure the spectral emissive characteristics of the fire. This section discusses the measured data using the radiometers and the calculated values for the thermal energy emitted by the flame (emissive power). For calculating the magnitude of the energy emission, atmospheric absorption corrections and geometrical view corrections (view factor) are taken into account. In effect, the flame emission characteristics are determined by assuming the flame to be a cylindrical, grey emitter (AGA 1974).

Five wide-angle and two narrow-angle radiometers were used in these pool fire tests to measure the radiant fluxes at various distances from the flame. Table 5.4 shows the location and orientation of these radiometers. The narrow-angle radiometers have a total cone angle of about 7° and are pointed at the flame. For the series of tests #1 to 6, they were located 60 m from the spill point and covered a flame surface area of approximately 7 m in diameter. The more recent series of tests, #12, 13 and 14, had the narrow-angle radiometers located at a distance of 30 m from the spill point. Therefore, the area of flame surface covered in these tests corresponded to a circle of about 3.5 m diameter. Since the

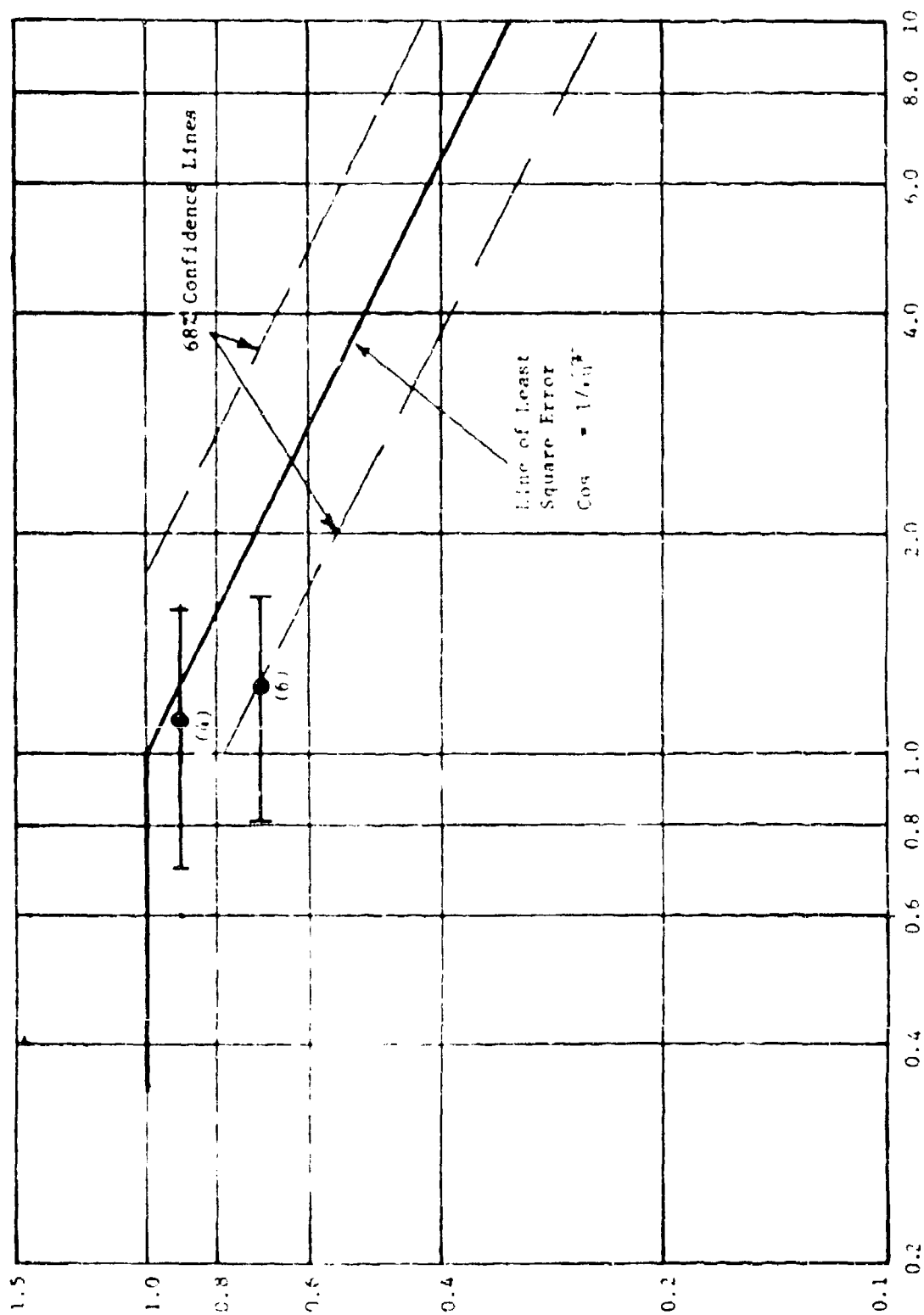


FIGURE 5.13: FLAME TILT ANGLE AS A FUNCTION OF DIMENSIONLESS WIND VELOCITY

LOCATION AND ORIENTATION OF RADIOISOTOPES

LWC TEST # 1 to 6					LWC TEST # 12, 13, and 14						
RADIOMETER #	SERIAL #	DISTANCE		TYPE OF MINERAL	SERIAL #	DISTANCE		TYPE OF MINERAL	HEIGHT ABOVE PORT LEVEL (m)		
		TYPE	FROM SPILL POINT (m)			TYPE	FROM SPILL POINT (m)				
1	56012	WA	OW 80	Quartz 2	Horizontal	65281	WA	60 NW	Sapphire	3	Horizontal
2	56013	WA	OW 60	Quartz 2	Horizontal	56015	WA	45 NW	Sapphire	3.4	Horizontal
3	56016	WA	OW 40	Quartz 1	Horizontal	56016	WA	45 NW	Sapphire	3.4	Horizontal
4	56014	WA	OW 55	Quartz 1	Horizontal	65283	WA	30 NW	Sapphire	1.5	Horizontal
5	56017	WA	OW 60	Sapphire	Spill Point	56017	WA	30 NW	Sapphire	1.5	Top of Spill Line
6	56018	NA	OW 60	Sapphire	4 m above spill point	56018	NA	30 NW	Sapphire	1.5	2.4 m above top of spill line
7	--					65284	WA	45 SW	Sapphire	3.4	Horizontal

WA = Wide-Angle Radiometer
NA = Narrow-Angle Radiometer

CW = Cross Wind Direction
OW = Down Wind Direction
NW = North West
SW = South West
OW = Upwind

* In tests 13 and 14 the window is ZnSe.

• in tests 13 and 14 the window is insip.

NOTE: All wide-angle radiometers in tests 1 through 6 were calibrated and used with quartz windows and all narrow-angle radiometers on all tests were calibrated and used with sapphire windows. In addition, radiometers 2, 3, and 4 were calibrated without windows.

narrow-angle radiometers view only flame surface, the measured quantity is directly related to the emissive power of the flame after corrections for atmospheric transmissivity are made.

The wide-angle radiometers have a field of view of approximately 150°. Therefore, only part of the field of view included the flame. The emissive powers can be obtained by back calculation, using the geometric view factor as one of the parameters.

5.4.1 Limitations of the Measured Radiometer Data

Unfortunately we have been unable to use all the radiometer data that were recorded for various pool fires. Table 5.5 shows the available radiometer data for various pool fires. A number of problems made some of the recorded data questionable. For instance, the two wide-angle radiometers #1 and 6 used in earlier series of tests #1 through 6 were subsequently damaged and could not be recalibrated. Also, in the calibration, low irradiance was obtained by lowering the temperature of the black body (resulting in the change in the spectral distribution of incident energy) while in field use the decrease in the irradiance was caused by the distance between the flame and the radiometer. A theoretical analysis was performed to estimate the average transmission through the window, but the results obtained by this method varied very widely. In the later delayed-ignition pool fire tests, #13 and 14, some of the radiometers were surrounded by the flame and the radiometer readings were off scale. One of the two narrow-angle radiometers used in tests #1 to 6 was aimed too low so that the flame covered only about half of the field of view. This resulted in a very low measurement of the emissive power of the flame (about half of that measured by another radiometer located next to it, but oriented in such a way as to have only flame surface in its field of view). Due to several of these unforeseen circumstances, the total amount of data that is reported in this section has been greatly reduced. A complete package of data gathered in the tests is given in Appendix D.

Tests #1-6 were conducted prior to any data analysis. The analysis indicated several instrument problems, so additional tests were conducted. Tests #12-14 represent the second series of tests where most of the early instrument problems were corrected.

TABLE 1

POOL FIRE RADIOMETER DATA FOR 1960 FIRE

Pool Fire Test #	Radiometer #							Remarks
	1	2	3	4	5	6	7	
1	RC	*		RC	0	UR	NA	U = The view of radiometer 3 covered only part of the flame. Hence the readings are far less than the ones measured using Rad #6.
2	UR	UR	UR	UR	UR	UR	NA	
3	RC	*		RC	0		NA	
4	RC	*		RC	0		NA	O = Off scale
5	RC	*	*	RC	0		NA	
6	RC	*		RC	0	/	NA	
12	/	*	*	/	/	IP	IP	R = The radiometer cali- bration curves without windows are not avail- ble.
13	/	*	OS	OS	/	*	*	
14	/	*	OS	OS	/	*	*	

NA = not used

UR = unrecognizable.

IP = instrument problem.

/ = useful data

* Radiometers 2 and 3 which are located at 60 m and 40 m from spill point measure same amount of radiant energy.

5.4.2 Analysis of Narrow-Angle Radiometer Data

As pointed out earlier, the narrow-angle radiometer looks at a portion of the flame and measures the radiated thermal flux from that portion of the flame. Since the field of view of the radiometers is typically small (of the order of few degrees), the measured thermal flux directly gives the local emissive power of the flame.

In Figure 5.16 are shown the measured narrow-angle radiometer data for LNG test #12. As can be seen from Figure 5.16, the measured thermal flux steadily increases with time after ignition and then remains fairly constant. At about 40 seconds the measured thermal flux starts to decrease reaching a low value of about 75 kW/m^2 just before the valve is closed. Then it increases rapidly to a value of 160 kW/m^2 just before the flame dies. The cause for this late increase in flux may be due to ethane and propane. During the steady burning of the pool, the radiometer reads an average flux of about 150 kW/m^2 . Due to an instrument problem, data from the second narrow-angle radiometer were not available for comparison.

In Figure 5.17 are shown the measured narrow-angle radiometer data for Test #5. As indicated earlier, radiometer #5 was aimed at the spill point and radiometer #6 was aimed at 4 m above the spill point. Therefore, only about half of the field of view of radiometer #5 was covered by the flame and the measured thermal flux is significantly lower than the flux measured by radiometer #6.

In Figure 5.18 and 5.19 are shown the measured narrow-angle radiometer data for the delayed ignition pool fire tests #13 and 14. As can be seen from the figure, the measured thermal flux fluctuates considerably for these two tests, and at times the instrument has recorded nothing. As pointed out earlier, in tests #13 and 14, the ignited vapor cloud starts burning about 2 seconds after it is formed and actually burns like a pool fire. Since the orientation of the narrow-angle radiometer is towards the spill point, the field of view of the instrument is completely covered by the flame only towards the end of the burning period. This is indicated by the pronounced peaks in the measured radiometer data towards the end of the burning period. We further note that during this period of burning, both Radiometers #5 and #6 read comparable values. This clearly indicates that the orientation of the radiometers were correct and the entire fields of view were covered by the flame.

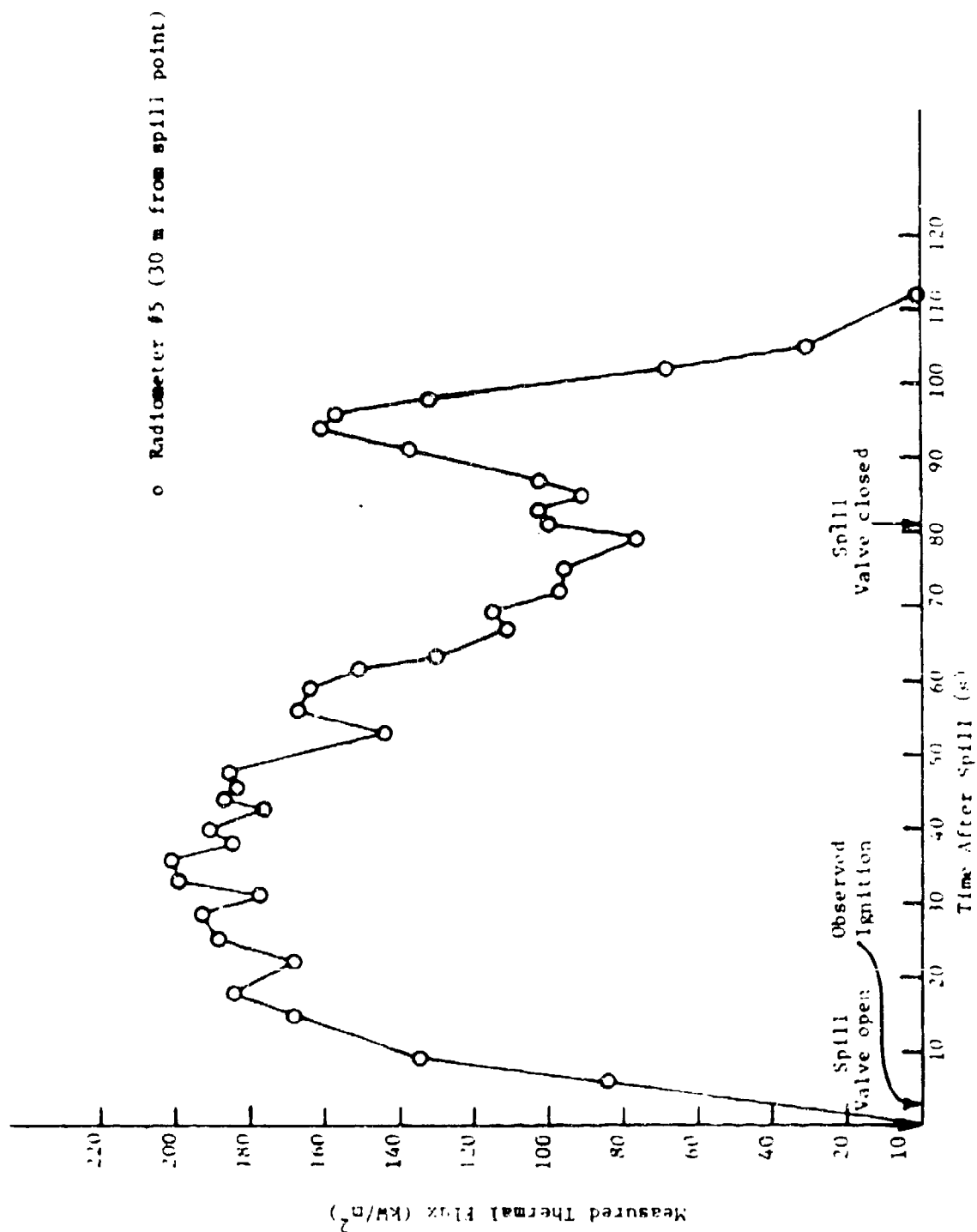


FIGURE 5.10: NARROW ANGLE RADIOMETER DATA FOR POOL FIRE TEST #12

□ Radiometer #6

○ Radiometer #5

Both radiometers located
just above the ground at
60 m from the spill point

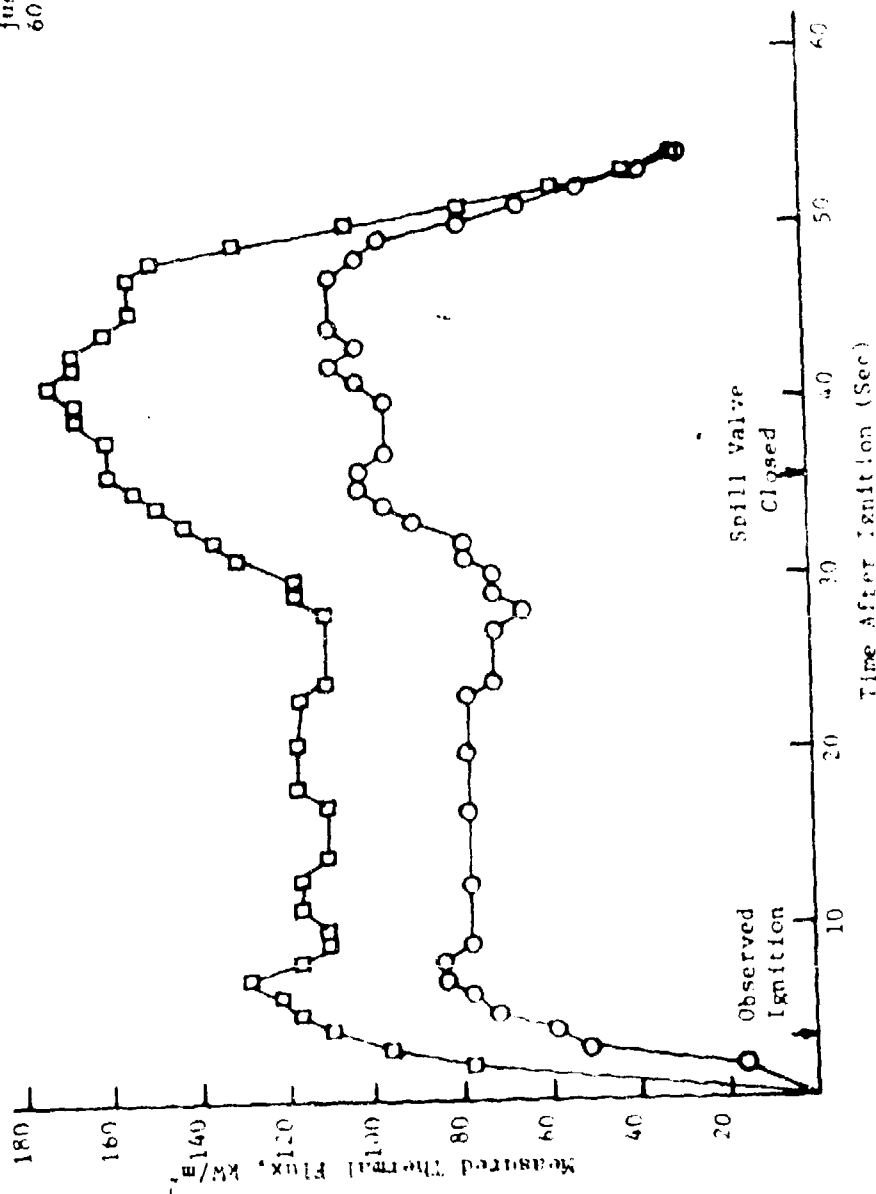


FIGURE 5.1.7: NARROW-ANGLE RADIOMETER DATA FOR TYPICAL TEST

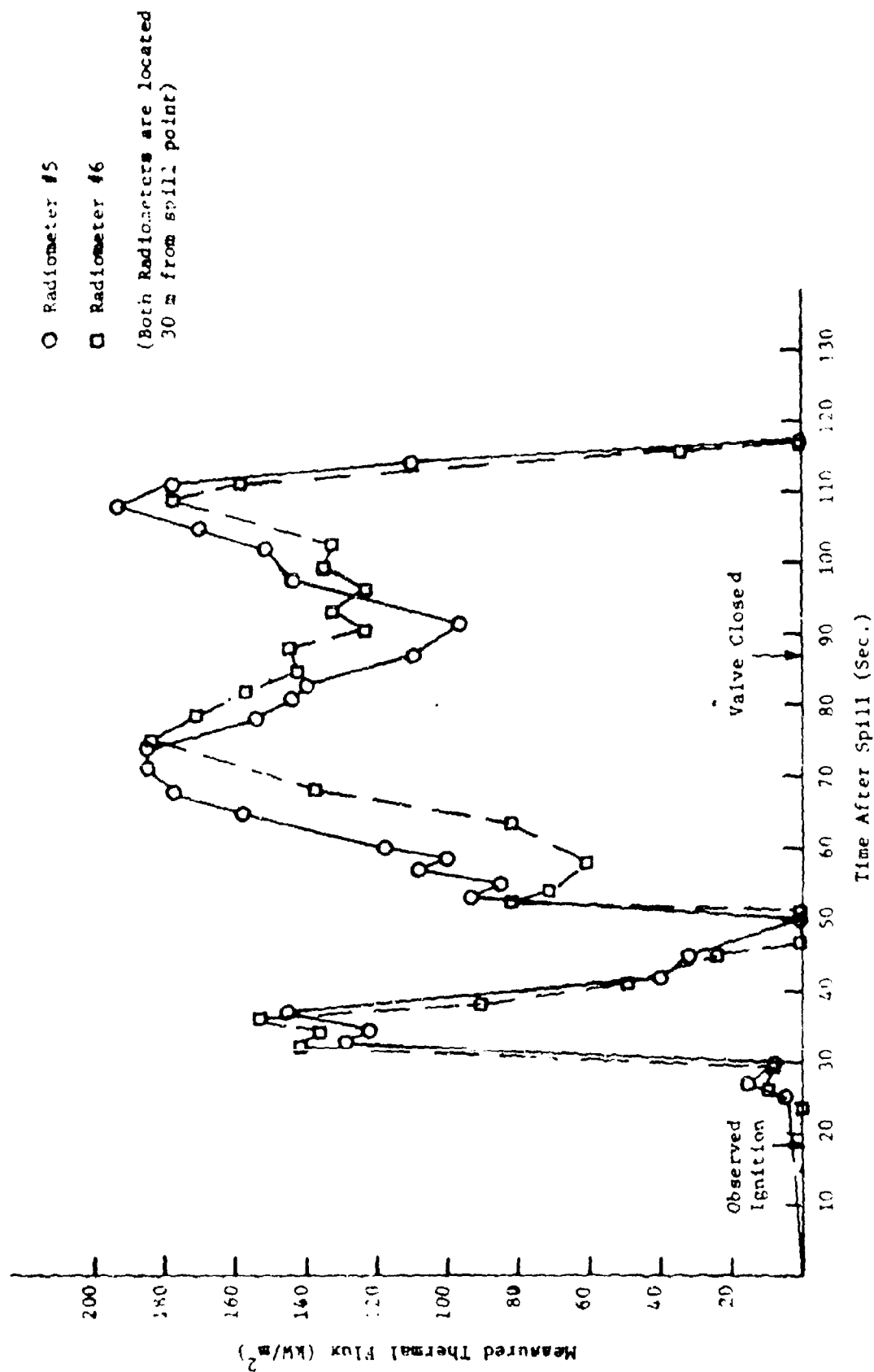


FIGURE 5.12: NARROW-ANGLE RADIOMETER DATA FOR DELAYED
 IGNITION POOL FIRE TEST #13

○ Radiometer #5
 □ Radiometer #6
 (Both Radiometers are located
 30 m from spill point)

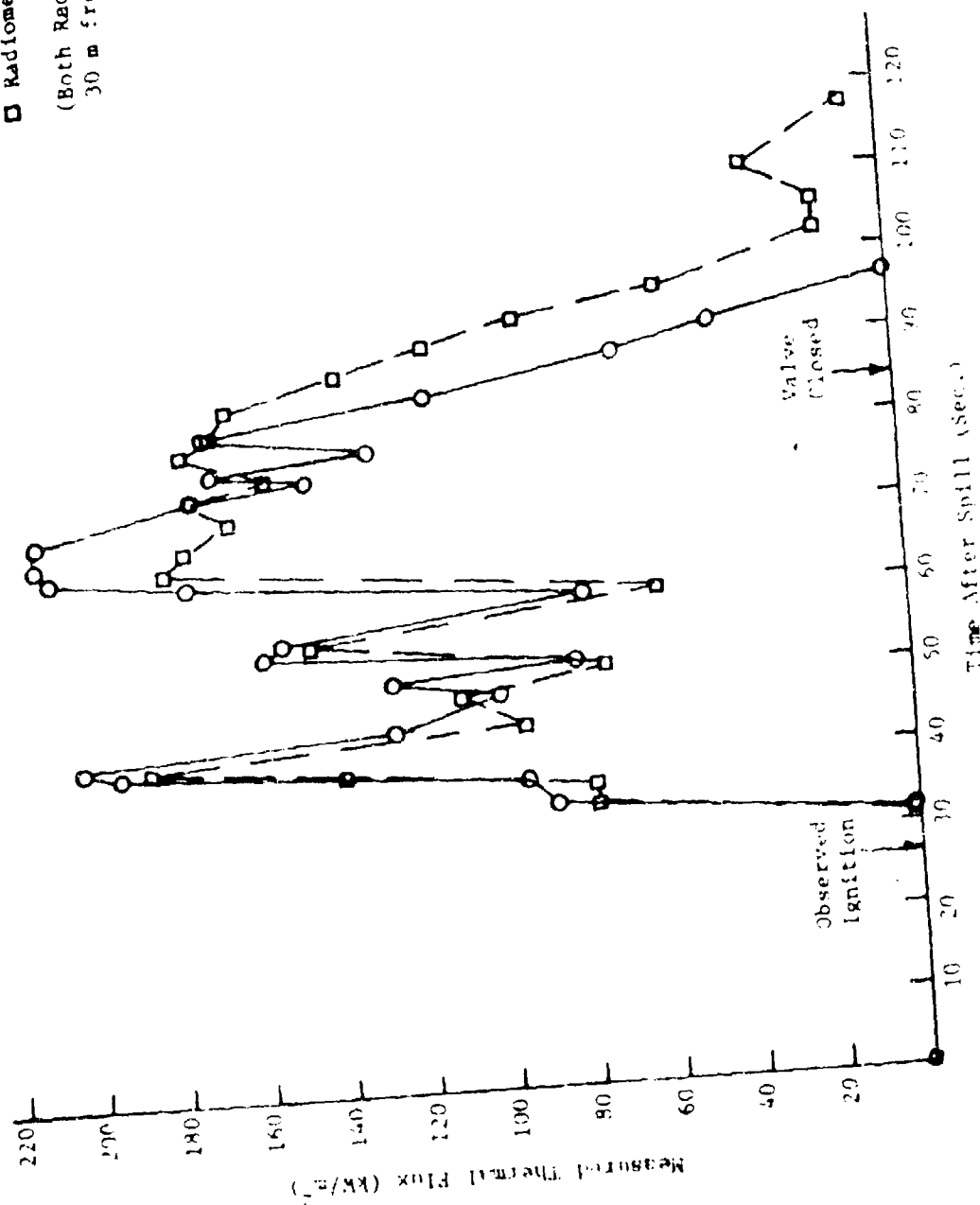


FIGURE 5.10: NARROW-ANGLE RADIOMETER DATA FOR DELAYED IGNITION POOL FIRE TEST #14

In Figure 5.20 are shown the thermal flux measured by the narrow-angle radiometers for various LNG pool fire tests. Here we have plotted the data obtained from radiometer #6 for the pool fire tests 3, 4, 5, and 6, radiometer #5 for the pool fire test #12 and the peak values registered by both radiometers #5 and 6 for the delayed ignition pool fire test #13 and 14. Since the view of the narrow-angle radiometer is completely covered by the flame, one can make estimates of the emissive power of the flame by properly correcting for atmospheric transmissivity.

Atmospheric transmissivity factor, τ , accounts for the attenuation of the thermal radiation caused by absorption and scattering along the intervening path by water vapor, carbon dioxide, dust and aerosol particles. This factor is a complicated function of the thermal and spectral characteristics of the emitter and the total amount of precipitable water in the path length through the atmosphere. (The amount of precipitable water in the atmosphere is directly related to the relative humidity.)

The LNG fire spectral radiation differs considerably from that of a black body spectrum. However, the lack of data on the nature of the spectral distribution of the thermal energy emitted from the fire precludes us from obtaining the correct transmissivity for any given path length through the atmosphere. To the extent that the measured irradiance has to be corrected for atmospheric absorption (and converted to the flame emissive power) we have used the black body spectral transmissivity curves. The variation of atmospheric absorptivity with distance and with relative humidities as parameters is shown in Figure 5.21, for a black body source of 1150 K. We have used this transmissivity data for correcting radiometer irradiances. We do recognize that this does create some error in the estimated value of the flame emissive power. However, the error is expected to be smaller than the standard deviation of the measured values. The flame emissive power thus estimated are shown in Figure 5.22.

It is seen that the emissive power of the flame is relatively independent of the time during the period of intense burning. Further, the emissive power does not appear to be a function of the total duration of spill. (It has already been indicated that the size of the fire increases with increasing spill rates.) The emissive power also does not seem to be a function of LNG composition in the range studied. A statistical averaging of the data shown in Figure 5.22 yielded a mean of 212 kW/m^2 as the emissive

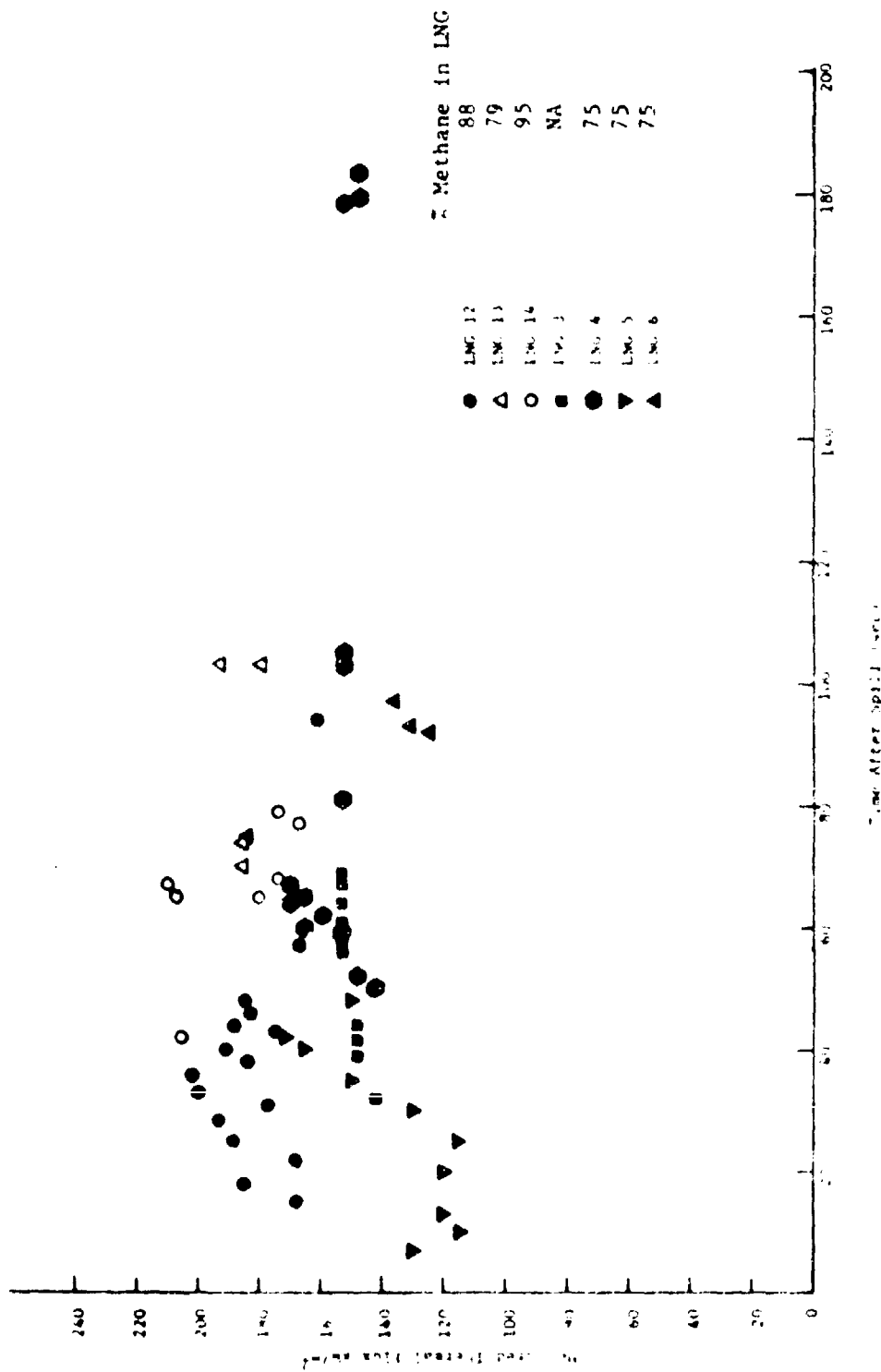


FIGURE 5.20: THE VARIATION OF MEASURED THERMAL FLUX WITH TIME AFTER SPILL FOR VARIOUS LNG POOL FIRES
(Using narrow-angle radiometers)

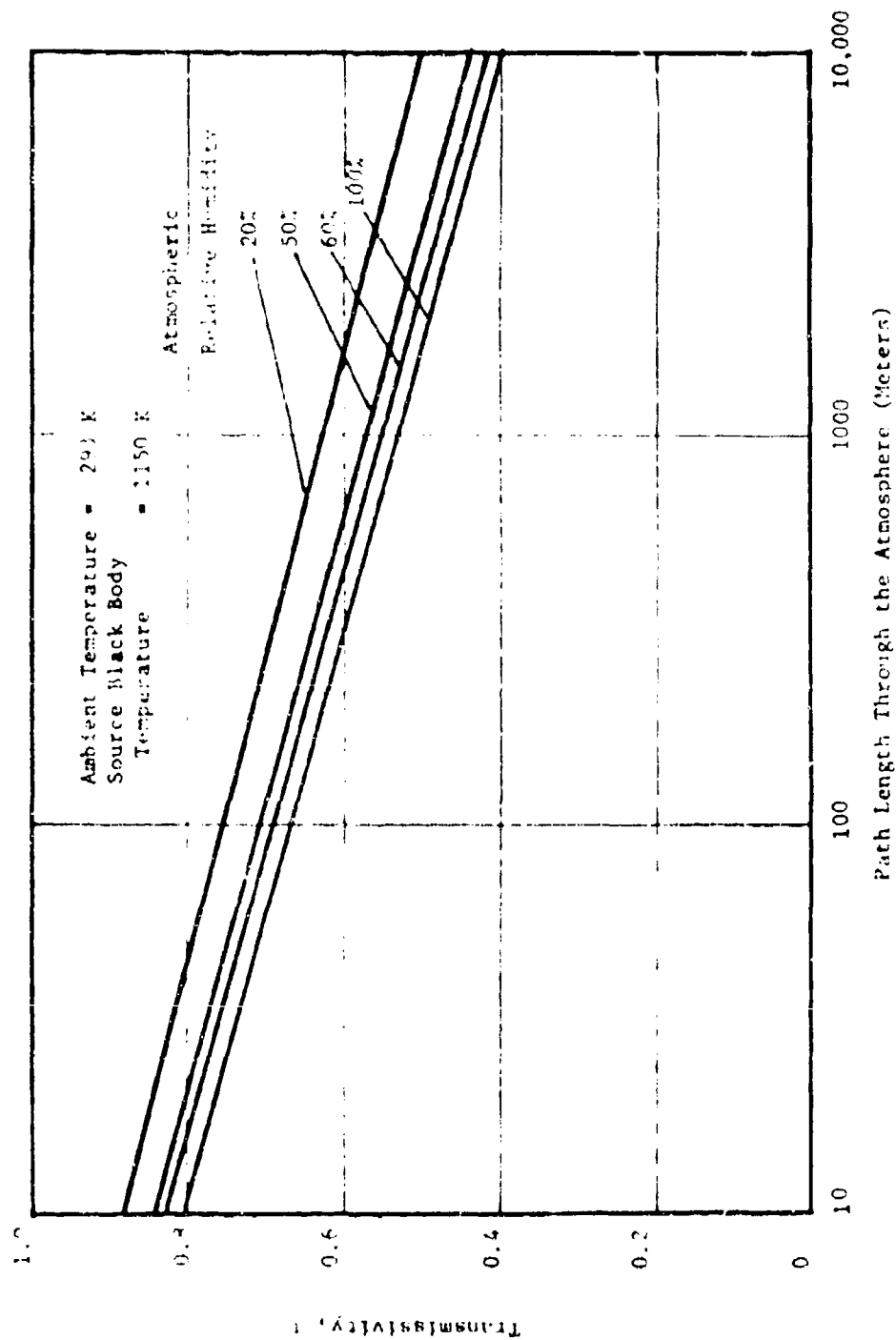


FIGURE 5.21: TRANSMISSIVITY OF ATMOSPHERE FOR THERMAL RADIATION FROM LNG FLAMES

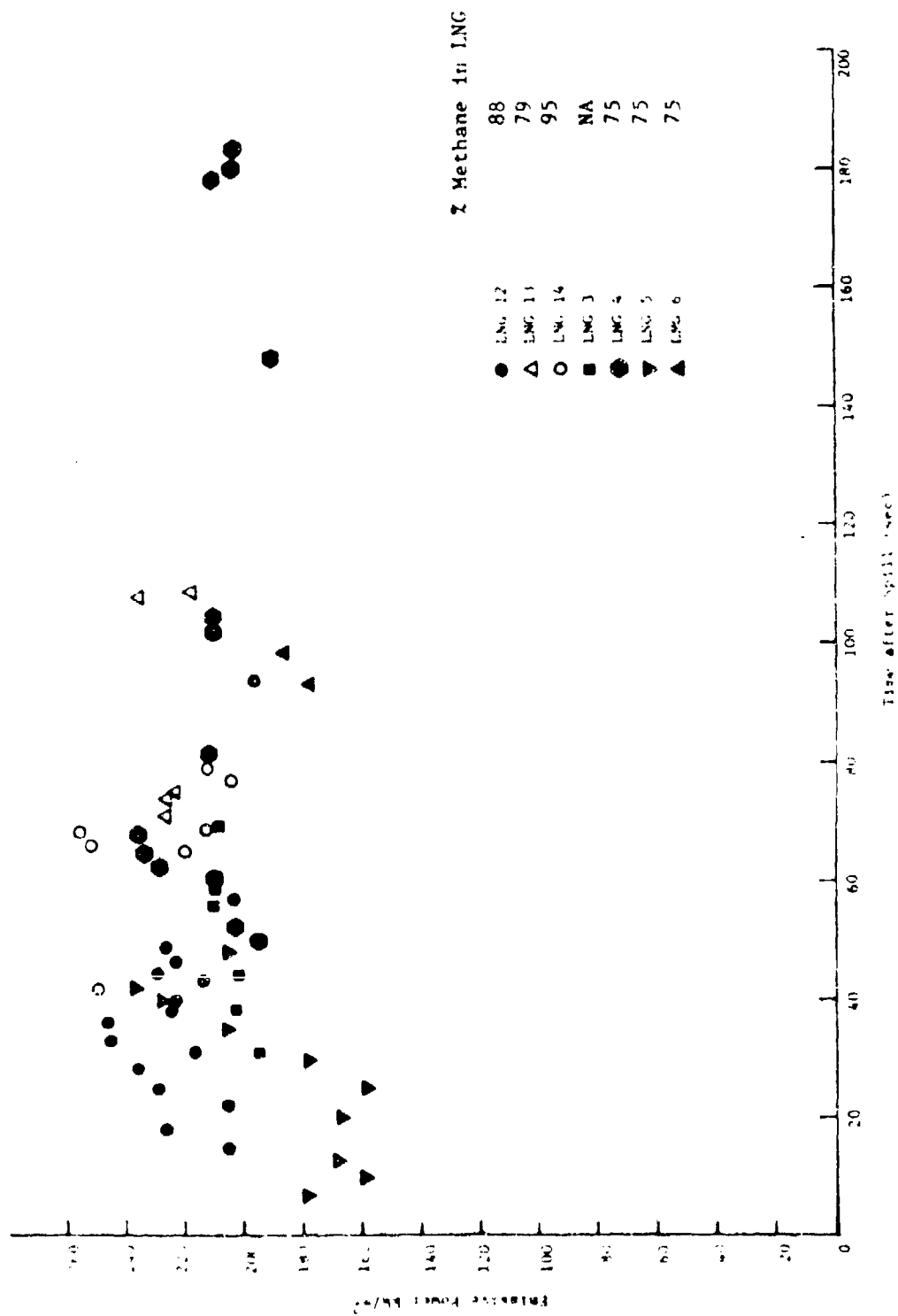


FIGURE 5.22: THE EMISSIVE POWER FOR VARIOUS LNG POOL FIRES DETERMINED USING NARROW-ANGLE RADIOMETER DATA

power of the LNG flames. The standard deviation of the data shown in Figure 5.22 is about 22 kW/m².

5.4.3 Wide-Angle Radiometer Data

Several wide-angle radiometers were located at various distances from the spill point to measure the overall thermal radiation from the pool fires. In Figure 5.1 and 5.2 are shown the exact location of wide-angle radiometers. As pointed out earlier, we have not been able to use all the wide-angle radiometer data. In Table 5.5 are indicated the valid wide-angle radiometer data that are analyzed in this section. The wide-angle radiometers were used with four different types of windows as indicated in Table 5.4. The average transmissivity through the window was calculated by using the transmissivity spectrum of the window and the spectrum of LNG flame measured in test #5.* The calculated average transmissivities of the radiometer windows are as follows:

Quartz 1	-	0.510
Quartz 2	-	0.441
Sapphire	-	0.787
ZnSe	-	0.720 (measured values were in 0.65-0.7 range)

In Figure 5.23 are shown the measured wide-angle radiometer data for pool fire test #12. This test was run under calm conditions, so the flame was essentially vertical. The radiometers were located at 30 m, 45 m and 60 m from the spill point. As can be seen from Figure 5.23, the measured thermal flux decreases steadily with increasing distance from the fire. The thermal flux measured by the two radiometers located at 45 m from the spill point are essentially the same. The radiometers measure zero thermal flux at the time of ignition and steadily increase to a stable value. During the period of intense burning, the fluctuations in the radiometer data appears to be periodic. It is likely that fluctuations in visible flame height result in fluctuation of radiometer data. The period of fluctuation of the latter, however, seem much larger than the former.

In Figure 5.24 is plotted the time averaged thermal flux measured by the wide-angle radiometers as a function of the distance from the surface of the flame for Test #12. Here we have assumed that during steady-state

* The use of a spectrum recorded at 236 m distance from the flame to correct the radiometer data obtained within 60 m does introduce errors. These are primarily due to the path length dependent spectral absorption characteristics of the atmosphere.

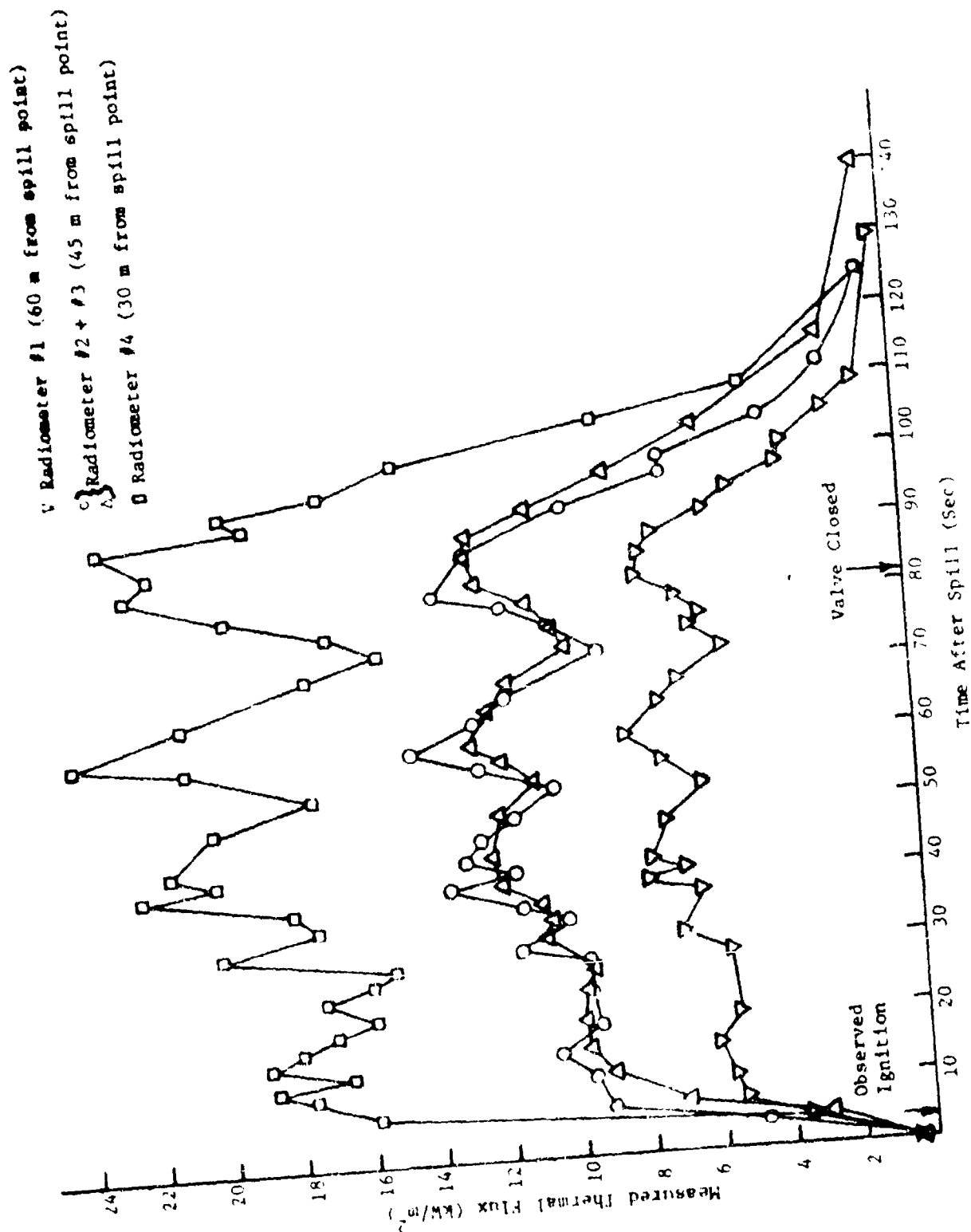


FIGURE 3. 20. WIDE-ANGLE RADIOMETER DATA FOR PWD, FIRE TEST #12

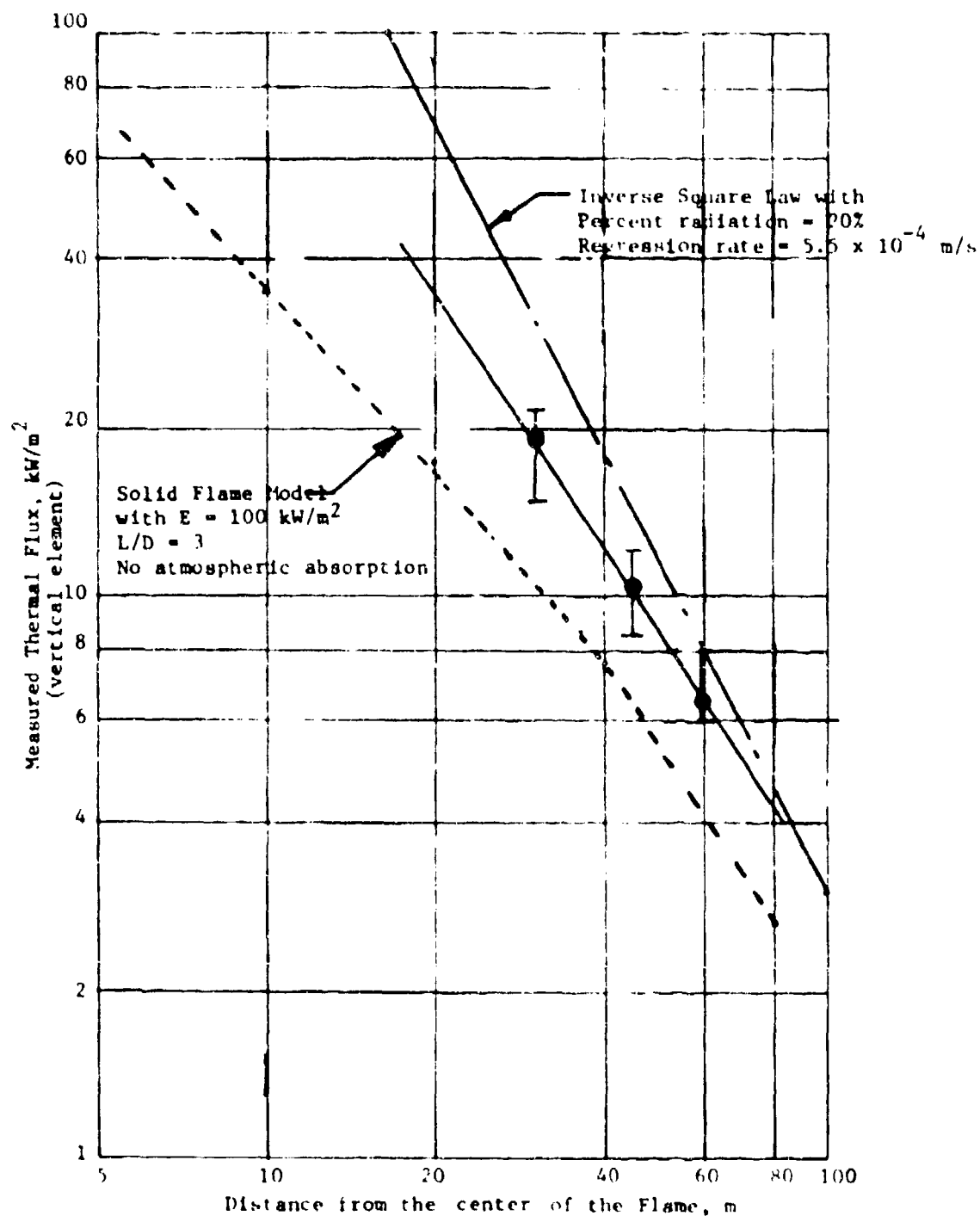


FIGURE 5.24: COMPARISON OF THE MEASURED THERMAL FLUX VARIATION WITH DISTANCE FROM THE CENTER OF THE FIRE FOR POOL FIRE TEST #12 AND PREDICTIONS FOR MODELS

burning, the flame shape can be approximated by a circular cylinder of diameter given in Table 5.2. The average thermal flux was determined by taking the arithmetic average of the instantaneous radiometer reading during the period of intense burning. Also indicated in Figure 5.24 is the measured peak and low values of the thermal flux from the various radiometers. The slope of the line passing through these data points will indicate the spatial variation of the thermal flux for the specific flame shape and size. In Figure 5.24 are also shown the predictions for test #12 based on two widely used existing models: the inverse square law model with 20% of the energy radiated and the solid flame model with $H/D = 3$ and $E = 100 \text{ kW/m}^2$. As can be seen from Figure 5.24, the measured variation in thermal flux is closer to the solid grey emitter model than the inverse square law model. The data are reasonably well modelled if one uses $E = 220 \text{ kW/m}^2$, $H/D = 3.1$ from Thomas' equation for a regression rate of $5.5 \times 10^{-4} \text{ m/s}$, and makes allowance for atmospheric absorption.

For the earlier series of pool fire tests 1 through 6, the data obtained by only two radiometers are valid. These two radiometers are located at 40 m and 60 m from the spill point, but measure essentially the same amount of incident thermal radiation in every test. For instance, in test #5, the radiometer located at 40 m measured an average flux of 15.6 kW/m^2 , with a peak and low values of 19.7 kW/m^2 and 12.9 kW/m^2 respectively. The radiometer located 60 m from the spill point measured an average of 14.4 kW/m^2 with a peak and low values of 19.6 kW/m^2 and 11.0 kW/m^2 , respectively. Such a spatial distribution of thermal radiation at far off distances does not correspond with either the inverse square law or the geometrical flame model variations. Hence, we have not used these data in making estimates of the emissive power of the flame, since an unexplained instrument problem seems likely.

The solid flame model assumes that the flame takes a specific geometric shape and emits radiation from its surface at a known rate. The radiative heat flux (\dot{q}'') received by an element at a distance from the flame may be calculated using the following expression:

$$\dot{q}'' = E \cdot F \quad (5.4)$$

Here the geometric view factor, F , represents the fraction of energy radiated from the fire which is intercepted by the object. The geometry of the

large-scale fires is generally assumed to be a circular cylinder. The variation of the geometric view factor with cylinder height and distance from the center of the fire is given by Raj (1977). In the computation of these view factors, it is assumed that the angle of view is 180° . Since the actual angle of view of wide-angle radiometers is 150° , a correction should be applied to the view factors. This correction term is as follows:

$$F_r = \frac{1}{2} (1 - \cos 2\theta_{\max}) \quad (5.5)$$

where θ_{\max} is the semi-cone angle of the radiometer. For $\theta_{\max} = 75^\circ$, the correction factor becomes 0.933. Therefore, the actual view factor between the fire and the radiometer is given by:

$$F = F_a / F_r \quad (5.6)$$

where F_a is the value of view factor obtained from the equation applicable for 180° view elements (Raj, 1977).

The variation of the atmospheric transmissivity factor τ with distance is already shown in Figure 5.21. In principle, it is possible to determine the emissive power of the flame knowing the instantaneous values of \dot{q}'' , F and τ . In Figure 5.25 are plotted the computed emissive powers of the flame for LNG pool fire test #12 using the wide-angle radiometer data. As can be seen from Figure 5.25, the emissive power calculated using different wide-angle radiometers read an average value of about 200 kW/m^2 and have a scatter of about 10 kW/m^2 during the initial stages of burning. Both the magnitude of the emissive power and the scatter in the data increase during the later stages of burning. The increase in magnitude of the emissive power can, at least in part, be attributed to the increase in luminous soot radiation. The increase in the scatter of the measured data, may be due to larger fluctuations in the flame height and width. During the period of intense burning, the average value of the emissive power of the flame for the pool fire test #12 was estimated to be 220 kW/m^2 . The variance of the measured data is about 47 kW/m^2 . The highest value of emissive power estimated using this procedure was 292 kW/m^2 and this was measured by the radiometer located at 30 m from the spill point. The flame height at this instance was about 57 m.

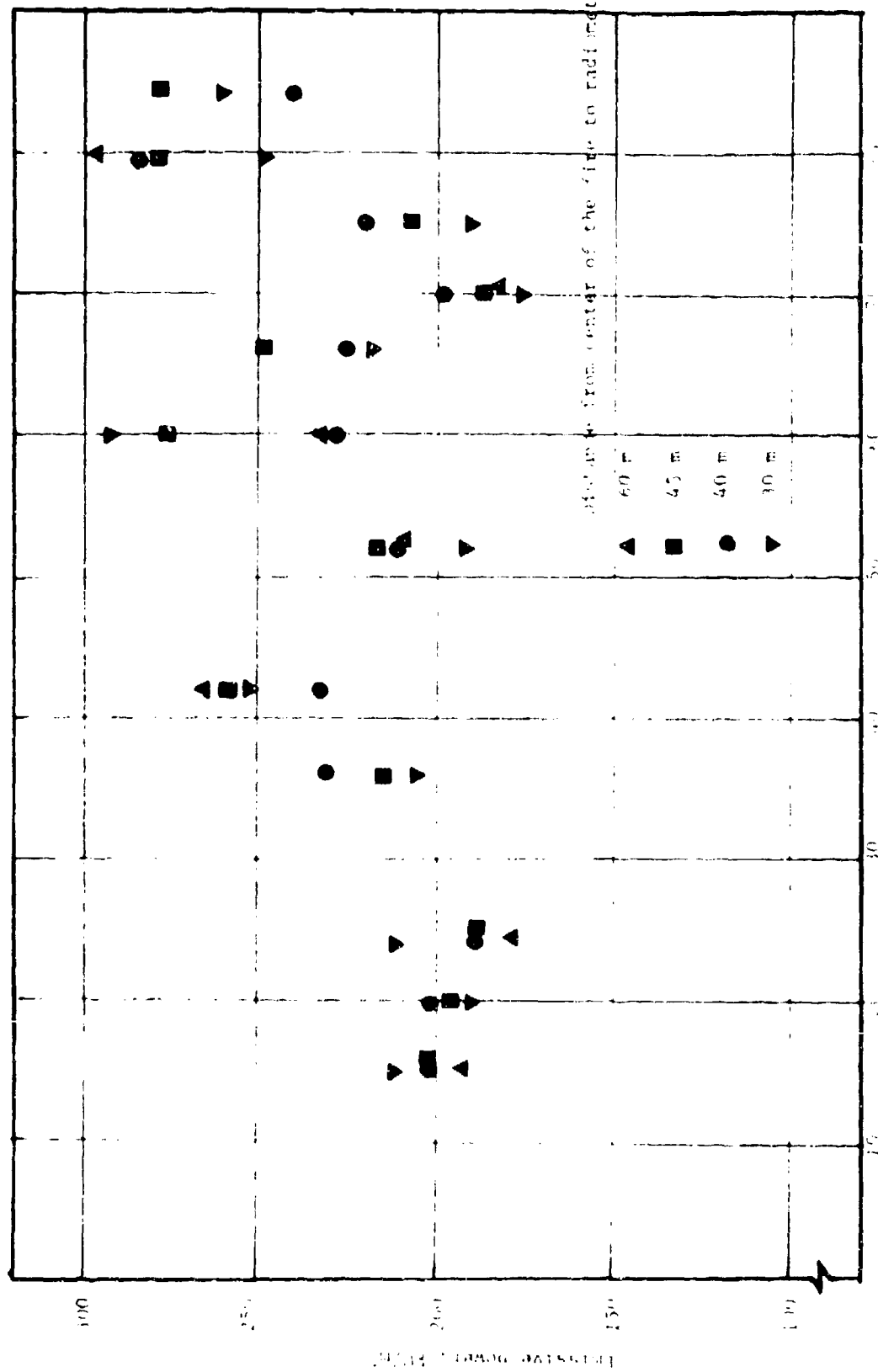


FIGURE 1.25 MISSILE POWER CALCULATED FROM THE DATA SHOWN IN FIGURE 1.24

5.4.4 Analysis of Wood Charring Data

In Tests 12 and 13 involving pool fires, wooden stakes were provided at different distances from the center of the spill. The purpose of providing these stakes was to observe the zone within which wood would ignite spontaneously from the thermal radiation from the fire. In other words, the stakes were used as additional, passive, radiation measuring instruments.

The stakes were construction grade timber of cross section 4 cm x 3.5 cm. These were used in "as available" condition and no attempt was made to pretreat the wood in any way. These stakes were driven into the soil in the pond such that about 0.5 m of the stake length would be projecting out of the water surface. Initial attempts to place the stakes at uniform spacings from the spill center failed due to practical difficulties. The actual distances are shown in Table 5.6. The general direction of the line of stakes was from the center of spill towards the NE corner of the pond.

The state of charring of the different stakes after the tests #12 and #13 is indicated in Table 5.6. Plate 5.1 shows the degree of charring of stakes located at different distances from the center in test #12. Test #13 was a delayed ignition pool fire test in which the vapors initially covered the downwind part of the pond before ignition. It is felt that the fire in this test swept past the wooden stakes. Hence, the charring data from test #13 are not considered in this analysis.

From the data of test #12, it is seen that the Stake #4 located at 18 m from the center does not seem to have ignited; only a slight blackening of the surface can be observed with beginnings to char. This can be assumed to represent the distance to unpiloted ignition of wood.

The mean flame emissive power can be inferred if we assume that spontaneous ignition of wood occurs at about 30 kW/m^2 (Lawson and Sims, 1953). However, we note that this is the ignition criterion for long durations of exposure. What constitutes "long" duration is somewhat uncertain. For short exposure times, ignition seems to be affected more by the total amount of energy absorbed by wood rather than by radiant energy flux alone. The calculation presented below should, therefore, be construed as giving an approximate value for the flame emissive power.

100
Centimeter Scale

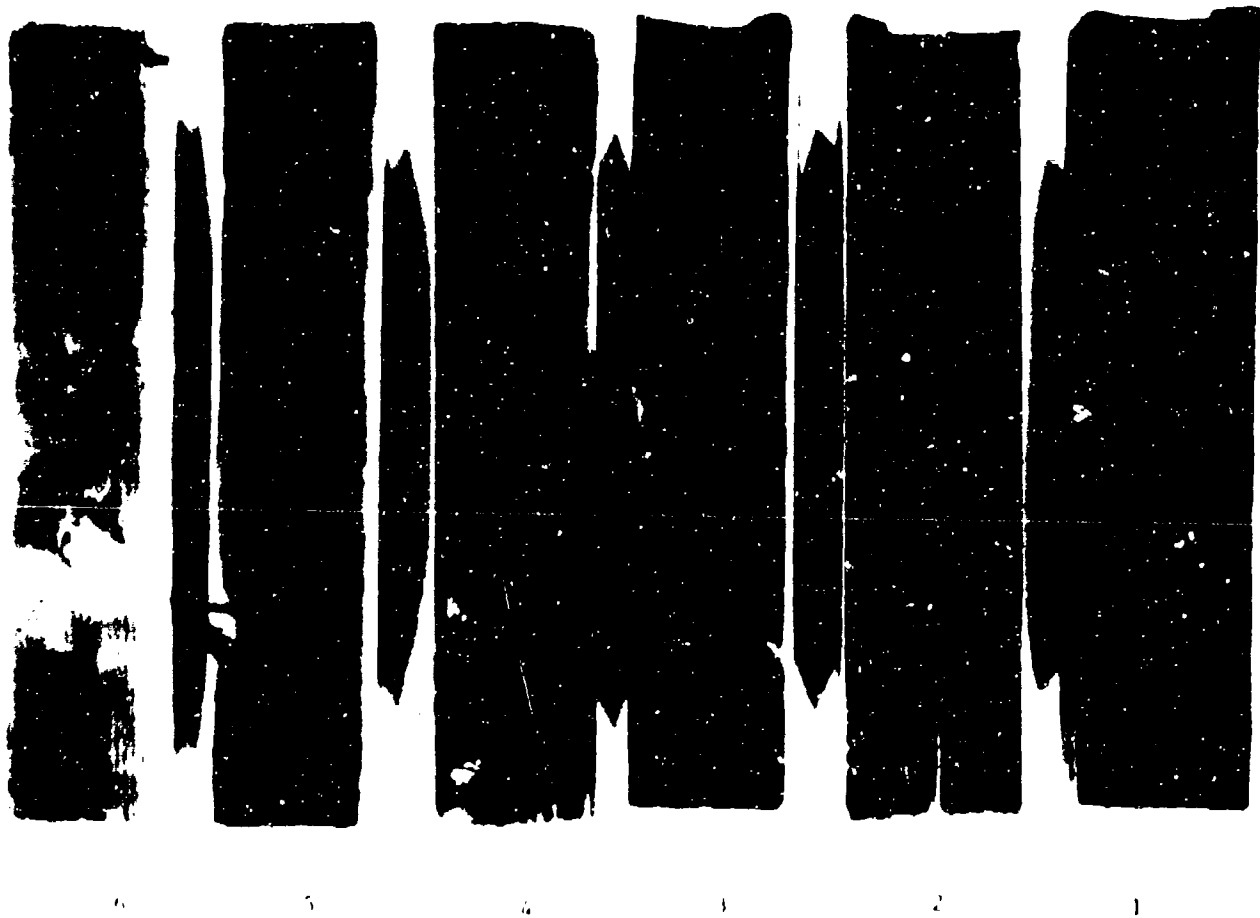


PLATE 5.1: PHOTOGRAPHS OF THE PIECES OF WOODEN STAKES
AFTER EXPOSURE TO POOL FIRE (TEST #12)

Flame Emissive Power Calculations

Measured radius to 30 kW/m² (wood ignition distance) X = 18 m (in test #12)

Mean flame height during steady burning period
(see Section 5.)

$$H = 44 \text{ m}$$

Flame base radius (R)

$$= 7 \text{ m}$$

View factor (F) between a fire which has H/R = 7.86, and a vertical element on the ground at X/R = 2.6 (for a table of view factor values see Raj (1977)).

$$= 0.193$$

Hence, the emissive power of flame = E =

$$\frac{30 \text{ kW/m}^2}{0.193}$$

$$= 155 \text{ kW/m}^2$$

In the above calculation we have ignored the effect of atmospheric absorption. This may be justifiable because the distance between the flame surface and the location of the stake is only a few meters. We note that the stakes receive significant part of the energy from the lower portions of the flame. We are uncertain, however, of the effect of the proximity of the radiation path to the water surface and its effect on the attenuation.

The second parameter that introduces uncertainties in the estimation of the emissive power is the flame diameter. In the above calculation we have used a mean value. However, it was noticed in all pool fire tests that the flame base was not circular but had a star shape. It is conceivable that the flame was much closer to the stakes than is implied by a mean diameter (i.e., an apex of the star may have been in the direction of the line of stakes. It is hard to tell this from the movies.). If this is the case, the above calculation over estimates the flame emissive power. The two errors have fortunately compensatory effects.

We note that the emissive power estimated above is somewhat lower than the emissive powers estimated using narrow-angle and wide-angle radiometer data for test #12. It is conceivable that the slight charring of stake #4 resulted from the maximum emission from the flame (which occurs towards the end of the burning time because of increased soot). There is some uncertainty in specifying which stake represents the 30 kW/m² ignition flux. For example, if stake #5 (located at 21 m) is assumed to represent the unpiloted ignition situation instead of stake 3 at 18 m, then the calculated emissive power would be 185 kW/m². This value, however, is much closer to the average emissive powers estimated using radiometer data.

The conclusion from the wooden stake data can be expressed in general terms; that the estimated emissive power of the fire is approximately 185 kW/m^2 .

5.5 DISCUSSION OF RESULTS

In the preceding parts of this section we have presented data and analysis of the geometric and the thermal radiation characteristics of LNG pool fires on water. In summary we wish to discuss some of the salient results obtained and to indicate the limitations of the analyses that have been performed.

In order to calculate potential hazard zones resulting from a LNG pool fire, two fundamental characteristics of pool fires need to be evaluated. The first one is the geometric description of the pool fire, namely, the mean diameter, height, and shape of the flame. The second, even more important parameter that needs to be defined is the emissive power of the flame. Using the motion picture data we were able to arrive at the geometrical description of the pool fire. We also noted that there were considerable uncertainties in the measured dimensions of the pool. In addition, the rate of burning was calculated using the duration of intense burning, which was determined from the motion picture data and the thermal radiation data. There is considerable uncertainty in determining the length of this period -- especially in the shorter tests.

In this section we have attempted to perform a sensitivity analysis on the measured data for pool fire test #12. The measured quantities for this particular test are as follows:

Quantity of LNG spilled	= 5.68 m^3
Duration of spill	= 81 seconds
Measured average diameter	= 14.1 m
Measured duration of intense burning	= 75 seconds

Since the measured pool diameter is subject to errors in measurement techniques, we have perturbed the diameter by 1.5 m (which corresponds to about 10%) over the mean. The duration of actual burning is likely to be between the duration of intense burning and the total duration of the spill. In Table 5.7 is shown the effect of variation of these parameters on the

TABLE 5.7
SENSITIVITY ANALYSIS ON LNG POOL FIRE
TEST #12 DATA

<u>Assumed Base Diameter, m</u>	<u>Assumed Duration of Burning (s)</u>	<u>Burning Rate m/s x 10⁴</u>	<u>Predicted Mean Flame Height, m</u>
12.6	81	5.62	46
	78	5.84	47.1
	75	6.07	48.2
14.1	81	4.49	43.3
	78	4.66	44.3
	75	4.85	45.4
15.6	81	3.67	41.1
	78	3.81	42.1
	75	3.96	43.1

Measured mean height of the flame = 44.0 m.

Variance of the height of the flame = 6.3 m.

predicted average visible height of the flame using Thomas' correlation. As can be seen from Table 5.7, the predicted flame heights are not very sensitive to the variation in diameters or the duration of burning. Also indicated in Table 5.7 is the measured mean and variance of the visible flame height for Test #12. We note that all the predicted flame heights are well within the standard deviation of the measured flame height data. Therefore, it is possible for us to conclude that Thomas' correlation predicts the mean height of the visible flame very well when the proper burning rates are used - which brings us to the question of defining the proper burning rate.

It was pointed out earlier in Section 5.2 that the estimated rates of burning indicated a tendency to increase with the spill rate. This implies that the maximum diameter is not as strong a function of spill rate as would be predicted from a simple evaporation model of the problem. In fact, one would expect to see an increase in spill dimensions with increase of spill rate, the dimensions being maximum for an instantaneous spill. Therefore, the apparent increase in the burning rate is not caused by the increase in spill rate, but possibly by increased velocity with which a jet of LNG impinges on to the water surface. Whenever an immiscible, buoyant, cryogenic liquid is released at low velocities in the form of a vertical jet on to a water surface, the liquid jet penetrates the water surface, sinks to a certain depth, rises due to buoyancy forces and then spreads and evaporates simultaneously. If we assume that the heat transfer rate from water to the liquid is constant, then the total evaporation rate is dependent on the surface area of the liquid pool. However, if the velocity of the liquid jet is large, the jet penetrates the water surface to considerable depth and part of the liquid breaks up into globules. The remainder of the liquid rises to the surface and spreads radially. The total amount of liquid evaporated is the sum of liquid evaporated from the pool surface and the globules which evaporate due to heat transfer from their surfaces. Hence the total quantity of liquid evaporated is larger than the quantity computed using the dimensions of the pool. This phenomenon is further augmented by the steel plate located directly below the spill point at the NWC test facility. While it is not possible to make quantitative estimates of the size and the total

quantity of liquid in the shape of globules, it is reasonable to assume that the total quantity will increase with the jet velocity and this may explain the observed increase in evaporation/burning rate. However, flame height is a function of actual vaporization rate, so the use of the apparent value in Thomas' correlation is valid.

The second quantity which is desired from the analysis of the thermal radiation data is the "emissive power" of the LNG flame. The narrow-angle radiometers, whose field of view are completely covered by the flame surface measure an average emissive power of about 212 kW/m^2 for the lower parts of the fire. Since the narrow-angle radiometers are viewing only the lower part of the flame in all the tests, the scatter in the measured data is not very large (about 20 kW/m^2).

The wide-angle radiometers measure the thermal flux received by the vertical element of the radiometers. The emissive power of the flame may be back calculated by assuming the flame to be a solid grey emitter. As pointed out earlier, we have the wide-angle radiometer data only from test #12 and the emissive power calculated using this procedure shows a wider scatter. The average emissive power was estimated to be 220 kW/m^2 and the scatter was about 47 kW/m^2 .

For the pool fire test #12, the mean emissive powers computed using narrow-angle and wide-angle radiometer data agree very well. However, the scatter in the emissive power computed using wide-angle radiometer data is nearly twice the scatter in the narrow-angle radiometer data. This large variation in the computed emissive power is partially due to the assumptions made regarding the shape and size of the flame. In computing the geometric view factors, we have assumed that the flame is a solid cylindrical body emitting equally in all directions. But, in practice, the flame is not a cylindrical emitter and, in fact, tends to pulsate. The large turbulent eddies rising from the lower part of the flame tend to distort the lateral dimensions of the flame. The narrow-angle radiometers, by virtue of viewing only part of the flame, may not be very sensitive to the flame size variation. But the thermal flux measured by wide-angle radiometers is affected by these pulsations in the lateral and vertical dimensions of the flame.

Using the narrow-angle radiometer data and the measured visible flame geometry we have calculated the percent of total combustion energy which is radiated out of the flame. The results are shown in Table 5.8 and are plotted in Figure 5.26 against the spill rate. Also plotted in the figure is a curve, which indicates the fractional energy radiated from a fire which has constant diameter and emissive power, but whose height varies with spill rate. In most of the present series of tests the diameter remained almost a constant. An extremely interesting observation can be made from the results. As the spill rate increases, the fraction of the energy radiated decreases. A physical explanation for this could be that not all of the vapors produced by the evaporating pool participate in combustion, and the faster they are liberated, the less the chance for combustion. Burgess and Zabatakis (1962) also found, in much smaller scale experiments (0.38 m diameter) involving the spill of LNG onto a warm tray, that about 70% of the vapor generated initially did not participate in combustion.

The question still remains as to what happens to the vapor that is generated by the boiling of LNG on water, but which seems to escape uncombusted. Burgess and Zabatakis (1962) infer from their results that these vapors mix with air and get diluted below the lower flammable limit and, therefore, escape unburned. This hypothesis which may explain an extremely transient phenomenon (such as occurred in Bureau of Mines' experiments) may not provide an adequate physical description for a long duration LNG fire. This is because the vapors liberated continuously from the pool are fuel rich and when they mix with enough air at the edges and reach flammable concentration, they are likely to burn. Besides the flow of air is radially inward and hence, no vapor can escape on the outside of the fire.

A more logical explanation could be provided if we assume a core of rich vapor that rises in the middle of the visible fire. This core may not burn in the initial stages because it is starved of oxygen (the reaction is taking place on the outer shell of the cylinder). Subsequently, this fuel rich core may be mixed with the inward flowing combustion products and rendered non-combustible even if it mixes with the right proportion of air at the higher elevations of the fire. The net result is that

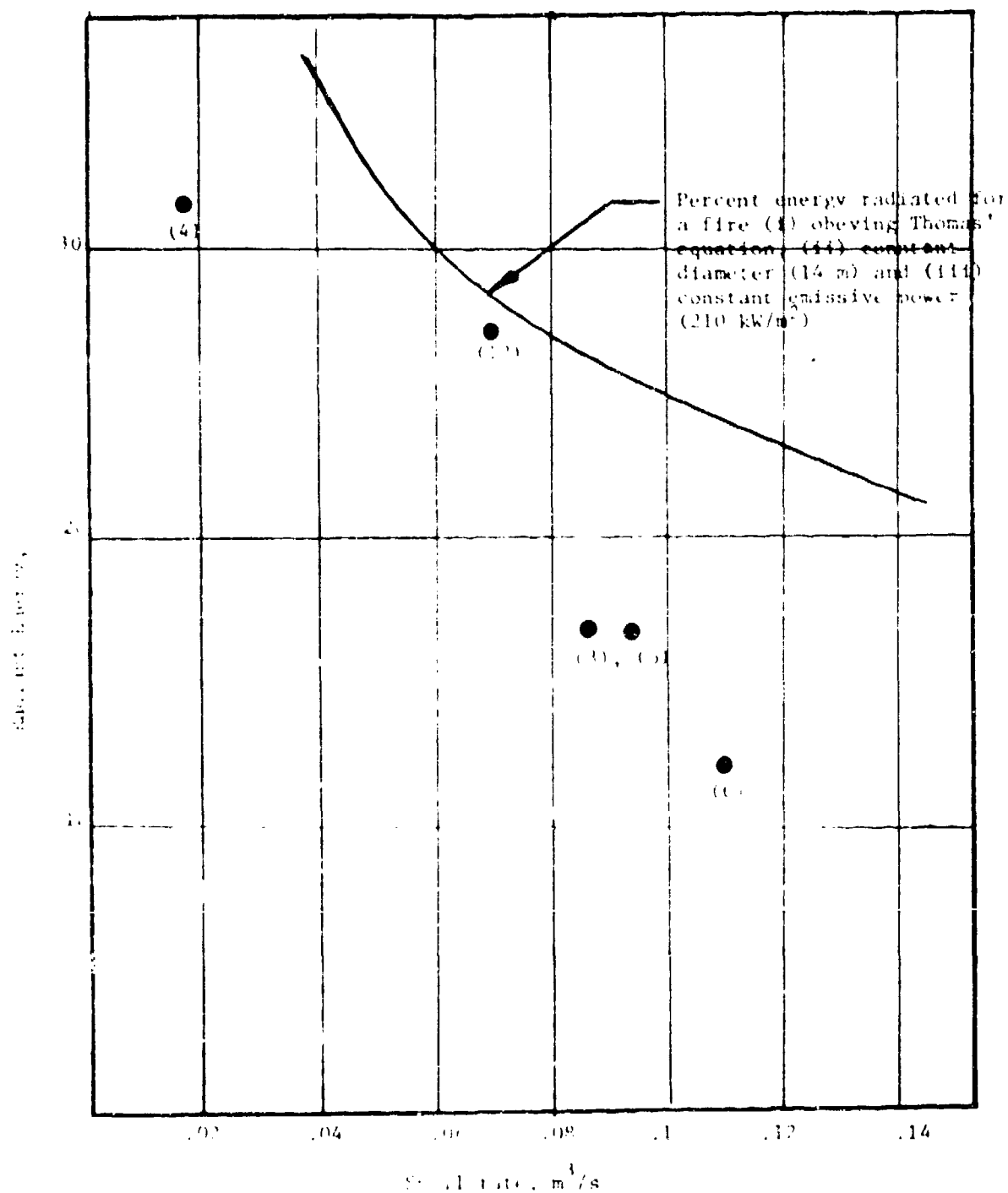


FIGURE 5.26 VARIATION OF FRACTIONAL COMBUSTION ENERGY RADIATED WITH SPILL RATE

TABLE 5.8
FRACTION OF COMBUSTION ENERGY RADIATED BY POOL FIRES

IN- Test #	Radiating* Surface Area m ²	Weight of Fuel (kgs)	Duration of Burning (s)	Emissive Power (kg/m ²)		% Combustion Energy Radiated	
				Narrow-Angle Radiometer	Wide-Angle Radiometer	Narrow Angle	Wide Angle
3	1720	1785	42	207 ± 5	-	16.8 ± 0.4	-
4	721	1785	195	200 ± 11	-	31.5 ± 1.7	-
5	2212	1275	26	187 ± 29	-	16.9 ± 2.6	-
6	1980	2423	40	135 ± 6	-	12.1 ± 0.4	-
12	1949	2414	75	224 ± 13	220 ± 47	27.1 ± 1.6	26.6 ± 3.7

5-59

* Radiating surface area is calculated using the average diameter and the length of the visible flame and considering only the cylindrical surface area.

a substantial part of the vapor produced goes at the top of the fire uncombusted. This model essentially implies that the fire is a cylindrical shell of reaction zone with an inner core that is relatively cool (compared to the combustion zone temperature). Perhaps this may even explain the emission that was observed in the 3 - 4 μm band from warm optically thick hydrocarbons (see Figure 4.7), observed in the spectrum of the pool fire in test #5. Test #5 is one of the high rate of spill tests and therefore the inner vapor core could be of substantial dimensions. That would explain the high optical thickness (which is generally a representation of physical thickness and the concentration). Since we are basing this inner warm vapor core hypothesis on only indirect data, it should be construed as being only tentative. Certainly, more direct measurements within the fire could shed more light on this issue.

5.6 CONCLUSIONS

The main conclusions of the analysis of the pool fire data are as follows:

- (i) For continuous release spills the maximum diameter of the pool fires does not increase with spill rate as rapidly as would be predicted by a model assuming a constant burning rate on water. In the highest spill rate tests, the burning rate was higher than anticipated, probably due to increased heat transfer area caused by the fragmentation of liquid by the spill jet.
- (ii) Thomas' correlation yields good agreement with measured visible flame heights when the apparent burning rates are used.
- (iii) The average emissive power of the bottom part of the flame was computed to be about 212 kW/m^2 using narrow-angle radiometer data of all the pool fire tests. The wide-angle radiometer data of pool fire test #12 indicated an average emissive power of about 220 kW/m^2 . However, the scatter in the wide-angle radiometer data of test #12 was about four times the scatter in the narrow-angle radiometer data for the same test.
- (iv) The wood charring data indicated the average emissive power of the flame for test #12 to be between 155 kW/m^2 and 185 kW/m^2 .

- (iv) The fraction of total combustion energy radiated is between 12.1% to 27.1% for rapid spill tests and 31.5% for the slower spill test. There seems to be a significant effect of the spill rate on the fraction of energy radiated. The higher the spill rate, the lower the fraction emitted as thermal radiation.

6.0 ANALYSIS OF LNG VAPOR FIRES

6.1 INTRODUCTION

The previous section focused on pool fires where LNG was spilled in the pond and was immediately ignited, resulting in a turbulent diffusion flame stationary over a pool of vaporizing LNG. In this section another type of fire is analyzed. The LNG is spilled onto the pond, but is not ignited immediately. The spilled LNG forms a pool that vaporizes due to heat transfer from the water. The vapors are then entrained by the prevailing wind, first over water and then over land. The vapors are ignited later, at about 70 m downwind of the spill point. A fire then spreads back through the vapor cloud and hence it is described as a "vapor fire."

Controlled vapor fire tests involving spills of LNG on water, dispersion of vapors and their subsequent ignition have not been conducted before. Only tests on land have been performed and even in these tests, there were no measurements of thermal radiation from the fires. Hence, the principal objective of the vapor fire test program was to perform relatively large-size field tests of vapor fires on water so as to characterize the fire behavior and its thermal radiation output. The ultimate objective of this part of the program is to improve the state of the art in the assessment of the potential hazards from vapor fires.

Six vapor fire tests were carried out in which about equal amounts of LNG (4.4 to 5.5 m³) were spilled in the center of a 50 x 50 x 1 m pond. The spill durations were comparable for all tests (65 to 85 s). The instrumentation included movie cameras, wide- and narrow-angle radiometers, and hydrocarbon gas analyzers.

It was found that vapor fires spread close to the ground in the form of a propagating plume flame. The experiments did not indicate that LNG vapors burn in the form of a fire ball. Three stages of fire development were identified. First, a transient turbulent flame (initially premixed and later diffusive) spread through the portion of the cloud over land while increasing in size. The flame speed relative to the vapors ranged from 8 to 17 m/s, increasing with an increase in wind speed. This result

is consistent with previous studies of vapor fires on land.

Secondly, as the flame approached the pond edge, its advance and growth ceased, producing a steady, stationary turbulent diffusion flame inclined at about 35 to 45° from the vertical under the effect of wind. This flame was bright orange in color with a width roughly three times its inclined length. The flame persisted at the edge of the pond for about half the fire duration yielding the maximum thermal radiation output at a fairly constant level.

During this stationary stage of the fire, time-averaged overall emissive powers were estimated. The values ranged from 104 to 320 kW/m² for the wide-angle radiometer data, and 183 to 260 kW/m² for the narrow-angle radiometers (pointed at the flame base). The wider spread of the wide-angle radiometers data can be attributed to uncertainties in the calculation of view factors between the flame and radiometer detectors. View factors are needed in reducing the wide-angle radiometer data but not for narrow-angle data. The average emissive power based on all radiometer data (fourteen measurements) was 210 kW/m² ± 30% (standard deviation).

The final stage of the vapor fire was a transient burn-out where the flame moved towards the LNG pool on the pond. The fire eventually resembled a pool fire with sooty and reddish flames.

The aforementioned behavior of the vapor fire, consisting of a rapid flame spread in the vapors over land followed by a stationary burn at the edge of the pond (over water) for a significant duration and finally a recontinued spread over water to the spill point, singularly distinguishes this fire from the vapor fires that have been observed over land. In the latter case, the fire spread continuously towards the spill point. Although we offer several hypotheses to interpret this behavior, further study is needed to determine whether it is intrinsic to vapor fires on water or merely a result of the test conditions at China Lake. Specific recommendations on future work are given in this section as appropriate.

6.2 TEST CONDITIONS



Six vapor fire tests were conducted at China Lake. The conditions for these tests are listed in Table 6.1 including date and time of test, amount and duration of the spill, the chemical composition of the LNG, the time of flare ignition, the ambient temperature and relative humidity, and the wind speed and direction at the pond and the bunker. As these tests were essentially repeat tests, the spilled volumes (4.4 to 5.5 m³) and the spill durations (65 to 85 s) were not varied significantly. Therefore, these two parameters are not expected to affect the results. (The tests were repeated until complete sets of successful measurements were obtained, namely in LNG 16 and 17.) However, the time between spill and ignition and the wind speed varied significantly between tests (from 22 to 64 seconds and from 4.1 to 7.2 m/s, respectively). We have examined the effects of these variations on the results.

Table 6.1 gives the atmospheric stability estimated for the wind and insolation conditions in each test, according to the procedure of Slade (1968). Note that the atmospheric stability varied from neutral (D) to moderately unstable (B). Table 6.1 gives also the amount of atmospheric precipitable water estimated for the ambient temperature and relative humidity in each test, according to the procedure of Hudson (1969).

The instrumentation consisted of cameras, wide- and narrow-angle radiometers (as for the case of the pool fire tests), and hydrocarbon gas sensors. The locations of instruments, scale markers and flares are shown in plot plans in Figure 6.1 and 6.2. Separate figures are given for test Nos. 8 to 11 and Nos. 16 and 17, respectively, to illustrate minor differences in the locations of the radiometers and the presence of an extra radiometer (No. 7) in the later tests.

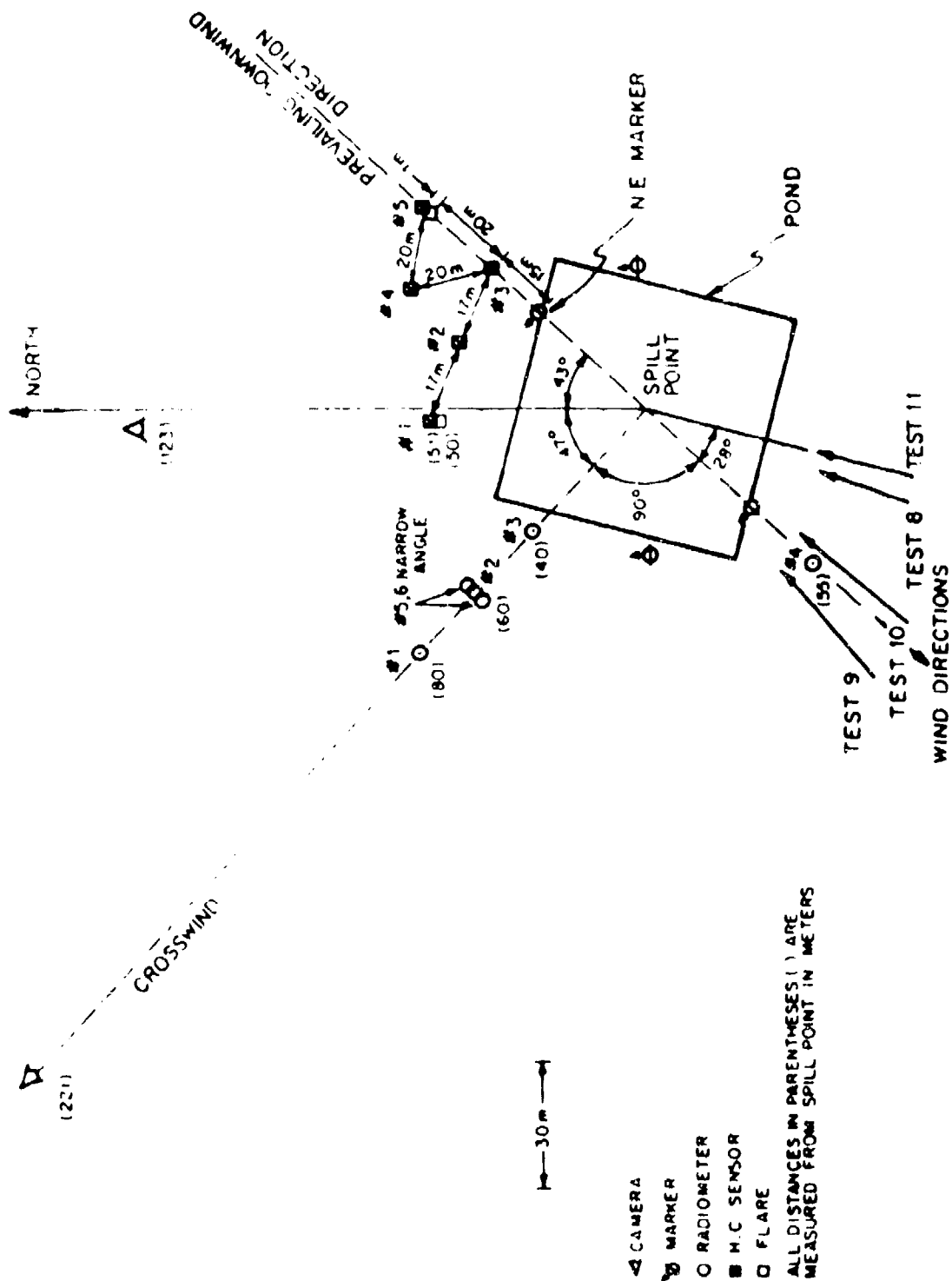
The wind direction for each test is also shown in Figure 6.1 and 6.2. Note that the variance from the general prevailing wind direction is smaller for tests 9, 10, 16, and 17 and larger for tests 8 and 11.

TABLE 6.1
TEST CONDITIONS OF VAPOR FIRE

ITEM	TEST NO.	8	9	10	11	16	17
Date of Test		5/26/77	6/1/77	7/12/77	7/13/77	6/12/78	6/13/78
Time of Test (Hr., Min.)		14:40	13:30	14:08	14:48	21:14	13:33
LHG Composition:							
Methane %		<div style="text-align: center;">  Uncertain  </div>	95.11	93.81	93.81	95.64	94.09
Ethane %			1.84	5.33	5.33	3.43	5.10
Propane %			1.73	0.79	0.79	0.71	0.71
Higher Hydrocarbon %			0.50	0.07	0.07	0.22	0.09
Nitrogen %			0.82	trace	trace		
Spill Parameters:							
Volume Spilled, (m ³)		5.1	5.1	4.9	5.2	4.4	5.1
Spill Duration, (s)		84	78	74	65	70	78
Rate of Spill (m ³ /s)		0.061	0.068	0.066	0.08	0.063	0.071
Time to Ignition (after spill), sec		22	50	44	60	33	25
Ambient Conditions:							
Air Temperature (°C)		27	37	39	39	29	36
Relative Humidity (%)		24	22	24	25	33	24
Wind Speed at Pond* (m/s)		4.1	7.2	4.1	4.1	7.2	7.1
Wind Direction* (deg)		200	230	220	195	230	210
Wind Speed at bunker (m/s)		4.1	6.1	5.1	4.1	5.7	6.2
Wind Direction (deg)		15	245	230	200	245	215
Location of Instrumentations		←	See Fig. 6.1		→	See Fig. 6.2	
Estimated Atmospheric Stability		B	C	B	B	B	C
Estimated Precipitable Water (g/m ³)		6.7	9.5	13.2	13.4	9.5	8.0
(mm eq.)		5.7	8.5	13.5	13.7	9.5	7.9

* measured 2.5 m above the water level for Ino. 8, 10, 11 and 2 and 10 m above water level for Ino. 16 and 17.

* Direction of wind is the compass angle from which the wind is blowing measured clockwise with respect to North.



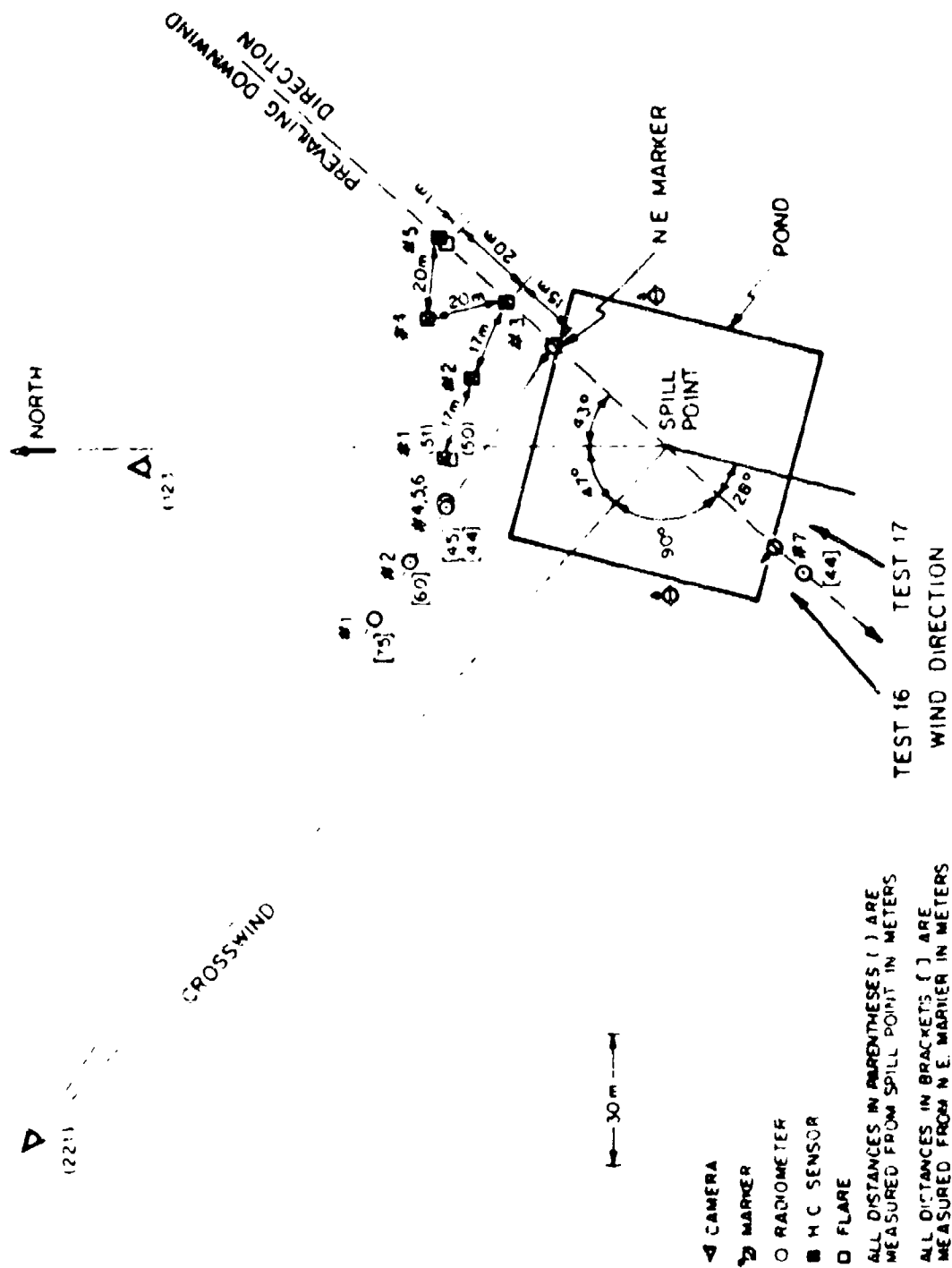


FIGURE 6.2: SPILL POINT TEST AREA AND WIND DIRECTION FOR TESTS No. 16 and 17

6.3 LISTING OF DATA COLLECTED

The collected data consisted of movie records (three to five views for each fire), four to five wide-angle radiometers, two narrow-angle radiometers, and five hydrocarbon sensors. To give the reader an overview of the data generated in these tests, we give a listing in Table 6.2 where the data are labelled as successful (✓), unrecognizable (UR), off-scale (OS), lost (L), or not taken in a particular test (blank). The basis for this labelling will be discussed as the data are presented within this section.

6.4 LNG RELEASE, CLOUD FORMATION, AND IGNITION

Upon the release of LNG onto the water surface, a pool was formed, reaching a constant diameter within a few seconds. The diameter at maximum size was about 12 to 35 m depending on the test. The LNG boiled due to heat transfer from the water and the vapors generated were carried with wind over water, then over land. The maximum height of the visible cloud prior to ignition was about four meters for all tests.

Two flares, located at about 70 m from the spill point (see Figures 6.1 and 6.2), were ignited 22 to 64 seconds after the spill (depending on the test). This ignition delay was sufficiently long to allow the LNG vapors to reach the flare prior to ignition. The time needed for the vapors to travel to the flare was estimated to be 10 to 20 seconds for the various ambient wind speeds. Thus, the vapors ignited immediately after flare ignition. The vapor was invisible at the location of the first ignition of the vapors. This indicates that the flammable region extends beyond the visible cloud, which is consistent with the low ambient relative humidity in all tests (22 to 33%).*

6.5 VAPOR FIRE DEVELOPMENT

Based on knowledge of the prevailing wind directions, the flares were positioned so as: 1) to ignite the cloud hopefully at its downwind tip and 2) to prevent cloud drift to the bunker where the observers were located.

* Note that in the pool fire tests, the humidity of the stagnant air over the pond may have been considerably higher than the humidity of the air over the land.

TABLE 6.2

RAW DATA FOR VAPOR FIRES

TEST NO.	3	9	10	11	16	17
<u>ITEMS</u>						
Films						
Crosswind	✓	•	•	•	✓	✓
Overhead	✓	✓	✓	✓	✓	✓
Upwind (southwest)	•	•	•	•		
West Close Up						✓
South Close Up						•
Wide Angle Radiometers						
1	OS	OS	L	OS	✓	•
2	OS	OS		OS	✓	✓
3	OS	OS		OS	✓	✓
4	•	1		•	✓	✓
7					✓	✓
Narrow Angle Radiometers						
5	UR	•		UR	✓	✓
6	•	OS		UR	•	•
Hydrocarbon Gas Sensors						
1	UR	UR		UR	+	•
2	↓	↓		↓	+	✓
3					•	✓
4					+	✓
5	↓	↓	↓	↓	✓	✓

Legend

- ✓ denotes successful data
- OS denotes off-scale data
- L denotes data taken but lost
- UR denotes negative or otherwise unrecognizable data
- denotes cloud missed sensor due to an unfavorable wind direction
- blank denotes data not measured in particular test

In tests 9, 10, 16, and 17 the wind directions were fairly close to the prevailing wind direction, as illustrated in Figures 6.1 and 6.2. Consequently, the cloud was ignited at its downwind tip and a fairly regular fire spread upwind towards the spill point. On the other hand, in tests 8 and 11, the wind was more southerly than the prevailing wind direction, thus, sending the cloud between the two flares (see Figure 6.1). Consequently, ignition occurred at two edges of the cloud, upwind of the cloud tip, resulting in a very non-uniform fire spread throughout the cloud.

The analysis of the development of the vapor fire, as given in this section, focuses on test Nos. 9, 10, 16, and 17 where a uniform fire was obtained. Test Nos. 8 and 11 were not considered, because their non-uniformity made the definition of a flame edge very difficult and not meaningful.

From the movie records, the locations of the upwind and downwind edges of the flame (or burning zone) were measured as a function of time and are given in Figures 6.3 to 6.6 for test Nos. 9, 10, 16, and 17, respectively. Flame edges were measured from the flare location and time from the instant of ignition. The flame width and length are also given in Figures 6.3 to 6.6. Flame width was measured along the direction of flame propagation, as the difference between the upwind and downwind edges of the flame. Flame length was measured in a vertical plane along the general direction of flame inclination under the effect of wind (see Figure 6.7). Figures 6.3 to 6.7 also give reference marks such as the spill point, the location of the NE marker (which is close to the pond edge), the time when the spill ended, and the cloud height and maximum LNG pool radius just prior to ignition. We also note on the time axis when the flame was in the cloud only, when a plume flame developed and when it turned red and sooty.

Three distinct stages of fire development were identified in each of the four vapor fire tests:

1. Transient flame growth;
2. Stationary flame near pond edge; and
3. Transient burn-out.

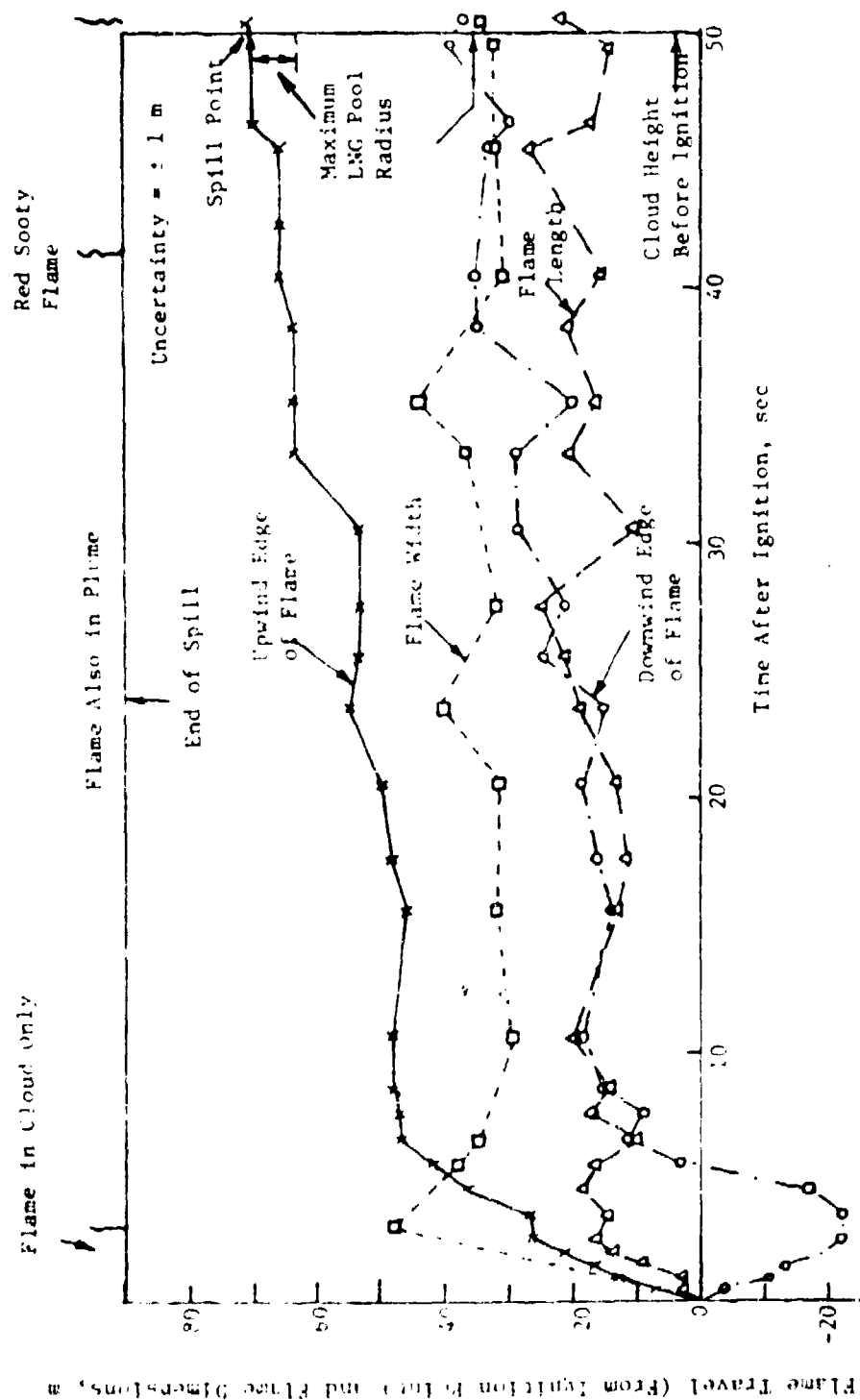


FIGURE 6.3: VAPOR FIRE DEVELOPMENT IN TEST #9 (5.3 m^3 SPILLED IN 78 sec AND IGNITED AFTER 50 sec: WIND SPEED = 7.2 m/sec)

Flame Travel (From Ignition Point) And Flame Dimensions, m

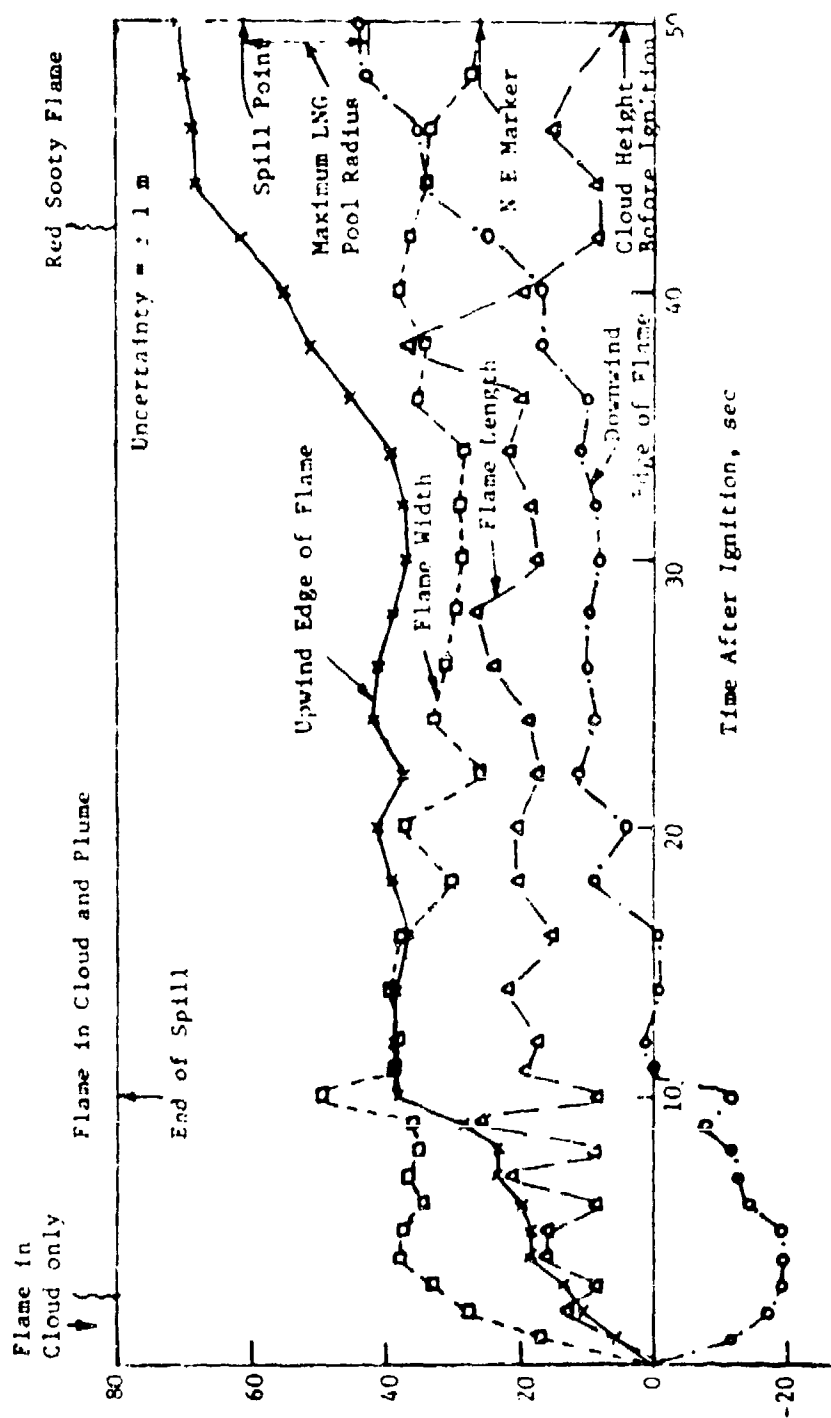


FIGURE 6.4: VAPOR FIRE DEVELOPMENT IN TEST #10 (4.9 m^3 SPILLED IN 74 sec AND IGNITED AFTER 64 sec; WIND SPEED = 4.1 m/sec)

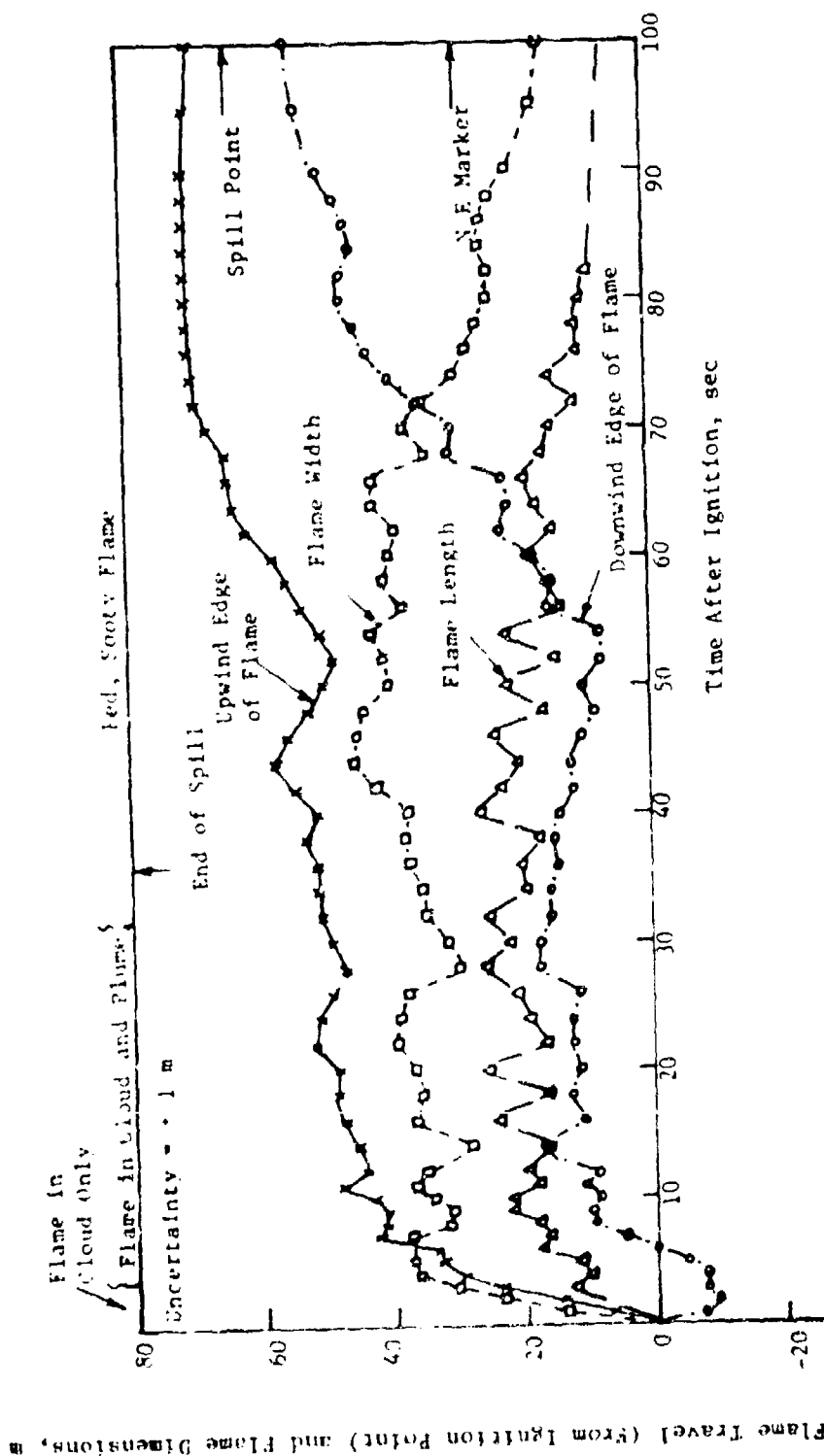


FIGURE 6.5: VAPOR FIRE DEVELOPMENT IN TEST #16 (4.4 m^3 SPILLED IN 70 sec. AND IGNITED AFTER 33 sec; WIND SPEED = 7.2 m/sec) (In this night test, the vapor cloud was not visible prior to ignition.)

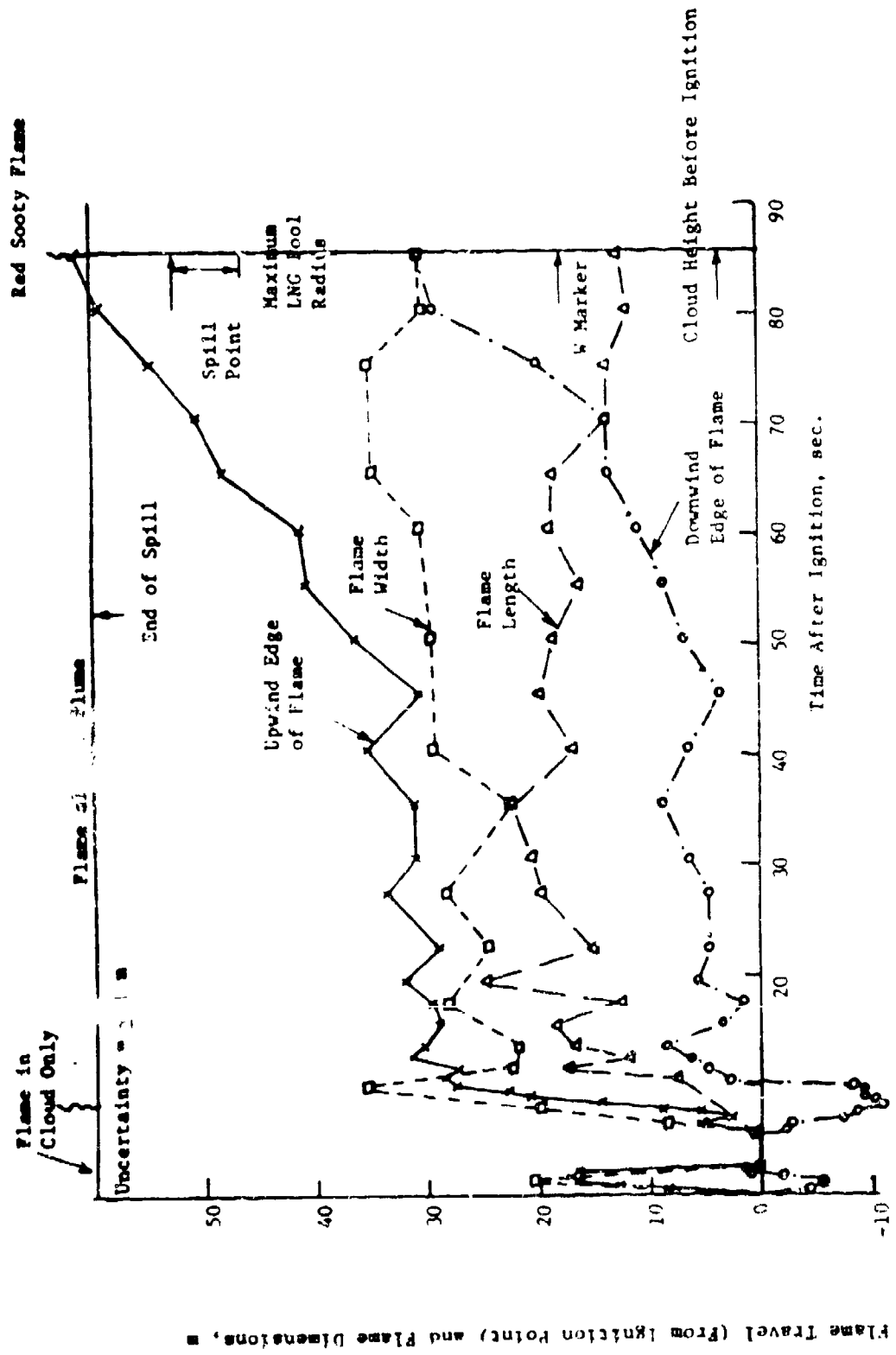
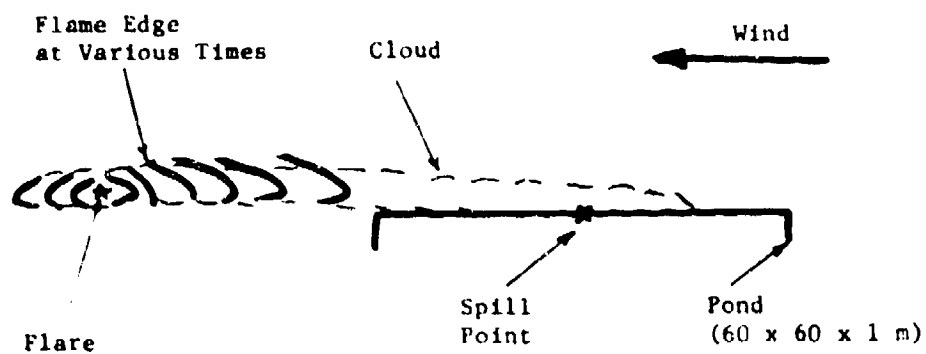
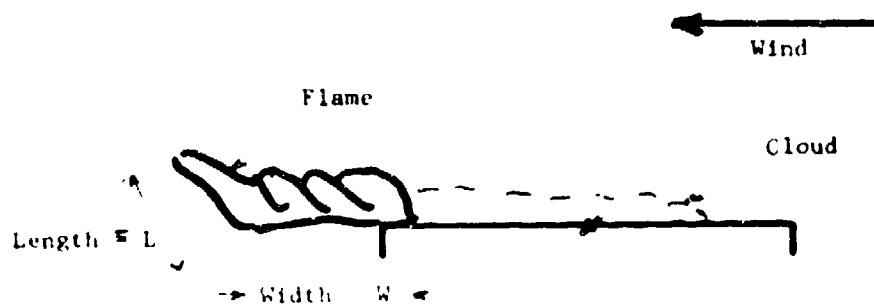


FIGURE 6.6: VAPOR FIRE DEVELOPMENT IN TEST #17 (5.5 m^3 SPILLED IN 78 sec AND IGNITED AFTER 25 sec; WIND SPEED = 7.2 m/sec)



(a) Transient Flame Growth



(b) Stationary Flame Near Pond

FIGURE 6.7: SCHEMATIC OF MAIN STAGES OF VAPOR FIRE

The main features of these stages are illustrated schematically in Figure 6.7 and are discussed in detail below.

6.5.1 Stage 1: Transient Flame Growth

Within the first ten seconds after ignition, flames spread quickly both upwind and downwind of the flare. Flame travel in both directions is consistent with the ignition of the flare after the flammable cloud had traveled over it. The flames were initially contained within the cloud but soon extended in a flame plume above the cloud, as schematically shown in Figure 6.7a. This is consistent with pre-mixed burning of the regions in the cloud that were within the flammable range prior to flame arrival, followed by diffusive burning of the richer regions in the cloud. At times, the edge of the upwind flame front was not easily visible. However, we could infer its location from a number of observations such as the recession of the visible water condensation cloud* ahead of it, the ignition of plants and brush within the flames and the general air motion around the flame as made visible by the water condensation cloud. The uncertainty in identifying the flame edge is estimated to be about ± 1 meter which is very acceptable for the scale of this experiment.**

Flame travel downwind of the flare lasted only a few seconds. After consuming the flammable vapors therein, the downwind edge of the flame started to recede toward the spill point. Generally, the flame zone was fairly normal to the wind direction.

During this transient flame growth, an average flame speed with respect to ground was calculated by taking the slope of the upwind flame location with respect to time in Figures 6.3 to 6.6. The flame speed with respect to the gases was obtained by subtracting the wind speed from the speed with respect to ground. The results are shown in Table 6.3 for both the upwind and downwind spread. As the duration of the downwind spread was very short, we focus only on upwind spread in the discussion below. Also shown in the table are wind speed at the pond, the delay in flare ignition (measured from the instant of spill) and the atmospheric stability for each test. (Note

* Due to evaporation of the water fog by heat from the flame.

** The uncertainty in measuring the flame length is higher (± 2 m) due to flame fluctuations and the lift off of small flamelets.

TABLE 6.3

CHARACTERISTICS OF MAIN STAGES OF VAPOR FIRE DEVELOPMENT

Test Number	9	10	16	17
Test Conditions				
Spilled quantity, m ³	5.3	4.9	4.4	5.5
Spill duration, s	78	74	70	78
Wind speed at pond, m/s	7.2	4.1	7.2	7.2
Time of flare ignition after spill, s	50	64	33	25
Estimated atmospheric stability	C	B	D	C
First Stage: Transient Flame Growth†				
Duration after ignition, s	6	9	11	10
Upwind flame speed w.r.t. ground, m/s	10	3.5	5	6
Upwind flame speed w.r.t. gases, m/s	17	8	12	13
Downwind flame speed w.r.t. ground, m/s	9	9	6	4
Downwind flame speed w.r.t. gases, m/s	1.5	5	-1.3	-3
Second Stage: Stationary, Steady Flame Near Pond Edge				
Duration after 1st stage, s	25	25	40	35
Average flame length, m ± 2 m	19	20	21	19
Average flame width, m ± 1 m	33	34	38	27
Average emissive power, kW/m ²	260	*	148	270
Average flame length/width ratio	0.58	0.59	0.55	0.70

* Radiation data of test No. 10 were lost.

† In this stage, all flame speed calculations are average values.

that the variation in the atmospheric stability is from neutral (D) to moderately unstable (B)). From Table 6.3, it is found that:

1. Test Nos. 16 and 17 had the same wind speed (7.2 m/s) and comparable ignition delays (33 and 25 sec), and resulted in essentially the same upwind flame speed with respect to the gases (within the experimental uncertainty);
2. Test No. 9 had the same wind speed (7.2 m/s) as test Nos. 16 and 17, but had a longer ignition delay (50 sec) and resulted in a 40% faster flame speed;
3. Test No. 10 had an ignition delay comparable to test No. 9 (60 vs 50 sec) but a much lower wind speed (4.1 vs. 7.2 m/s) and resulted in a flame speed slower by a factor of 2.

Because the above results are limited to four tests, only tentative qualitative observations can be made. It appears that the flame speed increases with an increase in wind speed and in the time between spill and flare ignition. This finding is reasonable because the mixedness of the LNG vapors with ambient air depends on the wind speed (which affects the rate of mixing) and the ignition delay (which determines the time over which mixing is allowed prior to flame arrival). Clearly, for the fuel-rich cloud at hand, an increase in mixedness, increases the flame speed. It is noteworthy, however, that for much longer ignition delays, as the cloud becomes leaner, an increase in ignition delay is expected to decrease the flame speed. In fact, for very long delays, the cloud may dissipate making ignition no longer possible.

The wind effect on flame speed in a vapor cloud has been investigated by Raj and Emmons (1975) using the liquid vapor fire data from several experiments (AGA, TRW, Gaz de France). The data on flame speed from the present study are in good agreement with the published data. A comparison of these results is shown in Figure 6.8. Note that the flame speed increases linearly with wind speed, in the range of winds investigated.

Unfortunately, there are no existing models that describe the aforementioned effects on the flame speed in a vapor fire. The most closely-related model has been presented by Raj and Emmons (1975) for the burning

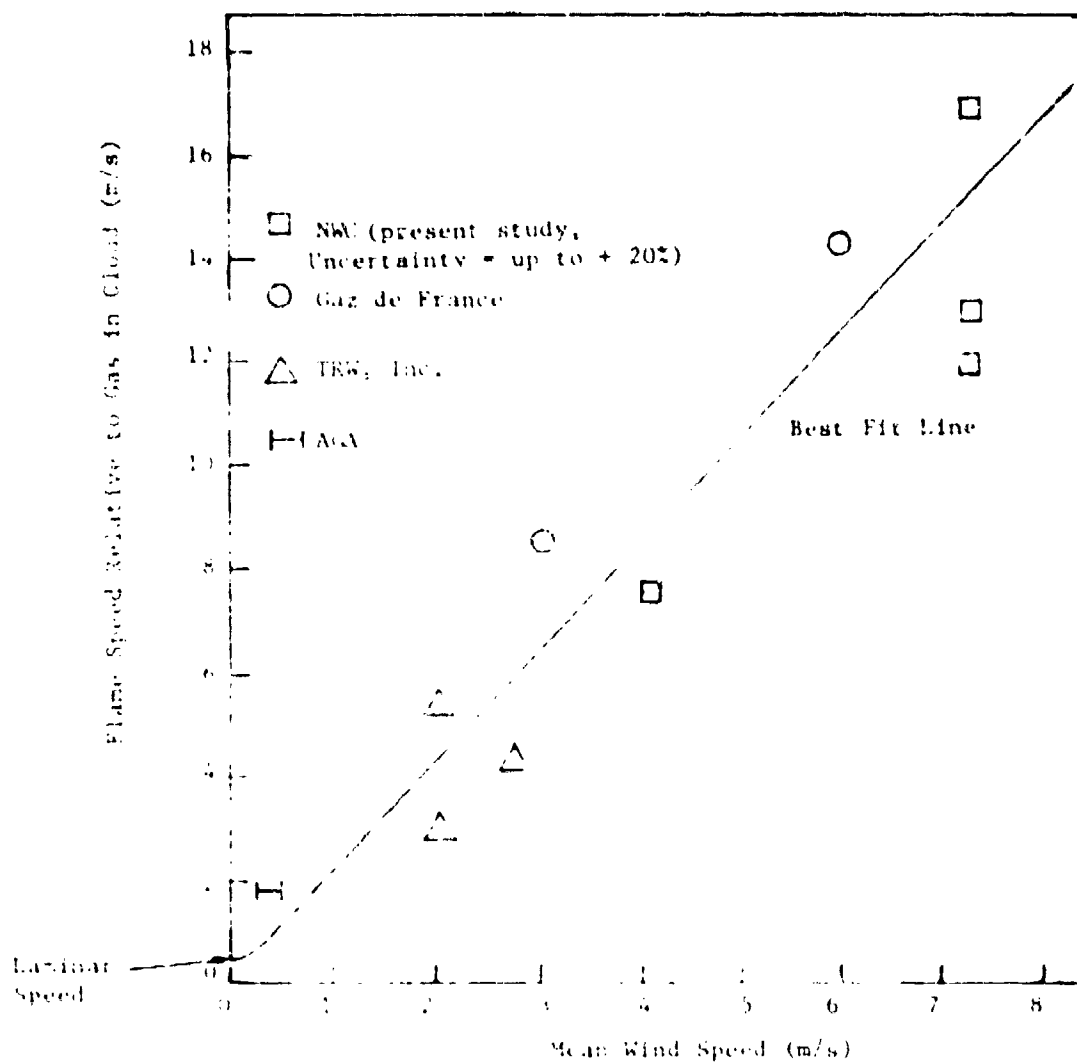


FIGURE 6.8: TURBULENCE FLAME SPEED RELATIVE TO GAS IN VAPOR CLOUD VS. MEAN WIND SPEED

of a large flammable vapor cloud. Yet, this model does not attempt to calculate the flame speed. Instead, it assumes a speed so as to calculate the width of the burning cloud. Consequently, we cannot test this model against the flame speed measurements of this study.

Another model for the unsteady burning of unconfined fuel vapor clouds has been presented by Fox and Lewis (1976). This model assumes burning to occur in a fire ball that rises (due to buoyancy) as the fuel is consumed. Clearly, this model is completely unrelated to the observed behavior in the present tests.

Future theoretical work should address the particular situation at hand; namely, a two dimensional vapor cloud carried in a wind and ignited at its downwind tip with subsequent flame propagation upwind.

6.5.2 Stage 2: Stationary Flame Near Pond Edge

Upon arrival near the pond edge, the transient flame growth and advance (described above) ceased. As illustrated in Figures 6.3 to 6.6, in this stage, the flame appeared stationary with a fairly constant width and length for a period of about 25 to 40 seconds. A fairly distinct turbulent diffusive plume flame was observed, at an inclination of 35 to 45° from the vertical. A schematic of this flame is given in Figure 6.7b. The flame height fluctuated around an average value at a period of about 1 second. The upwind flame edge usually extended a few meters into the pond. At times, small flamelets might "run" at the edge of the cloud, while the major portion of the flame remained stationary.

Table 6.1 gives the average flame length and width during this second stage of life development. (The thermal radiation measurements during this stage will be discussed in the following section.) Note that the flame dimensions are approximately the same for all the tests.

The flame behavior at the pond edge was very intriguing. In tests 8, 10, 11 and 16 the vapor cloud was approximately centered around a corner of the pond, due to the particular wind direction of the test (see Figure 6.9). The flame then stopped near the corner of the pond, but continued to spread on land along the sides of the pond as illustrated in Figure 6.9. On the other hand, this behavior was not observed in Test 17 despite a similar wind direction. Furthermore, in Test 9, the flame advanced into the center of the LNG pool before burning on the sides. In the center region where the flame advanced, the cloud was less opaque than elsewhere.

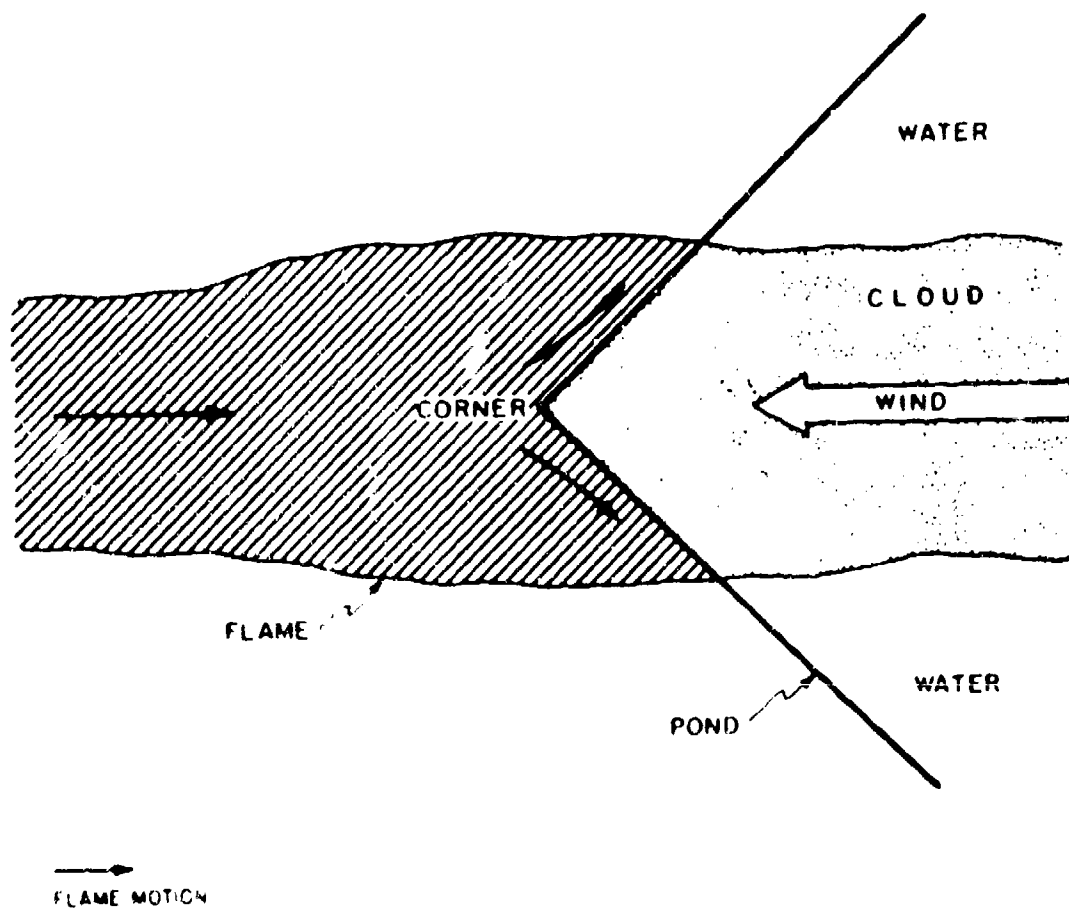


FIGURE 6-10. FLAME MOTION IN A CORNER

A number of explanations can be offered for the lack of motion of the flame near the pond edge. First, the flame may be slowed down due to the presence of water droplets or ice particles in the cloud over the water surface. The water droplets would act as heat sinks that inhibit chemical reactions within the flame resulting in a slower flame speed with respect to the gases. The water droplets result from the condensation of water vapors in a fog form due to heat transfer to the cold LNG. Since the relative humidity near water is much higher than that near land, a larger amount of water should condense therein. This is consistent with a visibly denser fog over water than over land. This water inhibition-based explanation is consistent with a general observation of faster flame spread in transparent clouds versus white clouds (where the water fog is present).

We found no experimental data in the literature on the effect of fine water droplets on the flame speed in a combustible vapor-air mixture. Only vaguely-related results are reported by Eggleston et al. (1975) for a jet of water sprayed into flammable mixtures of ethylene and vinyl chloride confined in a plastic enclosure of about 5 m x 3 m x 3 m (45 to 50 m³). They found an increase in flame speed, probably due to increased local turbulence caused by the water spray. Clearly, the situation is quite different in the present tests, where the water fog has no initial momentum to affect the turbulence level.

A second explanation for the lack of flame advance near the pond edge is that the cloud is locally too rich to burn. Utilizing a recently developed model for the gravity spread of LNG vapors released continuously from a source (DOE, 1979), we estimated the vapor concentration near the downwind edge of the pond to be significantly above the upper flammability limit of methane (15%) for the spill conditions of the tests. (In these calculations, we have utilized hydrocarbon gas sensor data -- to be discussed in Section 6.7 on gas analysis -- near the flare to determine the appropriate entrainment coefficient.) The presence of the pond edge becomes then purely coincidental. This rich cloud-based hypothesis is not very plausible, however, because it does not explain the general lack of flame spread in the cloud periphery where leaner concentrations should be present.

A third hypothesis is the formation of a circulation zone near the pond edge that stabilizes the flame. The circulation zone would be caused by the local topography, where land rises above the water level in the

pond. Because this difference in elevation is comparatively small (about a few meters) and because there is no visible evidence of a circulation zone, this hypothesis seems doubtful.

Further experimental and theoretical work is required to sort out the various hypotheses described above and to explain the reason for flame attachment near the pond. Suggestions on such work are given in the recommendations section.

6.5.3 Stage 3: Transient Burn-out

After being approximately stationary near the pond edge, for half the fire duration, the flame continued its upwind motion towards the spill point. For Tests 9, 16, and 17, this occurred approximately near the end of the spill, while it occurred much later in Test No. 10. This transient burn-out stage lasted for a fraction of a minute until all the LNC was consumed. At the very end of the test, the fire resembled a pool fire with a sooty and reddish plume.

6.5.4 Flame Length/Width Ratio

The flame length and width* throughout the vapor fire are plotted in Figure 6.7a for the four tests discussed above. Based on the present results, it is possible to make only a qualitative statement to the effect that flame length increases with flame width. There is too much scatter to provide any meaningful correlation. The significant quantitative result is that the flame height to width ratio is less than unity and is much closer to 1/2.

We note that the Raj and Emmons' model (1975) for a vapor fire assumed a constant ratio of 2 for the flame length to its width, for the entire duration of fire. This is in variance with the above data, although it would tend to give conservative estimates of thermal flux from the flame. Furthermore, even when this ratio is adjusted in the model so as to fit our experimental data, the predicted dependence of the maximum flame width on the flame speed is at variance with measurements. Clearly, the specific situation at hand has not been modelled and should be addressed in future work.

* Flame length = length of the visible flame plume from the ground to the tip.

Width = width at ground level of the zone of burning measured along the direction of propagation of flame. Length and width are defined in Figure 6.7b.

Test #9	○
Test #10	△
Test #16	□
Test #17	▽

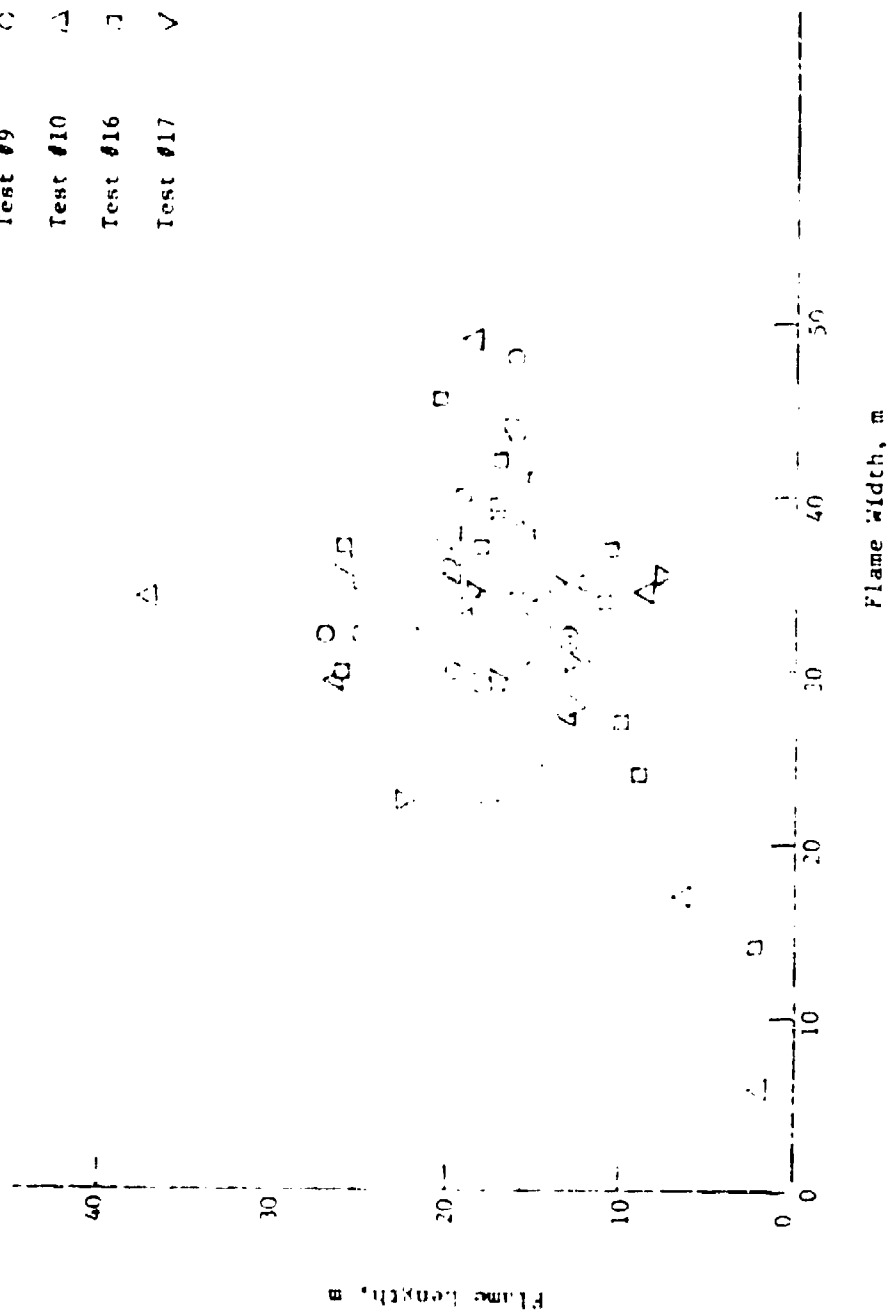


FIGURE 6.10: DIMENSIONS OF THE BURNING ZONE. WIDTH IS MEASURED ALONG THE DIRECTION OF FIRE PROPAGATION AND LENGTH IS MEASURED IN A VERTICAL PLANE ALONG THE DIRECTION OF FLAME INCLINATION (UNDER WIND).

6.6 RADIATION ANALYSIS

6.6.1 Data Collection and Evaluation

Radiation data were collected using wide-angle and narrow-angle radiometers placed at selected locations as indicated in Figures 6.1 and 6.2. The radiometer serial numbers, locations, elevation above the water level in the pond, orientation and window material are listed in Table 6.4. Most of the radiometers were oriented approximately along the crosswind direction so as to yield an unobstructed view of the fire. Two exceptions (Radiometer 4 in Tests 8 to 11 and Radiometer 7 in tests 16 and 17) were placed along the upwind direction.*

The output of each radiometer was examined individually to determine whether the measurement was successful or not. Clearly, all off-scale outputs were discarded. Furthermore, we checked the consistency of the radiometer output with the observed flame behavior shown in Figures 6.3 to 6.6, by comparing the time at which the radiometer started to respond and the response duration with the ignition delay and the duration of the fire, respectively. When such a consistency was lacking or when the readings were negative, the outputs were discarded as not recognizable (Radiometer 5 in Tests 8 and 11 and Radiometer 6 in Test 11). To check further the validity of the radiometer output, we compared its fluctuations with the flame fluctuations. This was very apparent in Test No. 17 where two successive ignitions occurred. A summary list of the collected radiometer data is given in Table 6.1. The data are labelled as successful, off-scale, unrecognizable, or lost. All data of Test No. 13 were lost. Blanks in Table 6.2 denote that the data were not collected.

A typical successful radiometer output is given in Figure 6.11 (from Radiometer 5). The figure shows that the maximum response occurs during the second stage of fire development (defined in Section 6.5.2), when the flame is stationary near the pond edge and is of maximum dimensions. The output also has a fairly constant average value (about 200 kW/m^2) except for some fluctuations (up to 240 kW/m^2 and down to 170 kW/m^2).

* The data from the upwind radiometers were not interpreted since corresponding view factors could not be estimated. In one test, downwind camera data were lacking; in the other tests portions of the flame were outside the field of view of the upwind camera.

TABLE 6.4

RADIOMETER ARRANGEMENTS FOR VAPOR FIRES

(Radiometers No. 5 and 6 are narrow angle; all others are wide angle)

Radiometer		Radiometer		Window	
Code	Serial No.	Location, m	Height Above Water Level, m	Radiometer Orientation	
For Test No. 8, 9, 10, 11					
(From Spill Pt.)					
1	56012	80	3.1	NE Marker-Horizontal	Quartz 2
2	56015	60	3.0	" "	Quartz 2
3	56016	40	2.7	" "	Quartz 1
4	56014	55	3.8	Spill Point	Quartz 1
5	56017	60	3.0	NE Marker	Sapphire
6	56018	60	3.0	H-C Sensor #3	Sapphire
For Test No. 16, 17					
(From Marker)					
1	65281	75 m	3.7 m	Horizontal over marker	Sapphire
2	56015	60 m	3.7 m	" "	Sapphire
3	56016		3.7 m	" "	Intran 4
4	65283	45 m	3.4 m	" "	Sapphire
5	65017		3.4 m	2.75 m AGL over marker	Sapphire
6	65018		3.4 m	2.75 m AGL 5.5 m NE of marker	Sapphire
7	65284	44 m	3.4 m	Horizontal over spill point	Sapphire
				AGL = above ground level	

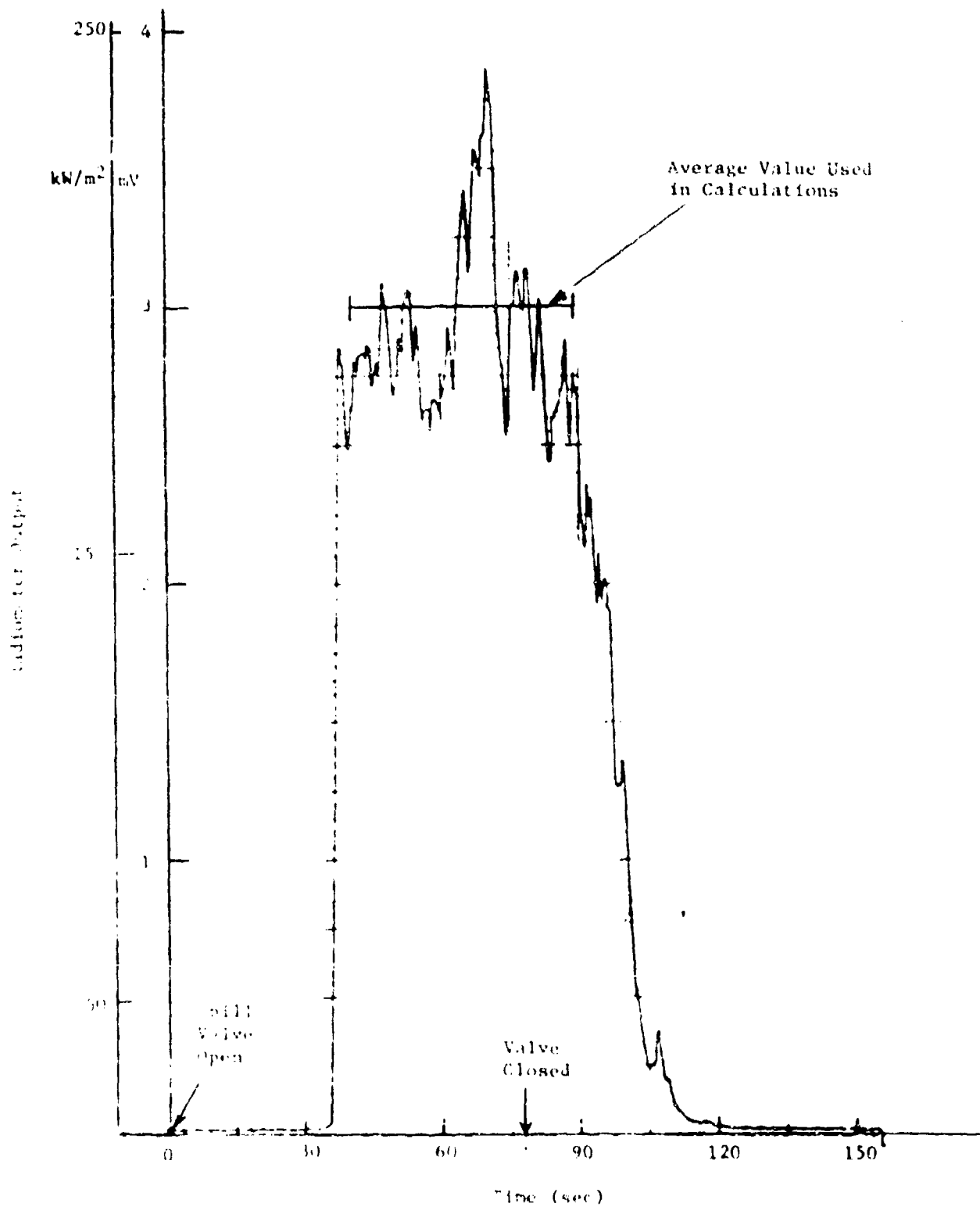


FIGURE 6.11: TYPICAL RADIOMETER OUTPUT (TEST # 17, NARROW ANGLE RADIOMETER # 5)

These radiometer fluctuations are attributable to fluctuations in flame size, both having a time constant of about 1 sec.

From the hazard point of view, targets exposed to flame radiation such as wood and steel structures would have response times much larger than 1 second. Consequently, they would integrate the radiation fluctuations over the exposure interval, thus effectively sensing only the average radiation (say 10 kW/m^2 in Figure 6.11). Consequently, we have focused our analysis on the time-averaged output of the radiometers. An analysis of the fluctuations would have required calculations of the instantaneous view factors and the synchronization of the movie and radiometer records (accounting for phase shifts due to the response time of the radiometers). Clearly, this is an awesome task that would also introduce large errors. Since this was not needed from the hazard analysis point of view, we did not analyze the fluctuations in the radiometer outputs, focusing only on average outputs.

6.6.2 View Factor Calculations

Based on the discussion of the previous section, we need only determine view factors between flame and radiometers that are averaged over the second stage of the vapor fire.

Wide Angle

To get the view factor between the wide-angle radiometer and the flame, we assumed that the flame can be represented by a rectangular plane. The average dimensions of this rectangle were calculated in two different methods by two different data analysts. The two methods are summarized in Table 6.5. The results, also shown in Table 6.5, indicate that the two methods may disagree by up to 23% in flame area (for Test No. 9), due to uncertainties in defining the irregular shape of the flame and in locating its edge. Fortunately, the disagreement is only within 2 to 8% for Tests 16 and 17. Only these two tests yielded successful wide-angle radiometer data for which the flame dimensions were needed to calculate view factors. Consequently, the uncertainty in our view factors is limited.

TABLE 6.5
FLAME DIMENSIONS FOR VIEW FACTOR CALCULATIONS

Test No.	1st Method*		2nd Method*	
	Flame Width (m)	Flame Height (m)	Flame Area (m ²)	Flame Average Area (For the 2 methods) (m ²)
9	32	10	200	260
10	34	11	410	400
16	38	11	440	430
17	27	9	280	260

* In the first method, flame width and height were obtained from Figures 6.3 to 6.6 and the movies. Then flame area = width x height.

In the second method, the flame area was measured directly from the movies (by projection on grid paper).

The two methods were carried out by separate data analysts.

The view factors were calculated using Hottel's Charts (1967) for radiation from a rectangular plane (the flame) to a parallel infinitesimal element (the radiometer) placed at one corner of the plane. We corrected for the fact that the flame was not exactly parallel to the element by geometric projection. The calculated view factors are given in Table 6.6. (This table will be discussed further below.)

Narrow-Angle Radiometers

For a narrow-angle radiometer, the view factor is unity when the field of view is completely filled by the flame. For a 7° (full cone) angle radiometer, the fields of view are 2.7 and 4.2 m in radius at distances of 44 and 69 m, respectively. We verified that these small fields of view were completely filled by the flame during the interval over which the outputs of the narrow-angle radiometers were used. Consequently, we utilized a view factor of unity.

6.6.3 Flame Emissive Power

The average radiometer outputs (as defined in Section 6.6.1) are given in Table 6.6 for all the successful measurements, along with the corresponding view factors (F), window and atmospheric transmissivities (τ_w and τ_a). The atmospheric transmissivity is only approximate as it assumes that the flame is a black body radiator at 1150 K and absorption occurs only in the water bands. In reality, the flame is a band emitter due to the presence of hot water and carbon dioxide, as explained in Chapter 4 on spectral measurements. This "approximate" atmospheric transmissivity for various path length and ambient humidity has been presented in a recent paper (Raj, 1977). Because of the relatively short path between flame and radiometers, the use of these transmissivities is expected to lead to insignificant errors.

TABLE 6.6

EMISSIVE POWER CALCULATIONS FOR VAPOR FIRES

Radiometer Number	Type of Meter	Average Radio-Output mv	View Factor	Transmissivity		Emissive Power (kW/m ²)
				Window	Atmosphere	
Test No. 8 (5/26/77)						Based on Calibration of 9/14/76
6	NA	0.70	1	*	0.77	210
Test No. 9 (6/1/77)						
5	NA	2.9	1	*	0.78	260
Test No. 16 (6/12/78)						Based on Calibration of 8/10/78**
1	WA	2.7	0.021	0.79	0.75	115
2	WA	2.9	0.031	0.79	0.76	118
3	WA	5.8	0.031	0.68	0.76	170
4	WA	5.5	0.048	0.79	0.78	104
5	NA	2.0	1	*	0.78	183
6	NA	2.1	1	*	0.78	200
Test No. 17 (6/13/78)						
1	WA	4.0	0.014	0.79	0.76	240
2	WA	4.5	0.021	0.79	0.77	260
3	WA	8.9	0.021	0.68	0.77	320
4	WA	10.7	0.035	0.79	0.79	300
5	NA	3.0	1	*	0.79	250
6	NA	2.3	1	*	0.79	<u>220</u>
Average =						210
Standard Deviation = ± 65 (or $\pm 30\%$)						

* No correction for window transmissivity as same sapphire window was used in both calibration and measurement.

** Except radiometer No. 3 which was calibrated on 3/21/78.

A = Narrow-Angle Radiometer

WA = Wide-Angle Radiometer

Because the flame depth is about 30 m, it is assumed to be optically thick, and the emissive power (E) is calculated according to:

$$E = \frac{\bar{q}''}{F_w \tau_a} \quad (6.1)$$

where:

\bar{q}'' = the radiometer output (in kW/m^2) averaged over the period where the flame is stationary near the pond edge.

The results calculated using the above equation are listed in Table 6.6 and are discussed below:

(1) Range of Emissive Powers

The range of calculated emissive powers covers from 104 to 320 kW/m^2 with Test 17 being on the high side, while Test 16 on the low side and Tests 8 and 9 in the middle range. The range is much narrower for emissive powers based on only narrow angle radiometer data, (186 to 260 kW/m^2) as shown in Table 6.7. It is noteworthy that the average in both cases is about the same (220 kW/m^2).

To check the repeatability of the results, we can compare only Tests 8, 16 and 17 for which complete sets of radiometer data have been obtained. For each of these tests, the individual wide- and narrow-angle radiometers (No. 1, 2, and 3)** give consistent results within + 7 to 13% of their averages. However, the wide-angle data for the two tests differ significantly from one another, while the narrow-angle radiometer data differ by much less.

A small portion of these differences may be attributed to radiative cooling of the radiometer detector by the cold sky which occurs only at night (in Test No. 16) and only for the wide-angle radiometers. In Test No. 16, the view factors between the cold sky and the wide-angle radiometers varied from 0.95 to 0.98 while they were zero for the narrow-angle radiometers (assuming that the

* In reducing the radiometer data, we used the original calibration curves (dated 9/14/76) for the 1977 tests (Nos. 8 and 9), and the most recent calibration curves (dated 5/10/78, except for radiometer No. 3 which was dated 3/1/78) for the 1978 test (Nos. 16 and 17). The radiometers were recalibrated after being engulfed in flames during Test 13 (5/26/78).

** Radiometer No. 3 has a different type of window and is discussed below.

flame is optically thick). Thus, from day to night tests, we should expect differences between the wide-angle radiometers data and no difference between the narrow-angle ones. These differences are estimated to be small (about 10%), however, since the sapphire windows on the radiometer minimized reradiation to space in the long wave-length region.

Most of the difference between the results from the two types of radiometers is probably attributable to errors introduced in the calculation of view factors which are needed only in the reduction of the wide-angle radiometer data. These errors are due to the irregular shape of the flame, the difficulty in determining flame tilt, and the uncertainty in locating its edges.

(2) Effect of Radiometer Windows on Results

In tests 16 and 17, Radiometers 2 and 3 were placed at the same location but with different windows, sapphire and Irtan 4, respectively. The spectral transmissivity of the sapphire window is about 0.80 up to 4.5 μm , but drops quickly thereafter and becomes zero beyond 8 μm ; while that of the Irtan 4 window is close to 1.0 up to 4.7 μm (see Appendix D).

The emissive powers calculated according to Radiometer 2 are less than those according to Radiometer 3 by 30% and 19%, for Tests 16 and 17, respectively. This trend is consistent with the spectral transmissivity of the two windows. However, a 30% difference is larger than expected, considering that about 1% of radiated energy lies in the region beyond 5.5 μm .

6.2 HYDROCARBON GAS ANALYSIS

Five hydrocarbon gas analyzers* were placed at selected locations downwind of the spill point, as illustrated in Figure 6.1 and 6.2. The elevation of the sensors above ground was 0.61 m. The sensor outputs from tests 8 to 11 were completely unrecognizable and were thus discarded. Successful data were obtained in tests 16 and 17, however. Still, three sensors were "blinded" by the cloud due to the particular wind direction in test 16 (see Figure 6.2).

* portable gas analyzer, Model I-500, manufactured by Mine Safety Appliances Company.

TABLE 6.7

EMISSIVE POWER BASED ON ONLY NARROW
ANGLE RADIOMETER DATA

<u>Test No.</u>	<u>Radiometer No.</u>	<u>Emissive Power</u> ($\mu\text{W}/\text{m}^2$)
8	6	210
9	5	260
16	5	183
	6	200
17	5	250
	6	<u>220</u>

Average = 220

Standard Deviation = ± 27 (or $\pm 12\%$)

The gas sensor response shows very rapid rise in hydrocarbon concentrations as the cloud moves over the sensor, shooting off scale (i.e., larger than 5% methane). The response also drops rapidly upon flame arrival over the sensor. For Test 17, the vapor cloud speed (without ignition) was estimated based on the gas sensor response. The speed was found to be equal to roughly half the sum of the wind speed and a gravity induced speed* of the negatively buoyant vapors. A similar agreement was not obtained for Test 17, presumably due to a slowdown or shifting of the wind.

6.8. RESULTS AND CONCLUSIONS

The results and conclusions based on the vapor fire tests are:

1. Ignition of dispersed vapors generated by the spill of LNG on water yields a spreading plume flame that remains close to the ground. A fire-ball type of vapor burning was not observed.
2. The fire spreads at a significantly faster rate in the portion of the cloud over land versus that over water. This may be attributed to the presence of larger amounts of condensed water and ice aerosols over water than over land, which inhibit the fire spread. Further work is needed to shed more light on this point.
3. The fire spread rate over land is found to increase with an increase in wind speed, as has been observed previously. The bulk of the data obtained so far suggests a linear relationship for winds of up to 7 m/s (16 mph).
4. Near the pool edge, the fire remained stationary with nearly constant dimensions over about half the burn interval. The burning zone dimensions were about the same for all tests with average values of 13 m x 1.5 m x 0.5 m for width (along the fire propagation direction), length (in the vertical plane), and depth.
5. Throughout the vapor fire, the ratio of burning zone length to width was always less than unity, which is smaller than has been reported previously.

*Gravity-induced speed (v_g) of a vapor cloud of height (H) and density (ρ_v) larger than air (ρ_a) is of the order of:

$$v_g = \sqrt{g \frac{(\rho_v - \rho_a)}{\rho_v} H} \approx 3 \text{ m/s for the present tests} \quad (6.2)$$

6. The radiant emissive power calculated for the stationary stage of the fire near the pond edge is found to range from 104 to 320 kW/m^2 with an average value of $210 \text{ kW/m}^2 \pm 30\%$ (standard deviation).
7. Although the number of tests was limited, a remarkable repeatability of the main fire behavior has been observed between tests. The radiant emissive power estimated based on the narrow-angle radiometer data was quite repeatable while that based on the wide-angle radiometer data varied significantly.

7. COMPARISON OF RESULTS AND RECOMMENDATIONS

In this chapter the results obtained from pool fire tests and vapor fire tests are summarized, compared, and contrasted. Also indicated are models for use in the assessment of thermal hazards from LNG fires on water. Finally a list of recommendations for future work is provided.

7.1 COMPARISON OF FLAME EMISSIVE POWER RESULTS FROM POOL FIRES AND VAPOR FIRES

The thermal radiative output of the pool fires and vapor fires have been calculated using the data from the narrow-angle radiometers, wide-angle radiometers, and in one experiment, from a spectrometer. In another test, wooden stakes were positioned to observe the degree of charring at various distances. These were discussed in detail in Chapters 4, 5, and 6. In this section, the thermal data and results are compared with a view to drawing conclusions about the nature of thermal radiation from pool fires and vapor fires.

The flame emissive power is one important physical quantity whose values were determined. This represents the energy emitted by a nominal surface area of the fire. Emissive power is estimated using data from receptors positioned at known distances from the fire. Wide-angle radiometers and the wooden stakes received thermal radiation from the entire flame sheet. Narrow-angle radiometers and the spectrometer were positioned so that only a portion of the lower part of the flame was viewed. Thus, the emissive power estimated from each data source represents an average value over the flame area viewed by the particular receptor instrument. The emissive power results from Chapters 5 and 6 and are repeated in Table 7.1. Results based on wide angle radiometer data for pool tests 1 through 6 give unreasonable values for the emissive power* and are, therefore, omitted in Table 7.1 (for a discussion on this see Chapter 5, Section 5.4.3). Also indicated in the table are the results from the spectrometer data and those obtained from the data on the charring of wooden stakes.

As can be seen from the results presented in Table 7.1 there does not appear to be any systematic variation in the value of the evaluated emissive power.

* This is due to instrument calibration problems.

TABLE 1. PLANT EMISSION DATA MEASUREMENTS FROM 150 FIRE TESTS

Numbers in the table represent the flame emissive power in Btu/hr.

Type of Test	Test No.	Min value measured	BASED ON WIDE-ANGLE DATA			BASED ON NARROW-ANGLE DATA			Spectrometer data (average values)	Wood ignition data
			Average over the duration of steady burning	Maximum value	Standard deviation	Min value	Average value	Max value		
Pool Fire	1	-	-	-	-	195	207	221	5	
	2	-	-	-	-	183	204	218	11	
	3	-	-	-	-	156	187	206	29	
	4	-	-	-	-	179	185	193	6	
	12	174	239	292	47	194	224	248	13	143
	13	-	-	-	-	218	226	235	6	
Delayed ignition pool fires	14	-	-	-	-	204	227	256	22	
	8	-	-	-	-	-	210	-	-	
Vapor Fire	9	-	-	-	-	-	260	-	-	
	16	115	127	170	30	183	192	200	8	
	17	240	280	320	36	220	235	250	15	

sive power. The narrow-angle radiometer data, which directly give the emissive power (except for a minor correction for the atmospheric absorption) vary from a low of 179 kW/m^2 to a high of 260 kW/m^2 over the entire experimental range, including both pool fire and vapor fire tests. The spectrometer, wood charring, and wide angle data are generally consistent with the narrow-angle data.

The purpose of the delayed ignition pool fire tests was to obtain a large diameter fire to determine whether the flame was optically thick. The emissive power results from these tests have wide scatter but indicate a somewhat higher mean emissive power than pool fires. It is likely, therefore, that the pool fires were not optically thick.

In general, vapor fire emissive power values are somewhat higher than those from pool fires. This may be due to two reasons. Vapor fires may be somewhat hotter because of the burning of a partially premixed vapor-air mixture. Hence, the combustion is likely to be more efficient. Secondly, the thickness of the vapor fires along the direction of sight of the narrow-angle radiometers were in general larger than those in the case of pool fires, i.e., the vapor cloud width was greater than the burning pool width. This suggests that vapor fires were perhaps more optically thick than pool fires. Also because the entire vapor cloud was partially premixed with air, combustion could occur throughout the width. In a large turbulent diffusion pool fire where the air is entrained from the outside of the flame plume, there are always pockets of cold air and burnt gas "trapped" within the folds of the flame sheets making the fire appear to be "cooler" overall than a turbulent premixed fire.

In Table 7.1, the average emissive power estimates are shown along with maximum and minimum values for the steady burning portion of each test. The maximum and minimum values represent trends during the period of steady burning and do not reflect the rapid fluctuations of thermal flux due to pulsations in the flame.

The variability in the narrow-angle emissive power between a minimum and a maximum (reckoned only in the quasi-steady state burning period) in the pool fire experiments is most probably due to the increased luminosity of the fire towards the end of the burning period. This appears to be due to the higher luminous soot concentrations caused by the combustion of increasing quantities of ethane, propane, and butane in the later stages of the fire. (Methane vaporizes preferentially in the early stages because it has a higher relative volatility.) The spectrometer data confirm this observation in test #5.

In the vapor fire tests, the flame emissive power remains fairly constant during the steady burning period and the range indicated in Tests 16 and 17 represent readings from two instruments. The instrument which read lower in Test 16 read higher in Test 17, so this does not appear to be an instrument calibration effect. In the vapor fire tests, methane composition of the LNG remained fairly constant. As a matter of fact, the ethane content in Test 9 is the lowest (1.8%), yet this test gives the highest emissive power. However, the propane content is highest in this test (1.7% compared to 0.8% in the others). Whether such small variations in propane content can lead to a wide variability in emissive power is doubtful. We have been unable to discern any systematic trend in the variability of the emissive powers obtained from the narrow-angle radiometer data. The explanation may be simply that because of nature of the vapor fire burning and the vagaries of the wind, the effective optical path along the radiometer axis varied from test to test. Such a conclusion, however, does not justify the variability in the emissive power data (from narrow-angle radiometers) obtained from the pool fires. In these tests one expects the optical depth to remain about the same considering that the flame diameters were all essentially the same (about 14 meters).

The results presented in Table 7.1 indicate larger standard deviations with wide-angle readings when compared to those with narrow-angle readings. The explanation for this may lie in the method by which the emissive power is calculated from the wide-angle radiometer data. This involves the determination of shape, size and orientation of the visible fire from movie records (a somewhat subjective operation) and then the calculation of the effective view factor. Because of the relatively small magnitudes of the view factors (compared to unity) relatively minor errors in the flame size contribute to significant variations in the estimated view factor and hence in the emissive power.

We also notice that the wide-angle results are in general higher than narrow-angle results. Several explanations can be considered. In the case of pool fires, the narrow angles were aimed at the lower sections of the flame. It is likely that luminous soot concentrations increased with

height in the flame making the flame more radiative at higher elevations. This would tend to make the wide-angle readings higher. The other possibility is that the effective fire diameter increases with height. That is, the infrared emitting gases form an inverted frustum of a cone with a visible core in the middle. It is this core which is seen in the motion pictures. The hot, but invisible gases (rising in the plume) surrounding the core may contribute to higher wide-angle radiometer readings and hence higher emissive power (which is based on visible flame area). Since no infrared pictures of the fire were taken, this hypothesis cannot be confirmed.

The emissive power of the flame obtained from the spectroscopic data is in close agreement with the results from narrow-angle data for Test #5. We recall that the emissive power from the spectral data was based on a flame temperature of 1500 K* and stoichiometric combustion. The fire is found not to be optically thick (over the entire infrared wave lengths) even though the visible diameter was 13 m. Using the spectral model, an equivalent flame emissive power would be about 210 kW/m^2 which is in good agreement with the narrow-angle radiometer data. It is unfortunate that the wide-angle result from this test cannot be compared with either narrow-angle or spectroscopic results because we suspect that the wide-angle radiometer calibrations were incorrect. However, the agreement of the results in Test 12, based on wide- and narrow-angle radiometers is very good. Results based on wood charring data give somewhat lower values. This may be because of the imprecise information on the thermal flux level at which the particular wood used starts to char. We have assumed this level to be 30 kW/m^2 , but it could be as high as 35 kW/m^2 in which case the estimated emissive power would be closer to the radiometer-based result.

The comparison above indicates the significant variability in the emissive power results. Several possible factors have been discussed. None of them can satisfactorily explain all of the differences. Under these conditions, the task of recommending a value for the emissive power to be

* Black body emissive power at this temperature is 287 kW/m^2 .

used in hazard calculations becomes difficult. We have more confidence in the spectroscopic data and the narrow-angle data. Our recommendation is for characterizing the LNG fire with a temperature of 1500 K and stoichiometric combustion and to use the physical thickness of the fire (diameter) for the optical path length. This gives a maximum emissive power of 287 kW/m^2 for an optically thick flame which is close to the observed maximum in vapor fires.

7.2 SUGGESTED MODEL FOR USE IN ASSESSING THERMAL RADIATION HAZARDS FROM LNG POOL FIRES ON WATER

The evaluation of the thermal radiation field around a LNG fire is made by calculating, in sequence, the following parameters:

1. The diameter of pool spread with a fire on the pool.
2. The time averaged mean flame height.
3. The emissivity of the fire (H_2O , CO_2 , and soot emissivities).
4. The view factor to an element at a given distance from the center of the fire.
5. The atmospheric transmissivity to the given distance.

Based on the data from the experiments indicated in this report and the analyses of the data, magnitudes of some of the physical quantities can be established for use in hazard models. Our recommendations for the values of the various quantities are indicated in Table 7.2. Further our recommendations for the equations include the following:

Pool Spread

$$D = \left[\frac{4}{\pi} \frac{\dot{V}}{\dot{v}} \right]^{1/2} \quad \text{For continuous spills} \quad (7.1)$$

$$D_{\max} = \left[\frac{V^3 \kappa (1 - \frac{1}{\kappa})}{\dot{v}^2} \right]^{1/8} \quad \text{For instantaneous spill} \quad (7.2)$$

in which the value of \dot{v} from Table 7.2 should be used.

TABLE 2-2. RECOMMENDED VALUES FOR VARIOUS PHYSICAL PARAMETERS FOR USE IN MODELS

No.	Physical Parameter	Symbol	Units	Range of Characteristic Values in the Tests	Recommended value or formula
1	Regression rate on water fire in the pool	\dot{r}	in/s	4×10^{-4} to 11×10^{-4}	7×10^{-4} in/min
2	Variable flame height in pool fire	h_f	ft	20 to 45	See Thomas' equation is recommended: $h_f = 4.7 \left[\frac{Q_{\text{net}}}{\pi \times 10^4} \right]^{1/4}$
3	Flame temperature for radiative calculations	T_f	K	1000-1500	1300
4	Condition of gases in the fire (expressed in partial pressures)	P	atm		Stoichiometric combustion values are recommended: $P_{\text{H}_2\text{O}} = 0.085$ atm, $P_{\text{H}_2\text{O}} = 0.19$ atm
5	Mean beam length for flame emissivity calculation	L_{av}	m	11 to 15	Use the flame diameter as the beam length
6	Water vapor and carbon dioxide emissivities (in the flame)	$\epsilon_{\text{H}_2\text{O}}$ ϵ_{CO_2}	-	0.85 and 0.9 respectively	Use Hottel charts (Hottel and Sarofim, 1967) or other equivalent charts
7	Luminous soot emissivity	ϵ_s	-	0.1-0.27	0.25

Flame Height

$$\frac{L_f}{D} = 42 \left[\frac{\frac{L}{\dot{V}_a}}{\frac{\dot{V}}{\sqrt{gD}}} \right]^{0.6} \quad (7.3)$$

Radiative Transfer

The thermal radiation flux at any point outside the fire is determined from the equation

$$\dot{q}'' = E_b F \left[\epsilon_{H_2O} + \epsilon_s - \epsilon_{H_2O} \right] \quad (7.4)$$

where

E_b = Black body emissive power at flame temperature

F = View factor

ϵ_{H_2O} = Combined band emissivities of H_2O and CO_2 in the fire

ϵ_s = Soot emissivity in the fire

ϵ_{H_2O} = Band absorptivity of water vapor and CO_2 in the atmosphere. This absorptivity is representative of only the following bands:

H_2O , 1.87, 2.7 and 6.3 microns

CO_2 , 2.7 (overlap), 4.3 and 15 microns

Also this absorptivity is to be calculated for a weighted mean radiation path through the atmosphere (see equations B9-B11).

7.2.1 Illustrative Example

Consider the spill of 25,000 m³ of LNG onto the water surface in 10 minutes. It is required to calculate the radiative heat flux to a vertical element at water level, located at 1 km from the center of spill. The temperature of the ambient is 20°C and relative humidity 60%.

In obtaining the result for the above problem we make use of the values recommended in Table 7.1.*

Diameter of pool (continuous spill formula, equation 7.1)

$$= 297 \text{ m}$$

Flame height = 1.52×297

$$= 450 \text{ m}$$

Partial pressure \times beam length for H_2O =

$$0.199 \times 297$$

$$= 56.4 \text{ atm m}$$

Partial pressure beam length for CO_2 =

$$0.095 \times 297$$

$$= 28.2 \text{ atm m}$$

At these partial pressure-length values the flame can be considered to be optically thick. Hence the total emissivity of the flame including the soot emission should be unity.

Total radiative energy released from the flame = $E_b = 287 \text{ kW/m}^2$

Atmospheric absorptivity over the 1 km distance is calculated using either Hottel charts (Hottel and Sarofim, 1967) or by using the band by band absorptivity calculations of Edwards and Balakrishnan (1973):

Partial pressure of water vapor in the atmosphere (20°C, 60% RH) = $1.38 \times 10^{-2} \text{ atm}$

Partial pressure of CO_2 in the atmosphere = $3 \times 10^{-4} \text{ atm}$

Hence,

$$(\text{PL})_{\text{H}_2\text{O}} = 1.38 \times 10^{-2} \times 10^3 = 13.8 \text{ atm m}$$

$$(\text{PL})_{\text{CO}_2} = 3 \times 10^{-4} \times 10^3 = 0.3 \text{ atm m}$$

Unfortunately, the charts provided in Hottel and Sarofim (1967) do not contain the range of PL for H_2O encountered in this problem. We therefore choose the (rather tedious) method of absorptivity calculations indicated by Edwards and Balakrishnan (1973). For detailed calculations the referenced paper should be consulted.

Total absorptivity of H_2O and CO_2 in 20°C, 60% RH, 1 km path = $a_{\text{atm}} = 0.370$

* In addition, $\rho_L = 425 \text{ kg/m}^3$ and $\rho_a = 1.2 \text{ kg/m}^3$

The view factor to a vertical element at 1 km from a fire of 297 m diameter and 450 m height = 0.0415 (see tables in Raj (1977)).

hence the thermal flux received at 1 km distance is:

$$\dot{q}''(1 \text{ km}) = E_b F (1 - \alpha_{\text{atm}}) = 287 \times 0.0415 \times 0.63 = 7.5 \text{ kW/m}^2$$

It is noted that in a path length of 1 km the effects of absorption by other gases such as carbon monoxide, nitrous oxide, methane, etc. in the atmosphere can begin to be noticeable. Therefore, the calculated flux received, indicated above, is probably the upper bound for the flux.

7.3 SUGGESTED MODEL FOR ASSESSING THERMAL RADIATION HAZARDS FROM UNCONFINED VAPOR CLOUD FIRES

The data from vapor fires have indicated the turbulent flame spread velocity in unconfined vapor clouds as well as the magnitude of radiative emission. Also the tests showed that there could be a significantly different type of vapor cloud fire behavior on a body of water compared to that on land. (The fire spread rate seems to be less on water.) Since additional direct data (such as the relationship between turbulent flame speed and density of water fog in a combustible vapor cloud) would be necessary before a vapor fire spread model on water can be developed and since the fire spread rate on land is higher, we recommend the use of the currently available vapor fire model for hazard assessment purposes.* Such a calculation would be conservative.

The recommended vapor fire hazard assessment model is therefore a "wall fire" model characterized by the burning of vapor in the form of a propagating (close to the ground) flame plume. The model calculation involves the following steps:

1. Calculating from the known initial vapor cloud spread, thickness and the concentration distribution in the cloud, an equivalent cloud thickness within which the concentration is uniform (and above lower flammable limit).

* This model is described in detail in a paper by Raj and Emmons (1975).

2. Obtaining from the (empirical) graph presented in Figure 6.8, the turbulent flame speed relative to the vapors corresponding to the prevailing wind speed.
3. Calculating the maximum burning zone width assuming a flame height to width ratio of 1 (see Chapter 6). This will also give the flame plume length.
4. Determining the radiation zone around the flame with flame emissive power for very large optical path lengths (very wide fire normal to the wind direction) taken as 287 kW/m^2 . If the flame is not optically thick in a given direction its emissivity has to be calculated by using the recommended values given in Table 7.2.

7.3.1 Illustrative Example

A vapor cloud has a mean vapor concentration of 20% (molar) and is of thickness 3 m. The wind speed is 5 m/s. Fire dimensions are calculated as follows:

From Figure 6.8

$$\text{The flame speed at 5 m/s wind speed} = S = 10.5 \text{ m/s}$$

$$\text{Thickness of cloud} = \delta = 3 \text{ m}$$

$$\text{Flame Froude number} = F_f = \frac{10.5^2}{3 \times 9.8} = 3.75$$

$$\text{Inverse volumetric expansion ratio of methane at 20\% concentration} = \omega = 5.18 \times 10^{-2}$$

[For the calculation of this parameter see Ra] and Emmons (1975)]

$$\text{Density of vapor cloud containing 20\% vapor by volume} = \rho_0 = 1.33 \text{ kg/m}^3$$

$$\text{Ratio of cloud density to air density} = \rho_0' = 1.13$$

$$\text{Air fuel mass ratio for the combustion of methane} = r = 17.2$$

Hence, using the equation from the above reference

$$\frac{W_a}{3} = 20 \left(\frac{W}{H} \right) \left[F_{12} + \frac{1}{6} \frac{(r + \sqrt{r^2 + 1})^2}{(1 - r)^3} \right]^{1/3}$$

for visible
flame

Hence, $W/3$ = 88.5

Therefore, width of burning zone = 88.5 x 3 = 265 m

Length of flame plume = 265 m

For calculating thermal radiation to a point outside the fire zone, conventional view factor calculations have to be made assuming the flame to be a tilted rectangle. We also note that the flame front is moving at a speed of $10.5 - 5 = 5.5$ m/s relative to the ground, against the wind direction.

7.4 RECOMMENDATIONS

With a view to providing better guidance for future LNG fire research and delineating the important information to be gathered we make the following recommendations.

1. Better spectral data on large LNG fires should be measured. This should include the following:
 - The spectrometer should be located as close as possible to the fire to minimize the absorption effects in the atmosphere. If necessary a nitrogen flushed optical system (which may involve providing a cooled pipe to almost the fire surface) should be considered.
 - The spectrometer should be provided with fore-optics to minimize the off center image problems.
 - If possible, the spectral scan range should be extended to 10 μ m.
 - Fast scanning interferometers (Michelson type) should be used. A very fast scanning monochromator may also be acceptable.

Considerations should also be given to the use of expendable spectrometers ("polychromator"). These are basically filter radiometers sensitive to only certain regions of the spectrum. However, they may offer low cost data acquisition at the expense of accuracy.

2. Spectral data should be obtained from different parts of the flame along its height to see if the upper parts of the flame are significantly more radiative than lower parts. This may be achieved by simply tilting the spectrometer axis (or a mirror in front of the spectrometer) to "see" different parts of the flame.
3. Spectrometers should be utilized to confirm or refute the postulate that large visible fires may be surrounded by a blanket of hot products of combustion which do not radiate in the visible but radiate in the infrared.

It may be possible to align the spectrometer carefully during an experiment so that the field of view does not contain any visible part of the fire but contains the hot combustion products assumed to be on the outside. This could also be augmented with still or motion pictures taken with infrared film.

4. Narrow angle radiometers should be movable in a vertical plane so that the emission from different parts of the flame can be recorded.

In this series of tests the narrow angle radiometer data have been more reliable than those from wide-angle radiometers. We therefore recommend using more narrow-angle radiometers than just the two that were used in the current series.

5. Use of wide angle radiometers should be continued, however, with Zn Se (Grtan) windows. The calibration of the radiometers should be performed without and with windows.
6. Direct in situ measurements of gas concentration and composition in the middle of a pool fire (say at about 10 cm above the pool surface) should be made to see if a significant quantity of unburned fuel vapor moves up in the center of the fire.

7. Larger tests would be useful to provide more data on optically thick pool fires and may also indicate that above a certain size, the fire burns in multiple cells rather than as a single plume. It would also be interesting to confirm that the quantity of unburned fuel increases with increasing fire size.
8. The effect on a pool fire of increasing vaporization rates by jetting LNG into the water should be investigated to verify the hypothesis that this should decrease hazard zones over those predicted by a model for a spreading pool on a smooth water surface.

For future vapor cloud fire study we recommend that:

9. Laboratory scale or medium field scale tests be performed to understand the effects of small droplets of water (fog) on the turbulent flame propagation in unconfined clouds.

This series of tests indicated a significantly different behavior of the vapor cloud fire on water compared to that on land. It has been postulated that the major reason for this may be the high density of water fog particles in the vapor cloud close to the water surface.

10. The feasibility of conducting a large vapor cloud fire test on a very large body of water should be considered. It is conceivable that the fire may not spread through the cloud as rapidly on water as on land.

For both pool and vapor fire tests, further investigation of the role of heavy hydrocarbons in the radiative character of the fires would be useful in understanding variations in emissive power during the course of pool fire tests.

NOMENCLATURE

<u>SYMBOL</u>	<u>DESCRIPTION</u>	<u>EQUATION NO.</u>	<u>UNITS</u>
A	Band width	4.4	cm^{-1}
A_f	Nominal area of the emitting flame surface		m^2
C	Calibration constant	4.4	mV/W
C_1	Planck first constant = 3.74×10^{-16}	4.1	W m^2
C_2	Planck second constant = 1.4388×10^{-2}	4.1	m K
D	Diameter of pool fire	5.1	m
E	Emissive power of flame	2.5, 4.2, 6.1	kW/m^2
E_b	Black body emissive power		kW/m^2
f_v	Volume fraction of soot	2.6	-
F	View factor	2.5, 6.1	-
g	Acceleration due to gravity	6.2	m/s^2
H	Cloud height	6.2	m
H	Average height of the visible flame	5.1	m
H_λ	Spectral irradiance	4.5	$\text{W/m}^2 \mu\text{m}$
i_λ	Spectral radiance of the flame	4.5	$\text{kW/m}^2 \mu\text{m sr}$
$i_{\lambda,b}$	Spectral radiance of black body	4.5	$\text{kW m/m}^2 \text{ sr}$
$k_{s,\lambda}$	Spectral absorption coefficient for soot	2.6	m^{-1}
L_f, L	Length of visible plume of the fire		m

NOMENCLATURE CONTINUED

<u>SYMBOL</u>	<u>DESCRIPTION</u>	<u>EQUATION NO.</u>	<u>UNITS</u>
L_B	Beam length		m
\dot{m}''	Mass rate of burning per unit area	2.2	kg/m ² s
N_λ	Spectral radiance of a source at wave length λ	4.7	W/m ² sr m
p	Partial pressure of species in the fire		atm
\dot{q}''	Thermal flux at any location	5.4	W/m ²
\dot{Q}	Thermal energy radiated in unit time	2.4	W
t	Time		s
t_s	Duration of spill		s
T	Temperature		K
u, U_w	Wind speed		m/s
u^*	Nondimensional wind velocity	2.2 , 5.3	-
v	Velocity of gravity spread	6.2	m/s
V	Total volume of spill		m ³
X, X_s	Distance to the radiation emitting source	2.3, 4.4	m
\dot{y}	Total liquid regression rate	5.1	m/s

NOMENCLATURE CONTINUED

<u>SYMBOL</u>	<u>DESCRIPTION</u>	<u>EQUATION NO.</u>	<u>UNITS</u>
<u>GREEK LETTERS</u>			
α	Absorptivity of a specie		
Δ	Fractional density defect	2.8	$(1 - \frac{\rho_L}{\rho_W})$
ϵ	Emissivity		
θ	Tilt angle of the flame axis with respect to vertical caused by wind		rad
θ_{max}	Maximum semi cone angle of wide angle radiometer	5.5	
k	Wave number	$1/\lambda$	m^{-1}
λ	Wave length		m or μm
ρ	Density	6.2	kg/m^3
τ	Atmospheric transmissivity	2.5, 5.4	
τ	Also used for optical depth parameter	Fig B.3	-
τ_w	Transmissivity of radiometer window	6.1	
τ_λ	Transmissivity for wave length λ		
Δ	Band width parameter		cm^{-1}
<u>SUBSCRIPTS</u>			
a	Air		
b	Black body		
f	Flame conditions		
i	Incident, initial		
L	Liquid		

NOMENCLATURE CONTINUED

<u>SYMBOL</u>	<u>DESCRIPTION</u>	<u>EQUATION NO.</u>	<u>UNITS</u>
<u>SUBSCRIPTS</u>			
max	Pertaining to the maximum value for the parameter		
s	Soot		
S	Source		
v	Vapor		
<u>SUPERSCRIPTS</u>			
.	Represents the rate of change of parameter with respect to time.		

REFERENCES

1. Abramowitz, M. and I. A. Stegun, "Handbook of Mathematical Functions," National Bureau of Standards, Washington, D.C., 1964.
2. American Gas Association, "LNG Safety Program," Report #2 Project # IV-2-1, Report Prepared by Arthur D. Little, Inc. for the AGA, January 1971.
3. American Gas Association, "LNG Safety Program - Interim Report on Phase II Work," IS-3-1, Section II, July 1974.
4. Becker, H.A. and D. Liang, "Visible Length of Vertical Free Turbulent Diffusion Flames," Combustion and Flame, Volume 32, p. 115-137, 1978.
5. Burgess, D. and M. Hertzberg, "Radiation from Pool Fires," Heat Transfer in Flames, edited by N. H. Afgan and J. M. Beer, Scripta Book Company, Washington, D.C., 1974.
6. Burgess, D. and M. G. Zabetakis, "Fire and Explosion Hazards Associated with Liquefied Natural Gas," Report # 6099, U.S. Bureau of Mines, Pittsburgh, Pennsylvania, 1962.
7. Dalzell, W. H. and A. F. Sarofim, "Optical Constants of Soot and Their Application to Heat Flux Calculations," Journal of Heat Transfer, Volume 91, Number 1, p. 100-104, 1969.
8. de Ris, J., "Buoyant Diffusion Flames," paper presented at the International Center for Heat and Mass Transfer, Dubrovnik, Yugoslavia, August 1976.
9. de Ris, J., "Fire Radiation - A Review," paper presented at the 7th International Symposium on Combustion, University of Leeds, England, August 1978.
10. DOE, 1979 "The Feasibility of Methods and Systems for Reducing LNG Tanker Fire Hazards" partial draft report (1979, by Arthur D. Little, Inc. to Division of Environmental Control Technology, Department of Energy, under contract EP-78-C-02-4734-A000. (Report not available for distribution as the work is on going.)
11. Edwards, D. K. and A. Balakrishnan, "Thermal Radiation by Combustion Gases," International Journal of Heat and Mass Transfer, Volume 16, Number 1, p. 25-40, 1973.
12. Eggleston, L. A., W. R. Herrera, and M. D. Pish, "The use of Finely Divided Water to Reduce the Hazard Potential of Vapor Clouds," report on Project # 3-3274, Southwest Research Institute, San Antonio, Texas, March 1975.
13. Fay, J. A., "Combustion of and Radiant Heat Emission from an Ignited LNG Vapor Cloud," Exhibit #525, Direct Testimony of the Intervenor's Union of Concerned Scientists Funds, Inc.; Docket # CP-132 et al., Distrigas Corporation et al.; Federal Power Commission Hearings, 1975.

14. Fay, J. and D. H. Lewis, "Unsteady Burning of Unconfined Fuel Vapor Clouds," 16th Symposium (International) on Combustion, 1976.
15. Gaz de France, "Essais D'Ependage de Gas Naturel Liquefie Sur de Sol," Report on the Experiments (Film Section of the Report). Also see "Flammable Mixture Penetration in the Atmosphere from Spillage of LNG," 3rd International Conference on LNG, Washington, 1972, Paper 4, pp. 1-34.
16. Hardee H.C., Lee D.O., and Benedick W.B. "Thermal Hazard from LNG Fire Balls." Combustion Science and Technology, Vol. 17, p. 189-197, 1978.
17. Hottel, H. C. and A. F. Sarofim, "Radiative Transfer," McGraw-Hill, 1967, New York.
18. Hudson, Jr., R. D., "Infrared Systems Engineering," Wiley-Interscience, John Wiley & Sons, New York, 1969.
19. Kruse, P. W., L. D. McGlauchlin, and R. B. McQuistan, "Elements of Infrared Technology, Generation, Transmission, and Detection," John Wiley & Sons, Inc., New York, 1962.
20. Lawson, D. I., and D. L. Simms, "The Ignition of Wood by Radiation," British Journal of Applied Physics, 3, 288-292 (1953).
21. Markstein, G. H., "Radiative Energy Transfer from Gaseous Diffusion Flames," 15th Symp. (Intl.) on Combustion, The Combustion Institute, 1974.
22. Markstein, G. H., "Radiative Energy Transfer from Turbulent Diffusion Flames," Combustion and Flame, V. 27, pp. 51-63, 1976.
23. Markstein, G. H., "Scaling of Radiative Characteristics of Turbulent Diffusion Flames," Tech. Rep. 22361-4, RC-B-66, Factory Mutual Research Corporation, Norwood, MA, June 1976.
24. Modak, A. T., "Radiation from Products of Combustion," Tech. Rep. FOAO16.BU-1, Factory Mutual Research Corporation, Norwood, Massachusetts, October 1978.
25. Otterman, B., "Analysis of Large LNG Spills on Water, Part I: Liquid Spread and Evaporation," Cryogenics, August 1975, pp. 455-465.
26. Raj, P.K.P., "A Criterion for Classifying Accidental Spills into Instantaneous and Continuous Types," Combustion Science and Technology, in print, 1979.
27. Raj, P.K.P., "Calculation of Thermal Radiation Hazards from LNG Fires - A Review of the State of the Art," paper 2, AGA Transmission Conference, St. Louis, May 1977.

28. Raj, P.K.P. and H. Immons, "On the Burning of a Large Flammable Vapor Cloud," presented at the meeting of the Western and Central States Section of the Combustion Institute, San Antonio, Texas, 1975.
29. Raj, P.K.P. and A. S. Kalelkar, "Fire Hazard Presented by a Spreading, Burning Pool of LNG on Water," paper # 73-25, presented at the meeting of the Western States Section of the Combustion Institute, October 1973.
30. Raj, P.K.P. and A. S. Kalelkar, "Assessment Models in Support of the Hazard Assessment Handbook (CG-446-3)," Chap. 9, Technical Report Prepared for the U.S. Coast Guard, NTIS publication #AD776617, January 1977.
31. Raj, P. K., and P. O. O'Farrell, "Development of Additional Hazard Assessment Models," Report to U. S. Coast Guard, NTIS # AD-A042365, March 1977.
32. Rehn, Jr., K. C., C. M. Sliepcevich and J. E. Welker, "Radiation View Factors for Tilted Cylinders," J. Fire & Flammability, Volume 1, p. 140, April 1970.
33. Slade, D. H., editor, Meteorology and Atomic Energy 1968, U.S. Atomic Energy Commission, 1968.
34. Sparrow, F. M., "Radiant Interchange Between Surfaces Separated by Non Absorbing Media," Sec. 15, on Radiation, Handbook of Heat Transfer, Rohsenow, W. M., and J. P. Hartnett (editors), McGraw-Hill Book Company, New York, 1973.
35. Steward, F. K., "Prediction of the Height Turbulent-Diffusion Buoyant Flames," Comb. Sci. Tech., Volume 2, pp. 203-212, 1970.
36. Thomas, F. H., "The Size of Flames from Natural Fires," 9th Symposium (Int'l) on Combustion, Academic Press, New York, pp. 844-854, 1963.
37. Thomas, F. H., R. Baldwin and A. J. M. Heselden, "Buoyant Diffusion Flames: Some Measurement of Air Entrainment, Heat Transfer and Flame Merging," 10th Symposium International Combustion, pp. 983-996, 1965.
38. University Engineers, Inc., "An Experimental Study on the Mitigation of Flammable Vapor Dispersion and Fire Hazards Immediately Following LNG Spills on Land," report to American Gas Association, Project 1S-100-1, Norman, Oklahoma, February 1974.
39. Valencia-Chavez, J.A. and R. C. Reid, "The Effect of Composition on the Boiling Rates of Liquefied Natural Gas for Confined Spills on Water," LNG Research Center Report, M.I.T., Cambridge, Massachusetts, June 1978.
40. Wolfe, W. L., editor, "Handbook of Military Infrared Technology," Office of Naval Research, Department of Navy, Washington, D.C., 1965.

APPENDIX A

1. THE SCANNING MICHELSON INTERFEROMETER

The principle of operation of this spectrometer is based on a multiplexing method. Conventional spectrometers are based on turning a monochromator - using a grating or a prism as a dispersive element - through the range of interest and recording the spectrum in sequence. In a multiplex spectrometer, the whole range is observed simultaneously. Much better signal-to-noise ratios are thus obtained and this advantage can be traded for speed of measurement, thus making the instrument particularly useful for taking spectra of time-varying sources. In effect, the spectrum is scanned so fast, that the fluctuation of the source does not have time to affect the shape of the recorded spectrum.

MULTIPLEX SPECTROMETERS

The classic example of a multiplex spectrometer is the Michelson interferometer in which one of the reflectors is able to move at a steady speed or in a series of small jumps, so as to change the interferometer path difference at a uniform rate. The elementary theory of what happens is as follows:

In Figure A-1 let the incident radiation have amplitude A and wave-number $\sigma = 1/\lambda$ at the moment when it reaches the beam-splitter. The primary beam is divided into two beams, one transmitted and one reflected. After passing along the two paths the beams return to the beam-splitter, where the amplitudes recombine. Taking into account their respective phases due to the different optical lengths of their respective paths. The resultant transmitted intensity can be shown to be:

$$I(\Delta) = \left(\frac{A^2}{2}\right) (1 + \cos(2\pi\sigma\Delta)) \quad (A1)$$

where Δ is the difference in the lengths of the two paths traversed by the two beams through the interferometer.

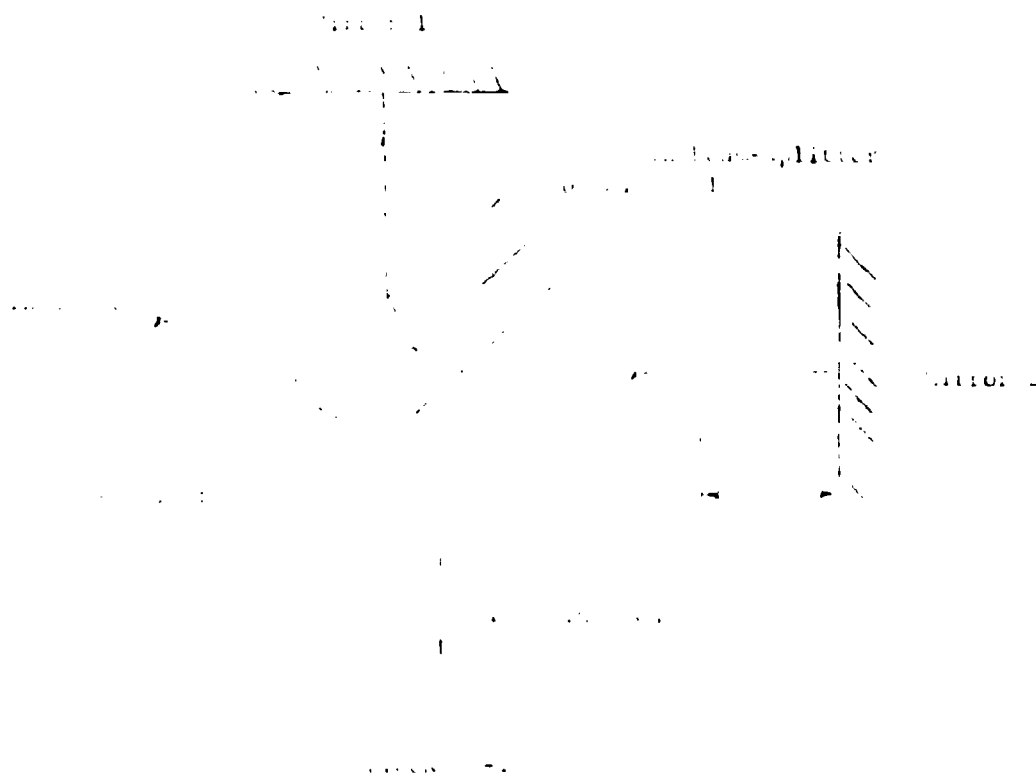


Figure A-1: Schematic Representation of a Spectrometer

Thus, the transmitted intensity varies sinusoidally with λ . The intensity and frequency of this wave are proportional to the intensity and wave-number of the incident radiation.

If the input radiation consists of a number of different wave-numbers, each with its own intensity, the output of the detector will be a number of cosine waves, each of different amplitude and period. The recording of the detector's output is called the interferogram.

This is the core of the multiplex system. Half of all the radiation passing into the instrument is collected by one detector, and the detector signal can be recorded and processed at leisure. The instrument looks at all the elements of the spectrum all the time, instead of dividing its time equally among the elements.

If there are N elements in the spectrum the instrument will show an improvement of the order of \sqrt{N} in its signal/noise ratio, as compared to a single channel spectrometer of the same optical throughput, and resolving power. This figure of \sqrt{N} is in the general case, where there is no a priori knowledge of the shape of the spectrum. The gain would be much less, for example, if the spectrum consisted of a small number of emission lines whose position was roughly known. The single channel spectrometer can skip the parts of the spectrum that are known to be empty, while the multiplex spectrometer must plod on through all the path differences from 0 to the maximum. This signal/noise advantage is termed the multiplex advantage or the Fellgett advantage.

In addition to the multiplex advantage (which only holds when detector noise is the principal source of noise in the system) the Michelson spectrometer has a large geometrical advantage in light gathering power over conventional spectrometers using prisms or gratings.

When viewing an extended source, the power collected by an optical instrument is:

$$P = N A \dots \text{(in watts)} \quad (A2)$$

where N is the radiance of the source ($\text{W/m}^2 \text{ sr}$) and $A \Omega$ is the product of area and solid angle, an invariant through the optical path from the source to the detector. This product $A \Omega$, sometimes called the throughput, is limited in a conventional spectrometer by the area of the entrance slit and by the F-number of the dispersive optics behind it. For given physical dimensions, a definite upper limit exists on the throughput limited by the size of available gratings and the aberrations of the collimating optics and for a given resolution, which defines the width of the entrance (and) exit slits.

In the Michelson interferometer, on the other hand, the collector area is limited only by the required optical precision and diameters as large as a few cms are possible. This is many times larger than the area of a typical monochromator slit. The permissible solid angle is of the same order of magnitude for a Michelson as for a conventional instrument - being governed by substantially similar considerations of optical path length and aberrations. The result is an advantage of typically a factor of 100 or more in throughput for the Michelson scanning interferometer over a conventional spectrometer.

2. CALIBRATION OF SPECTROMETER

The calibration of a spectrometer is performed by viewing the radiation from a standard black body and thereby establishing the intensity scale for the spectrometer's output.

For the spectrometer used in the experiment at NWC, the calibration in spectral intensity was done in terms of radiant intensity by viewing an uncollimated black body at 1116 K with an area of 1.99 cm^2 and located at 0.30 m (1 foot) from the aperture of the spectrometer. The spectrum of the 1116 K black body measured during the calibration procedure is shown in Figure 4.4. The spectrometer used had a 6° (full cone) angle of view. A cone of 6° angle subtends a diameter of $D = 3.2 \text{ cm}$ at 0.3048 m distance. Considering that the black body had a nominal diameter of 1.6 cm (area 1.99 cm^2) the calibration source filled about half the diameter of the field of view.

The scale factor for the spectral curve (ordinate) is determined by comparing the peak spectral radiance for the known black body and the output from the spectrometer. Using this information the actual intensity of radiation received by the spectrometer (when it was used 236 m away from the flame) is calculated. The procedure given below indicates the method of obtaining the ordinate scale for the experimental spectral results.

The spectral radiance (N_λ) of a black body radiation is given by Planck equation (Hottel and Sarofim, 1967).

$$N_\lambda = \frac{C_1}{\pi \lambda^5 \left[\exp\left(\frac{C_2}{\lambda T}\right) - 1 \right]} \quad (A3)$$

where N_λ = Spectral radiance ($\text{W/m}^2 \text{ st m}$) for a black body

λ = wave length (m)

T = temperature of black body (K)

C_1 = Planck's first constant = $3.74 \times 10^{-16} \text{ W m}^2$

C_2 = Planck's second constant = $1.4388 \times 10^{-2} \text{ m K}$

It is known that the maximum spectral radiance at any given temperature is given by:

$$N_{\lambda, \text{max}} = 4.093 \times 10^{-6} T^5 \text{ (W/m}^2 \text{ st m)} \quad (A4)$$

and the maximum intensity occurs at a wave length given by:

$$(\lambda)_{N, \text{max}} = \frac{2.8978 \times 10^{-3}}{T} \text{ (m)} \quad (A5)$$

For the 1116 K black body calibrating source, the peak spectral radiance has a value $7.085 \times 10^9 \text{ W/m}^2 \text{ st m}$, (i.e., $7.085 \text{ kW/m}^2 \text{ st } \mu\text{m}$) and this occurs at a wave length of $2.597 \times 10^{-6} \text{ m}$. The theoretical black body curve for 1116 K source is plotted on Figure 4.4 normalized to the peak intensity being represented by 0.7 apparent units.

Assuming that the spectrometer has the same calibration constant (i.e. output signal strength to input power) at all wave lengths, the signal output from the spectrometer can be related to the power input at any wave length by:

$$e = \frac{C}{N_{\lambda,s}} \frac{d\lambda}{A_s} \frac{d\Omega_1}{\tau_\lambda} \quad (A6)$$

$\underbrace{e}_{\text{Signal output (say mV)}}$	$\underbrace{C}_{\text{Instrument conversion constant (mV/W)}}$	$\underbrace{N_{\lambda,s}}_{\text{Rate of energy emitted by the source (W/m}^2 \text{ sr)}}$	$\underbrace{A_s}_{\text{Source area (m}^2 \text{)}}$	$\underbrace{d\Omega_1}_{\text{Solid angle subtended by the instrument aperture at the source (sr)}}$	$\underbrace{\tau_\lambda}_{\text{Atmospheric transmissivity between the source and the spectrometer.}}$
--	---	---	---	---	--

We note that:

$$d\Omega_1 = \frac{A_1}{X_s^2}$$

where A_1 is the spectrometer aperture area and X_s the distance between the source and the instrument aperture. From the calibration with black body source we have, by assuming the atmospheric transmissivity to be unity,

$$0.7 \text{ ordinate scale units} = CA_1 \frac{7.085 \text{ (kW/m}^2 \text{ sr } \mu\text{m)} \times d \text{ (}\mu\text{m)} \times 1.99 \times 10^{-4} \text{ (m}^2 \text{)}}{0.3048^2 \text{ (m}^2 \text{)}} \quad (A7)$$

Similarly, when the instrument is used in the field we have:

$$1.0 \text{ ordinate scale units (full scale)} = CA_1 d \frac{N_{\lambda,f}}{236^2} \quad (A8)$$

where $N_{\lambda,f}$ is the spectral radiance of the flame corresponding to the full scale. In this it is assumed that the same signal strength attenuation was maintained on the spectrometer output when exposed to the black body and when exposed to the fire. Substituting for the instrument constant CA_1 from equation A7 into equation A8 and assuming $\tau_\lambda = 1$, the apparent radiant intensity of the flame represented by the full scale reading is:

$$N_{\lambda,f} \text{ (full scale)} = \frac{7.085}{0.7} \times \left(\frac{236}{0.305} \right)^2 \times 1.99 \times 10^{-4}$$

$$= 1210 \text{ kW/sr } \mu\text{m}$$

In the course of the actual experiment, it was necessary to change the attenuation on the instrument so that the data could fit within the physical size of the plot. This was necessary because of the more than expected spectral radiance of the flame. Therefore, considering this additional attenuation, the full scale on the spectral graphs presented should be read as:

$$N_{\lambda,f} \text{ (full scale)} = 7000 \text{ kW/sr } \mu\text{m}$$

APPENDIX B
SPECTRAL CALCULATIONS

1. Calculation of the Emissive Power of the Flame Using the 4.3 μm CO_2 Band Data Received by the Spectrometer

In this part of the appendix calculations have been made to obtain the band absorptivities and band emissivities of the 4.3 μm CO_2 . Knowing the transmitted spectrum of the 4.3 μm at 236 m, the emissive power of the flame is calculated.

The general approach to the calculation of the band emissivity and absorptivity is similar to that indicated by Edwards and Balakrishnan (1973).^{*} In fact, many of the figures given in their paper are reproduced here. The following is the sequence of steps for calculating the flame emissive power.

1. Assuming a flame temperature the absorptivity of the 4.3 μm CO_2 band in the atmosphere, for 236 m path length, is calculated.
2. The energy received by the spectrometer in the 4.3 μm band is determined from the spectral data. This energy is divided by the black body energy to obtain the apparent emissivity of the band.
3. The sum of apparent emissivity and the atmospheric absorptivity gives the true band emissivity ($\epsilon_{4.3}$) at 4.3 μm band.
4. From the above emissivity the equivalent bandwidth for total absorption (Δ) is calculated at the flame temperature.
5. Using the above information the partial pressure beam length product for CO_2 is obtained.
6. Noting the CO_2 and H_2O partial pressure-beam length product and using Hottel charts, the total gas emissivity is calculated. To this is added the soot emissivity.
7. The total emissivity times the black body emissive power gives the flame emissive power.

Calculation of CO_2 Band Absorptivity in the Atmosphere

The atmosphere temperature = 300 K

^{*} The purpose of the calculation by these authors was to obtain gas emissivity given a temperature, specie composition and beam length. Our calculation is somewhat opposite of this.

Partial pressure of CO_2 in the atmosphere = $p_{\text{CO}_2} = 3.3 \times 10^{-4} \text{ atm}$
(see Table 4.1)

Total path length through the atmosphere = $L = 236 \text{ m}$

Hence, $(p_{\text{CO}_2} L)_{\text{atmosphere}} = 7.8 \times 10^{-2} \text{ atm m}$

Optical depth parameter (τ_H) for 300 K = 104
from Figure B-1 and $4.3 \mu\text{m CO}_2$

$$\tau_{H,i} = \tau_H (p_{\text{CO}_2} L)_{\text{atm}} = 7.8 \times 10^3 \quad (\text{B1})$$

In the above equation the pl. parameter should be in the units of meter atmosphere.

Value of line width parameter β from Figure B.2 for 4.3 CO_2 band = 0.3

Value of bandwidth parameter ω_0 from Table B.1 for 4.3 CO_2 band = 11.2 cm^{-1}

Now,

$$\omega(300 \text{ K}) = \omega_0 \left[\frac{300}{100} \right]^{\frac{1}{2}} = 19.1 \text{ cm}^{-1} \quad (\text{B2})$$

The equivalent pressure P_e defined by Edwards and Balakrishnan is in general equal to unity in most cases of practical applications. We now use Figure B.3, the universal band absorption curve. Corresponding to an abscissa of 7800, the ordinate on the curve $\eta = 0.3$ cannot be obtained. We therefore use the equation:

$$A^* = \ln(\eta \tau_{H,i}) + 2 - \eta \quad (\text{B3})$$

Hence $A^* = 7.16$.

Therefore, total band absorption width

$$A = A^* \omega = 136.67 \text{ cm}^{-1} \quad (\text{B4})$$

The band head for the $4.3 \mu\text{m CO}_2$ band is located at $K = 2410 \text{ cm}^{-1}$.
The spectral intensity of a black body ($i_{K,b}$) at this wave number is calculated using the formula:

TABLE F.1

EXPONENTIAL WIDE-BAND PARAMETERS

Gas	Vibrations ν_1, ν_2 (cm^{-1})	Bands $\Delta \nu, \Delta \nu_2$ "	Pressure parameters ^a		Spectral location			Band absorption parameters		
			β	γ	ν_1	ν_2	ν_0	β_0	γ_0	ν_0
					($T_0 = 1000\text{ K}$)	(cm^{-1})	(cm^{-1})	($\text{cm}^{-1}\text{gm}^{-1}$)		(cm^{-1})
1. H_2O	$m = 3$ $\nu_1 = 3652$ $\nu_2 = 1595$ $\nu_3 = 3.56$ $\nu_4 = 1$ $\nu_5 = 1$ $\nu_6 = 1$	1. Rotational								
					$1.867 \cdot 10^3 + 0.5$			5200.0*	0.14311*	28.4*
		2. 6.3μ			$8.6 \cdot 10^3 \cdot T_0^{-1} + 0.5$	1600		412	0.09427	56.4
		3. 2.7μ								
								0.19		
								2.30	0.13219	60.0
								22.40		
								3.0	0.08169	43.1
		4. 7.87μ			$1.867 \cdot 10^3 + 0.5$	5350		3.0	0.08169	43.1
		5. 3.38μ			$1.867 \cdot 10^3 + 0.5$	7250		2.5	0.11628	32.0
		10.1								
2. CO_2	$m = 3$ $\nu_1 = 1351$ $\nu_2 = 667$ $\nu_3 = 2396$ $\nu_4 = 1$ $\nu_5 = 2$ $\nu_6 = 1$	1. 15μ								
		2. 10.4μ	0.7	13		667		19.0	0.06157	12.7
		3. 9.4μ	0.8	13		960		2.47×10^{-6}	0.04017	13.4
		4. 4.3μ	0.8	13		1060		2.48×10^{-6} *	0.11888*	10.1
		5. 2.7μ	0.8	13		2410		110.0	0.24723	11.2
		10.1	0.65	13		3660		4.0	0.13341	23.5
3. CO	$m = 1$ $\nu_1 = 2143$ $\nu_2 = 1$	1. 4.7μ								
		2. 2.35μ	0.8	11		2143		20.9	0.07506	25.5
4. NO	$m = 1$ $\nu_1 = 1876$ $\nu_2 = 1$	1. 5.9μ								
		2. 1μ	0.65	10		1876		9.0	0.18050	20.0
5. SO_2	$m = 3$ $\nu_1 = 1151$ $\nu_2 = 519$ $\nu_3 = 1361$ $\nu_4 = 1$ $\nu_5 = 1$ $\nu_6 = 1$	1. 10.27μ								
		2. 8.55μ	0.7	128		519		4.22	0.05291	31.08
		3. 7.35μ	0.7	128		1151		3.674	0.05952	24.83
		4. 4.34μ	0.65	128		1361		29.97	0.49299	8.78
		5. 2.09μ	0.6	128		2350		0.423	0.47513	16.45
		10.1	0.8	128		2512		0.346	0.58937	10.91
6. CH_4	$m = 4$ $\nu_1 = 2914$ $\nu_2 = 1526$ $\nu_3 = 3020$ $\nu_4 = 1306$ $\nu_5 = 1$ $\nu_6 = 2$ $\nu_7 = 3$ $\nu_8 = 1$	1. 7.66μ								
		2. 3.31μ	0.8	13		1310		28.0	0.8698	21.0
		3. 2.37μ	0.8	13		3020		46.0	0.06923	56.0
		4. 2.7μ	0.8	13		4220		2.9	0.35429	60.0
		11.01	0.8	13		5861		0.42	0.68598	45.0

* For the rotational band of H_2O , $\nu(T) = \nu_0$ and $\gamma(T) = \gamma_0(T/T_0)^{-1}$.Otherwise ν_0 and γ_0 comply to equations (6) and (10) respectively.* Because of Fermi resonance between the ν_1 and $2\nu_2$ levels, the Ψ and Φ functions for the 1060 cm^{-1} band are to be those of the 960 cm^{-1} band, i.e. use the set of β 's for the 960 cm^{-1} band to get Ψ and Φ for either band.

Source: Edwards and Balakrishnan (1973)

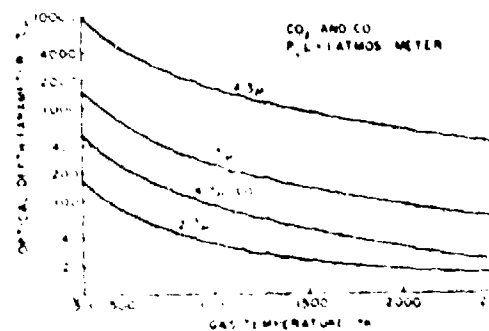
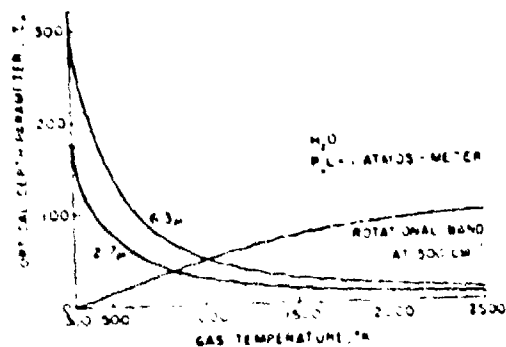


FIGURE B.1: NORMALIZED OPTICAL DEPTH PARAMETERS FOR H_2O , CO_2 , AND CO BANDS VS GAS TEMPERATURE

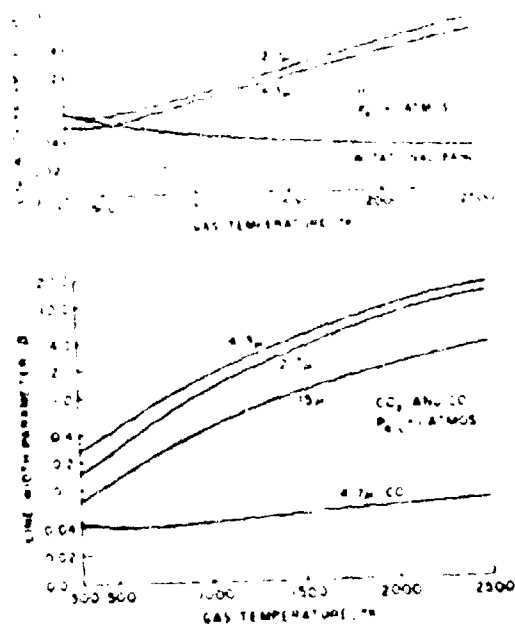


FIGURE B.2: LINDE WIDTH PARAMETER VS GAS TEMPERATURE

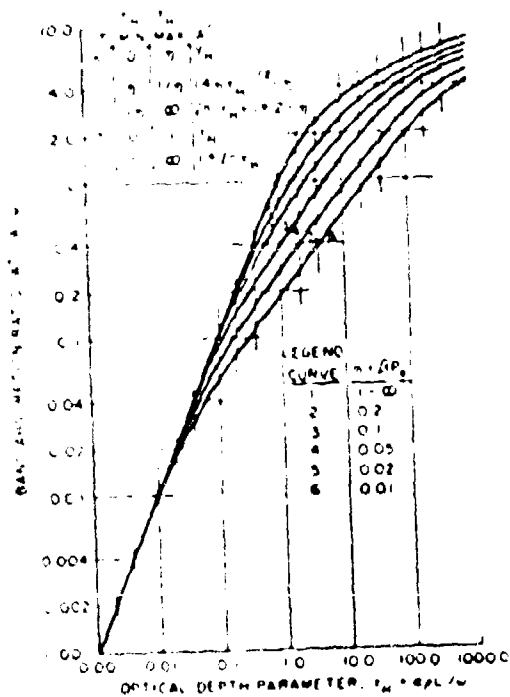


FIGURE B.3: UNIVERSAL BAND ABSORPTION CURVES

Source: Edwards and Balakrishnan (1973)

$$i_{\kappa,b} = \frac{1}{\pi} \frac{C_1 \kappa^3}{\left[\exp\left(\frac{C_2 \kappa}{T}\right) - 1 \right]} \quad (\text{kw m}^{-2} \text{ sr}) \quad (B5)$$

where κ the wave number is in m^{-1} and C_1 and C_2 are Planck's first and second constants (Hottel and Sarofim, 1967, p. 14) given by:

$$C_1 = 3.74 \times 10^{-16} \text{ w m}^2$$

$$C_2 = 1.4388 \times 10^{-2} \text{ m K}$$

Using equation B5 and the absorption bandwidth obtained from equation B4 the atmospheric absorptivity for the 4.3 CO_2 band is calculated by:

$$\alpha_{4.3} = i_{\kappa,b}(T, \kappa = 2410 \text{ cm}^{-1}) A \frac{\pi}{E_b(T)} \quad (B6)$$

where $E_b(T)$ is the black body emissive power at temperature T .

The results of these calculations for several different flame temperatures are shown in Table B.2.

Apparent Emission from CO_2 Band based on the Energy Received by the Spectrometer from 4.3 CO_2 Band

Figure B.4 shows the spectral data recorded 20 s into the burn (Scan #60). The line structure beyond about $4.7 \mu\text{m}$ is due to the water vapor absorption band (at $6.47 \mu\text{m}$). The atmospheric transmissivity over a 300 m path length, for the region beyond $4.5 \mu\text{m}$ is also shown (Ref. Wolfe, 1965, p. 253). This attenuation is caused principally by N_2O in the atmosphere up to $4.65 \mu\text{m}$ and beyond that the water vapor effect is dominant.

In order to distinguish between hot CO_2 emission (4.3) and hot H_2O emission (6.47) from the flame, we first plotted the ratio of observed spectral intensity divided by atmospheric transmissivity. The resulting spectral line is shown in Figure B.4 and titled "atmosphere absorption corrected line." The $4.3 \mu\text{m}$ CO_2 energy emitted from the flame that reaches the spectrometer is then set equal to the hatched area shown in Figure B.4. Admittedly, there is some judgment involved in assigning the proper amount of energy received to the CO_2 emission.

TABLE B.2
ATMOSPHERIC ABSORPTIVITY $\alpha_{4.3}$ FOR THE 4.3 μ CO_2 BAND FOR A PATH LENGTH OF 236 m

Assumed Flame Temperature (K)	Bandwidth Parameter at 300 K ω (cm^{-1})	Total Absorption Bandwidth A (cm^{-1})	Black Body Spectral Intensity (I_b) at $\lambda = 2410, \text{cm}^{-1}$ ($\text{kW cm}^{-2} \text{sr}$)	Total Black Body Energy Absorbed in a Unit Solid Angle ($\text{kW/m}^2 \text{sr}$)	Black Body Intensity $I_b = E_b / \pi$ ($\text{kW/m}^2 \text{sr}$)	Atmospheric Absorptivity for 4.3 μ band $\alpha_{4.3}$
1300	19.4	136.67	1.24×10^{-2}	2.28	51.55	3.29×10^{-2}
1350	19.4	136.67	1.28×10^{-2}	2.53	59.94	3.14×10^{-2}
1400	19.4	136.67	1.53×10^{-2}	2.80	69.33	3.01×10^{-2}
1500	19.4	136.67	1.83×10^{-2}	3.36	91.37	2.74×10^{-2}
1550	19.4	136.67	1.99×10^{-2}	3.66	104.17	2.61×10^{-2}
1600	19.4	136.67	2.15×10^{-2}	3.95	118.30	2.49×10^{-2}

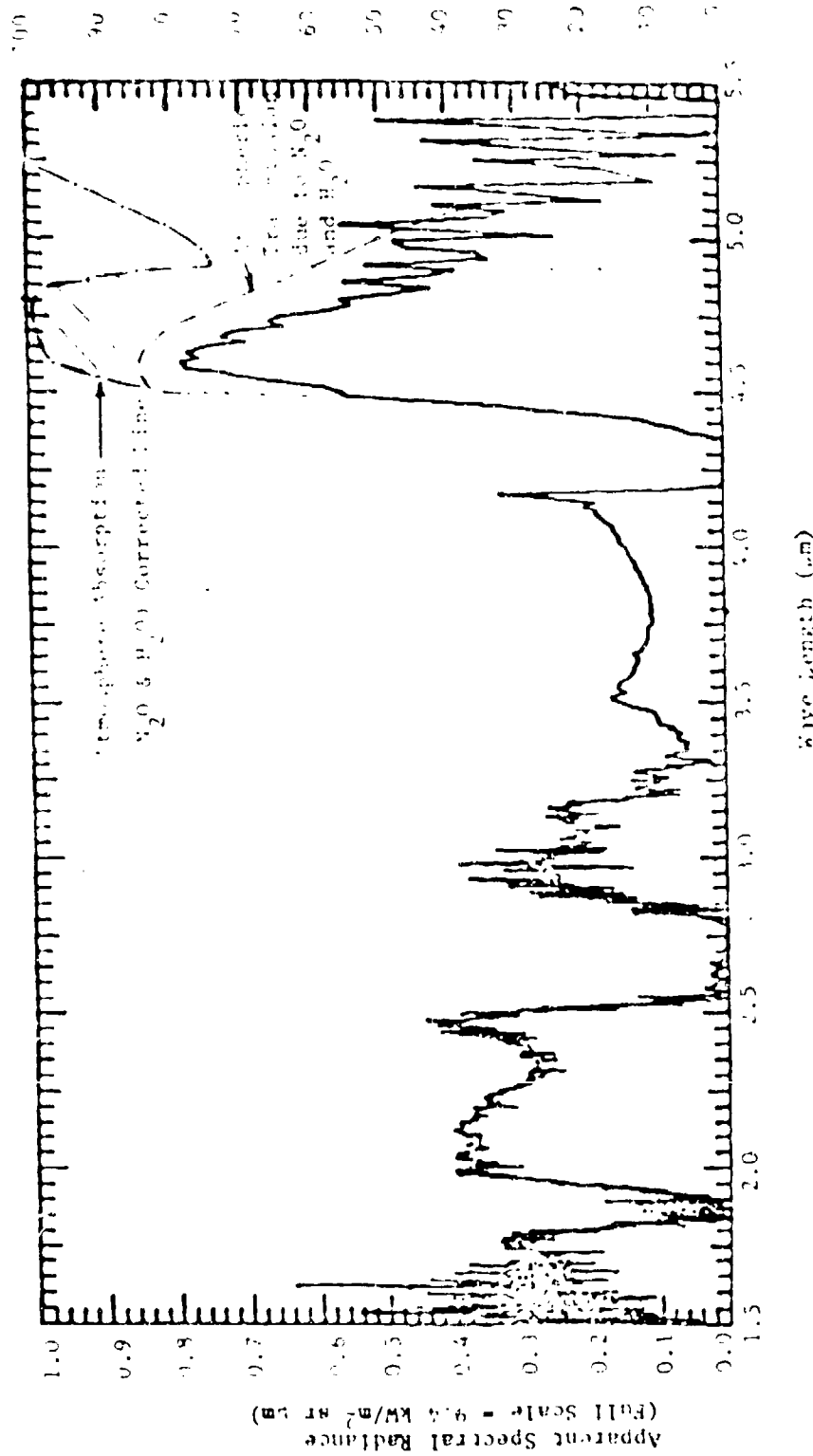


FIGURE B.4: ILLUSTRATION OF THE EVALUATION OF THE APPARENT ENERGY RADIATION FROM THE 4.3 μm CO_2 BAND

Area of hatched part of Figure B.4 = $3.8 \text{ kW/m}^2 \text{ sr}$

Therefore, total energy per unit area of flame surface emitted by $4.3 \mu\text{m}$ CO_2 band that is received by the spectrometer = $\pi \times 3.8 = 11.9 \text{ kW/m}^2$

Hence,

$$\text{Emitted energy in the } 4.3 \mu\text{m band} = \text{apparent energy emitted} + \text{energy absorbed in the band in the atmosphere} \quad (\text{B7})$$

Therefore,

$$\text{band emissivity} = \frac{\text{Apparent energy emitted per unit area}}{\text{Black body emissive power}} + \frac{\text{Atmospheric band absorptivity}}{\quad} \quad (\text{B8})$$

The result of applying equation (B8), for various flame temperatures assumed is shown in Table B.3. The methods of calculation of various parameters shown in the table are indicated below the table.

DISCUSSIONS

The calculation of the partial pressure of carbon dioxide in the flame is extremely sensitive to the value assigned to the energy received by the spectrometer in the $4.3 \mu\text{m}$ CO_2 band. This sensitivity is due to the fact that the absorption bandwidth varies as the logarithm of the optical depth in the region of our calculations. That is the partial pressure (which is proportional to the optical depth) varies exponentially with the calculated band emissivity (see Note 5 in Table B.3). Therefore, any small error that results in the estimation of energy received is amplified exponentially in the estimate of the CO_2 partial pressure. Because of this the partial pressure results should be analyzed very carefully.

The apparent emissive power of the 4.3 CO_2 band is estimated (from the energy received by the spectrometer) to be 11.9 kW/m^2 . Consider for example what this implies if the flame temperature is 1300 K. The atmospheric absorptivity is 0.0142 and therefore the band emissivity is 0.1177 (see Table B.3). This leads to a predicted CO_2 partial pressure of 4.31 atm!! Clearly this is physically unacceptable because the ambient pressure is only one atmosphere and the fire is burning in the open. In fact, the

partial pressure of CO_2 cannot be larger than the value corresponding to the stoichiometric combustion of methane and air. This value is $P_{\text{CO}_2} = 0.095$ atm. Also the amount of CO_2 that is convected into the fire by the entrained air is small. Calculations have been made with different (assumed) flame temperatures. Only in the case of flame temperature of 1500 K does the calculated CO_2 partial pressure value occur in the physically acceptable range. This temperature is close to the temperatures occurring in other hydrocarbon fuel fires (Burgess and Hertzberg, 1974).

The evaluation of flame temperature is based on the apparent radiance of the $4.3\text{ }\mu\text{m}$ CO_2 band. This is shown in Figure B.4 by a crossed area. The value of this radiance is 11.9 kW/m^2 .

There are different types of errors that may contribute to the inaccuracy in the estimation of $4.3\text{ }\mu\text{m}$ band energy emitted. These arise as a consequence of the (1) improper choice of the upper wave length for the $4.3\text{ }\mu\text{m}$ band, (2) uncertainty in the magnitude of atmospheric absorption and CO emission, (3) lack of precise knowledge of the total area of the flame which is within the view of the spectrometer.

The procedure by which the upper wave length limit of the $4.3\text{ }\mu\text{m}$ CO_2 band was determined has been described in an earlier part of this appendix. This procedure relied on the atmospheric transmissivity data obtained for 300 m path length. (The spectrometer was used at 236 m distance.) First of all, only the mean transmissivity values corresponding to wave lengths were used; whereas in the actual atmospheric transmissivity, there are significant line structures (see Wolke, 1965). Secondly, the transmissivity for a 236 m length is higher than for 300 m length. The ordinates for the line titled "Atmosphere absorption corrected line" in Figure B.4 were obtained by dividing spectrometer output by atmospheric transmissivity corresponding to 300 m path. If the correct transmissivity pertaining to 236 m path length were used, the ordinate of the atmosphere absorption corrected line will be lower and hence the estimated apparent emissive power in the

4.3 μm band will be lower. Also this correction will probably decrease the position of the upper band wave length resulting in a further reduction in the area of the hatched portion in Figure B.4 and hence a lower flame emissive power. Assuming that the absorptivity in the atmosphere is directly proportional to path length then accounting for 236 m path length rather than using the data for 300 m path length results in about 10% reduction in the apparent emissive power of the 4.3 μm CO_2 band.

The second uncertainty is the presence CO in the fire and the magnitude of its emission. CO emits relatively strongly at 4.7 μm ; however, its bandwidth is small and hence the energy emitted is small. It is conceivable that 5% to 10% of the apparent emissive power is due to CO emission but this is being interpreted as CO_2 emission because the bands overlap. There is no known way of resolving the CO and CO_2 emission from the observed data.

Finally, there is some uncertainty introduced in the calculations because of the lack of precise information on the area of the flame seen by the spectrometer. The axis of the spectrometer was aimed at 3 to 5 m above spill point. We have used for the calculations the flame area corresponding to the aim 4 m above water level. If the aim was say 5 m above, then the flame area seen by the spectrometer is about 5% higher than the nominal flame area used in our calculations. In that case, the apparent emissive power of the flame will be about 5% lower than indicated in our calculations. Secondly, we are using the visible flame area in our calculations. The spectrometer on the other hand is able to see infrared radiation from hot gases outside the flame which may not radiate in the visible. In this case also the effective flame area seen by the spectrometer is higher and hence the effective band emissive power (which power emitted per unit flame area) of the 4.3 CO_2 band will be lower.

The discussions above indicate that all of the errors, if properly accounted for tend to reduce the apparent emissive power of the 4.3 μm CO_2 band, compared to the value indicated in this appendix. In other words

* This is not necessarily a valid assumption for all wave lengths because of band absorptions.

the flame temperature consistent with physically acceptable partial pressure for CO_2 could be lower than 1500 K. It could also mean that the flame temperature is 1500 K with excess air in the fire. There is no way of obtaining, with the present data, the correct values for the flame temperature and the fraction of excess air.

The conclusion from this analysis is that the correct temperature that should be assigned to the flame is 1500 K and the CO_2 partial pressure estimated at this temperature is equal to the stoichiometric value (0.095 atm). The use of spectral data to obtain information more precisely than the above results cannot be accomplished.

2. Calculation of Total Radiant Energy Received at the Position of a Specific Radiometer Using the Characteristics of the Flame Determined by Spectral Data

In the first part of this appendix the emissivity of the flame in the $4.3 \mu\text{m}$ CO_2 band is calculated. From this is inferred the partial pressure length product for CO_2 and also for H_2O . Assuming these to represent the real situation in the flame and assuming a flame temperature of 1500 K, the radiant flux received by a specified wide-angle radiometer is calculated. This calculated energy is compared with the radiant flux actually measured by the radiometer. The procedure for performing these sets of calculations is indicated below.

The calculation procedure consists of the following steps:

1. Calculation of effective path length for radiant energy between the flame and radiometer. Then using the atmospheric conditions, obtaining the partial pressure length product for H_2O and CO_2 in the atmosphere.

2. Calculation of band emissivities of various bands of CO_2 and H_2O in the flame for the given flame temperature and partial pressure length product values for the two species.
3. From the atmospheric path length and temperature, the band absorptivities for different H_2O and CO_2 bands are calculated.
4. The view factor between the flame and the radiometer is calculated.
5. The total energy received by the radiometer is equal to the sum of individual band emissivity less the atmospheric absorptivity multiplied by the black body emissive power and the view factor. To this is added the soot emission which is assumed to go through the atmosphere unattenuated.

The calculation procedure is illustrated for a wide-angle radiometer located at 40 m from the center of the spill. The following conditions and parameters are assumed:

1. Test # 5
2. Atmospheric conditions
 - Temperature = 21°C
 - Relative Humidity = 54%
3. Mean flame height (see Figure 5.12) = 65 m
4. Steady state flame diameter = 13 m
(see Figure 5.5)
5. Luminous soot temperature = 1500 K
6. Emissivity of soot (Table 4.4) ϵ_s = 0.74
7. Partial pressure length product within the flame (Table 4.6)

}	$(\text{PL})_{\text{H}_2\text{O}}$	= 1.83 atm m
	$(\text{PL})_{\text{CO}_2}$	= 0.914 atm m

Calculation of Mean Path Length Through the Atmosphere

The wide-angle radiometer is located close to the ground level about 3 m above the base level of the fire. Because of this it receives a larger fraction of energy from the lower portions of the flame. The energy emitted by the lower flame regions travels through a shorter

distance through the atmosphere before reaching the radiometer compared to the longer distance for the energy emitted from the top of the flame. The absorption in the atmosphere being dependent on the path length of travel, the mean absorption depends on a energy weighted travel path. This mean travel path can be determined approximately by the formula:

$$\bar{X} = \frac{\sum X f}{\sum f} \quad (B9)$$

where f is the fraction of energy received by the radiometer from the flame surface at distance X . (Implicit in the above equation is the assumption that absorptivity in the atmosphere is proportional to path length.) Now:

$$f \propto \frac{\cos^2 \theta}{X^2} \quad (B10)$$

where θ is the angle between the line joining the radiometer element and an area on the flame surface and the normal to the radiometer element (which is assumed to be vertical as also is the axis of the flame).

For our calculation purposes we divide the flame into 3 parts: the base, the middle, and the top. The various path lengths and the angles are calculated to give:

Distance from the radiometer to the nearest flame surface = 33.5 m

Distance from the radiometer to the flame surface at mid-height = 46.7 m

Distance from the radiometer to the flame surface at the top = 73 m

The angles between horizontal and the lines joining the top of the flame and middle of the flame with the radiometer are respectively 44.1° and 62.73° . Hence,

$$\bar{X} = \frac{\sum \frac{\cos^2 \theta}{X}}{\sum \frac{\cos^2 \theta}{X^2}} \quad (B11)$$

$$\bar{X} = \frac{\frac{1}{33.5} + \frac{0.52}{46.7} + \frac{0.21}{73}}{\left(\frac{1}{33.5}\right)^2 + \frac{0.52}{46.7^2} + \frac{0.21}{73^2}} = 37.5 \text{ m} \quad (B12)$$

Atmospheric Partial Pressures

Saturated water vapor pressure at 21 °C	$= 2.52 \times 10^{-2} \text{ atm}$
Actual water vapor pressure at 54% relative humidity	$= 0.54 \times 2.52 \times 10^{-2}$ $= 1.36 \times 10^{-2} \text{ atm}$
Partial pressure of CO_2	$= 3 \times 10^{-4} \text{ atm}$
Hence, $(P)_{\text{H}_2\text{O}}$ in the atmosphere	$= 1.36 \times 10^{-2} \times 60$ $= 0.816 \text{ atm m}$
$(P)_{\text{CO}_2}$ in the atmosphere	$= 0.018 \text{ atm m}$

Band Emissivities and Absorptivities

The band emissivities and absorptivities are calculated for various (important) bands of H_2O and CO_2 by the method indicated by Edwards and Balakrishnan (1973). Complete details are not given. The results for important bands are shown in Table B-4.

View Factor

The view factor between a cylindrical flame of height 65 m and diameter 13 m and a vertical element on the ground at 40 m from the center is calculated using the formula presented in the paper by Raj (1977, Appendix).

$$F_v \left(\frac{H}{R} = 10, \frac{S}{R} = 6.15 \right) = 0.0774$$

Black body emissive power at 1500 K = 287.0 kW/m²
(E_b)

Hence, the total thermal flux received by the radiometer is given by:

$$\dot{q}'' = E_b F [\epsilon_s + \sum \epsilon_\lambda - \sum \alpha_\lambda] \quad (\text{B11})$$

$$= 287.0 \times 0.0774 (0.14 + 0.449^\dagger - 0.203^*)$$

$$= 8.58 \text{ kW/m}^2$$

If Hottel charts are used instead of the above band wise calculation, the estimated value of heat flux at the position of the radiometer is:

$$\dot{q}'' = 9.9 \text{ kW/m}^2$$

† Using Hottel charts this value is found to be 0.47.

* Using Hottel charts this value is found to be 0.165.

TABLE 2.4

CALCULATION OF SPECTRAL EMISSIVITY OF FLAME IN SEVERAL BANDS
AND THEIR ABSORPTION IN 37.5 m ATMOSPHERE

Emitting or Absorbing Species	Band Wavelength (μ m)	Band Location in Wave Number (cm^{-1})	Flame Species		Atmospheric Species		Remarks
			Black Body Spectral Radiance ($\text{W m}^{-2} \text{m}^{-1} \text{sr}^{-1}$)	Absorption (cm^{-1}) A	Spectral Emissivity (cm^{-1}) A	Absorption (cm^{-1}) A	
H_2O	Rotational band	0.055 μm 18181	-	419	0.027	0	Black body Emissive Power at 1500 K = 287 W/m^2
	6.3	15900	1.34×10^{-2}	973.4	0.141	457	22.10
	2.7	3760	1.77×10^{-2}	883.3	0.173	446	24.40
	1.87	5350	1.08×10^{-2}	323.9	0.038	210.6	3.73
	13	667	3.94×10^{-3}	419.3	0.018 overlap	61.5	- 0.57
CO_2	4.3	2310	1.83×10^{-2}	347.6	0.07	111.4	13.78
	2.7	3660	1.80×10^{-2}	393.4	0.078 overlap	52.4	-

NOTE: Total band emissivity of the flame

Total band absorptivity in the 37.5 m atmosphere

Flame Temperature = 1500 K

(pL) H_2O : flame = 2.47 atm m

(pL) CO_2 : flame = 1.233 atm m

0.203

Atmospheric temperature = 293 K

(pL) H_2O : Atmosphere = 0.816 atm m

(pL) CO_2 : Atmosphere = 0.018 atm m

APPENDIX C
DEFINITIONS OF COMMON TERMS AND
VALUES OF CONSTANTS OCCURRING IN
RADIATIVE TRANSFER CALCULATIONS

It is unfortunate that there exist differences between the terminologies used by Engineers, Physicists and Spectroscopists to denote an identical physical quantity. We have followed, perhaps because of our engineering background the definitions encountered in engineering radiative transfer analyses. However, we felt that a comparative table indicating the differences in terminology was essential. This is given in Table C-1.

The engineering terms and symbols are taken from the book by Hottel and Sarofim (1967). The terms used by Spectroscopists and Physicists is taken from the Handbook of Military Infrared Technology (Editor, Wolfe, 1965). The latter are based on the recommendations of the Working Group on Infrared Backgrounds.*

The common constants used in radiative transfer are indicated in Table C-2.

*Report of the Working Group on Infrared Backgrounds, Part II, "Concepts and Units for the Presentation of Infrared Background Information," Report #2389-3 S. The University of Michigan, Ann Arbor, Michigan, 1956, AD123-007.

TABLE 1
DEFINITION OF TERMS USED IN RADIATION TRANSFER

No.	Physical Quantity	Units	Engineers' Terminology	Symbol	Spectroscopists' Terminology	Symbol
1.	Radiant Energy contained in a Unit Volume of Space	W/m^3	Energy Density	u	Radiant energy density	u
2.	Energy Radiated by a Source in Unit Time	W	Radiant Power	Q_R	Radiant Power	P
3.	Energy Radiated per Unit Time per Unit Normal Area	W/m^2	Emissive Power	E	Radiant Emittance	W
4.	Energy Incident normally upon a Surface in Unit Time	W/m^2	Incident Flux	q	Irradiance	H
5.	Energy Radiated per Unit Time from a point Source into a Unit Solid Angle	W/sr	---	---	Radiant intensity	J
6.	Energy Radiated per Unit Time normal to a unit area in a unit Solid Angle	$\text{W/m}^2\text{sr}$	Intensity (emitted)	I	Radiance	N

(TABLE C-1) (Cont'd)
 DEFINITION OF TERMS USED IN RADIATIVE TRANSFER

No.	Physical Quantity	Units	Engineers' Terminology Name	Symbol	Spectroscopists' Terminology Name	Symbol
7.	Radiant Energy emitted per Unit Time in Unit Wave Length Interval	W/m	---	---	Spectral Radiant Power	P_λ
8.	Rate of Energy emitted per Unit Time, Unit Normal Area in Unit Wave Length Interval	W/m ²	Monochromatic Emissive Power	E_λ	Spectral Radiant Emittance	M_λ
9.	Radiant Energy Incident normally upon a Unit Area in Unit Time and contained within a Unit Wave Length Interval	W/m ²	---	---	Spectral Irradiance	H_λ
10.	Radiant Energy emitted by a point source in Unit Time in a Unit Solid Angle in a Unit Wave Length Interval	W/sr m	---	---	Spectral Radiant Intensity	J_λ
11.	Energy emitted Per Unit Area per Unit Time in a Unit Solid Angle and in Unit Wave Length Interval	W/m ² sr m	Monochromatic Intensity	I_λ	Spectral Radiance	L_λ

TABLE C.2

SOME COMMON CONSTANTS USED IN RADIATIVE TRANSFER CALCULATIONS

No.	Name of the Constant	Symbol	Value	Units	Remarks
1.	Stefan Boltzmann Constant	σ	5.669×10^{-8}	$\text{W/m}^2\text{K}^4$	
2.	Planck Constant	h	6.626×10^{-34}	J s	
3.	Planck First Constant	C_1	3.74×10^{-16}	W m^2	(see equation
4.	Planck Second Constant	C_2	1.4388×10^{-2}	m K	(A3
5.	Boltzmann Constant	k	1.3806×10^{-23}	J/K	
6.	Velocity of Light in vacuo	c	2.998×10^8	m/s	

APPENDIX D

1. RADIOMETER CALIBRATION DATA

Six radiometers were used in LNG tests 1 through 11 and seven radiometers were used in LNG tests 12 through 17. Two of these are narrow-angle radiometers and the remaining are wide-angle radiometers. The radiometers are identified by their serial numbers.

All the narrow-angle radiometers were calibrated with sapphire windows and were used with sapphire windows. The wide-angle radiometers were calibrated without windows, but were used with different types of windows. The location of the radiometers and the type of windows with which they were used in each experiment are indicated in Tables 5-4 and 6-4.

The radiometers were calibrated with a black body of known temperature. To obtain low irradiance, the temperature of the black body was decreased. In the following pages are given the calibration plots of the radiometers. Indicated in each plot are the radiometer identification number and the date of calibration. These calibration plots are used in determining the incident thermal flux outside the radiometer window.

CERTIFICATE OF CALIBRATION

DATE 8-10-78

CUSTOMER Naval Weapons Ctr

P. O. NO. N60530-78-W-1867

INST TYPE Radiometer

MODEL R-8015-CX-15-120

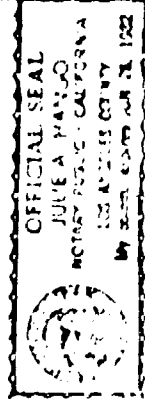
ABSORPTIVITY 0.99

CERTIFIED RECORD OF CALIBRATION
DATA IN THE INSTRUMENT ASSIGNED
SERIAL NO. 10000 WAS OBTAINED IN
AT CAL ENGINEERING'S THERMAL FLUX
FACILITY

REFERENCE STANDARD 10069

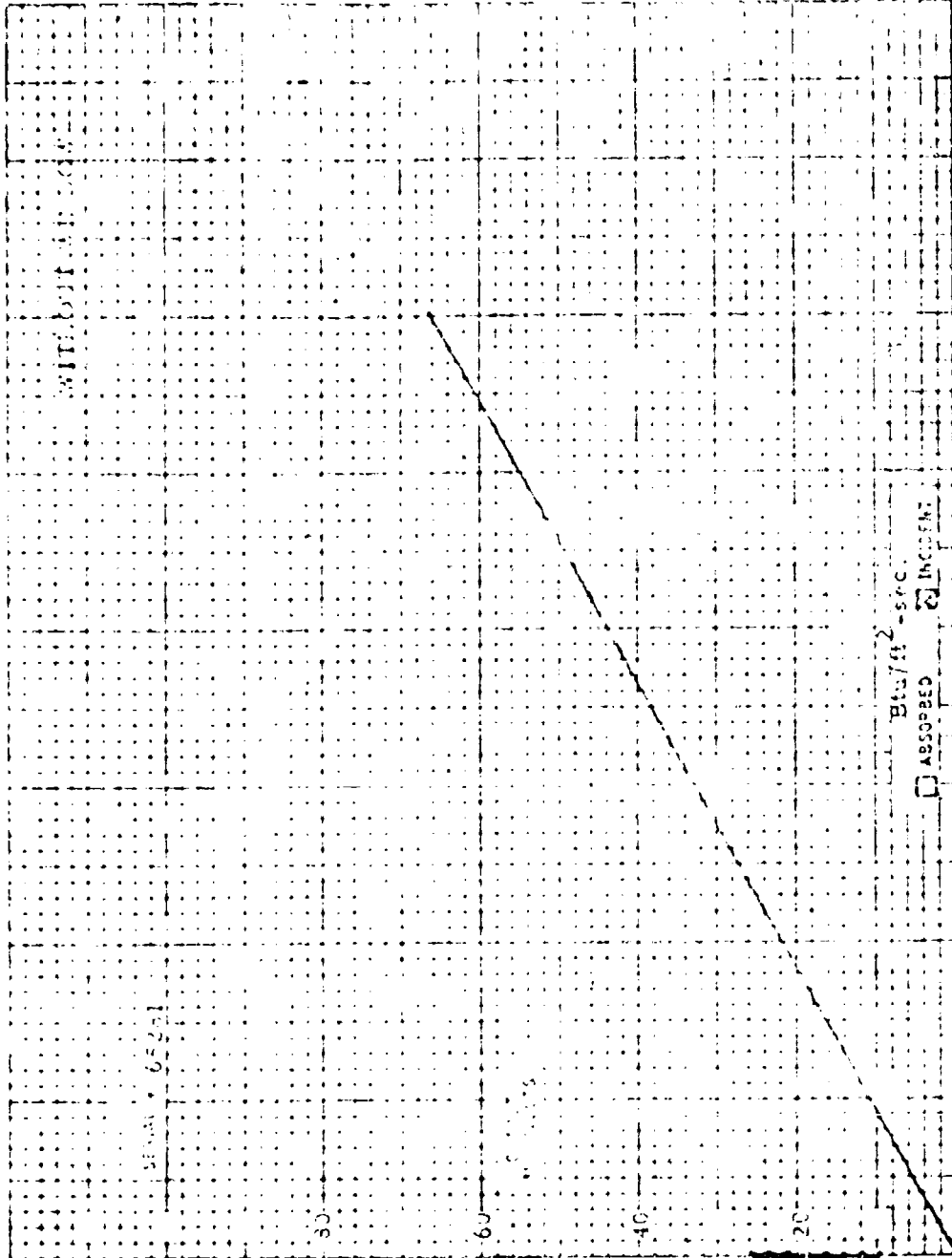
TESTED BY J. H. J.

QC APPROVAL [Signature]



SUBMITTED AND JUDGED TO
BEFORE ME THIS 10th DAY
OF August 19 78

[Signature]



ASAP/92 - SPC

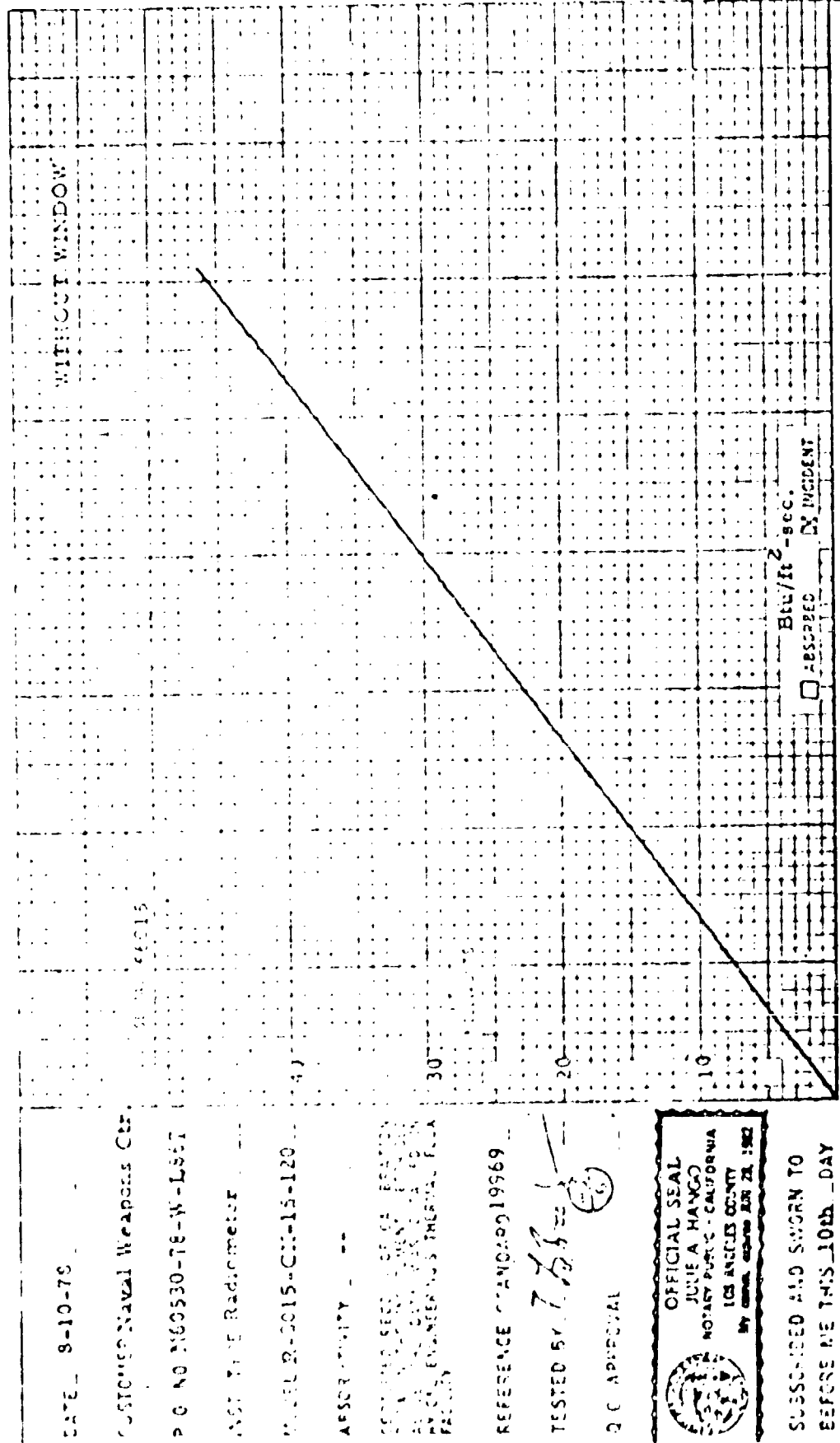
☐ ABSORBED ☒ INCIDENT

P. 1

THE THERMISTOR BECOMES
 MORE SENSITIVE TO TEMPERATURE
 AS THE TEMPERATURE DECREASES

CERTIFICATE OF CALIBRATION

Red 2.



DATE 8-10-78

CUSTOMER Naval Weapons Ctr.

P.O. NO. N60530-78-W-L567

MODEL R-2015-CR-15-120

ASSEMBLY --

CONTAINING SEVEN (7) OF SEVENTEEN (17) THERMISTORS
 IN A SINGLE PACKAGE. THE THERMISTORS
 ARE CALIBRATED AT THE THERMAL FLUX
 FACILITY.

REFERENCE CHANGING 19969

TESTED BY 7.53

QC APPROVAL

OFFICIAL SEAL
 JUDIE A. HANCO
 NOTARY PUBLIC - CALIFORNIA
 LOS ANGELES COUNTY
 My Comm. Expires JAN 28, 1982

SUBSCRIBED AND SWORN TO
 BEFORE ME THIS 10th DAY
 OF August 19 78

Judie A. Hanco

CERTIFICATE OF CALIBRATION

DATE 3-21-78

CUSTOMER Naval Weapons Ctr

P O NO 560530-78-W-L345

INST TYPE Radiometer

MODEL R-8015-C-115-130

ACCURACY --

TESTED BY [Signature]

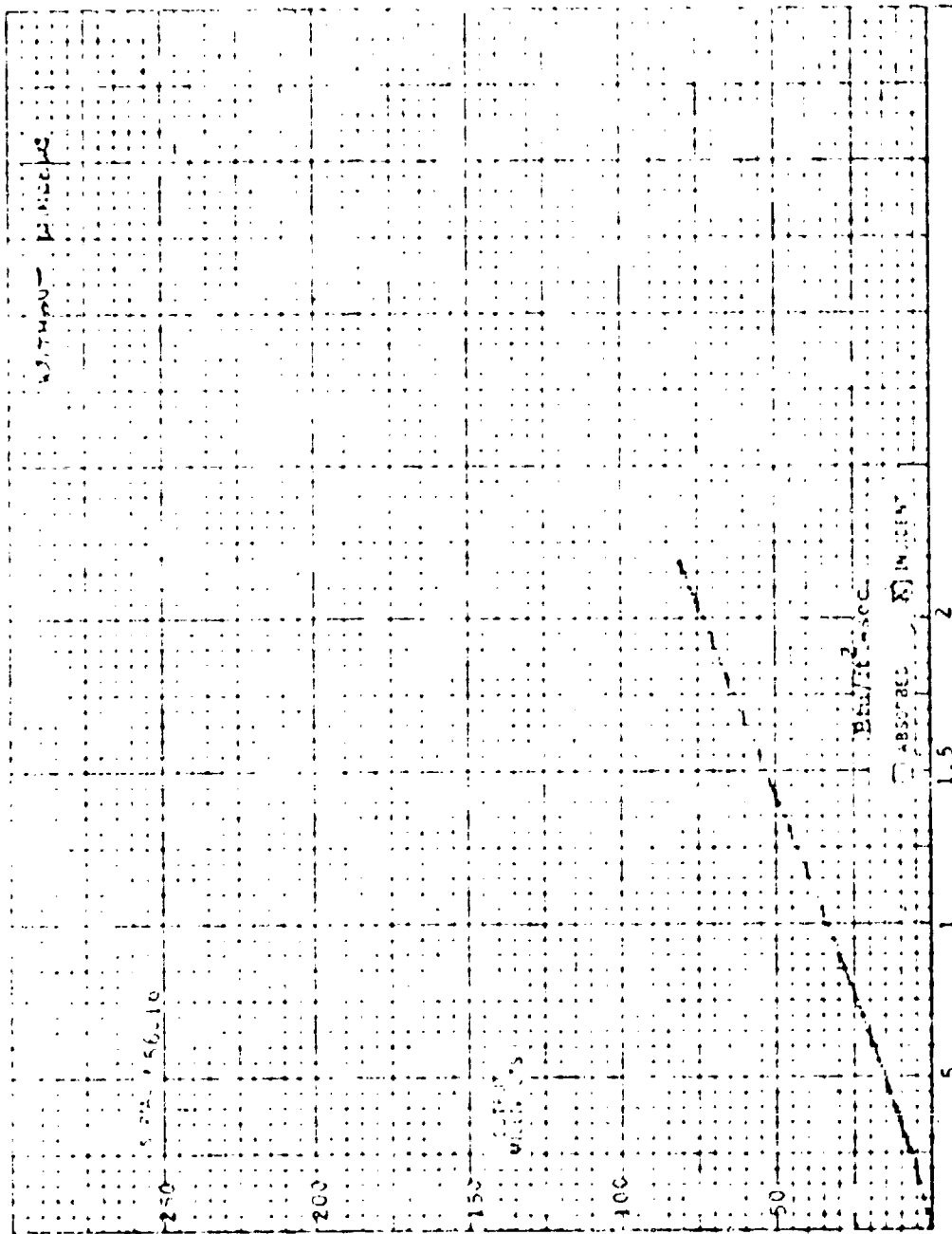
REFERENCE STANDARD 19969

TESTED BY [Signature]

Q C APPROVAL [Signature]

ENCLOSURE (1)

SUBSCRIBED AND SWORN TO
BEFORE ME THIS 21st DAY
OF March 1978



THE CALIBRATION SOCIETY OF AMERICA

(This form is to be filled out by the user of the instrument being calibrated.)

CERTIFICATE OF CALIBRATION

DATE 8-10-78
 CUSTOMER'S NAME Naval Weapons Lab
 P O NO N60530-74-W-LS67
 INSTRUMENT Radio-meter
 MODEL NO. 5015-CX-15-120

ASSURANCE
 CERTIFICATE OF CALIBRATION
 GIVEN ON THE 10th DAY OF August
 1978 AT Los Angeles, California
 BY James H. H. H.
 PRESIDENT, CALIBRATION SOCIETY OF AMERICA

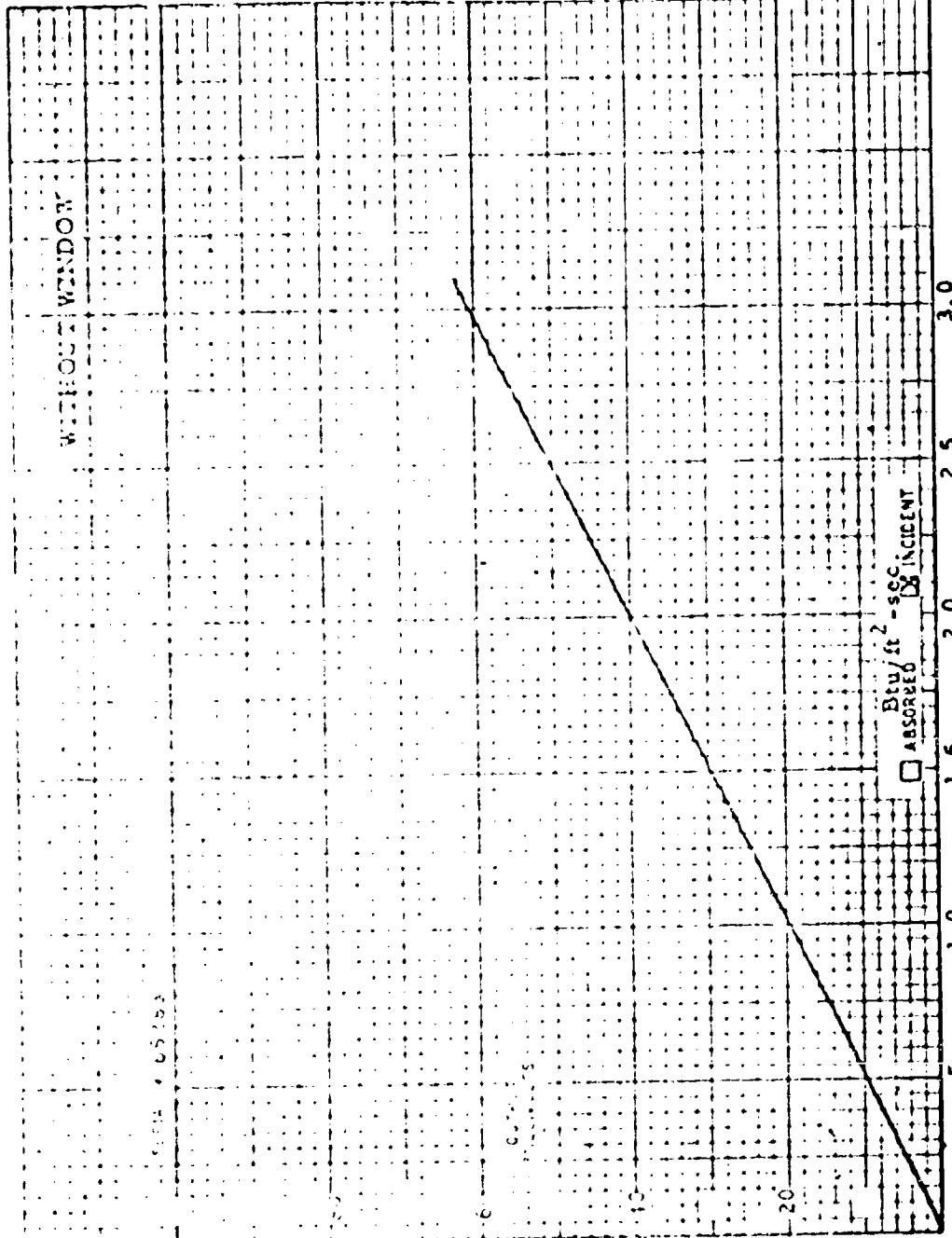
REFERENCE STANDARD 1969

TESTED BY J. H. H.

Q C APPROVAL [Signature]

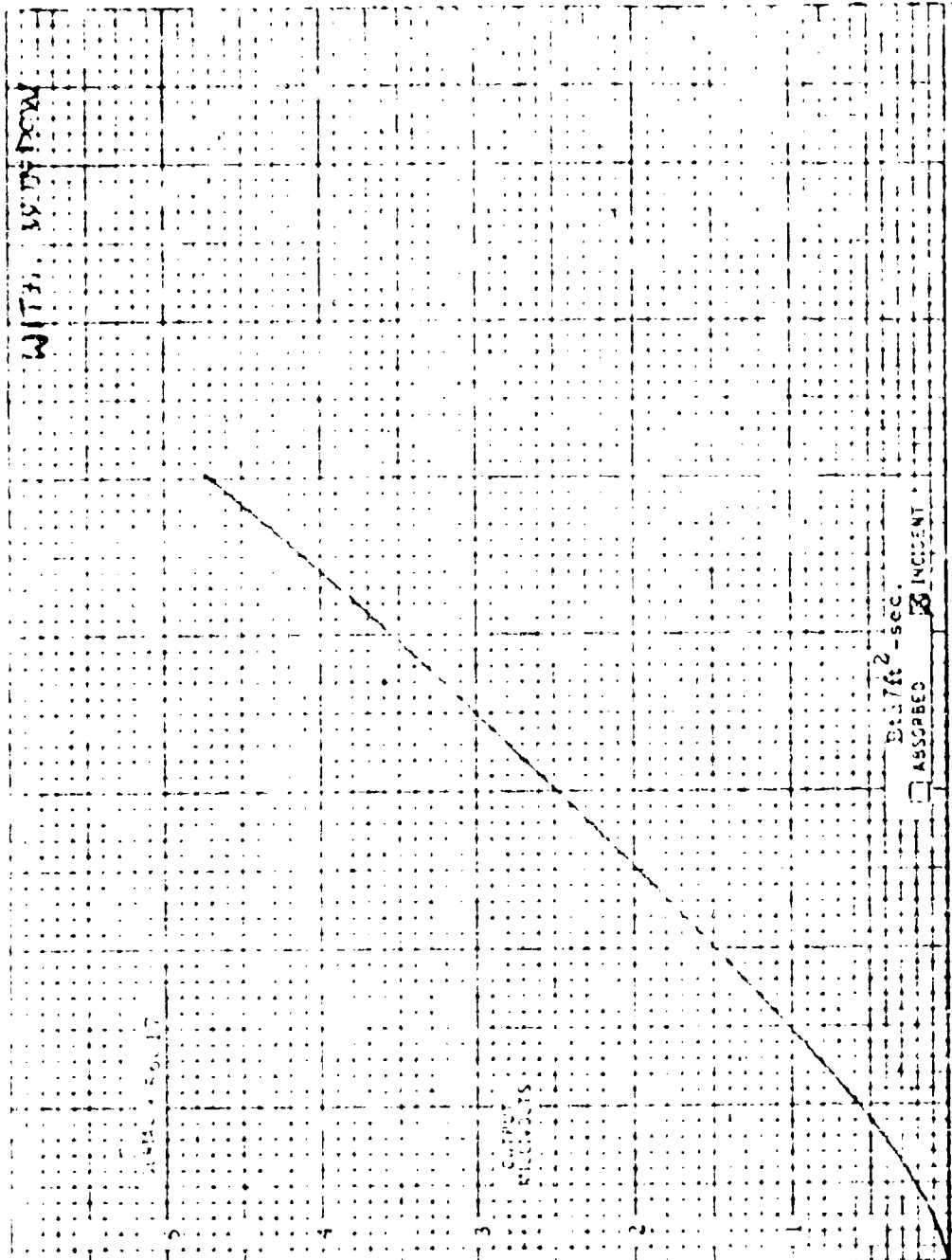
OFFICIAL SEAL
 JAMES H. H. H.
 NOTARY PUBLIC - CALIFORNIA
 LOS ANGELES COUNTY
 My Comm. Expires Jan 28, 1982

SUBSCRIBED AND SWORN TO
 BEFORE ME THIS 10th DAY
 OF August 19 78
James H. H. H.



CERTIFICATE OF CALIBRATION

FORM 502 ADV
 10-10-78
 10-10-78



DATE 8-10-78

CUSTOMER Naval Weapons Ctr

P.O. NO N60530-73-W-L867

INST TYPE Radiometer

MODEL R-8101-B-30-120

ABSORPTIVITY --

CERTIFIED RECORD OF CALIBRATION
 MADE ON THE INSTRUMENT DESCRIBED
 ABOVE. THE DATA HAS BEEN OBTAINED IN
 ACCORDANCE WITH THE THERMAL FLUX
 FACTORY.

REFERENCE STANDARD 9791

TESTED BY T. S. S. S.

Q.C. APPROVAL

OFFICIAL SEAL
 JUDITH A. HANCOCK
 NOTARY PUBLIC - CALIFORNIA
 LOS ANGELES COUNTY
 MY COM. EXPIRES JAN 21, 1982

SUBSCRIBED AND SWORN TO
 BEFORE ME THIS 10th DAY
 OF August 19 78

CERTIFICATE OF CALIBRATION

DATE 8-10-75

CUSTOMER Naval Weapons Ctr.

P.O. NO. 160510-74-N-1967

ITEM Radio Meter

MODEL R-6101-B-30-120

ASSOCIATION ---

CERTIFICATE RECORD OF CALIBRATION
 THIS CERTIFICATE IS VALID FOR THE
 PERIOD OF 12 MONTHS FROM THE DATE OF
 CALIBRATION. IT IS THE POLICY OF THE
 CALIBRATION ENGINEERING CENTER TO
 RECALIBRATE ALL INSTRUMENTS AT THE
 END OF THE CALIBRATION PERIOD.

REFERENCE STANDARD 9731

TESTED BY T. B. J.

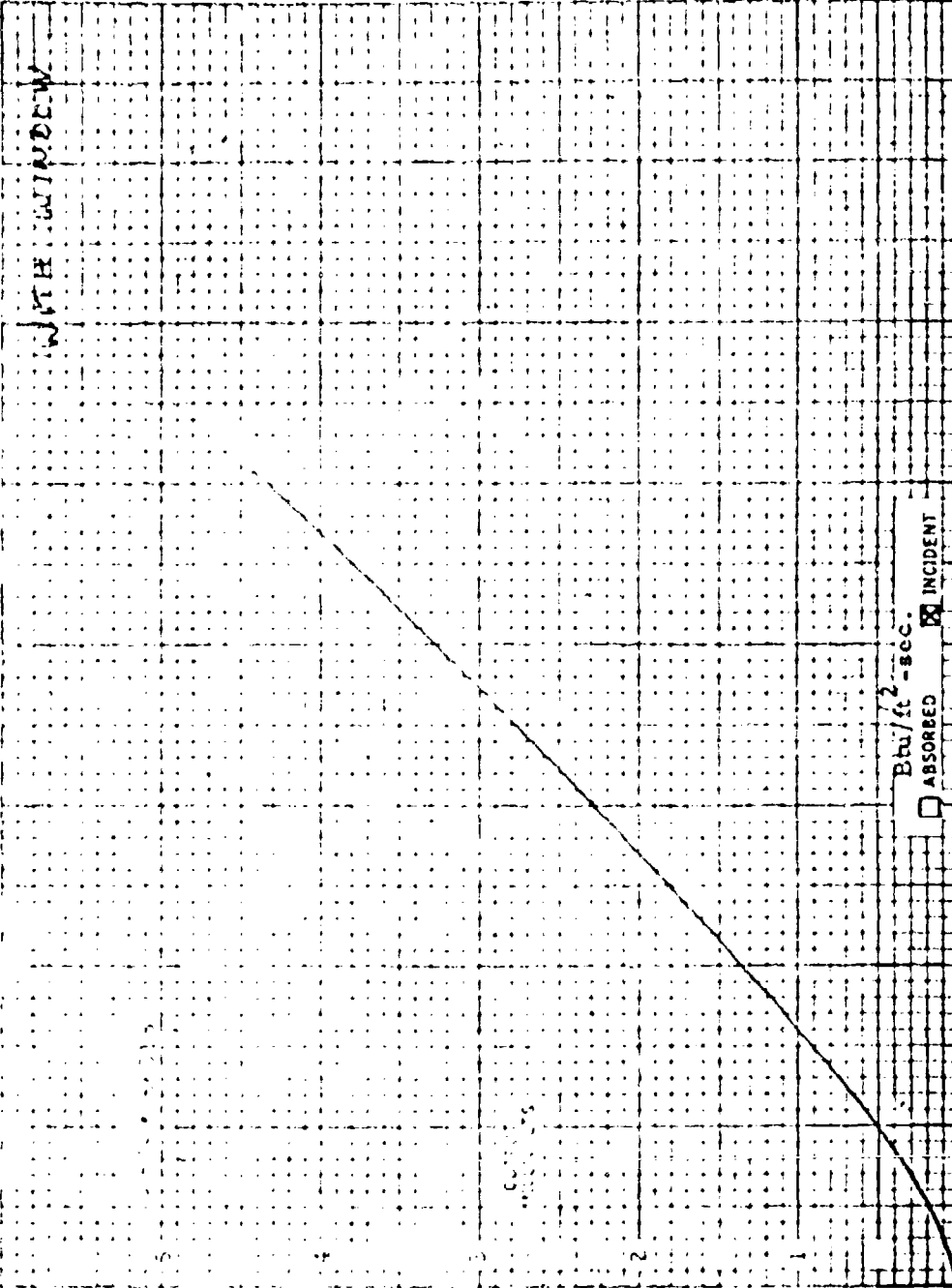
QC APPROVAL

OFFICIAL SEAL
 JULIE A. HARGO
 NOTARY PUBLIC - CALIFORNIA
 LOS ANGELES COUNTY
 MY COM. EXPIRES JAN 28, 1982

SUBSCRIBED AND SWORN TO
 BEFORE ME THIS 10th DAY
 OF August 19 78

P 8

THE FOLLOWING IS A SUMMARY
 OF THE TEST RESULTS
 FOR THE CALIBRATION
 OF THE RADIO METER
 MODEL R-6101-B-30-120
 ON 8-10-75



TH

CERTIFICATE OF CALIBRATION

DATE 8-10-78

CUSTOMER Naval Weapons Ctr.

P O NO N60530-78-W-L867

INST TYPE Radiometer

MODEL P-8015-CX-15-120

ABSORPTIVITY --

CERTIFIED RECORD OF CALIBRATION
DATE: 8-10-78
BY: J. A. HANCO
FACILITY: PHYSICAL ENGINEERING THERMAL FLUX FACILITY

REFERENCE STANDARD 10959

TESTED BY J. A. Hanco

D C APPROVAL

OFFICIAL SEAL
JUNE A. HANCO
NOTARY PUBLIC - CALIFORNIA
LOS ANGELES COUNTY
My Comm. Expires 04-27-1982

SUBSCRIBED AND SWORN TO
BEFORE ME THIS 10th DAY

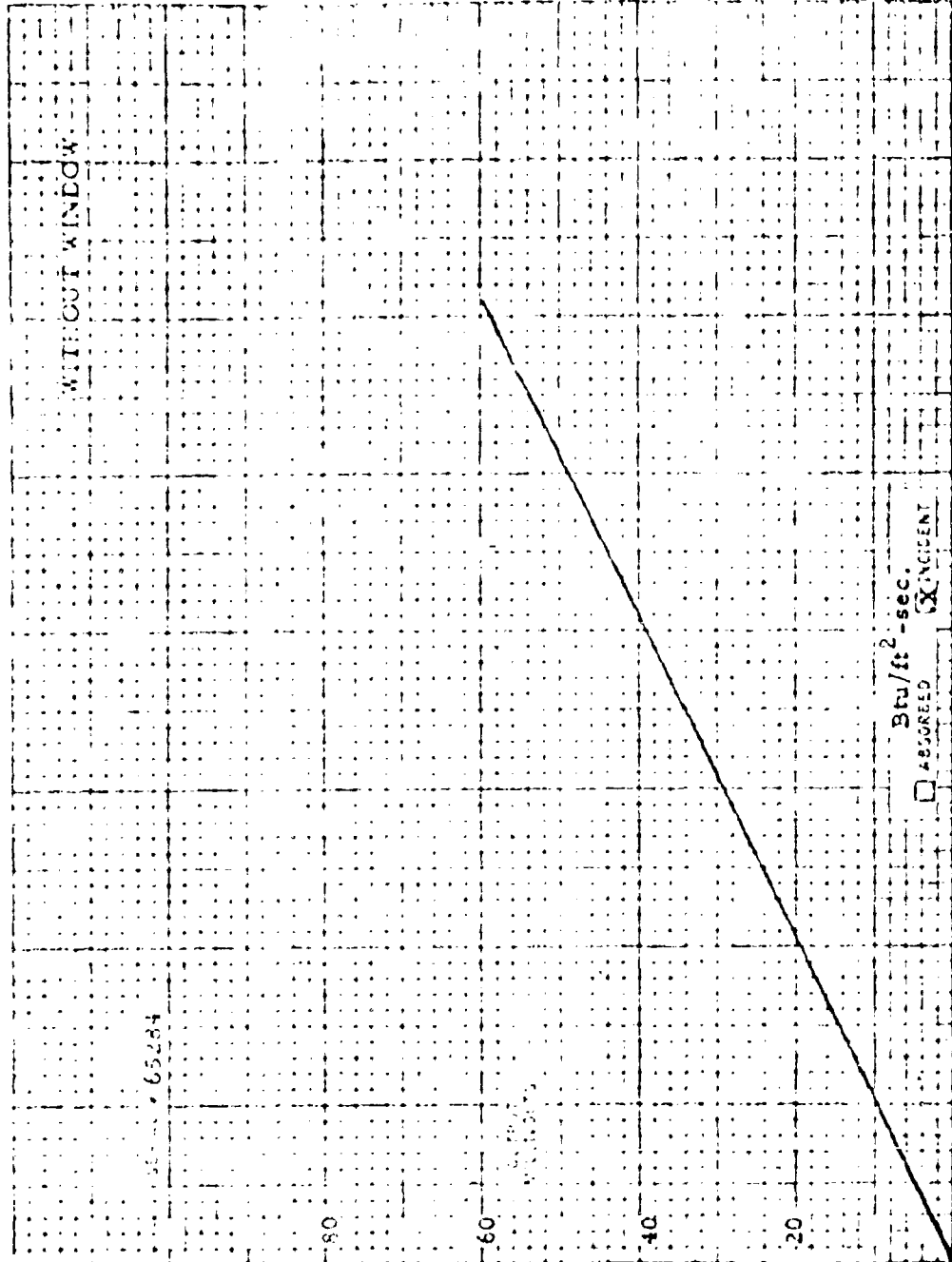
OF August 19 78

P 9

232-57

FORM 15-A THERMAL FLUX FACILITY

FORM 200 507

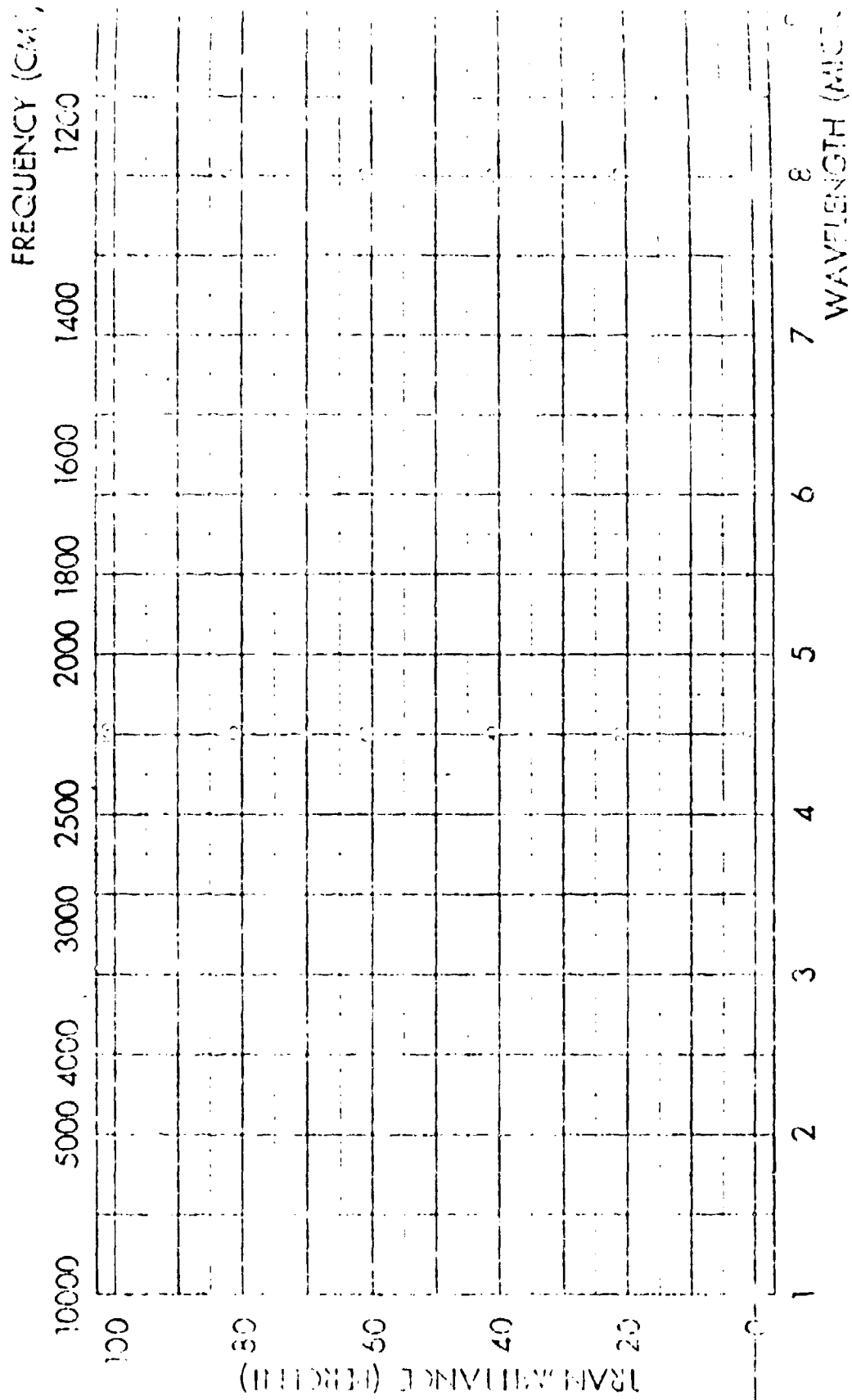


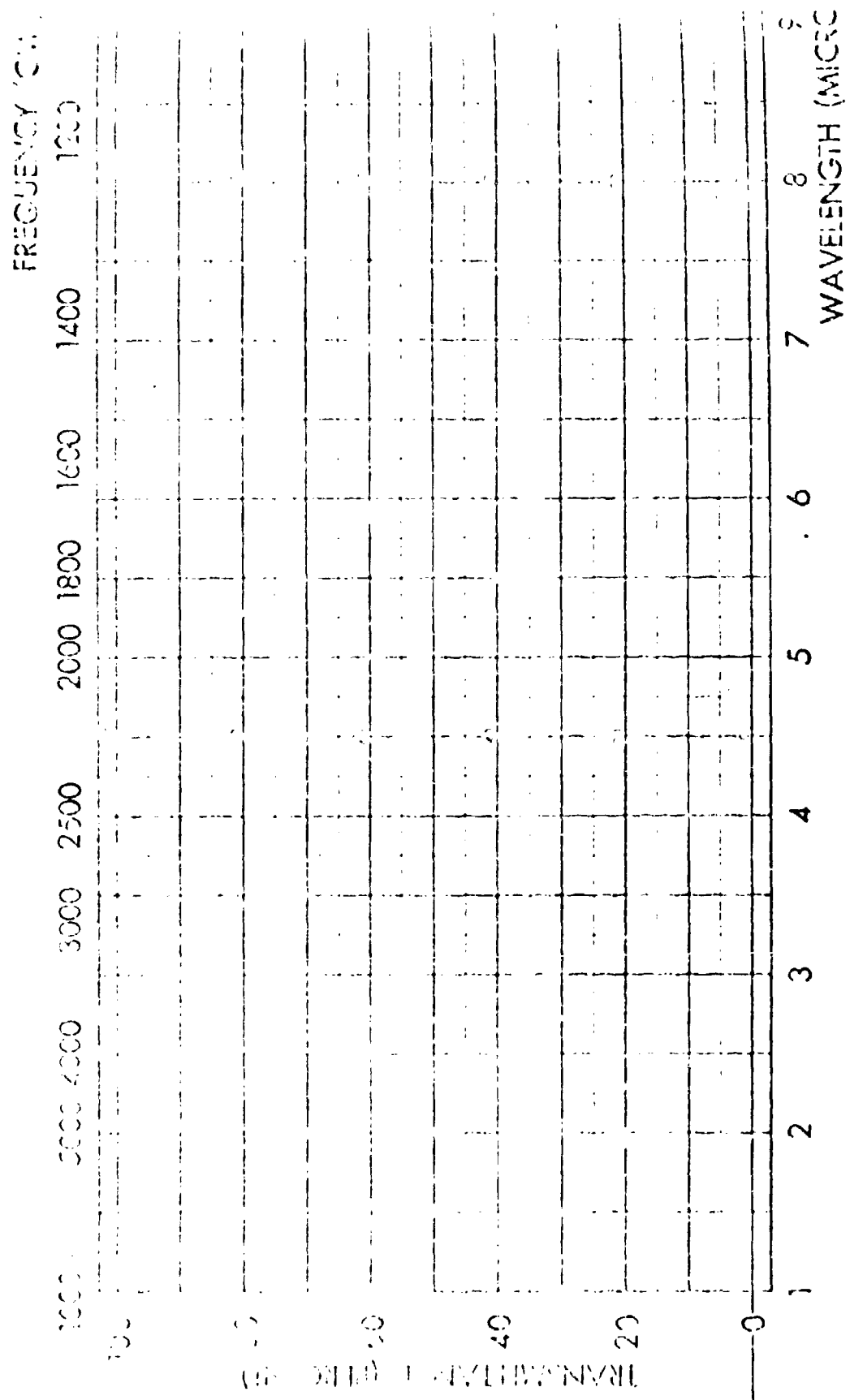
PA.

2. TRANSMISSIVITY OF RADIOMETER WINDOWS

The narrow-angle radiometers were used with sapphire windows. The wide-angle radiometers were used with quartz windows in tests 1 through 11 and sapphire windows in tests 12 through 17. One of the wide-angle radiometers (serial number 56016) was used with an Irtran-4 (ZnSe) window in tests 13 through 17.

In this section are given the transmissivity of various radiometer windows as a function of the wave length of incident radiation.





FREQUENCY (CM⁻¹)

1200

1400

1600

1800

2000

2500

3000

4000

5000

10000

100

20

10

5

2

0

TRANSMITTANCE (%)

WAVELENGTH (MICRONS)

1

2

3

4

5

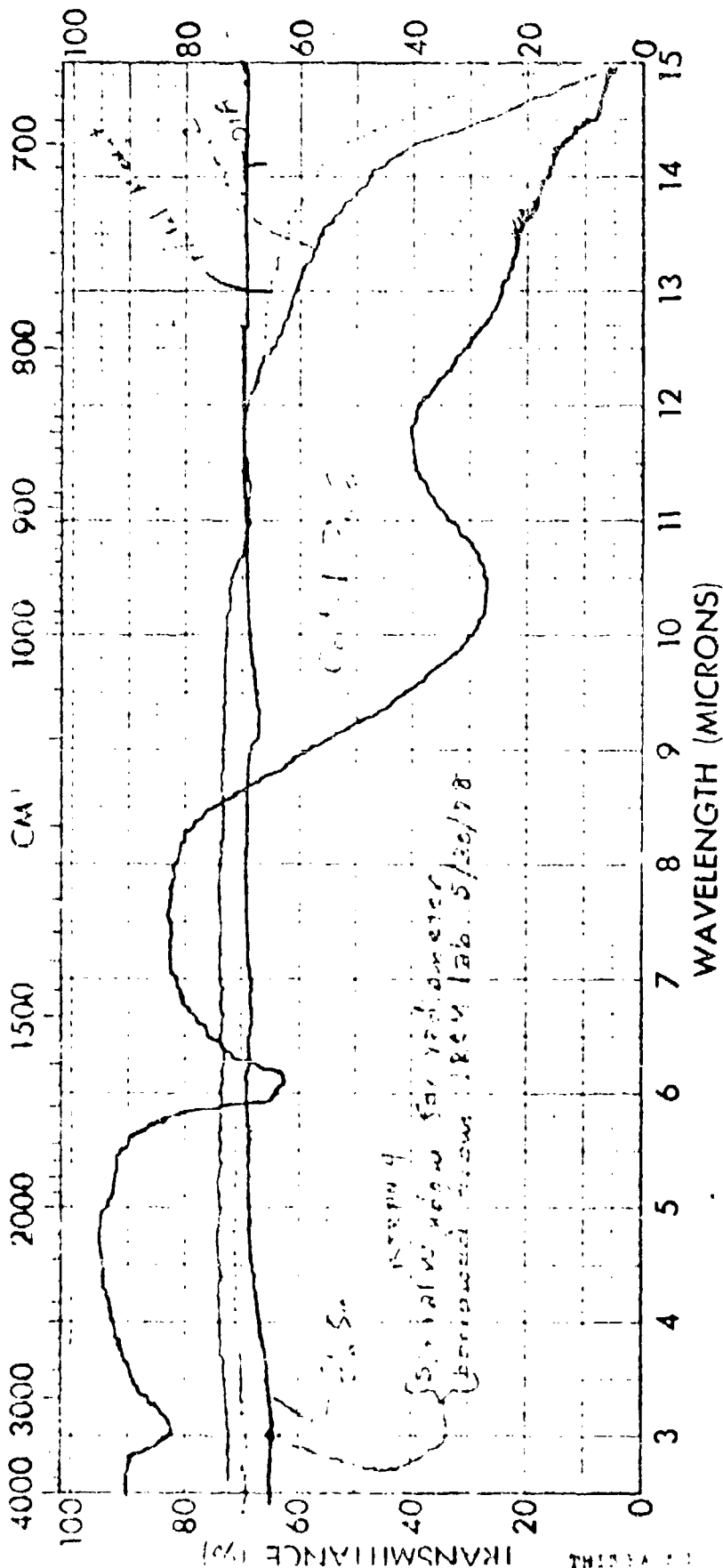
6

7

8

9

WAVELENGTH (MICRONS)

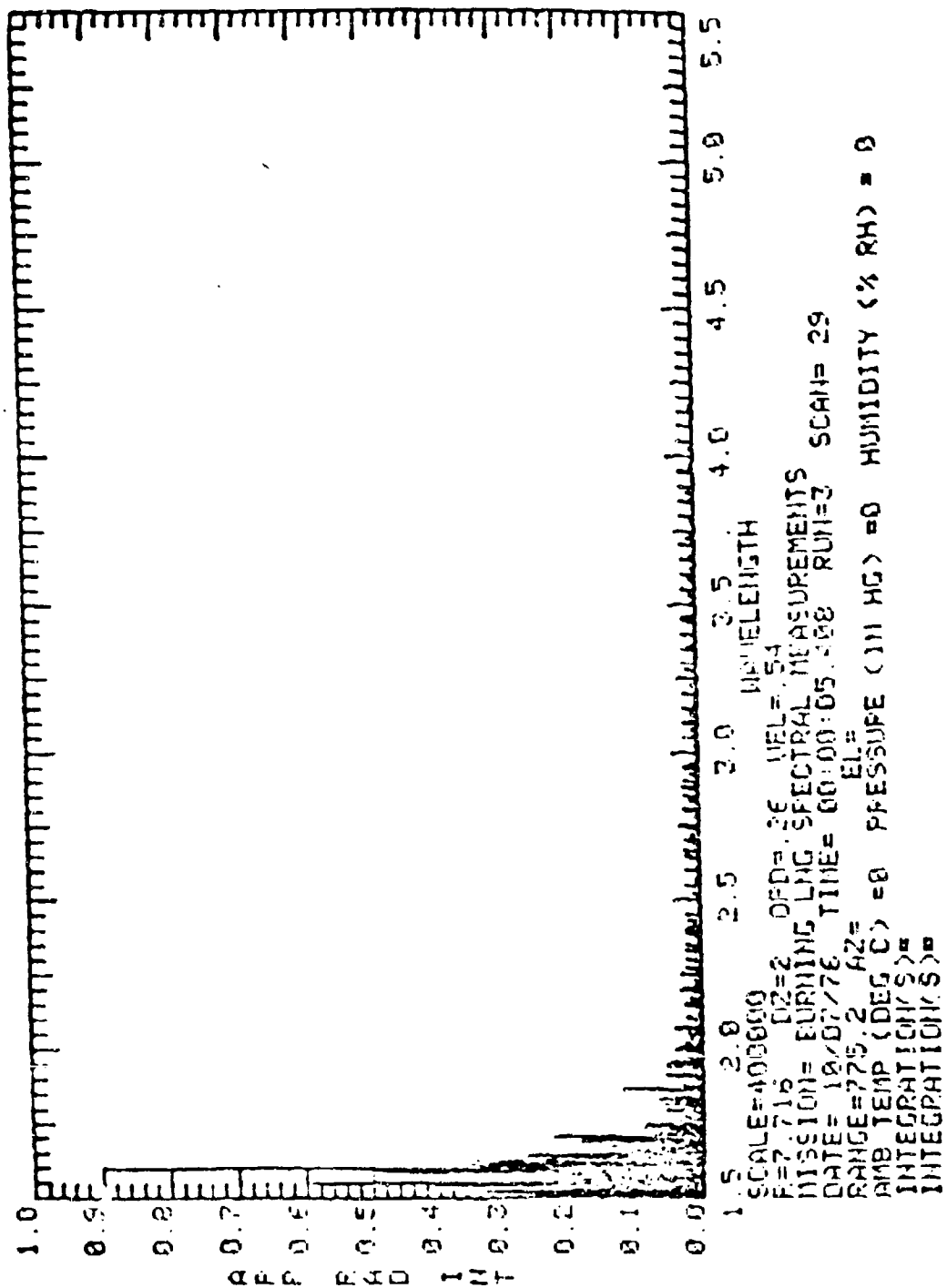


SPECTRUM NO. _____		SAMPLE _____	
ORIGIN _____		LEGEND _____	
PURITY _____		1. _____	
PHASE _____		2. _____	
THICKNESS _____		DATE _____	
_____		OPERATOR _____	
REMARKS _____		REMARKS _____	

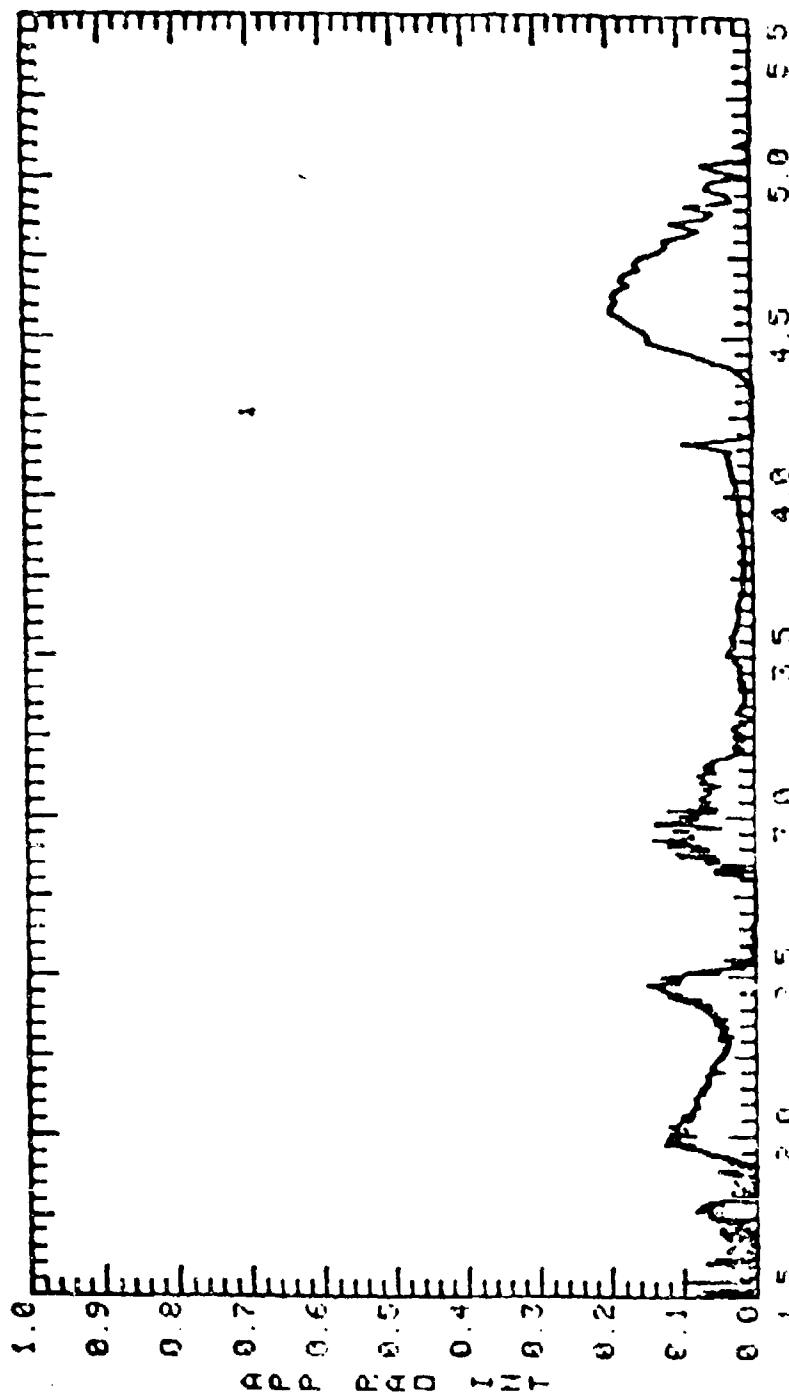
LNG FLAME SPECTRA? DATA

A series of one hundred and twenty eight (128) fast scan spectra was measured during test #5 involving a pool fire on water. The duration of each scan was approximately 0.5 seconds. The spectral range scanned wavelengths from 1.5 μm to 5.5 μm with a resolution of 7.7 cm^{-1} . The data obtained from different scans were reduced at approximately 5 second intervals. Starting with the first at 5.4 s after initiation of ignition.

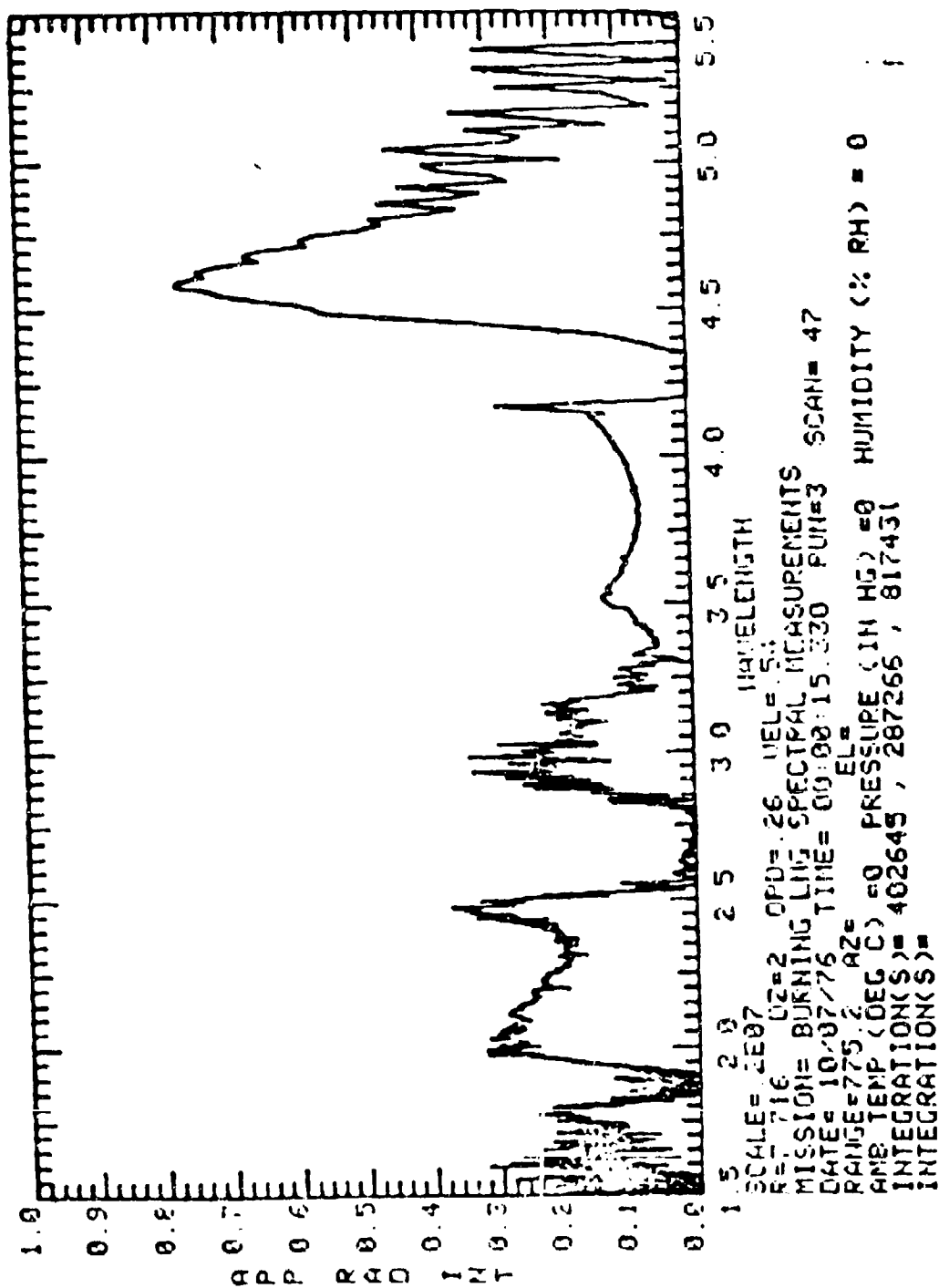
The reduced LNG flame spectra from 5.4 to 60 at 5 seconds intervals (twelve spectra) are indicated in the following pages.



ENCLOSURE (1)

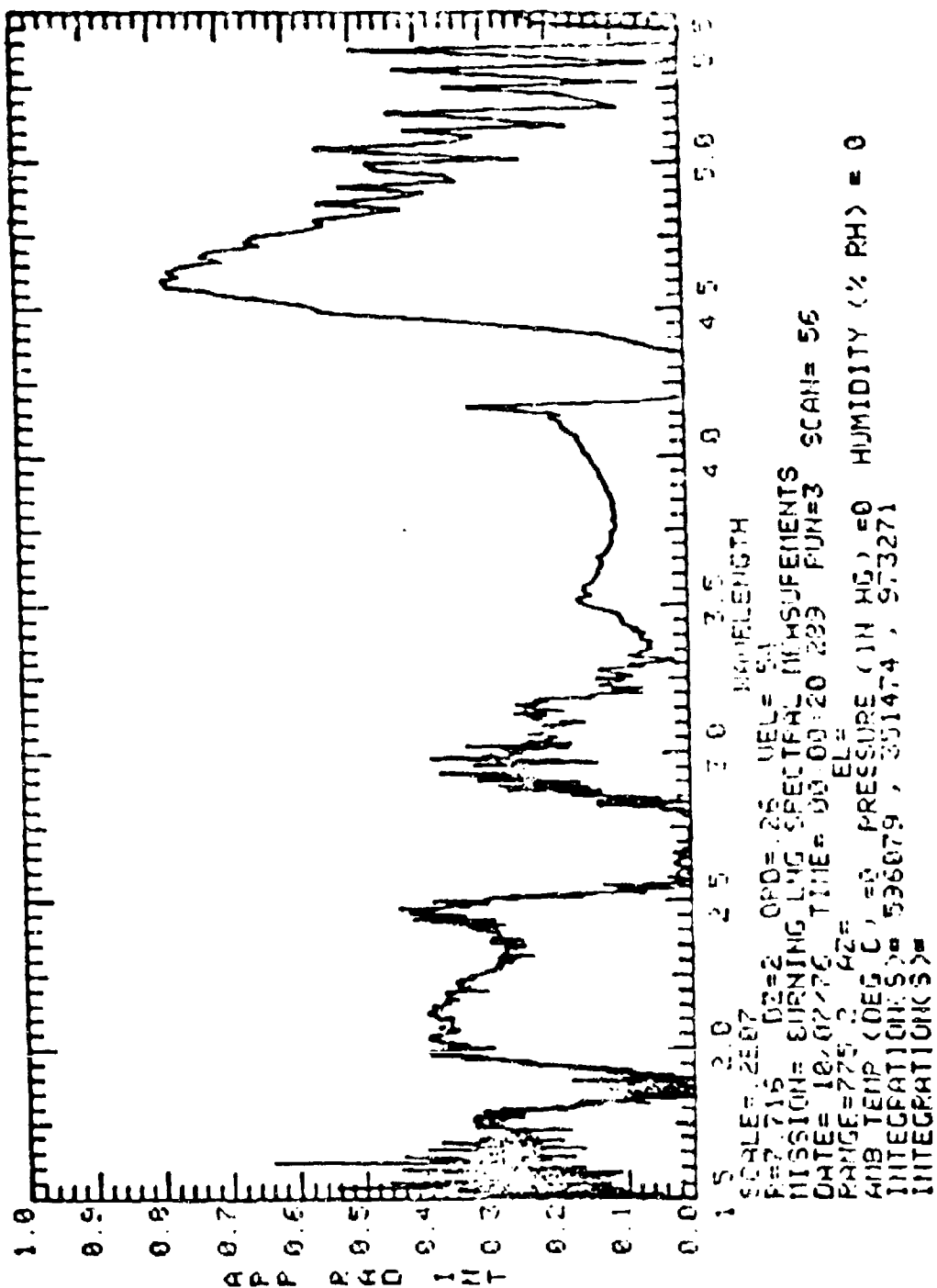


SCALE=2007
 P=7.716 D2=2 OFD=126 WEL=51
 MESSION= PURVING LAG SPECTRAL MEASUREMENTS
 DATE= 10/07/76 TIME= 00:20:10 RUN=3 SCAN= 33
 RANGE=75.2 A2= EL
 AIR TEMP (DEG C) =0 PRESSURE (IN HG) =0 HUMIDITY (% RH) = 0
 INTEGRATION(S)= 112717, 85330.2, 163940
 INTEGRATION(KS)=

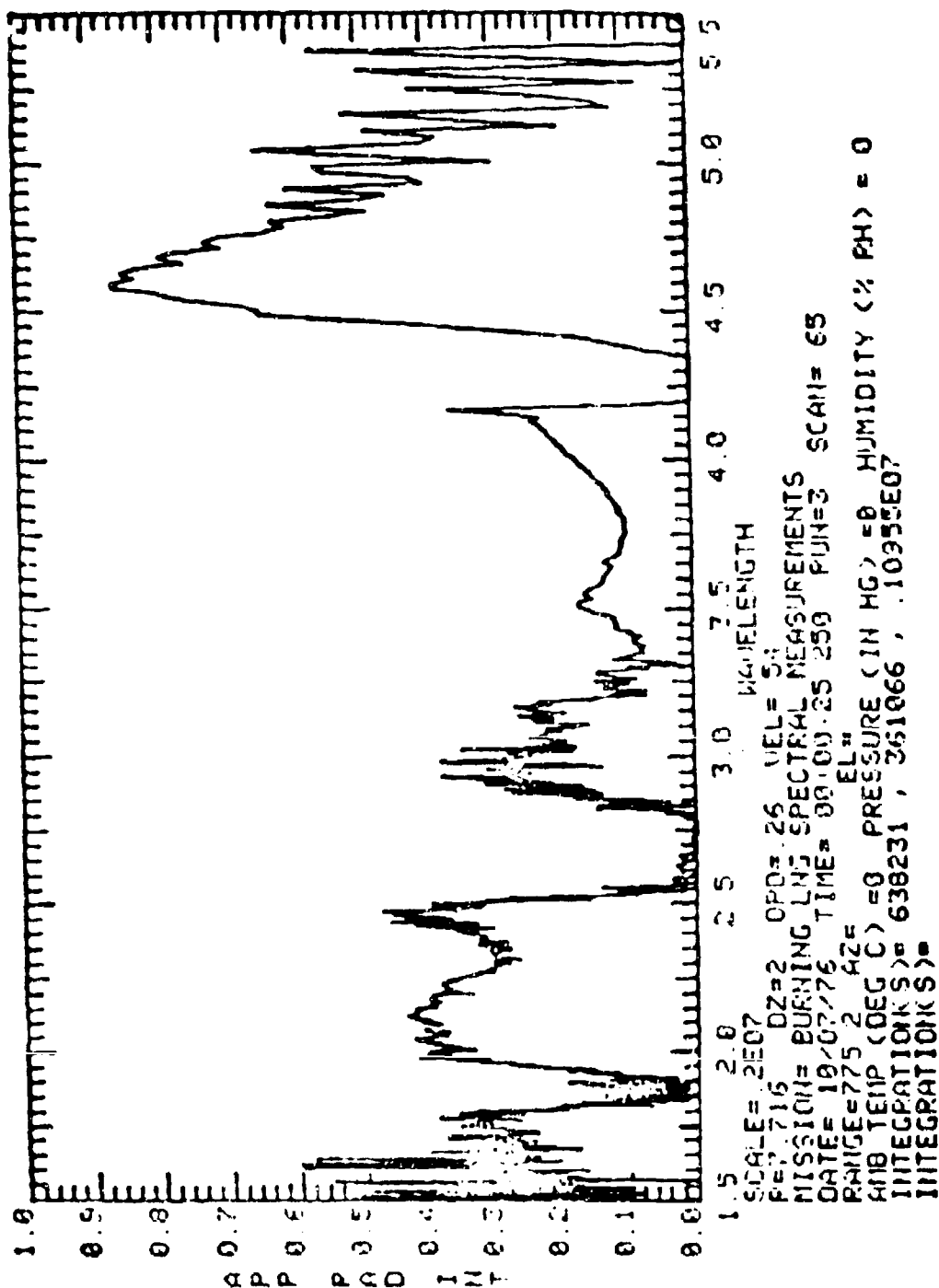


D-18

100% RELATIVE HUMIDITY FLAGGED
 100% RELATIVE HUMIDITY FLAGGED

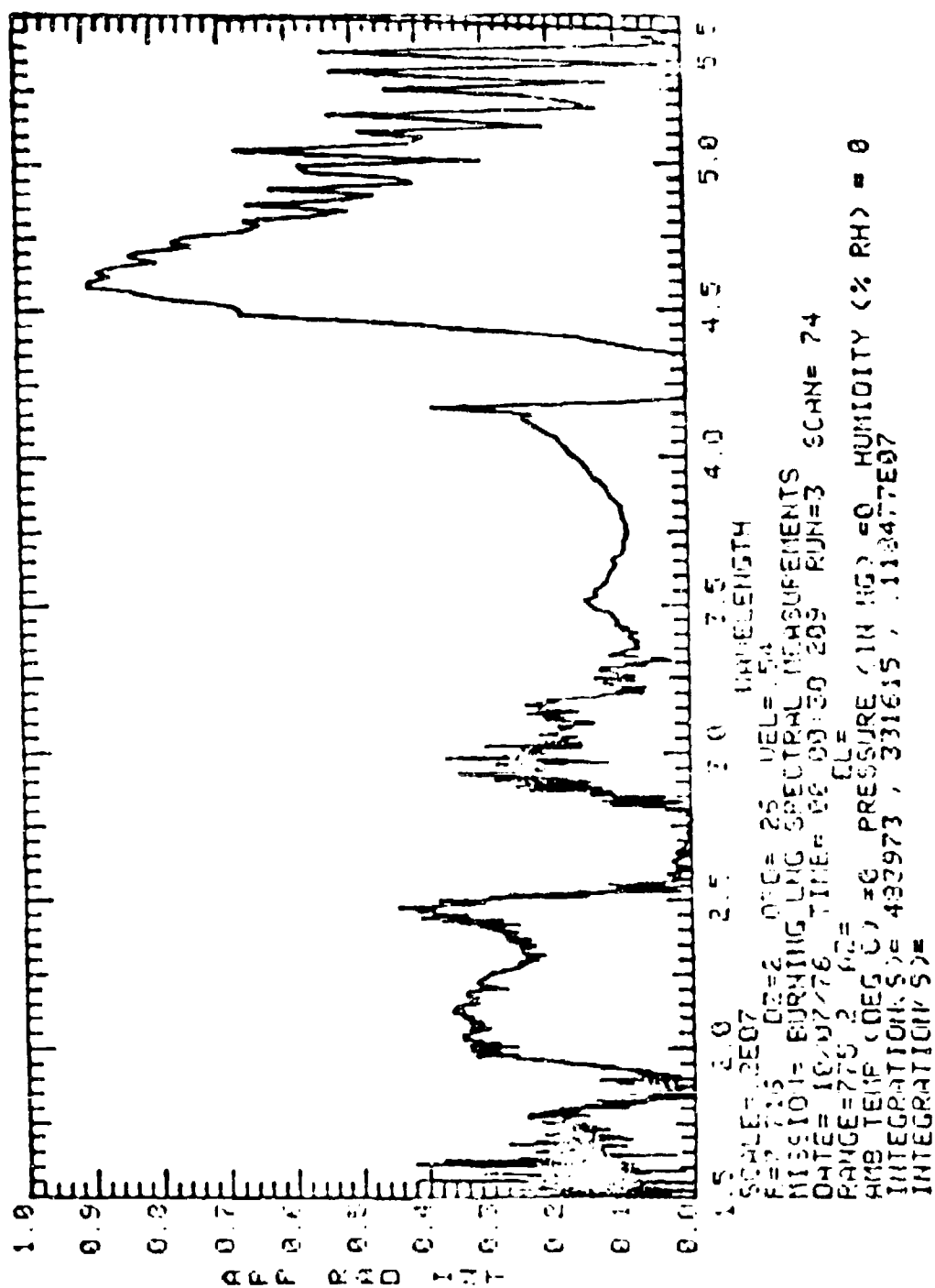


15-00000-1
 15-00000-1
 15-00000-1

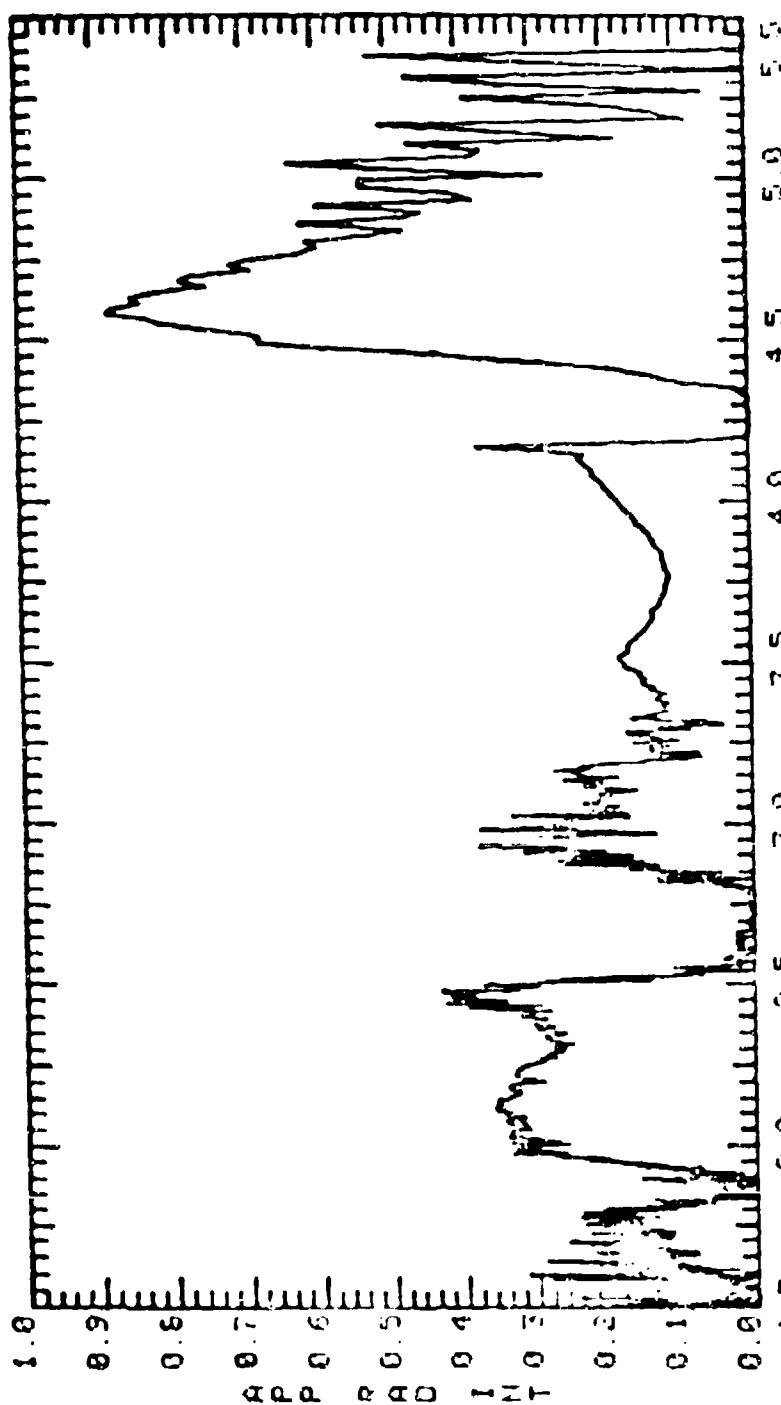


D 20

ADITY PRASAD



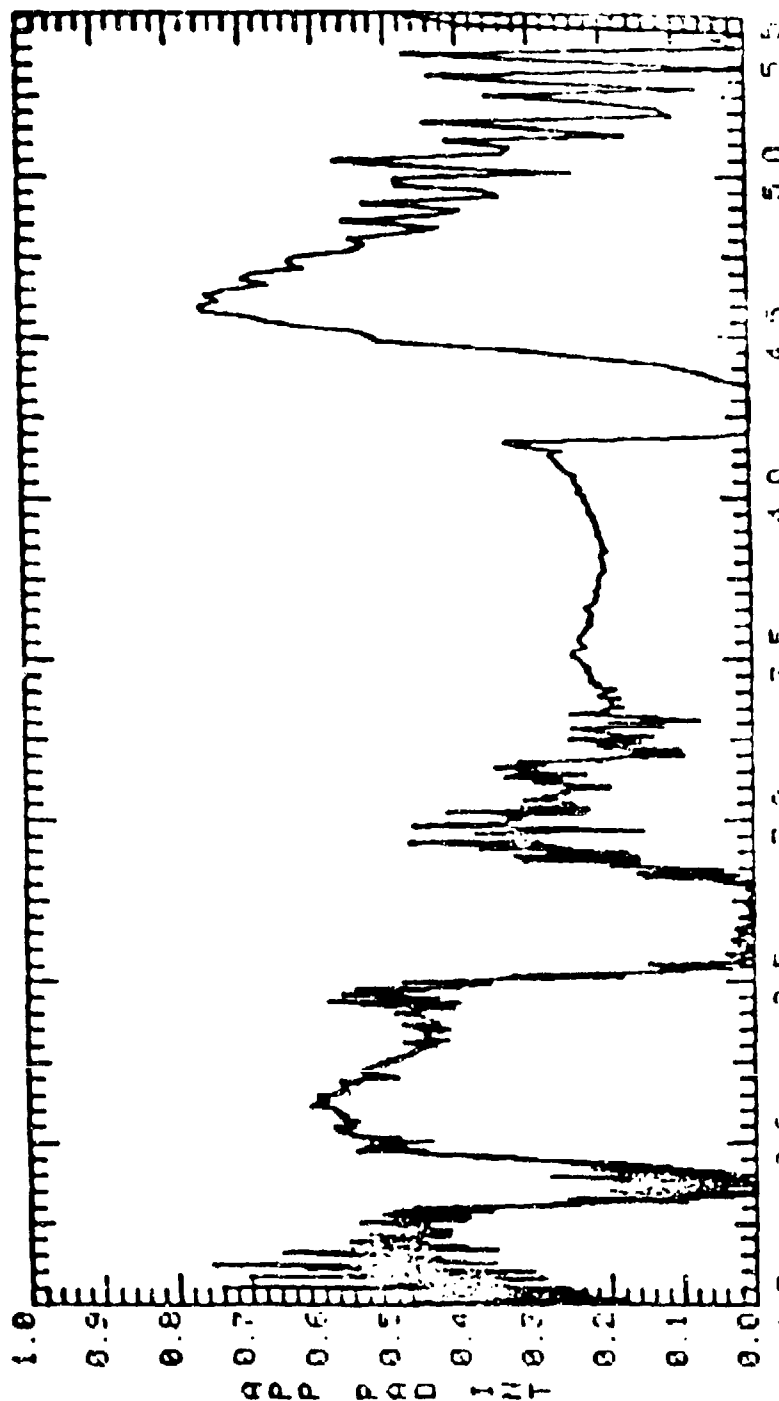
10/07/76 09:00:20
 10/07/76 09:00:20



SCALE=12807
 R=7.15 DZ=2 GFD=26 UEL=5
 MISCION= BURNING LING SPECTRAL MEASUREMENTS
 DATE= 10/07/75 TIME= 00:00:35.169 RUN=3 SCAN= 82
 RANGE=775.2 AZ=
 EL=
 AIR TEMP (DEG C)=0 PRESSURE (IN HG)=0 HUMIDITY (% RH)= 0
 INTEGRATION(S)= 476462 , 367904 , 10985607
 INTEGRATION(S)=

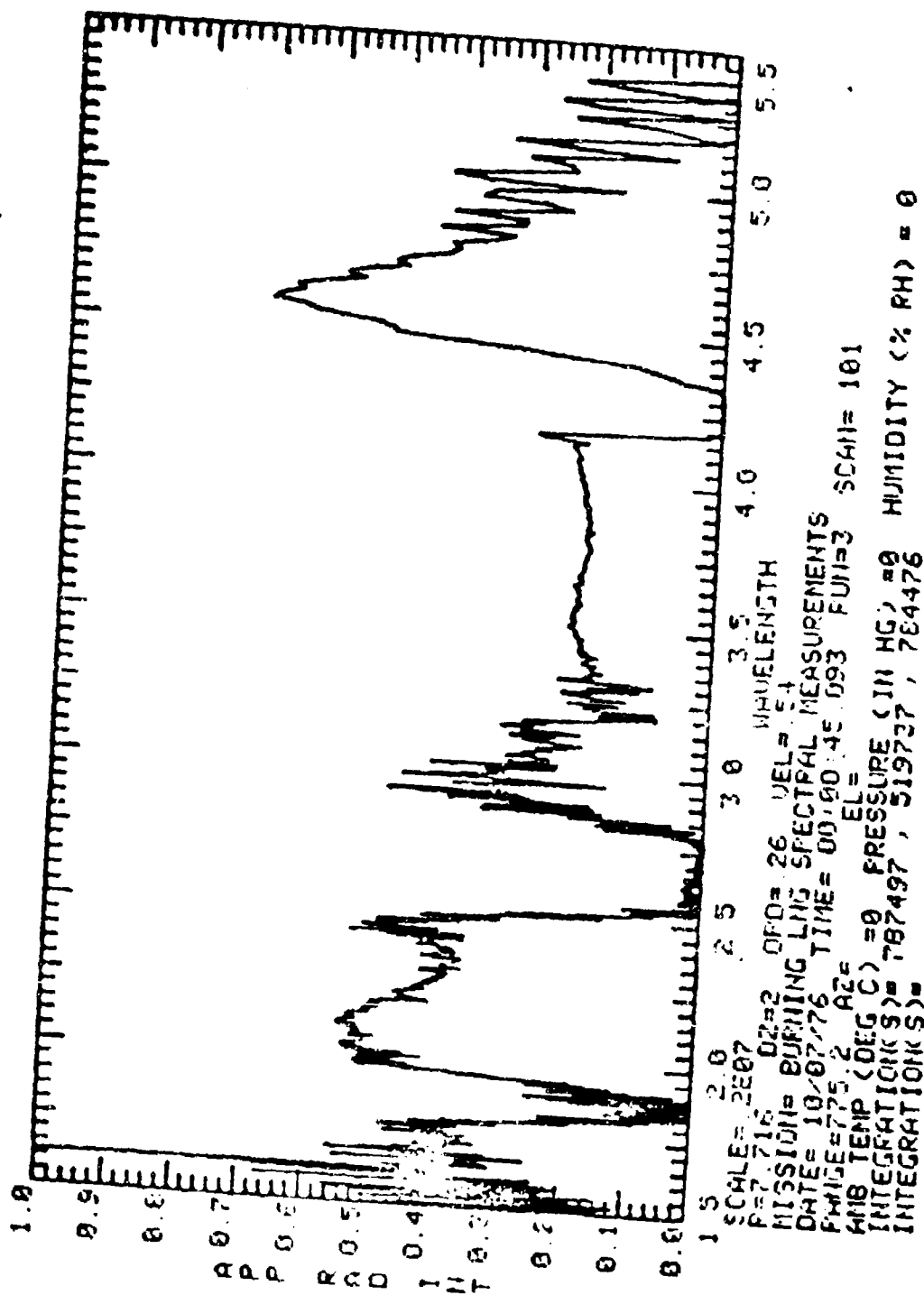
D-12

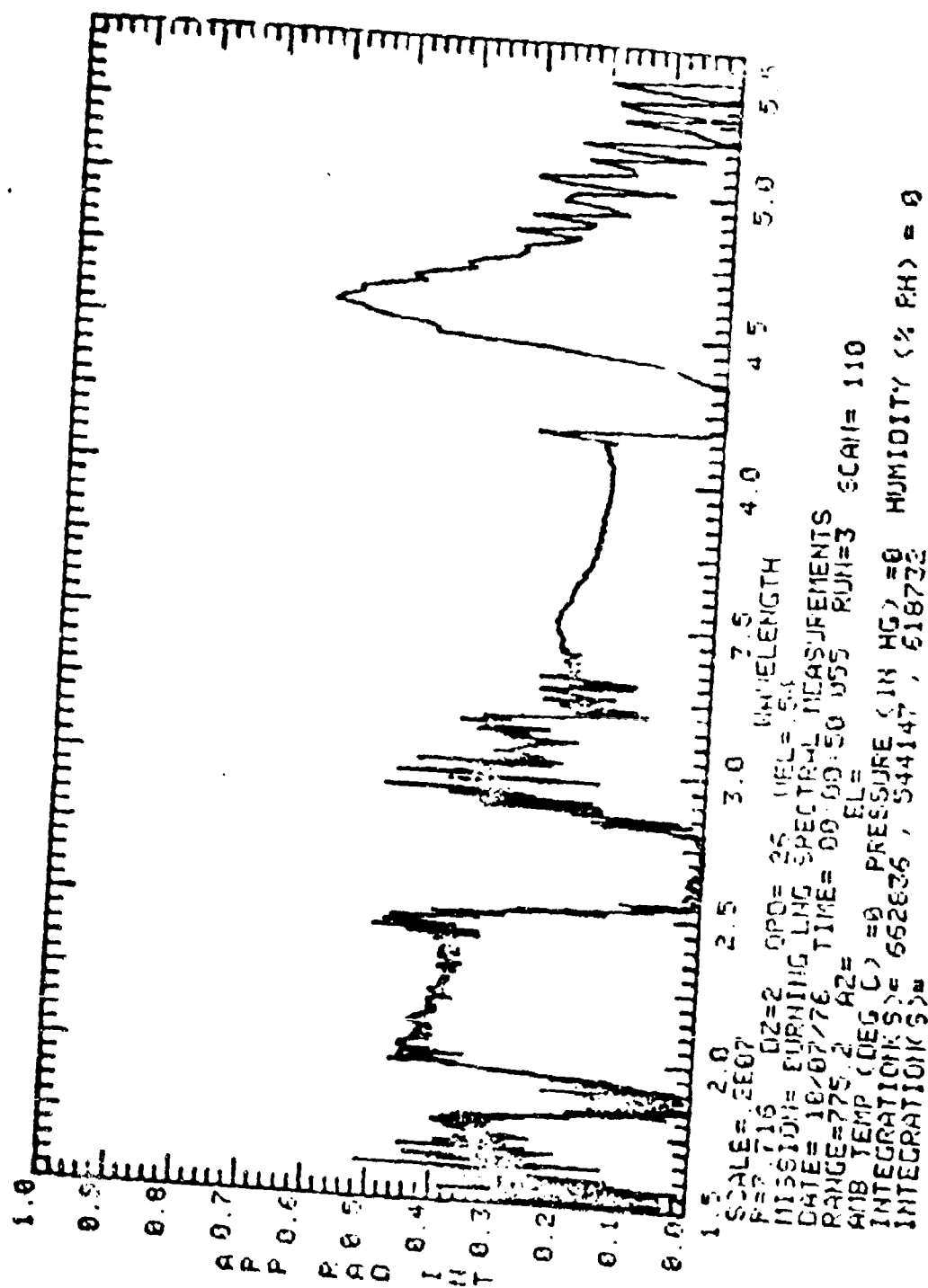
UNIVERSITY OF CALIFORNIA
 LIBRARY
 1975



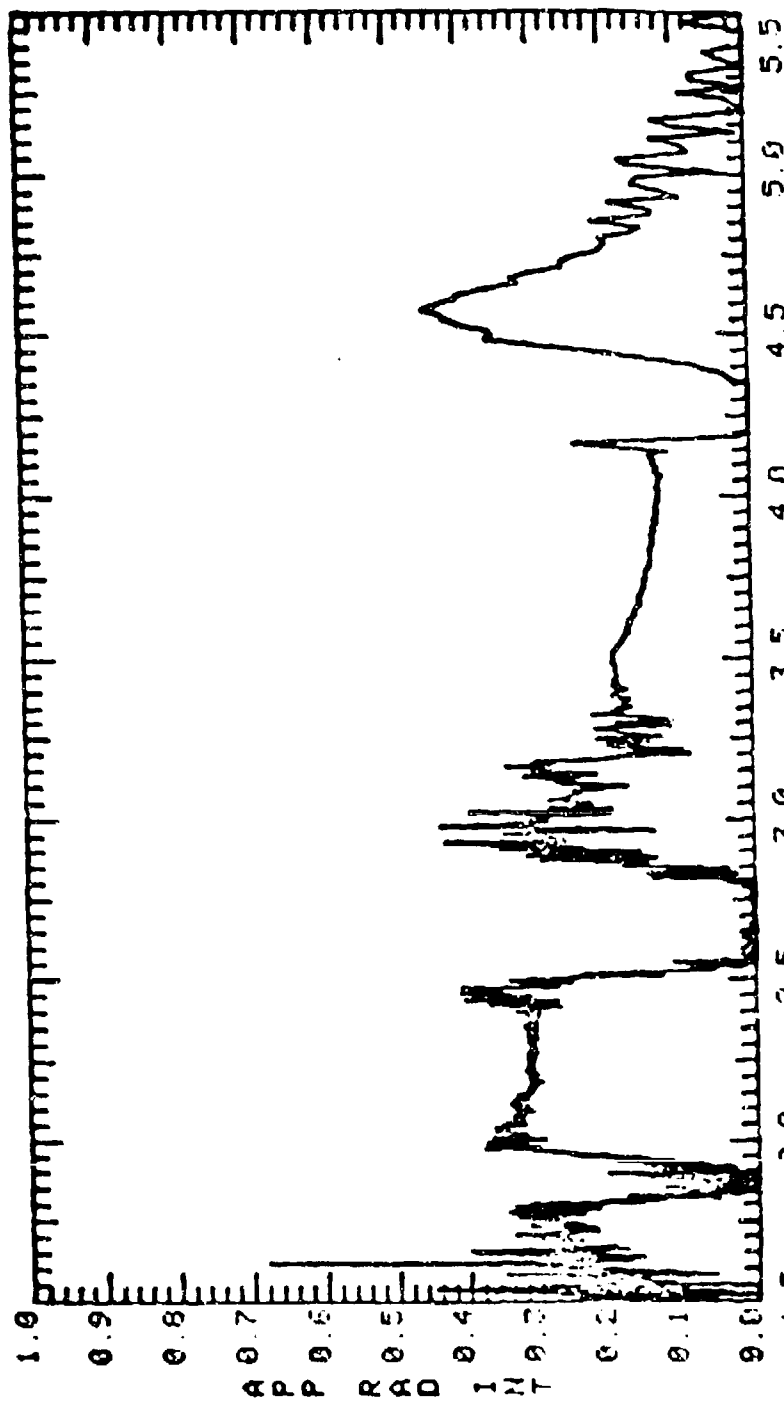
SCALE=2007
 REF=716 QZ=2 QY=28 VEL=70
 MISSION= BURJING LING SPECTRAL MEASUREMENTS
 DATE= 10/07/76 TIME= 00:00:40 RUN=3 SCAN= 92
 PATH=175.2 MZ= EL= 0
 AIR TEMP (DEG C)= 00 PRESSURE (IN HG)= 0 HUMIDITY (% RH)= 0
 INTEGRATION(S)= 902182, 546851, .102527E07
 INTEGRATION(S)=

10/25/76 10:10:10

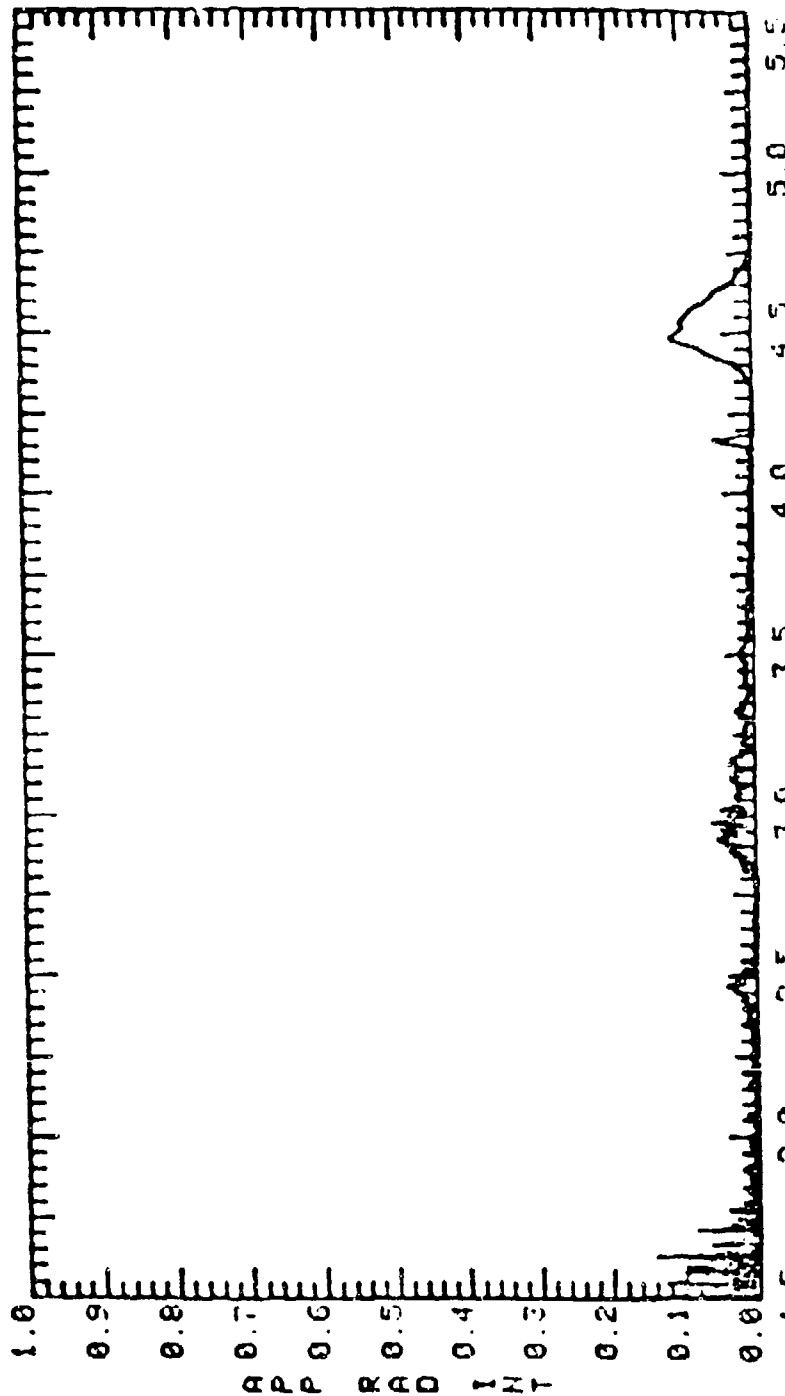




REPORTING TO THE DIRECTOR
 OF THE ARMY



SCALE=12E07
 F=7.716 DZ=2 OPD=26 VEL=54
 MISSION= BURNING LNG SPECTRAL MEASUREMENTS
 DATE= 10/07/76 TIME= 00:00:55.015 FUN=3 SCAN= 119
 RANGE=775.2 KZ= EL=
 AIRB TEMP (DEG C)=0 PRESSURE (IN HG)=0 HUMIDITY (% RH)= 0
 INTEGRATION(S)= 551930 , 245030 , 411342
 INTEGRATION(S)=



Scan No	Time (T+)	Integrations (w/ster)		
		1.5 - 2.6	2.6 - 4.0	4.0 - 5.5
38	10.370	112717	85330.2	163949
47	15.330	402645	287266	817431
56	20.289	596079	351474	973271
65	25.250	638231	361066	1095500
74	30.209	483973	331615	1184770
83	35.169	476462	387904	1086660
92	40.130	902182	546851	1025270
101	45.093	787497	519737	784476
110	50.055	662836	544147	618732
119	55.016	551930	446038	4113-2
128	59.976	19313.7	34852.4	43804

ENCLOSURE (2)

SPC 002 001

